IntechOpen

# Intermetallic Compounds

## Formation and Applications

*Edited by Mahmood Aliofkhazraei*

# INTERMETALLIC COMPOUNDS - FORMATION AND APPLICATIONS

Edited by **Mahmood Aliofkhazraei**

**Intermetallic Compounds - Formation and Applications**
http://dx.doi.org/10.5772/intechopen.68256
Edited by Mahmood Aliofkhazraei

**Contributors**

Muhamad Faiz Md Din, Jianli Wang, Mohd Taufiq Ishak, Núria Cinca, Abdessamad Sekkal, Janusz Cebulski, Dorota Pasek, Adrian Habanyama, Craig Comrie, Magdalena Jabłońska, Williams S. Ebhota, Tien-Chien Jen, Mathias Galetz, Alexander Donchev, Knut E. Aasmundtveit, Thi-Thuy Luu, Hoang-Vu Nguyen, Andreas Larsson, Torleif A. Tollefsen, M. Raviathul Basariya, N. K. Mukhopadhyay



**Notice**



First published in London, United Kingdom, 2018 by IntechOpen
eBook (PDF) Published by IntechOpen, 2019
IntechOpen is the global imprint of INTECHOPEN LIMITED, registered in England and Wales, registration number: 11086078, The Shard, 25th floor, 32 London Bridge Street
London, SE19SG – United Kingdom
Printed in Croatia

British Library Cataloguing-in-Publication Data
A catalogue record for this book is available from the British Library

Additional hard and PDF copies can be obtained from orders@intechopen.com

Intermetallic Compounds - Formation and Applications
Edited by Mahmood Aliofkhazraei

p. cm.

Print ISBN 978-1-78923-178-6

Online ISBN 978-1-78923-179-3

eBook (PDF) ISBN 978-1-83881-298-0

# Meet the editor

Dr. Mahmood Aliofkhazraei works in the corrosion and surface engineering group at the Tarbiat Modares University. He is the head of Aliofkhazraei research group (www.aliofkhazraei.com). Dr. Aliofkhazraei has received several honors, including the Khwarizmi award and the best young nanotechnologist award of Iran. He is a member of the International Association of Corrosion Engineers (NACE International) and International Society of Electrochemistry (ISE). His research focuses on materials science, nanotechnology, and its use in surface and corrosion science.

# Contents

# Preface

Intermetallic compounds are usually brittle with high melting points. Their properties are often found among ceramic and metallic materials. In most cases, their hot corrosion resistance and simultaneously hardness are important. Also their toughness and simplicity of fabrication must be considered. Sometimes intermetallic compounds are used due to their magnetic or superconducting properties. They are also considered in the applications of various novel materials such as hydrogen storage materials. One of the main applications of intermetallic compounds is for superalloy turbine blades in which they show appropriate high-temperature-related properties.

This book collects new developments about intermetallic compounds and their recent usages. I like to appreciate all contributors to this book and thank them for their high-quality manuscripts. I wish open access publishing of this book helps all researchers benefit from this collection.

**Dr. Mahmood Aliofkhazraei**
Tarbiat Modares University
Iran

Chapter 1

# FeAl Intermetallic Alloy: Its Heat-Resistant and Practical Application

Janusz Cebulski and Dorota Pasek

Additional information is available at the end of the chapter

http://dx.doi.org/10.5772/intechopen.73184

**Abstract**

Intermetallic phases, as a group of materials which have a great practical importance, both in the past and in the present day, are subject of research on the basis of physicochemical and mechanical properties. The presented studies were conducted for Fe40Al5Cr0.2TiB intermetallic alloy, their purpose was to determine the corrosion resistance of this alloy in an oxidizing environment, at temperatures up to 1373 K. The test material was made of Fe40Al5Cr0.2TiB intermetallic alloy after plastic processing. The kinetics of corrosion, allotropic variants according to the temperature of the process and the surface condition after corrosion were determined during the study. Based on the results obtained, the verification was performed under operating conditions. Taking into account the properties of the FeAl alloys, the working conditions and material requirements of turbochargers, studies have been undertaken to determine the possibility of the use of Fe40Al5Cr0.2TiB intermetallic alloys for components of the hot turbocharger of the automobile with compression ignition engines. The components of the hot turbocharger parts were used from the test material. The tests distance of turbocharger was 80,000 km.

**Keywords:** FeAl, corrosion, high temperature, application, $Al_2O_3$ layer

## 1. Introduction

Introducing the new materials to industrial practice enables us to build more and more durable and reliable components for machines and equipment that are suitable for use in high temperature and other special conditions. Undoubtedly, this group of innovative and advanced construction materials introduced over the past 30 years includes intermetallic alloys [1] The wide interest in these alloys is mainly due to their unique properties, which in particular include: excellent oxidation, carburizing and sulphate resistance, good corrosion resistance in seawater and melted salts, high resistivity at room temperature (which also increases with

the increase of temperature), as well as high abrasion, erosion and cavitation resistance [2–4]. So much interest in FeAl alloys is due to the fact that during the high temperature processes in the oxidizing atmospheres a protective layer of aluminum oxide is formed on the surface of these materials forms. The layer prevents the degradation of the metallic core. These materials can therefore be used as construction material for working in the atmospheric industrial gases, contaminated with $SO_2$, $O_2$ and steam [5].

Bystrzycki and others asserted that a set of favorable properties induces the use of intermetallic alloys as a material working at elevated temperatures in industrial atmosphere. The limitation may, however, be the fragility of these materials [6].

The structure of the alloy is stable however the presence of a pro-eutectoid phase in FeAl leads to a deterioration in the creep resistance [7].

As one of the major limitations of the practical application of FeAl alloys is their low plasticity (which makes it impossible to process with conventional methods). In the first step, FeAl alloys were focused on the feasibility of alloys. The result of this work was a doctoral thesis entitled "Ways to increase the plasticity of the alloy on the matrix of FeAl" [8]. The positive results of the conducted research became the inspiration for further research and development of these materials. The result of the study was the determination of corrosion resistance in a liquid environment, but above all resistance to high temperature gas corrosion. The next step was to verify the results obtained under real-life conditions in turbocharged performance tests where some components were made from FeAl [9, 10]. Alloys of aluminum and iron intermetallic compounds are considered to be future-proof materials for applications in environments with high temperature corrosion, due to their good oxidation resistance (especially in an environment containing sulfur and chlorine). This has been confirmed by the results of the research presented in this paper.

The initial development of research concerning of the Fe-Al intermetallic alloys was aimed at modifying them with suitable alloying elements, such as zirconium, yttrium, boron, manganese, chromium, vanadium, titanium, cobalt and nickel. The research of modified intermetallic alloys with a variety of modifying elements has been conducted by numerous research centres around the world. It has been found that the most effective additives that improve the strength of intermetallic alloys at elevated temperatures and also plasticity and corrosion resistance both for isothermal and cyclic oxidation were: zirconium, boron and fine dispersion of $Y_2O_3$. Furthermore, the positive effects of alloying additives, both in oxygen and aggressive oxygen and sulfur-containing gas mixtures, on the kinetics of oxidation of intermetallic alloys have been found. The results, obtained by numerous authors, clearly demonstrate the slowdown of the process of the $Al_2O_3$ scale development due to the modification of the FeAl phase with the appropriate amount of the element. The addition of Cr and Ti results in an increasing of the Fe-Al oxidation rate during the early stages of the reaction, but these additives have improved the adhesion of the scale and the morphology. In addition, they reduced the reaction rate for long periods [11–13].

For the FeAl alloys, elements of bathtubs for bath aluminizing and grate bars for furnaces (which have successfully passed long-term operating tests at 1273 K) are already being made [4]. Practical applications also include intermetallic (FeAl) pallets and racks for furnaces used in heat-chemical treatment as well as rails for roller hearth furnaces and rolls for transporting hot rolled steel sheets [1, 4].

## 2. Oxidation kinetics and $Al_2O_3$ morphology after heat-resistance tests

The test material was made of Fe40Al5Cr0.2TiB intermetallic alloy after plastic processing. The smelting process was carried out under vacuum. To homogenize the chemical composition, homogenizing annealing was performed at a temperature of 1323 K for 72 h. The resulting material was plastically extruded to improve the mechanical properties of the alloy for practical application. Fine-tuning was carried out using a proprietary technology that is patentable. The developed method makes it possible to perform reprocessing of hard-to-change materials in a repetitive manner without cracks [14].The chemical composition of the test alloy is shown in **Table 1**.

The oxidation kinetics of the Fe40Al5Cr0.2TiB intermetallic alloy at 1173, 1223, 1273 and 1373 K for 500 h is shown in **Figures 1** and **2**. The processes of complex diffusion in the Fe40Al5Cr0.2TiB intermetallic alloy and the aluminum oxide layer determine the speed of the process. The kinetics studies (**Figures 1** and **2**) show that the process is parabolic in accordance with the relation $dX/dt = k'_p\,(t)/X$. The measured rates of reaction did not strictly reflect this law, i.e. at constant temperature $k'_p = f(t) \neq const$ deviations from the standard parabolic equation result from the formation of different $Al_2O_3$ oxide variants, grain growth and / or formation of mixed oxides that appear during the oxidation reaction. Thus, in spite of the above limitations, it is convenient to approximate the reaction rates to the classical formula (Eq. (1)):

$$x^2 - layer\ thickness,\ cm^2 \quad 2k'_p - constant\ rate\ of\ oxidation,\ \frac{cm^2}{s} \quad t - time,\ s \tag{1}$$

**Table 2** shows constants of the oxidation rate for the respective process temperatures, values of which correspond to the parabolic oxidation course (**Figures 1** and **2**).

The research on corrosion products made with scanning electron microscope is presented in **Figures 3–10**. The type of oxides on the surface of oxidized samples was determined by X-ray phase analysis. The results are shown in **Figures 11–13**. At a temperature of 1173 K, the $\alpha$ and $\theta$ form of $Al_2O_3$ oxides were observed (**Figure 11**). After oxidation at a temperature of 1273 K, a small amount of metastable $\theta - Al_2O_3$ and a stable $\alpha - Al_2O_3$ form of oxides were observed (**Figure 12**). Only stable $\alpha$-$Al_2O_3$ is present at 1373 K (**Figure 13**). The growth rate of $Al_2O_3$ scale, in the palaces where it has lost contact with the alloy, is similar to places that where the contact remains. This phenomenon occurs because the rate of evaporation of aluminum from the surface of the metallic phase and its transport in the gas phase towards the inner surface of the scale is faster than diffusion of oxygen through the $Al_2O_3$ scale. The whiskers appear on the surface of $Al_2O_3$ scale. This effect is related to the presence of compression stresses in the oxide, which are formed under isothermal conditions following the transverse growth phenomenon. Despite the presence of Fe and Cr in the alloys, the created oxides of these metals

| Fe40Al5Cr0.2TiB | Fe | Al | Cr | Ti | B |
|---|---|---|---|---|---|
| % Mass | 68.21 | 23.66 | 5.77 | 0.15 | 0.015 |

**Table 1.** Chemical composition Fe40Al5Cr0.2TiB alloy.

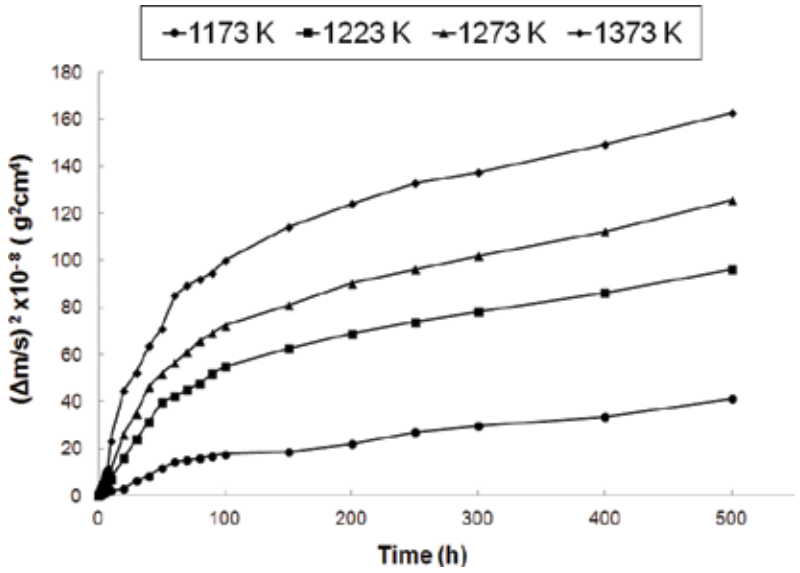


**Figure 1.** The total weight gain (sample + chips oxide in the crucible) measured after oxidation.

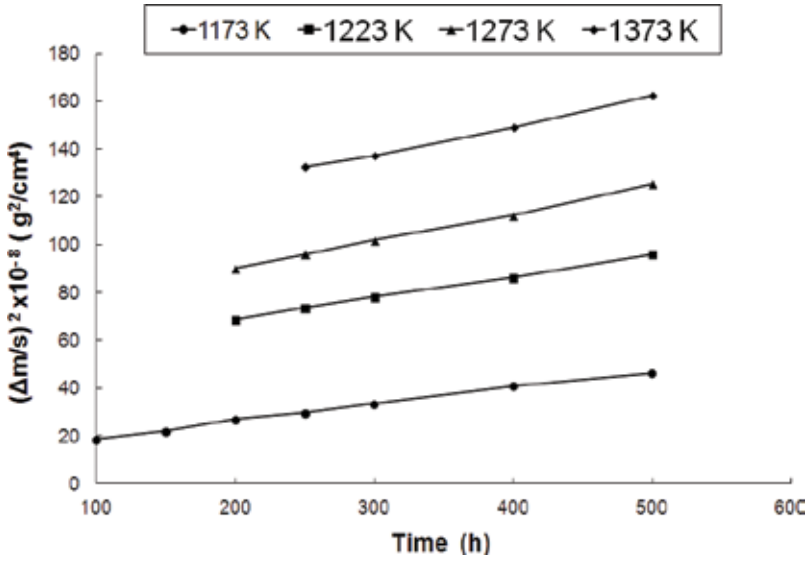


**Figure 2.** The change in mass intermetallic alloy Fe40Al5Cr0.2TiB in time to 500 h in parabolic coordinates.

have several orders of magnitude higher compressibility decomposition than the oxides forming the protective scale of $Al_2O_3$. For this reason, Al in the Fe40Al5Cr0.2TiB intermetallic alloy can be selectively oxidized to stable form of $Al_2O_3$ oxides on the melt surface. From a thermodynamic point of view, the only protective oxide that is likely to form as a stable layer on the Fe40Al5Cr0.2TiB intermetallic alloy is $Al_2O_3$ [15].

| Temperature [K] | $k_p''$ [$g^2 \cdot cm^{-4} \cdot s^{-1}$] |
|---|---|
| 1173 | $1.93 \cdot 10^{-13}$/100–500 h |
| 1223 | $2.51 \cdot 10^{-13}$/200–500 h |
| 1273 | $3.26 \cdot 10^{-13}$/200–500 h |
| 1373 | $3.30 \cdot 10^{-13}$/250–500 h |

**Table 2.** Kp″ constant values for the Fe40A5Cr0.2TiB intermetallic alloy.

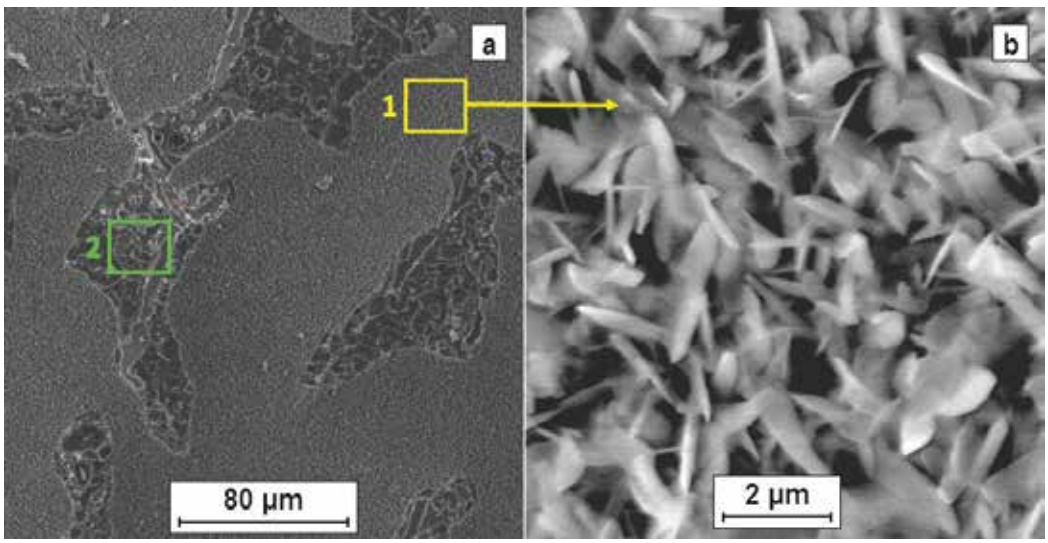


**Figure 3.** The surface condition of the sample after the corrosion tests at 1173 K for 100 h: a – oxidized surface, b – formed on the surface morphology of the oxide.

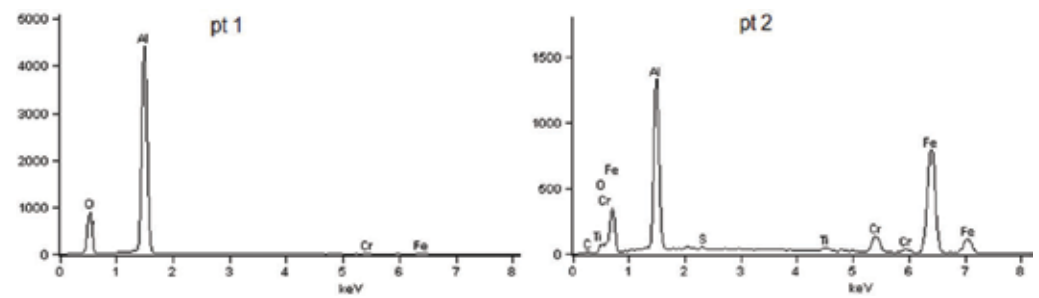


**Figure 4.** X-ray microanalysis of the chemical composition of the areas indicated on the sample surface after corrosion research at 1173 K for 100 h.

The structure and growth mechanism of the protective $Al_2O_3$ scale on heat-resistant alloys depends to a great extent on the type of metal in the matrix. Alloys on the FeAl intermetallic phase throughout the entire temperature range remain single phase. For this reason, the $Al_2O_3$

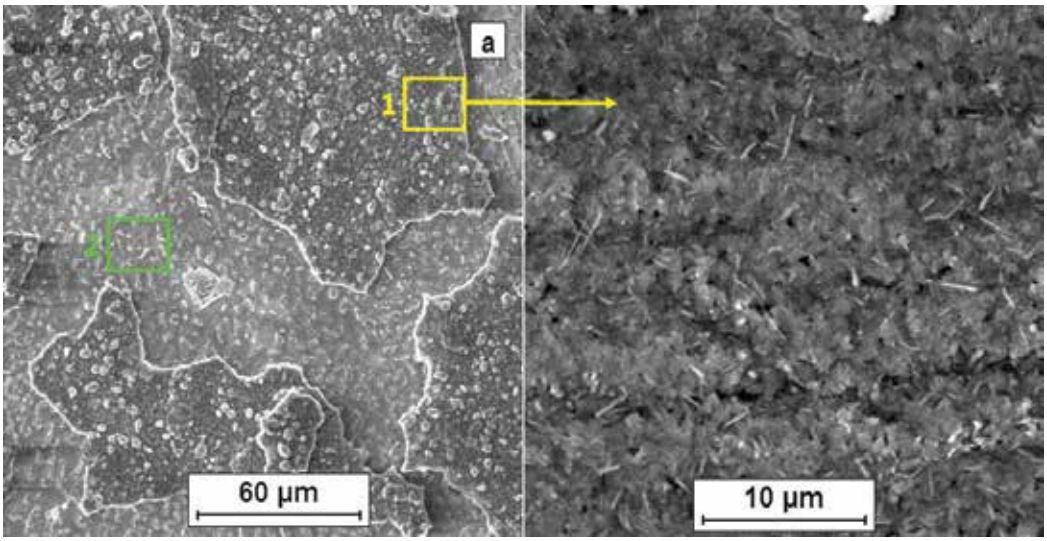


**Figure 5.** The surface condition of the sample after the corrosion tests at 1223 K for 100 h: a – oxidized surface, b – formed on the surface morphology of the oxide.

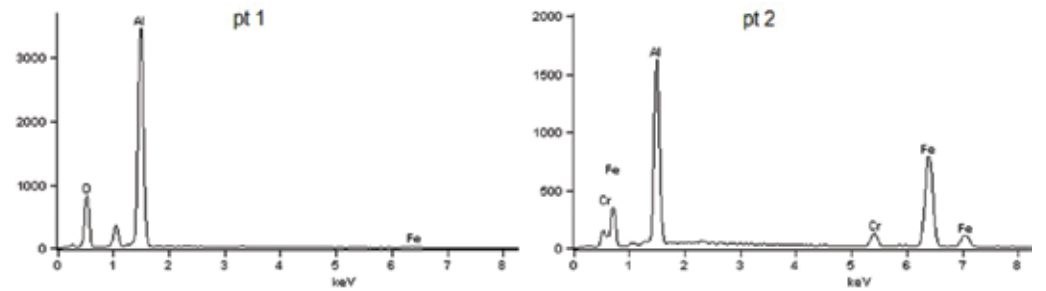


**Figure 6.** X-ray microanalysis of the chemical composition of the areas indicated on the sample surface after corrosion research at 1223 K for 100 h.

layer is formed throughout its surface at the time of contact of the hot metallic phase with oxygen, regardless of temperature.

The thermal expansion of the alloy affects the level of stress that forms between the oxide and the metallic phase during temperature changes. Relaxation of these stresses can occur when the oxide layer comes off the metallic substrate.

The phase composition of the $Al_2O_3$ scale, which is formed on the alloys and intermetallic phases on the iron matrix, is influenced by: their chemical composition, the crystallographic structure of the metallic substrate and the temperature at which the oxidation process is carried out. Within the temperature range of 1073–1223 K, in the initial oxidation state, on the surface of many iron alloys, especially the FeAl intermetallic phase, an increase in metastable alumina $\theta$, $\gamma$ and $\delta$ is observed. After a period of time, a protective layer from the $\alpha$-$Al_2O_3$ phase is produced. The addition of chromium to the FeAl alloy accelerates the phase transformation $\theta \rightarrow \alpha$ and increases its corrosion resistance [16–18].

http://dx.doi.org/10.5772/intechopen.73184

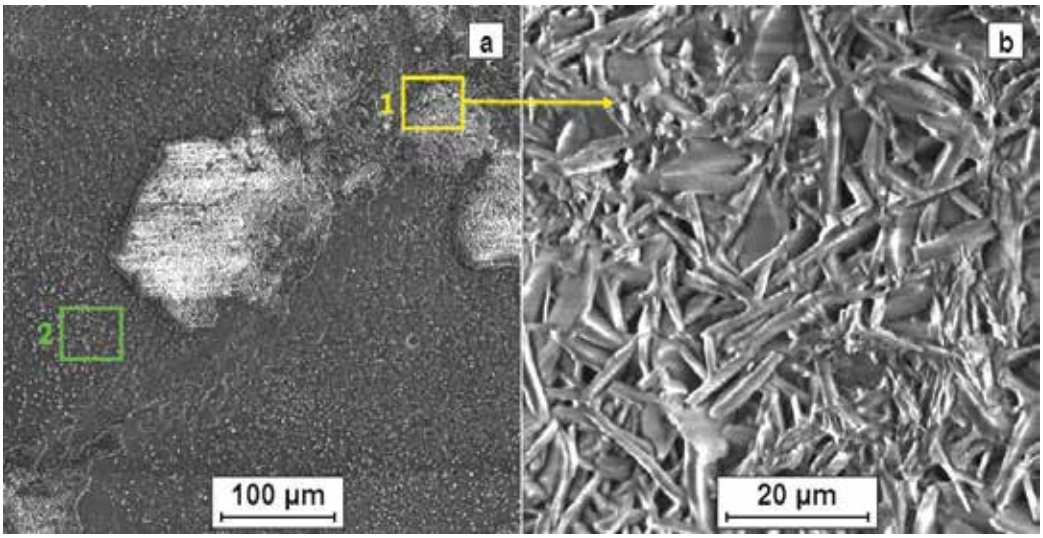


**Figure 7.** The surface condition of the sample after the corrosion tests at 1273 K for 100 h: a – oxidized surface, b – formed on the surface morphology of the oxide.

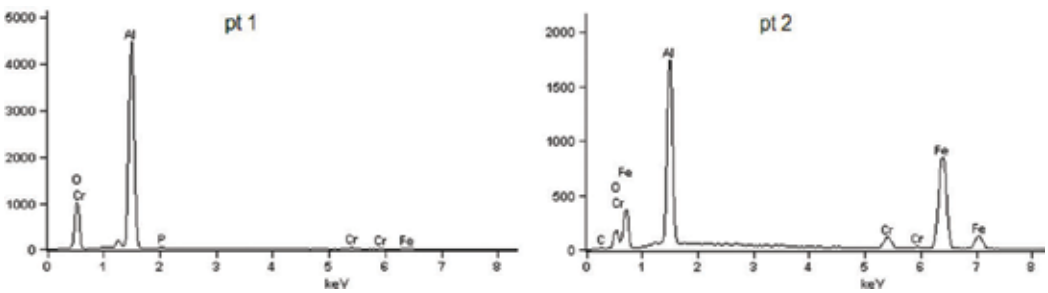


**Figure 8.** X-ray microanalysis of the chemical composition of the areas indicated on the sample surface after corrosion research at 1273 K for 100 h.

One hypothesis assumes that the growth of metastable phases is related to the phenomenon of epitaxia.

Most of the metallic phases as well as metastable alumina crystallize in the regular grid, whereas alumina – in the hexagonal network. The growth velocity of the θ-$Al_2O_3$ phase is larger by one order of magnitude than in the case of $\alpha$-$Al_2O_3$ phase, and its increase occurs as a result of core metal diffusion and depends on the concentration of vacancies in the cation subnetwork. The period of time required to form the continuous $\alpha$-$Al_2O_3$ layer is reduced with increase of oxidation temperature [19].

The morphology of $Al_2O_3$ oxides varies depending on the process temperature: from the needles appearing at 1173 K to the oxides in the form of grains at 1373 K.

The θ-$Al_2O_3$ phase grows on FeAl alloys in the form of lamellar grains allowing the external surface of the scale to become strongly developed. Transformation of metastable alumina phases into the $\alpha$-$Al_2O_3$ phase starts at the metal-oxide border [18, 19]. This transformation is

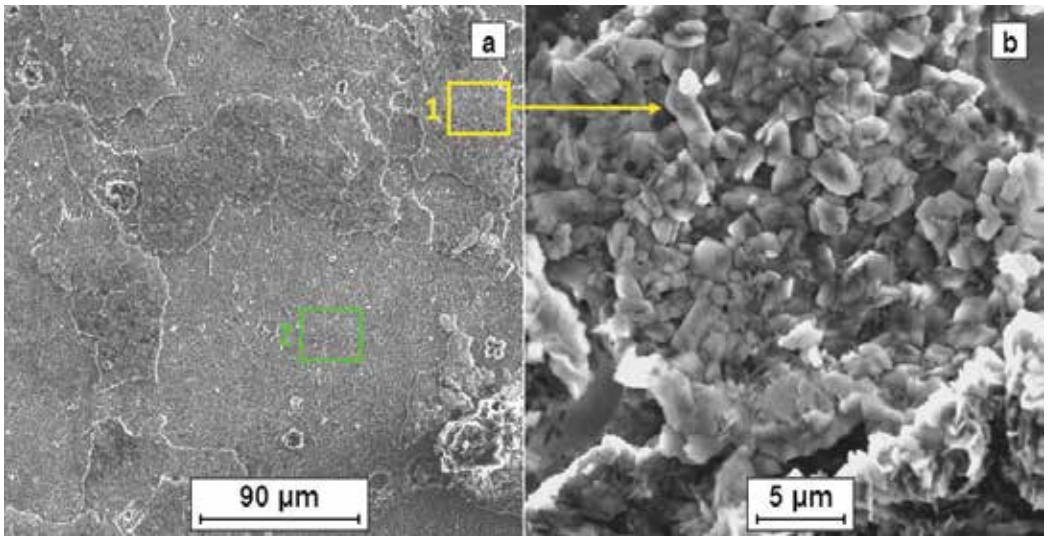


**Figure 9.** The surface condition of the sample after the corrosion tests at 1373 K for 100 h: a – oxidized surface, b – formed on the surface morphology of the oxide.

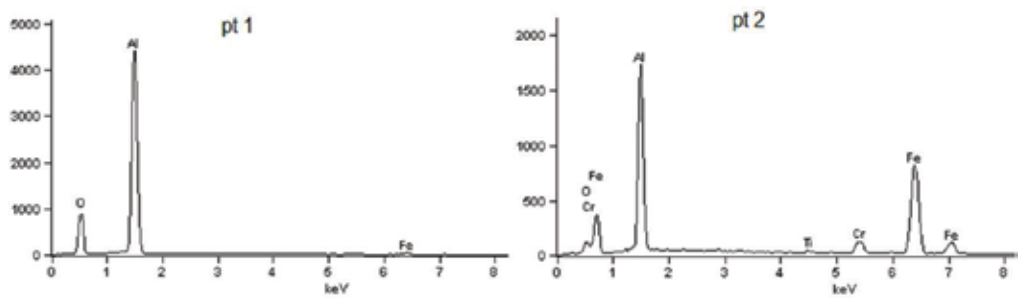


**Figure 10.** X-ray microanalysis of the chemical composition of the areas indicated on the sample surface after corrosion research at 1373 K for 100 h.

accompanied by a reduction in the volume of the oxide phase, which results in tensile stresses in the layer. The relaxation of these stresses results in numerous microcracks in which the new alumina is built up. Such microcapsules, filled with oxides, form a characteristic grid on the surface of the scale, which resembles a spider web [20, 21].

The growth of $\alpha$-Al2O3 scale occurs as a result of the predominant, intra-articular transport of oxygen across the grain boundaries in the oxide. Because of low concentration of point defects in the $\alpha$-$Al_2O_3$ phase, the aluminum and oxygen network diffusion in this oxide is not taken into account in the balance of mass transport through the layer of corrosion product [22, 23].

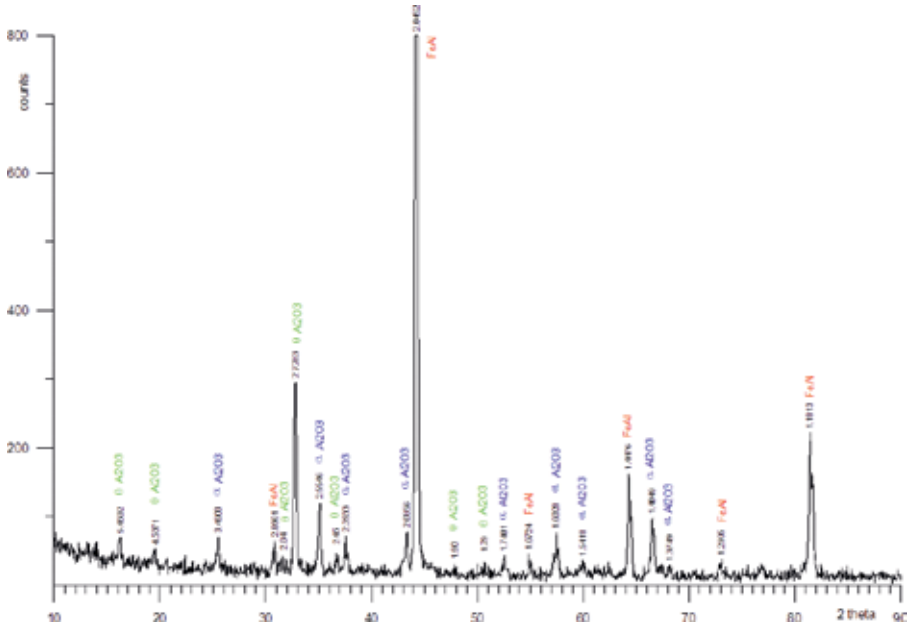


**Figure 11.** X-ray diffraction of the products of corrosion of the sample after oxidation at the temperature 1173 K in time 48 h.

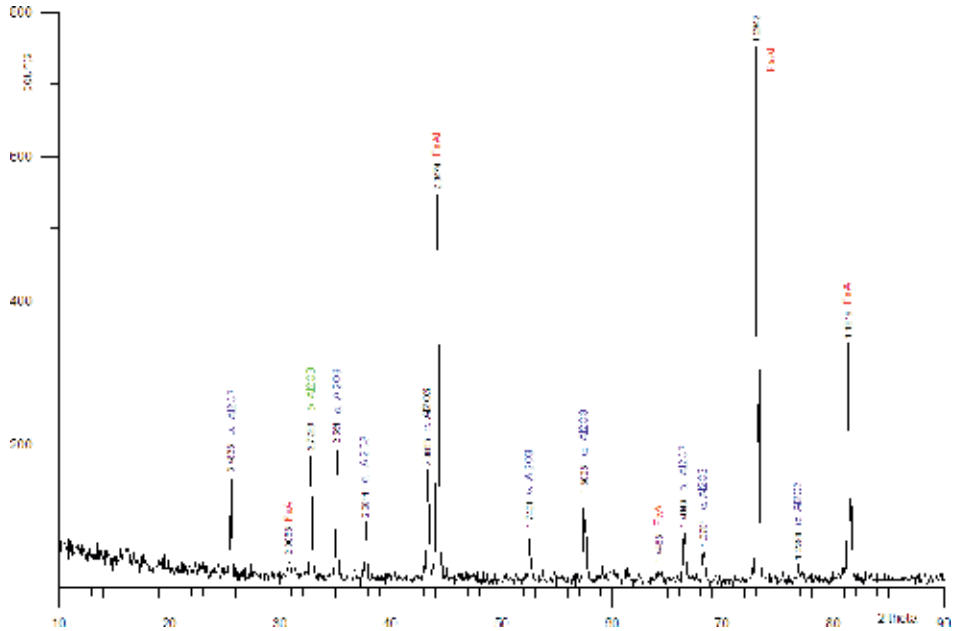


**Figure 12.** X-ray diffraction of the products of corrosion of the sample after oxidation at the temperature 1273 K in time 48 h.

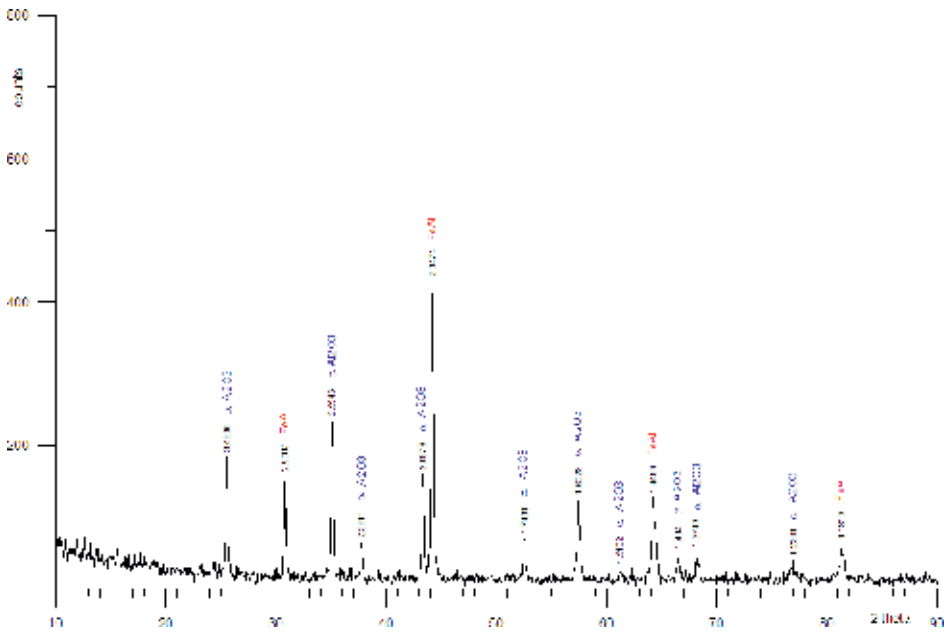

**Figure 13.** X-ray diffraction of the products of corrosion of the sample after oxidation at the temperature 1373 K in time 48 h.

### 3. The thickness of the corrosive layer

The kinetics of the corrosion process and the parabolic constant of the oxidation process ($k_p$) were the basis for determining the thickness of the corrosive layer. The $k_p$ values for temperatures of 1173, 1223, 1273, 1373 K were calculated from the relation (Eq. (2)):

$$\begin{gathered} k_p'' - \ constant\ rate\ of\ oxidation, \left(g^2 \cdot cm^{-4} \cdot s^{-1}\right) \\ \left(\frac{\Delta m}{s}\right)^2 - weight\ change\ \left(\frac{g2}{cm^4}\right)\ t - time\ (s) \end{gathered} \tag{2}$$

The results obtained for individual oxidation times are presented in **Table 2**.

Taking into account the corrosion kinetics and the oxygen density of the $Al_2O_3$ compound, the theoretical thickness of the corrosion layer (based on the oxidation time and process temperature) was calculated. The thickness of the corrosion layer was calculated from the relation (Eq. (3)):

$$\frac{\Delta m_O}{s} - weight\ change\ \left(\frac{g}{cm^2}\right) \tag{3}$$

$\rho_{Al2O3}$ = 1.98 g / cm$^3$ – calculated oxygen density in $Al_2O_3$ compound, X – layer thickness [cm].

The results of the calculations are shown in **Figure 14**. The real (occurring on the surface) thickness of the corrosion layer is lower because, during its growth, part of this layer comes

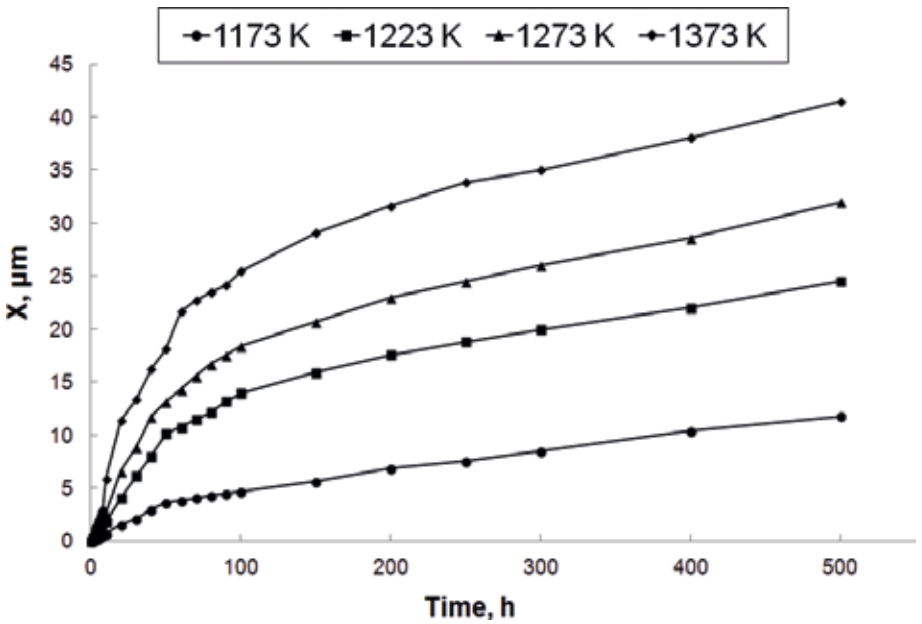


**Figure 14.** Diagram of the layer thickness calculated from the density of oxygen in $Al_2O_3$ compound for the time of 500 h.

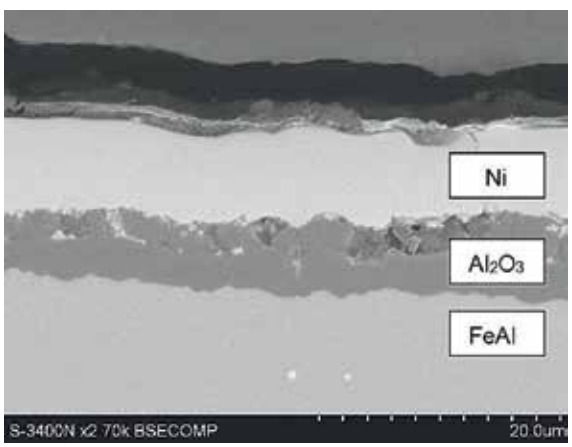


**Figure 15.** The $Al_2O_3$ layer after corrosion tests at temperature 1173 K in time 500 h.

off due to different coefficients of thermal expansion of the substrate and corrosion products. **Figures 15** and **16** show a cross-sectional image of a sample after corrosion tests. In order to protect the corrosion layer, the surface was covered with nickel (**Figure 15**). It has been shown that the corrosion layer consists of an area coherently adjacent to the substrate when tested at a temperature of 1173 K for 500 h and a corrosive layer inconsistent with numerous discontinuities for samples subjected to corrosion testing at 1373 K. This phenomenon does not depend on the process time.

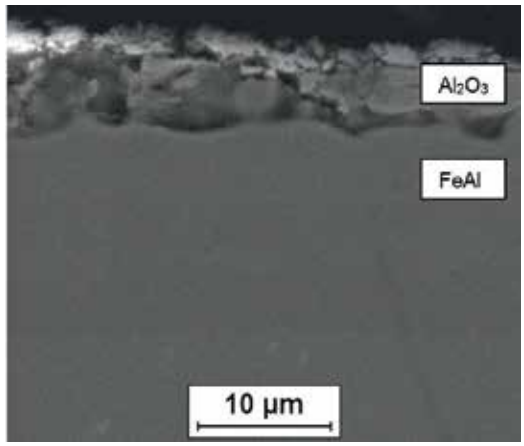


**Figure 16.** The $Al_2O_3$ layer after corrosion tests at 1373 K in time 100 h.

## 3. The operating tests on the intermediate phase of FeAl

Many Fe40Al alloy tests have shown its high resistance to high temperature corrosion in environment rich in chlorine and sulfur compounds. This confirms the possibility of using these materials for elements operating at high temperatures in the atmosphere of exhaust and industrial gases. The high-temperature strength of FeAl alloys is better than the strength of polymer composites and typically used aluminum alloys, so FeAl Fe alloys can be used on rotating elements [24]. Such conditions occur for example in turbochargers of car engines.

Turbochargers are one of the basic components of an internal combustion engine that influence its parameters. They consist of a turbine (the so-called hot part), driven on the flue side and a compressor (so-called cold part) on the compressed air side, set on a common shaft. The rotating assembly is the main element of its structure, which is held in the central body with plain bearings [25].

Due to high temperature of operating turbine, the basic issue is the selection of a material resistant to high temperatures, oxidation, aggressive working environment and creep (deformation). The exhaust gas temperature of the compression-ignition engine is about 973 K, and for spark-ignition engines it can be over 1273 K.

Due to the high temperature of exhaust gas and continuous changes of pressure, as well as a high rotational speed of up to 200 000 rpm it is necessary to use heat resistant materials [26, 27].

The durability of the turbocharger is also influenced by the presence of impurities entering the interior of the intake system, exhaust system and lubrication, and therefore the materials used for its components should exhibit abrasion resistance [28].

Taking into account the properties of alloys on the FeAl alloy phase and the working conditions and material requirements of turbochargers, studies have been undertaken to determine the feasibility of the use of Fe40Al5Cr0.2TiB intermetallic alloys for components of the hot parts of turbocharger of a car with a compression ignition engine.

The tests were performed on the Fe40Al5Cr0.2TiB intermetallic alloy which has been used as a material for making the axles of rollers for pressure control system in the suction manifold and the sleeve at the sealing ring of the turbocharger impeller (**Figures 17**, **18**). These elements are made of Fe40Al5Cr0.2TiB intermetallic alloy. The turbocharger was operated in road conditions for a distance of 80 000 km. After the tests, the turbocharger was dismantled and the components of the Fe40Al5Cr0.2TiB intermetallic alloy were tested.

The comparison of appearance of surface elements made from intermetallic Fe40Al5Cr0.2TiB alloy, after operating at a distance of 80 000 km indicates that there are no signs of tribological wear on them, and the surface is damage free.

The study of the rolls axis surface after their lifetime has been done with Hitachi S-4200 electronic scanning microscope. On the rollers surface small amounts of corrosion products and so-called carbon deposit (compounds derived from burnt engine oil) were found. The presence of single surface inequalities, which may be the result of the occurrence of metallurgical faults of the type of rupture, was also shown (**Figures 19**, **20**).

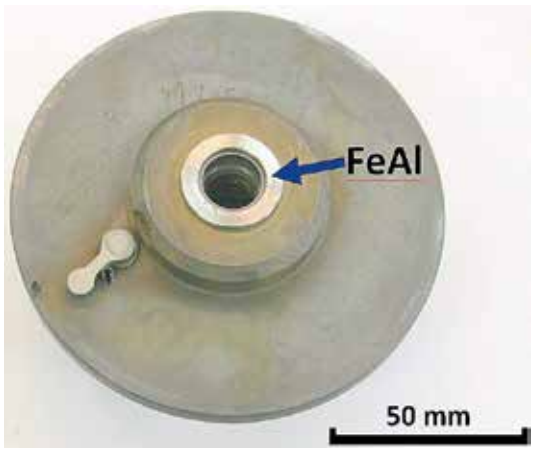


**Figure 17.** Turbine lid. The arrow indicates the sealing made of the alloy based on FeAl intermetallic phase matrix.

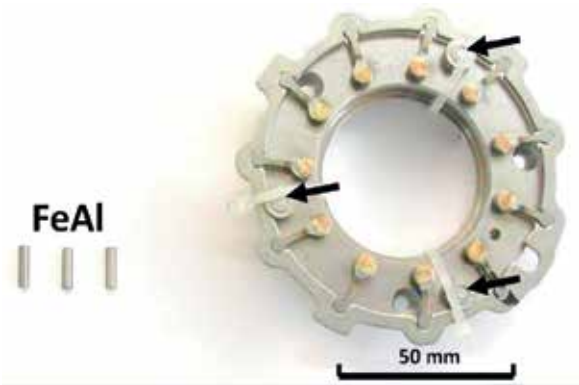


**Figure 18.** The axles of the pressure control regulator rollers before the test and the place in embedded.

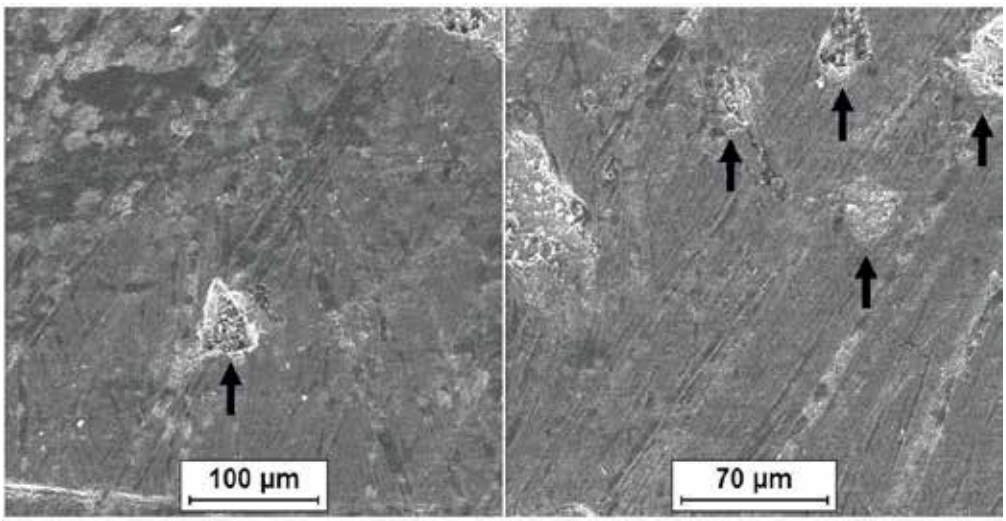


**Figure 19.** Surface view of the roll axis control system made Fe40Al5Cr0.2TiB intermetallic alloy. Visible metallurgical defects in the form of shrinkage porosity.

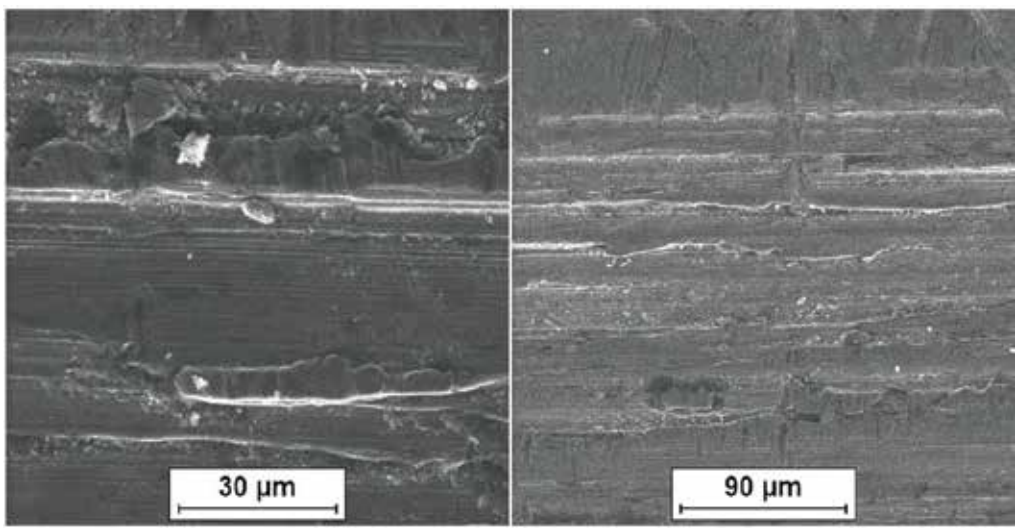


**Figure 20.** Surface of the roller axle of the control unit made of intermetallic alloy Fe40Al5Cr0.2TiB.

The turbocharger operating conditions (high temperature, corrosive environment) make the turbocharger one of the most unreliable components of the engine. This failure can be reduced by using modern materials, including alloys based on FeAl's intermetallic phase.

In the research, the tests of application FeAl alloys on the axle of the variable-geometry steering wheel control vanes were made. Conventional solutions often cause the turbocharger to malfunction due to the clogging of the rollers and their mounting axles, resulting in the lack of proper pressure control in the suction manifold. The use of FeAl alloys on the exhaust control

rollers axis was characterized by the correct operation of a turbocharger operated under high engine load conditions over a distance 80,000 km.

Determining the predictable lifetime of alloys based on FeAl's intermetallic phase as heat-resistant components working in the hot turbocharger section requires further investigation in this field, including verification for longer operating distances.

## 4. Summary

Summarizing the description of the processes involved in the high temperature corrosion of FeAl alloys, it seems appropriate to analyze key achievements concerning this issue in recent years.

Protecting metals from oxidation at high temperatures is one of the important problems of modern technology. Understanding the rate of process under certain conditions is essential both in theory and in practice. The phenomenon of gas corrosion is a source of many serious technical problems due to the large number of different technological processes running at high temperatures. The process which is limiting the growth of the protective oxide scale is volumetric diffusion. In industrial conditions we usually deal with different atmospheres, often very of variable composition, and also with non-isothermal conditions.

The possibility of reaction on metal surfaces and the composition of gas corrosion products can be predicted on the basis of thermodynamic data. Oxidation of metals of good heat-resistance is a type of evenly spread corrosion that is uniform across the entire surface to produce a layer of products having the same thickness throughout the corroded area. The rate of corrosion is most often determined by the growth of the mass of the sample or the volume of obtained products or spent gas substitutions calculated per unit of surface of the corroding metal surface, sometimes by determining the reaction rate of the reaction zone (depth of the corrosion zone) [29, 30]. When analyzing the kinetics of the metal oxidation process, it is important to define the kinetic law that the process follows and also to determine the reaction rate. The activation energy of the oxidation process (determined from kinetic measurements) is the energy of the slowest-running partial process, which determines the speed of the scale growth. It is assumed that the primary requirement for the oxide layer is to be airtight and to protect the metal from further corrosion is its greater volume relative to the volume of metal from which the oxide is formed, in accordance with the Pilling-Bedworth rule.

In case of large differences in volume, strong stresses, layer cracks and rapid oxygen diffusion paths may occur [31, 32]. Oxidation studies based on intermetallic compounds from the Fe-Al system show that a continuous layer of aluminum oxide forms on the surface of the coatings. Such an $\alpha$-$Al_2O_3$ oxide layer generated on the coatings during cyclic oxidation at 1373 K and 100 h shows significantly better corrosion resistance than $\theta$-$Al_2O_3$ oxide produced on the alloy surface of the FeAl alloy [33].

FeAl alloys should be used for construction materials, protective coatings and materials working in high-temperature corrosion conditions. The high-temperature strength of FeAl alloys is better than composites and used aluminum alloys, thus FeAl alloys can be used on spinning components [24].

Studies have shown that the growth of $\alpha$-$Al_2O_3$ scale occurs with the involvement of oxygen transport at the intracellular boundaries in the oxide. Because of the low concentration of point defects in the $\alpha$-$Al_2O_3$ phase, the network diffusion of aluminum and oxygen in this oxide is not included in the mass balance sheet by the corrosion product layer [22, 23]. The calculations and experiments carried out show that aluminum transport in the absence of contact of corrosion products with melt substrate (pore occurrence) occurs by the aluminum alloy evaporation. It is sufficient for the formation of oxide. X-rays showed that at 1373 K after 48 h $\alpha$-$Al_2O_3$ is the dominant component of the scale.

Taking into account the properties of the FeAl alloy, the working conditions and material requirements of the turbochargers, studies have been carried out to determine the feasibility of the use of the Fe40Al5Cr0.2TiB intermetallic alloy for hot-dipped turbocharger components. Axis of the pressure control rollers in the suction manifold and the sleeve at the sealing ring of the turbocharger rotor ring were made. Operation was performed under extreme turbocharger operation conditions (high load engine operation). The conditions produced during the test often lead to a turbocharger failure, which results in damage to the exhaust control system due to the seizure of the control mechanism. Performance tests have yielded a positive result, preserving turbocharger performance for 80 000 km.

## 5. Conclusion

1. The kinetics of the corrosion process of the high temperature alloy Fe40Al5Cr0.2TiB after the incubation period is in accordance with the parabolic law. Deviations from the parabolic course in the initial period are due to the fact that different allotropic variants of $Al_2O_3$ oxide and grain growth occur.
2. The $\alpha$-$Al_2O_3$ scale formed on the surface is characterized by different thermal expansion compared to the thermal expansion of the FeAl phase. Diffusion of the thermal expansion coefficient results in the formation of microcracks in the case of cyclic reduction and temperature rise, leading to the falling of the protective oxide layer. The rate of growth of the scale in places where it has lost contact with the alloy (porosity) is the same as where the contact was maintained.
3. In the multicomponent alloy Fe40Al5Cr0.2TiB corrosion products formed on the surface of the material in the temperature range 1273 -1373 K the dominant oxide is $\alpha$-$Al_2O_3$. The proportion of other oxides, e.g. $Cr_2O_3$, is negligible. This is due to the fact that the oxides of the remaining elements in the alloy, such as iron, chromium, have several orders of magnitude higher decomposition. For this reason Al in the Fe40Al5Cr0.2TiB alloy is selectively oxidized to form stable $\alpha$-Al2O3 oxide on the melt surface.
4. Morphology and phase composition of the scale are characterized by differentiation depending on the temperature at which the oxidation process takes place. In the temperature range up to 1223 K, metastable θ oxides are observed. Over time, the crystallographic network rebuilds to the $\alpha$-$Al_2O_3$ phase. At higher temperatures, the time at which the continuous $\alpha$-$Al_2O_3$ layer is produced decreases. Only $\alpha$-$Al_2O_3$ phase was observed at 1373 K after 48 h.

5. The thickness of the corrosion layer determined on the basis of the kinetics of the discontinuous process shows differentiation compared to the results of thermogravimetric measurements. The thickness of the corrosion layer measured on the surface of the oxidized samples in the crucibles is lower, as it decays during the cooling process due to the different coefficients of thermal expansion of the substrate.
6. The use of the Fe40Al5Cr0.2TiB intermetallic alloy for hot turbocharger parts as nickel alloy alternatives with compression ignition has allowed operation while preserving the nominal compressor characteristics during the entire operating test. Surface condition tests carried out on elements after the course of 80 000 km showed no signs of tribological wear and the surface of these elements was free of corrosion damage.

## Acknowledgements

During the implementation of the research, the knowledge and experience of the employees of the Faculty of Materials Science and Ceramics of the Department of Physicochemistry and Process Modeling of the AGH University of Science and Technology were used. I sincerely thank Prof. PhD Eng. Marek Danielewski for help in carrying out research.

## Author details

Janusz Cebulski and Dorota Pasek*

*Address all correspondence to: dorota.pasek@polsl.pl

Silesian University of Technology, Katowice, Poland

## References

[1] Jóźwiak S. Aluminki żelaza. Sekwencja przemian fazowych w procesie nieizotermicznego spiekania proszków żelaza i aluminium. Bel Studio, Warszawa; 2014

[2] Deevi SC, Sikka VK. Nickel and iron aluminides: An overview on properties, processing, and applications. Intermetallics. 1996;**4**:357-375

[3] Liu CT, Stringer J, Mundy JN, Horton LL, Angelini P. Ordered intermetallic alloys: An assessment. Intermetallics. 1997;**5**:579-596

[4] Sikka VK, Wilkening D, Liebetrau J, Mackey B. Melting and casting of FeAl-based cast alloy. Materials Science and Engineering. 1998;**A258**:229-235

[5] Formanek B, Szczucka-Lasota B. Odporność na korozję wysoko-temperaturową stopów międzymetalicznych z układu Fe-Al. Ochrona przed korozją. 2009;**513**:583-588

[6] Bystrzycki J, Varm RA, Bojar Z. Postępy w badaniach stopów na bazie uporządkowanych faz międzymetalicznych z udziałem aluminium. Inżynieria Materiałowa. 1996;**5**:137

[7] Schmitta A, Kumarb KS, Kauffmanna A, Lic X, Steinc F, Heilmaiera M. Creep of binary Fe-Al alloys with ultrafine lamellar microstructures. Intermetallics. 2017;**90**:180-187

[8] Cebulski J. Sposoby podwyższania plastyczności stopu na osnowie związku międzymetalicznego FeAl. Rozprawa doktorska. Gliwice: Politechnika Śląska; 1998

[9] Schindler I, Kratochvíl P, Prokopčáková P, Kozelský P. Forming of caste Fe – 45at.% Al alloy with high content of carbon. Intermetallics. 2010;**18**:745-747

[10] Barcik J, Cebulski J. Plastify of alloy based on the matrix of intermetallic FeAl phase. Archives of Metallurgy. 2000;**45**(3):315-330

[11] Grabke HJ. Oxidation of NiAl and FeAl. Intermetallics. 1999;**7**:1153-1158

[12] Danng Ngoc Chan C, Huvier C, Dinhut JF. High temperature corrosion of some B2 iron aluminides. Intermetallics. 2001;**9**:817-826

[13] Formanek B, Szymański K, Beliayev A: Composite carbide powders and HVOF sprayed coatings with a plastic matrix. Journal of Achievements in Materials and Manufacturing Engineering. 2006;**13**(1/2):351-354

[14] Cebulski J, Tytko K. Przeróbka plastyczna metodą wyciskania zwłaszcza stopów na osnowie fazy międzymetalicznej FeAl. Patent No. 208310, decyzja Urzędu Patentowego Rzeczypospolitej Polskiej z dnia Nov 26, 2010

[15] Cebulski J. Żaroodporność stopów na osnowie fazy międzymetalicznej FeAl, Wydawnictwo Politechniki Śląskiej, Gliwice. 2014

[16] Mrowec S. Teoria dyfuzji w stanie stałym. Warszawa: Państwowe Wydawnictwo Naukowe; 1989

[17] Brumm W, Grabke HJ. The oxidation behaviour of NiAl-I. Phase transformations in the alumina scale during oxidation of NiAl an NiAl-Cr alloys. Corrosion Science. 1992;**33**:1677-1690

[18] Schumann E. The effect of Y-ion implantation on the oxidation of β-NiAl. Oxidation of Metals. 1995;**43**:157-172

[19] Young JC, Schumann E, Levin I, Ruhle M. Transient oxidation of NiAl. Acta Materiala. 1998;**46**:2195-2201

[20] Hindam HM, Smeltzer WW. Growth and Microstructure of $\alpha$ - $Al_2O_3$ on Ni-Al Alloys: Internal Precipitation and Transition to External Scale. Journal on the Electrochemical Society. 1980;**127**(7):1622-1630

[21] Doychak J, Ruhle M. TEM studies of oxidized NiAl and $Ni_3Al$ cross sections. Oxidation of Metals. 1989;**31**:431-452

[22] Clemens D, Bongartz K, Speier W, Hussey RJ, Quadakkers WJ. Analysis and modelling of transport processes in alumina scales on high temperature alloys. Fresenius' Journal of Analytical Chemistry. 1993;**346**;318-322

[23] Clements D, Bongartz K, Quadakkers WJ, Nickel H, Holzbrecher H, Becker JS. Determination of lattice and grain boundary diffusion coefficients in protective alumina scales on high temperature alloys using SEM, TEM and SIMS. Fresenius' Journal of Analytical Chemistry. 1995;**353**:267-270

[24] Kupka M. Technological plasticity studies of the FeAl intermetallic phase-based alloy. Intermetallics. 2004;**12**:295-302

[25] Schweizer B, Sievert M. Noulinear oscillations of automotive turbocharger turbines. Journal of Sound and Vibration. 2009;**321**:955-975

[26] Romagnoli A, Martinez-Botas R. Heat transfer analysis in a turbocharger turbine: An experimental and computational evaluation. Applied Thermal Engineering. 2012;**38**:58-77

[27] Tetsui T. Development of TiAl turbocharger for passenger vehicle. Materials Science and Engineering. 2002;**A329-331**:582-588

[28] Pint BA, Haynes JA, Armstrong BL. Performance of advanced turbocharger alloys and coatings at 850-950°C in air with water vapor. Surface & Coatings Technology. 2013; **215**:90-95

[29] Jabłońska M, Jasik A, Hanc A. Structure and some mechanical properties of Fe(3) Al-based cast alloys. Archives of Metallurgy and Materials. 2009;**54**(3):731-739

[30] Formanek B, Hernas A, et al. Structre and Applications, Materials Week. International Congres on Advanced Materials, their Processes and Applications, Monachium. 2000

[31] Cebulski J. Odporność korozyjna stopów na osnowie fazy międzymetalicznej FeAl po krystalizacji i po przeróbce plastycznej. Hutnik-Wiadomości Hutnicze. 2012;**8**:557-561

[32] Cebulski J, Lalik S, Michalik R. Corrosion resistance of FeAl intermetallic phase based alloy in water solution of NaCl. Journal of Achievements in Materials and Manufacturing Engineering. 2008; **27**:15-18

[33] Hernas A, Piliszko B, Imosa M. Resistance to high-temperature corrosion of new materials for power industry. Archiwum Combustionis. PAN. 2007;**27**(1):4-7

Chapter 2

# Intermetallics Formation and Their Effect on Mechanical Properties of Al-Si-X Alloys

Williams S. Ebhota and Tien-Chien Jen

Additional information is available at the end of the chapter

http://dx.doi.org/10.5772/intechopen.73188

**Abstract**

This study focuses on primary impurities, called intermetallics, in the microstructure of Al-Si-X alloys, their formation, effects and treatments to eliminate or ameliorate their deleterious effects. Intermetallic compounds are usually formed when alloying elements, such as Fe, Cu, Mn, Mg and Sr. are added to Al-Si based alloys. These elements are depicted by X in the alloys formation expression. The chapter noted that the most common intermetallics are iron (Fe) based, and several of these Fe-phases, including the most harmful Fe-phase, β-$Al_5SiFe$, are listed and discussed. Fe-phase intermetallics are deleterious to the mechanical properties of Al-alloys; however, addition of <0.7% Fe helps prevent soldering in die casting mould. The effects of Fe-phase and other intermetallics formed by Cu, Mg and Mn were examined. Further, some techniques of eliminating or mitigating the negative influences of intermetallics were discussed.

**Keywords:** Al-Si alloys, Fe intermetallics, aluminium alloys intermetallics, impurities in aluminium alloys, alloying elements

## 1. Introduction

Eutectic and near-eutectic alloys of Al-Si-X (ternary systems) have many areas of applications, particularly in the automotive, airspace and marine industries, due to their exceptional properties. X in Al-Si-X formation represents one or more alloying elements, such as copper (Cu), magnesium (Mg), nickel (Ni), iron (Fe), etc. Large quantities of aluminium (Al) alloys (Al-Si-X) are required in engineering applications, especially in automotive and airspace industries [1–4]. The mean aluminium consumption in automobiles in Europe is shown in **Figure 1**. The increasing demand and studies on these alloys seem to be proportionate, as several studies have been reported on Al-Si-X alloys' microstructure, mechanical properties and

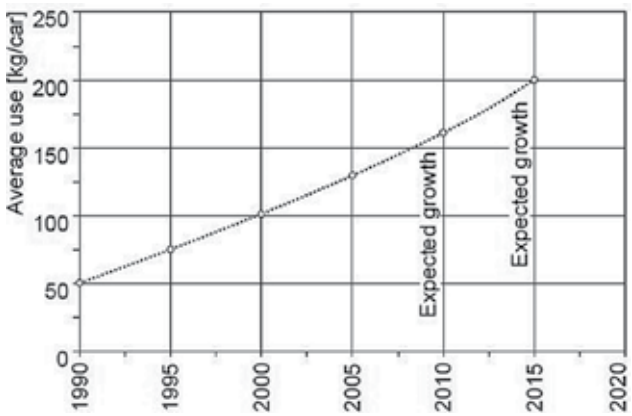


**Figure 1.** The mean aluminium consumption in automobiles in Europe [15].

their modifications [5–11]. The high demand is due to the excellent high strength-to-weight ratio, abrasion and corrosion resistance and low coefficient of thermal expansion possess by aluminium alloys. Besides these properties, aluminium alloys application is limited by certain mechanical property drawbacks, such as partially inherited as-cast microstructure, existence of unavoidable metastable intermetallics and intra-dendritic zones of microstructure [12, 13]. Eutectic and near-eutectic Al–Si-X alloys depend on chemical composition, morphology of dendritic $\alpha$-Al, and intermetallics that are present in the microstructure for mechanical properties. Coupled with the size and morphology of eutectic Si and the precipitation hardening phases during heat treatment, describing the myriad variables responsible for mechanical properties is quite complex.

These alloys are usually produced from secondary alloys and recycling processes. Many of their based alloys contain impurities, while the levels of impurities in the recycled ones are multiplied during recycling process. Alloying elements, such as Mg, Cu and silicon (Si) are deliberately added to Al alloys to enhance their mechanical properties. Apart from the intentionally added elements, impurities such as Fe, Cu, Cr, Manganese (Mn), and transition metals are usually present [14]. Although these impurities are at trace levels in the alloys, they form new phase components called intermetallics that significantly influence the properties of the microstructures. Quite often, these impurities are strong sites for crack initiation that serve as weak points for decohesion failure. However, intermetallics of Al or Si show resistance to corrosion and oxidation due to their adherent surface oxides; intermetallics of light elements are applied in light weight areas due to their attractive low density, which gives rise to highly specific properties.

The total amount of intermetallics in as-cast alloys is below 5% volume. Despite a few intermetallics in the cast microstructure, the detrimental effects on the ductility and service performance of alloys are huge. Controlling and manipulating the development of the metastable intermetallics during non-equilibrium solidification are of technological interests. This chapter, therefore, centres on the understanding of intermetallics in Al-Si-X alloys, their formation, nature, their effects on mechanical properties and methods of mitigating their adverse influences. There are several published studies on the type of intermetallics in Al-Si-X alloys and their effects as presented in **Table 1.**

| Ref | Al-Alloy | Intermetallics | Effects on mechanical properties |
|---|---|---|---|
| [16, 17] | Al-Fe-Fe is highly soluble in molten Al but low in solid Al (max 0.05 wt.%, 0.025 atm.%) | $Al_3Fe$ | It cracks and reduces formability and fatigue resistance but Improves wear resistance |
| | | $Al_6Fe$ | The effect of $Al_6Fe$ fibres on fatigue properties of Al-Fe alloys is not very clear yet, though is said to be finely dispersed. |
| [18–22] | Fe combines with other elements to form intermetallic phase particles of various types | | |
| | Al-Si-Fe | β-$Al_5FeSi$; | Deleterious; stress raiser |
| | | α-$Al_8Fe_2Si$ | Less harmful |
| | | δ-$Al_4FeSi$ | Metastable |
| | Al-Si-Mg-Fe | π-$Al_8Mg_3FeSi_6$ | It has negative impact on ductile properties; lower strength and ductility |
| | | $Al_9FeMg_3Si_5$ | improved significantly after the T6 heat treatment |
| | | $Mg_2Si$ | Detrimental to the alloys' ductility |
| [23] | Al-Mn-Fe | $Al_6(Fe,Mn)$ | Significantly deteriorate the mechanical properties of alloy |
| | Al-Si-Mn-Fe (Excess Mn + $Al_5FeSi$) | α-$Al_{15}(FeMn)_3Si_2$ (China script) | Not very harmful but reduces the machinability |
| [24, 25] | Al-Cu (Cu 1–4%) | θ-$Al_2Cu$ | Improve mechanical properties-they decrease the grain size and increase the fatigue life |
| | Al-Si-Cu-Mg (Cu 1–4%) | (Q) $AI_5Cu_2Mg_8Si_6$ | |

**Table 1.** Studies on the types of intermetallics in al-Si-X alloys and their effects on mechanical properties.

## 2. Formation processes of intermetallic compounds and their identification

The equilibrium and non-equilibrium reactions that occur during the casting of Al alloy account for intermetallic phases. Coarse intermetallic particles are formed in the interdendritic regions during solidification or at a relatively high temperature in the solid state during solution treatment, homogenisation, or recrystallization [14]. Most metals, except for Mg and Cu, exhibit a low solid solubility in Al. When the amount of solute element exceeds the limit of solid solubility, an intermediate phase, also called second phase, is developed. The composition of the intermediate phase is in between two pure metals (primary components) and has a varied crystal structure from the primary components. The intermediate phase, with unchanging composition, is called an intermetallic compound. Therefore, intermetallics are products of incomplete solid solubility by alloy systems. Intermetallic compounds identification in Al alloys is critical to complex structure examination. Microstructural examination is one of the primary ways of evaluating the evolution of phases in materials. This evaluation promotes the understanding of the effects of composition, production technique, heat treatments and deformation process on

alloys' mechanical behaviours. Also, it is used to investigate the influences of new fabrication processes and to analyse failure mechanisms and causes.

## 2.1. Identification of intermetallics

### *2.1.1. Fe-Intermetallics*

The known intermetallic compounds in aluminium and its alloys are categorised into two systems: binary (Al-Fe and Fe-Si) and ternary systems. The following phases have been reported to exist in Al-Fe binary systems: $Al_5Fe_2$, $Al_3Fe$, $Al_2Fe$ $Al_{13}Fe_4$ and $Al_8Fe_5$ [26–28]. In the case of a Fe-Si system, the following stable compounds were found: FeSi, $Fe_2Si$, $FeSi_2$, and $Fe_5Si_3$ [29, 30]. Phase equilibria of the binary systems are generally well known. The ternary system is characterised by a large number phases, both metastable and stable. Several review papers on Al-Fe-Si ternary phases have been published [23–25]. Gosh appraised over 150 research papers on ternary phases that covered unto 1986 [30, 31]. More updates have been provided by other authors [30] and in 2008, Du et al. presented about 24 Al-Si-Fe ternary compounds [32]. A summary of all the significant phases of both binary and ternary systems are presented in **Table 2**.

In a study, the effects of Cu, Fe, Mg, Mn, and Sr. additions on the type of intermetallic compounds formed in Al-Si eutectic alloys were investigated and reported [33]. Many eutectic alloys (SP0, SP1 SP2, SP3, SP4, and SP5) were developed by adding elements Cu, Fe, Mn, Mg and Sr. to A413.1. The chemical compositions of the various alloys produced for the experiment are presented in **Table 3**.

Microstructural examination shows the presence of $\alpha$-Fe Chinese script phases in alloys SP0, SP4 and SP5, with a reasonable amount of Mn, as shown in **Figure 2**. The morphology of Chinese script of the $\alpha$-Fe phase arises during solidification of eutectic alongside $\alpha$-Al. The appearance of $\alpha$-Fe phase could be polyhedrons if it solidifies before the eutectic reaction occurs [34].

| **Binary systems** | | | **Denary systems (Al-Si-Fe)** | |
|---|---|---|---|---|
| Al-Fe | Al-Si | Fe-Si | $Al_2Fe_3Si_3$ | $Al_{4.5}FeSi$ |
| AlFe ($\alpha_2$) | HT-$FeSi_2$ ($Fe_2Si_5$) | FeSi | $Al_3FeSi$ | $Al_3Fe_2Si_3$ |
| $AlFe_3$ ($\alpha_1$) | LT-$FeSi_2$ | $FeSi_2$ | $Al_{21.5-45}Fe_{36.5-37.5}Si_{8.5-41.5}$ [a] | $Al_{64.5-67.5}Fe_{15.5-16.5}Si_{17-19}$ [a] |
| $Al_2Fe$ | $Fe_2Si$ | $Fe_2Si$ | $Al_2FeSi$ | $A_{l2}Fe_3Si_4$ |
| $Al_5Fe_2$ | $Fe_5Si_3$ | $Fe_5Si_3$ | $Al_{53.9-65.3}Fe_{19.5-20.5}Si_{15.2-25.6}$ [a] | $Al_{39.2-48.7}Fe_{23.5-24.5}Si_{27.8-36.3}$ [a] |
| $Al1_3Fe_4$ | FeSi | | $Al_3FeSi_2$ | $Al_{24.1-28.6}Fe_{31.9-32.9}Si_{39.5-43}$ [a] |
| $Al_8Fe_5$ (e) | | | $Al_{53-56}Fe_{23.5-24.5}Si_{20.5-22.5}$ [a] | $Al_{57-59}Fe_{24-25}Si_{17-18}$ [a] |
| | | | $Al_{7.4}Fe_2Si$ | $Al_4Fe_{1.7}Si$ |
| | | | $Al_{45.5-54}Fe_{15.5-16.5}Si_{30.5-38}$ [a] | $Al_{64-66.5}Fe_{24-25}Si_{9.5-11}$ [a] |
| | | | $Al_{68-72}Fe_{18-19.5}Si_{10-12.5}$ [a] | |

**Table 2.** A summary of both binary and ternary systems.

| Phase type | Alloy code | Al | Si | Cu | Fe | Cr | Mn | Mg | Sr/ ppm* | Suggested composition |
|---|---|---|---|---|---|---|---|---|---|---|
| $\alpha$-Fe | Sp0 | 60.30 | 9.93 | 0.48 | 18.43 | 1.83 | 8.99 | | 120 | $Al_{12.7}(Fe,Mn,Cr,Cu)_3Si_2$ |
| | Sp0 | 60.32 | 9.93 | 0.49 | 19.17 | 1.67 | 8.41 | | 00 | $Al_{12.7}(Fe,Mn,Cr,Cu)_3Si_2$ |
| | Sp0 | 59.81 | 9.58 | 0.98 | 21.10 | 0.96 | 7.57 | | 00 | $Al_{13.6}(Fe,Mn,Cr,Cu)_{3.3}Si_2$ |
| | Sp0 | 66.36 | 9.90 | 0.88 | 14.72 | 1.42 | 6.71 | | 00 | $Al_{14}(Fe,Mn,Cr,Cu)_{2.3}Si_2$ |
| | Sp0 | 65.14 | 9.52 | 0.58 | 16.07 | 1.48 | 7.19 | | 180 | $Al_{12.6}(Fe,Mn,Cr,Cu)3Si2$ |
| | Sp0 | 61.09 | 10.10 | 0.39 | 19.05 | 1.87 | 9.11 | | 42 | $Al_{12.1}(Fe,Mn,Cr,Cu)_{2.9}Si_2$ |
| | Sp0 | 60.10 | 10.13 | 0.40 | 18.28 | 1.90 | 8.78 | | 110 | $Al_{12.3}(Fe,Mn,Cr,Cu)_{2.8}Si2$ |
| | Sp4 | 59.9 | 10.5 | 1.29 | 14.7 | 1.79 | 12.8 | 0.01 | 132 | $Al_{11.7}(Fe,Mn,Cr,Cu)_{2.9}Si_2$ |
| | Sp5 | 60.59 | 10.4 | 0.79 | 17.0 | 2.32 | 10.3 | 000 | 109 | $Al_{12.2}(Fe,Mn,Cr,Cu)_3Si_2$ |
| | Sp5 | 70.51 | 8.92 | 1.44 | 12.88 | 0.63 | 4.94 | 0.08 | 000 | $Al_{16.5}(Fe,Mn,Cr,Cu)_{2.2}Si_2$ |
| | Sp5 | 61.83 | 9.63 | 0.67 | 20.10 | 1.29 | 8.79 | 000 | 452 | $Al_{13.4}(Fe,Mn,Cr,Cu)_{3.3}Si_2$ |
| | Sp5 | 61.8 | 9.43 | 0.60 | 20.62 | 1.26 | 8.30 | 000 | 000 | $Al_{13.7}(Fe,Mn,Cr,Cu)_{3.3}Si_2$ |
| | Sp5 | 61.09 | 10.4 | 0.90 | 19.04 | 1.58 | 8.77 | 000 | 000 | $Al_{12.3}(Fe,Mn,Cr,Cu)_{2.9}Si_2$ |
| | Sp5 | 61.46 | 10.1 | 1.10 | 20.77 | 1.02 | 8.03 | 0.01 | 236 | $Al_{12.7}(Fe,Mn,Cr,Cu)_{3.1}Si_2$ |
| | Range | 59.8–70.6 | 8.9–10.5 | 0.4–1.44 | 14.7–21.1 | 0.63–2.3 | 4.9–12.8 | | | $Al_{11.7–16.5}(Fe,Mn,Cr,Cu)_{2.2–3.3}Si_2$ |
| | Average | 62.2 | 9.9 | 0.79 | 18.0 | 1.5 | 8.5 | | | $Al_{13}(Fe,Mn,Cr,Cu)_{2.9}Si_2$ |
| $\beta$-Fe | Sp1 | 66.25 | 18 | 0.21 | 14.1 | 0.11 | 4.68 | | 00 | $Al_{7.1}(Fe,Mn,Cr,Cu)Si_{1.8}$ |
| | Sp1 | 71.2 | 9.66 | 0.33 | 13.56 | 0.11 | 4.23 | | 241 | $Al_{8.0}(Fe,Mn,Cr,Cu)Si$ |
| | Sp1 | 56.7 | 17.68 | 0.05 | 22.8 | 0.03 | 3.8 | | 00 | $Al_{4.4}(Fe,Mn,Cr,Cu)Si_{1.3}$ |
| | Sp1 | 68.5 | 17.3 | 0.25 | 16.5 | 0.05 | 3.55 | | 00 | $Al_{7.0}(Fe,Mn,Cr,Cu)Si_{1.7}$ |
| | Sp2 | 72.3 | 14.8 | 0.13 | 10.7 | 0.07 | 2.72 | | 352 | $Al_{10.7}(Fe,Mn,Cr,Cu)Si_{2.1}$ |
| | Sp2 | 60.9 | 17.9 | 0.05 | 20.0 | 0.05 | 4.5 | | 00 | $Al_{5.0}(Fe,Mn,Cr,Cu)Si_{1.4}$ |
| | Sp4 | 55.7 | 17.9 | 0.10 | 22.2 | 0.05 | 3.88 | 0.11 | 129 | $Al_{4.39}(Fe,Mn,Cr,Cu)Si_{1.36}$ |
| | Sp4 | 54.7 | 18.4 | 0.15 | 21.3 | 0.06 | 3.72 | 1.69 | 000 | $Al_{4.47}(Fe,Mn,Cr,Cu)Si_{1.59}$ |
| | Sp4 | 55.6 | 17.9 | 0.10 | 22.1 | 0.03 | 3.61 | 0.44 | 000 | $A_{l4.43}(Fe,Mn,Cr,Cu)Si_{1.41}$ |
| | Sp4 | 56.4 | 18.1 | 0.06 | 23.0 | 0.03 | 3.79 | 0.02 | 000 | $Al_{4.33}(Fe,Mn,Cr,Cu)Si_{1.34}$ |
| | Range | 54.4–72.3 | 9.6–18.4 | 0.05–0.33 | 10.7–23 | 0.03–0.11 | 2.72–4.68 | | | $Al_{4.3–10.7}(Fe,Mn,Cr,Cu)Si_{1–2.21}$ |
| | Average | 61.8 | 16.7 | 0.14 | 18.6 | 0.06 | 3.8 | | | $Al_6(Fe,Mn,Cr,Cu)Si1.5$ |

| Phase type | Alloy code | Al | Si | Cu | Fe | Cr | Mn | Mg | Sr/ ppm* | Suggested composition |
|---|---|---|---|---|---|---|---|---|---|---|
| $Mg_2S$ Pi phase | Sp3 | 0.33 | 37.3 | | | | | 62.4 | 00 | $Mg_{1.9}Si$ |
| | Sp3 | 49.3 | 26.5 | 0.13 | 8.16 | 0.10 | 1.66 | 14.76 | 00 | $Al_{10.3}(Fe,Mn,Cr,Cu)Si_{5.3}Mg3_{.4}$ |
| | Sp3 | 52.3 | 25.8 | 0.19 | 7.89 | 0.05 | 1.23 | 13.27 | 00 | $Al_{11.8}(Fe,Mn,Cr,Cu)Si_{5.6}Mg_{3.3}$ |
| | Sp3 | 48.6 | 26.1 | 0.08 | 9.19 | 0.01 | 0.96 | 15.03 | 00 | $Al_{9.9}(Fe,Mn,Cr,Cu)Si_{5.1}Mg_{3.4}$ |
| | Sp2 | 51.0 | 25.4 | 0.11 | 8.11 | 0.08 | 1.44 | 13.87 | 00 | $Al_{11.0}(Fe,Mn,Cr,Cu)Si_{5.3}Mg_{3.3}$ |
| | Sp2 | 49.6 | 26.5 | 0.20 | 8.77 | 00 | 0.63 | 14.22 | 00 | $Al_{10.9}(Fe,Mn,Cr,Cu)Si_{5.6}Mg_{3.5}$ |
| | Sp2 | 48.0 | 26.8 | 0.12 | 9.30 | 00 | 0.79 | 14.97 | 127 | $Al_{9.9}(Fe,Mn,Cr,Cu)Si_{5.3}Mg_{3.4}$ |
| | Sp4 | 46.7 | 27.4 | 0.18 | 7.91 | 0.04 | 1.91 | 15.9 | 000 | $Al_{9.6}(Fe,Mn,Cr,Cu)Si_{5.4}Mg_{3.6}$ |
| | Sp4 | 47.5 | 27.4 | 0.27 | 8.50 | 0.02 | 1.26 | 15.9 | 000 | $Al_{9.9}(Fe,Mn,Cr,Cu)Si_{5.5}Mg_{3.7}$ |
| | Sp4 | 48.4 | 26.7 | 0.46 | 9.58 | 0.13 | 2.44 | 15.1 | 000 | $Al_{8.1}(Fe,Mn,Cr,Cu)Si_{4.3}Mg_{2.8}$ |
| | Sp4 | 46.9 | 27.4 | 0.15 | 8.15 | 0.03 | 1.98 | 15.9 | 000 | $A_{l9.4}(Fe,Mn,Cr,Cu)Si_{5.2}Mg_{3.5}$ |
| | Range | 46.7–52.3 | 25.4–27.4 | 0.08–0.46 | 7.9–9.6 | 0–0.13 | 0.6–2.44 | 13.3–15.9 | | $Al_{8.1–11.8}(Fe,Mn,Cr,Cu)_{Si4.3–5.6}Mg_{2.8–3.7}$ |
| | Average | 48.9 | 26.6 | 0.19 | 8.6 | 0.04 | 1.43 | 14.9 | | $Al_9(Fe,Mn,Cr,Cu)Si_{5.3}Mg_{3.4}$ |
| Q phases | Sp3 | 16.56 | 31.6 | 19.23 | 0.10 | 0.01 | 0.01 | 34.67 | 000 | $Al_4Mg_{9.4}Cu_2Si_{7.4}$ |
| | Sp3 | 17.56 | 31.6 | 20.36 | 0.04 | 000 | 000 | 36.51 | 117 | $A_{l4}Mg_{9.4}Cu_2Si_7$ |
| | Sp3 | 18.62 | 31.4 | 19.51 | 0.12 | 000 | 0.01 | 36.29 | 000 | $Al_{4.5}Mg_{9.7}Cu_2Si_{7.3}$ |
| | Sp3 | 20.88 | 26.6 | 17.25 | 0.02 | 00 | 00 | 38.01 | 000 | $Al_{4.4}Mg_{8.4}Cu_2Si_7$ |
| | Sp4 | 22.51 | 28.5 | 18.9 | 0.14 | 0.01 | 0.01 | 39.28 | 000 | $Al_{4.6}Mg_8Cu_2Si_{6.8}$ |
| | Sp4 | 21.7 | 30.2 | 18.4 | 0.10 | 0.02 | 000 | 37.89 | | $Al_{4.1}Mg_{7.8}Cu_2Si_{7.7}$ |
| | Range | 16.6–22.5 | 26.6–31.6 | 17.2–20.3 | 0.02–0.14 | | | 28–36.5 | | $Al_{4–4.4}Mg_{7.8–9.7}Cu_2Si_{6.8–7.7}$ |
| | Average | 23.6 | 30 | 18.9 | 0.8 | | | 32.8 | | $Al_4Mg_{8.8}Cu_2Si_{7.2}$ |

**Table 3.** Analysis of chemical composition of intermetallic phases [33].

### *2.1.2. α- and β-Fe phases*

The platelet β-AlFeSi particles are found in the Sp1, Sp2 and Sp4 alloys. The β phase is known to be a primary phase, with a three-dimensional form of a platelet that looks like needles in a two-dimensional optical micrograph, as shown in **Figure 3**. The β-Fe phase chemical composition observed vary within $Al_9Fe_2Si_2$, $Al_9FeSi$, $Al_{13.6}Fe_3$ $Si_{3.05}$, $Al_{13.3}Fe_3Si_{3.3}$ and $Al_{13.6}Fe_3Si_{3.4}$ [35]. The phases are generally represented by the chemical formula $Al_5FeSi$, despite the non-inclusion of alloying elements such as Cu, Mn, etc. The *α*-phase is the second type of the script-like; it has a lower amount of Fe which is between 23.88 and 26.79 wt.%, with Si in the range of 6.87 and 8.38 wt.%. The chemical formula of the phase is $Al_{10.42–11.67}Fe_2Si_{1.08–1.25}$. The second type of

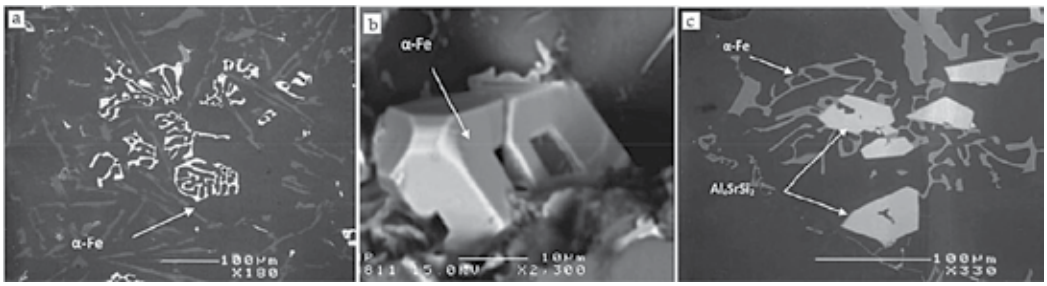


**Figure 2.** Refs. [33, 34] shows (a) non-modified PS0 alloy; (b) shows compact SEM image of phase; (c) structure of over modified PS4 alloy –note the presences of Al4SrSi2 particles on top of a-Fe morphology.

the script-like a phase has a lower iron content, between 23.88 and 26.79 wt.%, a silicon content lying between 6.87 and 8.38 wt.%, and a chemical formula of $Al_{10.42–11.67}Fe_2Si_{1.08–1.25}$.

*2.1.3. δ- and pi-phase α- and β-Fe phases*

Apart from $\alpha$- and $\beta$-AlFeSi phases commonly found in Fe intermetallic compounds, there are other phases that are occasionally found [33]. These phases include $\delta$-$Al_4FeSi_2$ and pi-$Al_8Mg_3FeSi_6$ compounds, shown in the micrographs in **Figure 4**. The formation of the $\delta$-$Al_4FeSi_2$ phase is favoured by high amount of Si in Al-Si eutectic alloys. This phase is considered to be the richest in Si of the Al-Fe-Si phases, and looks like platelet morphology and shows grey level under optical microscope like $\beta$-phase [21, 36]. The disparity in the Fe/Si atomic ratio in the examined $\beta$-phase particles is most likely the outcome of the partial conversion of the $\delta$-phase to the $\beta$-phase via the peritectic decomposition as in the expression [37]:

Liq. + $\delta$-$Al_4FeSi_2$ → $\beta$-$Al_5FeSi$ + Si.

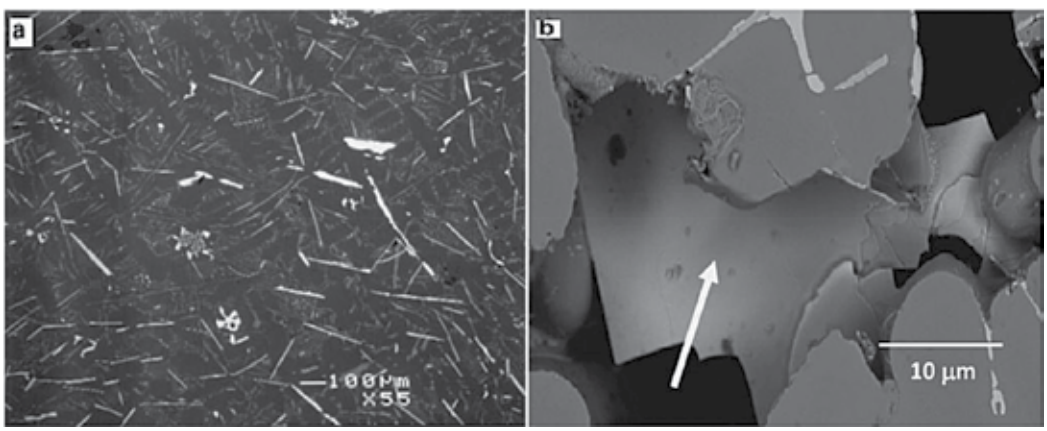


**Figure 3.** Optical micrograph of (a) β-Fe phase (needles) in alloy Sp1 and (b) SEM image showing 3-D platelet morphology of β-Fe phase [33].

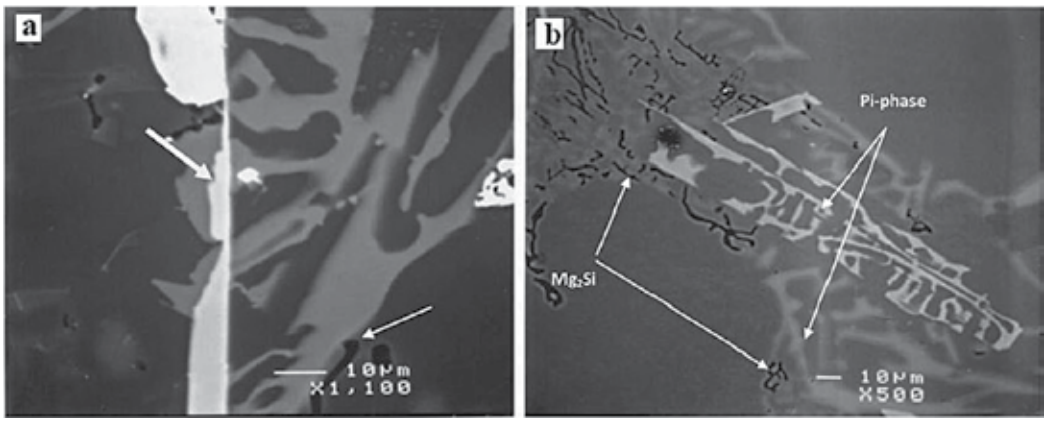


**Figure 4.** (a) β-$Al_5FeSi$ transforming into pi-phase in Sp4 alloy; (b) presence of pi-phase and phases of $Mg_2Si$ Chinese script in SP3 alloy [33].

The pi-$Al_8Mg_3FeSi_6$ phase is usually present in the precipitates of an alloy containing relatively high Mg, such as Sp3 and Sp4 in **Table 3**.

### 2.2. Mg2Si phase

The precipitate, Mg2Si, is usually observed to in all Al–Si–Mg alloys, at the edge of pi phase particles. It appears in the form of black Chinese script particles, as shown in **Figure 4**. The precipitate can also be found at the edge of primary Si and the average chemical analysis of the $Mg_2Si$ provided in **Table 3**.

### 2.3. $Al_2Cu$ and Q-phases

Copper concentration increases with the solid fraction and segregates to the liquid during solidification. Al–$Al_2Cu$ is formed to the end of solidification. A study has suggested that addition of alloying elements, such as Mg and Sr phase, does not alter the stability of the Al2Cu [33]. During final solidification, the Q-phase, Q-$Al_5Mg_8Si6Cu_2$, grows out from $Al_2Cu$

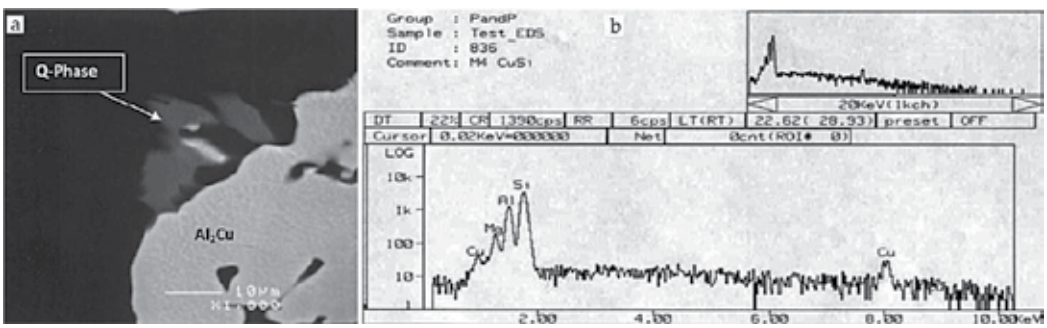


**Figure 5.** (a) Q-phase growing out of Al2Cu phase; (b) energy dispersive spectroscopy corresponding to Q phase in (a) [33].

particles. The EDX spectrum in **Figure 5**, shown that Q-phase has a reflection of elements, such as Al, Cu, Si and Mg, in the alloy.

Secondary alloys were prepared from recycling of cast Al alloys scrap of AlSi9Cu3, AlSi12Cu1Fe and AlSi8Zn10Mg were investigated for intermetallic compounds [38]. The chemical compositions of the recycled alloys are presented in **Table 4**.

The intermetallics found in recycled cast alloys, AlSi12Cu1Fe, AlSi8Zn10Mg and AlSi9Cu3, are presented **Figures 6** and **7**.

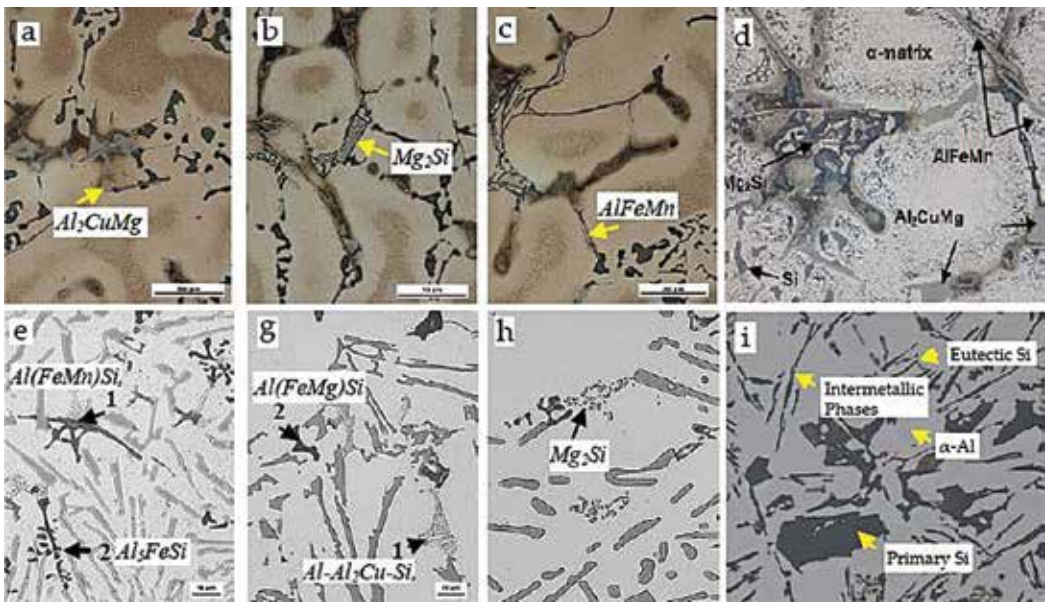


**Figure 6.** Intermetallic phases in the microstructures of recycled al-Si-X cast alloys [38] (a–c) intermetallics in AlSi8Zn10Mg cast alloy; (e–h) intermetallics in AlSi12Cu1Fe cast alloy; (d & i) microstructures of secondary AlSi8Zn10Mg and AlSi12Cu1Fe alloys respectively.

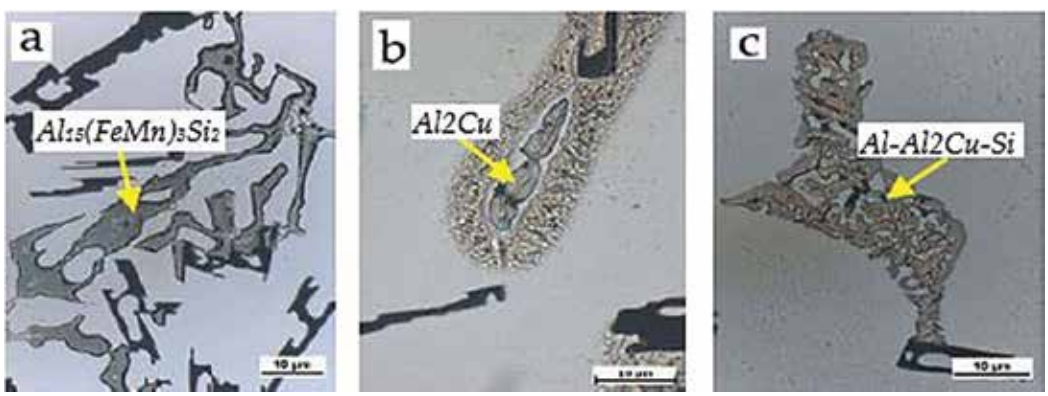


**Figure 7.** Intermetallic compounds in recycled AlSi9Cu3 cast alloy.

| Materials elements | AlSi9Cu3 | AlSi12Cu1Fe | AlSi8Zn10Mg |
|---|---|---|---|
| Si | 9.4 | 12.5 | 8.64 |
| Cu | 2.4 | 0.85 | 0.005 |
| Mn | 0.24 | 0.245 | 0.181 |
| Mg | 0.28 | 0.347 | 0.452 |
| Zn | 1 | 0.42 | 9.6 |
| Ni | 0.05 | 0.039 | 0.0022 |
| Fe | 0.9 | 0.692 | 0.1143 |
| Pb | 0.09 | 0.055 | — |
| Ti | 0.04 | 0.026 | 0.0622 |
| Cr | 0.04 | 0.023 | 0.0014 |
| Sn | 0.03 | 0.01 | — |
| Hg | — | — | 0.0006 |
| Ca | — | 0.001 | 0.0002 |
| Cd | — | — | 0.0001 |
| Bi | — | — | 0.0003 |
| P | — | — | 0.0001 |
| Sb | — | — | 0.0007 |
| Al | Remainder | Remainder | Remainder |

**Table 4.** Chemical composition of the recycled of cast al alloys scrap (wt.%).

## 3. Effect of intermetallic on mechanical and physical properties of al-Si alloys

The presence of intermetallic compounds in Al alloys is of a great concern to materials engineers due to their harmful effects on mechanical properties. Mechanical properties of Al-Si-X alloys are greatly affected by the structures of the intermetallic. Intermetallics compounds appear more in recycled Al-Si based alloys, however, cycling which is a secondary production process of Al and its alloys is cheaper than primary production process. Therefore, producing Al alloys devoid of deleterious intermetallic phases will positively affect Al and its alloys recycle market and decrease the use of primary method that requires high fabrication power consumption.

The β-phase platelets are usually potential sites for crack initiation, where eventual breakup failure occurs. Iron-based intermetallics dominate Al-Si-X alloys' intermetallics studies. Commercially available alloys contain Fe impurities in the form of Al and Si and other elements phases. In conductive liquids, the presence of certain Fe-phases, $Al_3Fe$ and

$\alpha$-AlFeSi, on the surface stimulates pitting attacks on the surface because $\alpha$-AlFeSi is cathodic in the Al matrix. The greatest disadvantage of intermetallics is their low ductility, especially at low and transitional temperatures. This has been attributed to several factors, such as [39]:

**i.** A restricted number of simple deformation modes to suit the von Mises criterion,

**ii.** Dislocations operation with large slip vectors

**iii.** Restricted cross-slip

**iv.** Transmitting slip across grain boundaries complexity

**v.** Inherent grain boundary weakness

**vi.** Isolation of harmful solutes to grain boundaries

**vii.** High Peierls-Nabarro stress and covalent bonding

**viii.** Environmental vulnerability.

### 3.1. Fe intermetallics

The presence of the dispersed brittle intermetallic $ß$-$Al_5FeSi$ phase in the structure is one of the primary barriers that impede the bendability of Al-Si based alloy sheet and consequently, poor mechanical formability. During sheet bending and forming processes, these particles create damage and premature failure. Intermetallic, $ß$-$Al_5FeSi$, forms thin brittle platelets that cause weak bond strengths within the matrix of $\alpha$-Al, thus initiating crack sites around the structure. This deleterious behaviour is especially severe in sheets produced by strip casting, a cost-effective fabrication method, which should be economically suitable for automotive Al alloys production [40]. In Al-Si based casting, Fe is the most common deleterious impurity element and forms the intermetallic compound $ß$-$Al_5FeSi$ when levels of Fe in an alloy exceed critical percentage. Solid solubility of Fe in Al is very low and consequently combines with other impurities or alloying elements to form intermetallic compounds. The type of compound formed depends on the other available impurities. An optical micrograph of the Al-Si-1.8Fe-0.8Mn microstructure is shown in **Figure 8**.

However, Fe is required in pressure die casting to prevent liquid metal from soldering to the die [42, 43]. For optimal thermal performance, Fe is desirable for Al-Si alloys to maintain stable mechanical properties at high temperatures. The Al alloys formed by Cu and Mg addition, are known for high strength due to precipitation hardening. These alloys, however, lose their strength at elevated temperatures because of unstable precipitates formed by Cu and Mg. Addition of Fe to alloys makes them stable at high temperatures compared to alloys with Cu and Mg addition. Transition elements such as Fe, upon addition to Al alloys, yield thermally stable intermetallics. The composition of eutectic Al-Si-Fe alloy is about 0.8 wt.% Fe. The liquid metal does not show affinity of dissolution with the steel mould, once the iron content is at approximately this level. The desirable Fe content in alloys in most Al pressure die casters is in the range of 0.8–1.1 wt.% Fe.

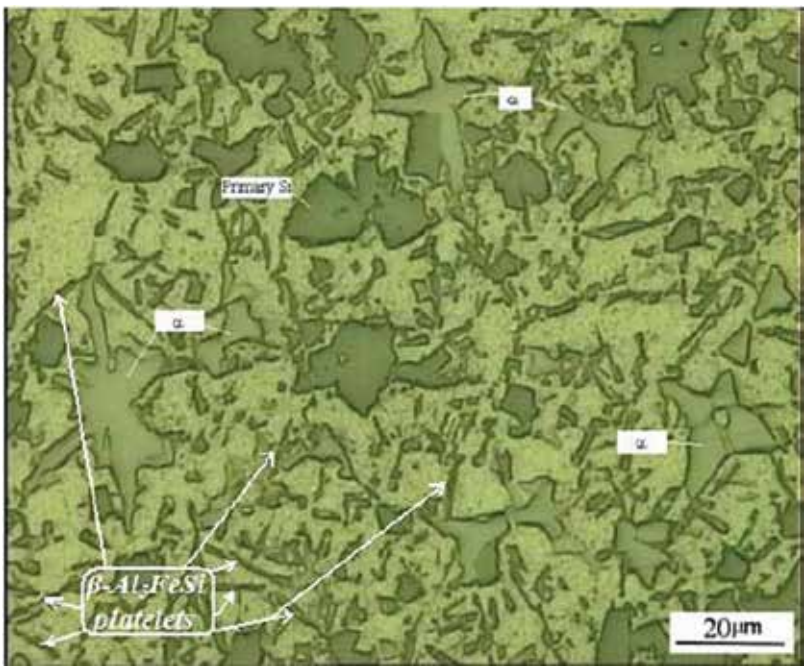


**Figure 8.** Optical micrograph of al-Si-1.8Fe-0.8Mn microstructure [41].

The class of wrought Al alloys, 6xxx series, is known for good corrosion resistance and high strength to density ratio. These alloys are good substitutes for steel in the manufacturing of automobile body panels. Apart from their principal compositional elements, Al, Mg, and Si, 6xxx alloys also possess Fe, Cu, Mn, and Cr, which sometimes are not deliberately added. The presence of these elements, especially Fe, promotes the development of different brittle iron-containing intermetallic compounds [44]. These Fe intermetallics cause poor formability and consequently, stimulate premature failure and damage during bending and forming operations. This drawback limits the application of 6xxx alloys in both automotive and aerospace industries [40, 45, 46].

### 3.2. Other Fe-phases

Other phases that have a detrimental influence on the alloy properties are $Al_3Fe$ and $\alpha$-AlFeSi, which is cathodic to the $\alpha$-Al matrix. Their presence on the surface accelerates pitting attacks in conductive liquids. Subsequently, these affect the mechanical property of the alloy by decreasing its ductility and resulting in de-cohesion failure. Equally, the platelets and needles of β-phase intermetallic, may adversely affect the alloy's castability, fluidity, and dendrites channel feeding, which results in cast defects. The different intermetallic phases in Al-Si eutectic alloys depend on the composition of the alloys. However, the phases in the microstructure with Cu and Mg, β-Al–Fe–Si–X and Sr, which are usually called Chinese script phases, are most studied. Virtually in all the alloys microstructures, $\alpha$-AlFeSiCuMg phases

with the Chinese script morphology are the dominant Fe intermetallic phases [47]. The composition of the alloy affects the morphology and location of intermetallic phases in $\alpha$-Al or in the interdendritic regions.

### 3.3. Manganese, Mn

Often, Mn is found in secondary metal made from recycled wrought product and is usually not deliberately added to virgin cast alloys. Manganese can transform iron-rich ($Al_5FeSi$) phases morphology of Al-Si-X alloy from platelets to a more cubic or globules ($Al_{15}(MnFe)_3Si_2$) and this improves the alloy's ductility and tensile strength. **Figure 9** shows micrographs of Al-Si-X structure with (a) iron-rich $A_{l5}FeSi$ phase; and (b) Cubic $Al_{15}(MnFe)_3Si_2$ form.

It is recommended that Mn should be over 50% of Fe when the amount of Fe exceeds 0.45 wt.%. Manganese (Mn) is more influential in causing gravity segregation than Fe. Application of Mn concentration that exceeds 0.6 wt.% causes segregation whether the Fe content is 0.8 or 2.3 wt.% [48]. Further, Mondolfo [21] reported that Mn marginally improves strength at the expense of ductility, while Kashyap et al. [49] indicate that presence of Mn weakens the strength of Al-7Si-Mg alloy.

Several literatures have indicated that Mn enhances yield strength and ultimate tensile strength of wrought Al-Si alloys [50, 51]. Formation of fine dispersoids of about 0.03–0.3 μm by the addition of Zr, Cr and Mn to commercial aluminium alloys was reported in these studies. Dispersoids significantly affect alloy's fracture toughness, strength, grain structures and recrystallization characteristics. Investigation has revealed that commercial 6000, 7000 and 8000 series aluminium alloys are improved by the addition of manganese with it ductility retailed [52].

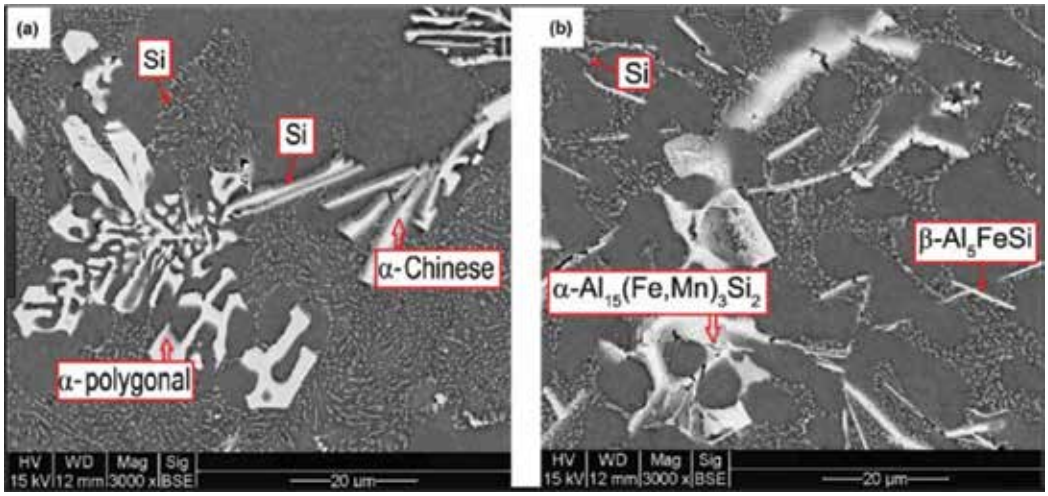


**Figure 9.** (a) Formation of a thick polyhedral $\alpha$-$Al_{15}(Fe,Mn)_3Si_2$ phase in the microstructure of the Al9Si0.8Fe alloy containing 0.7 wt.% of Mn; (b) micrograph of the Al9Si0.8Fe alloy containing 0.7 wt.% of Mn showing the presence of the β-Al5FeSi particles [2].

## 4. Processes to eliminate or ameliorate intermetallic deleterious effects

Many studies have reported various approaches and techniques in improving the mechanical properties of Fe-bearing intermetallics by the application of modification principle. Rapid solidification process increases the solubility fields and alters the morphology and size of microstructural elements but does not eliminate intermetallics. Das et al. demonstrated the effect of rapid cooling on alloy by processing Rheocast A380 alloy, using cooling slope (CS) technique to generate semisolid slurry from the superheated alloy melt [53]. The study observed finer, near spherical grains within the cooling slope fabricated slurry and in the solidified castings. This structure is different from the dendritic grains bounded by large eutectic phase within the conventionally cast A380 alloy. However, the most harmful intermetallic phase, β-$Al_5FeSi$ (monoclinic), was found to be present, accounting for the alloy's low ductility and consequent poor mechanical formability [54].

The Al–Si–Cu ternary system alloy, A380, has minute fractions of Fe, Mg, Mn, Ni and Zn. These impurity elements interact to form intermetallic compounds near the grain boundary and occasionally in the parent matrix. The expected intermetallics phases in A380 alloy are $\alpha$-phase, $\beta$-phase ($Al_5FeSi$), and ($Al_{15}(Fe,Mn)_3Si_2$). $\beta$-phase morphology is platelet-like (needle-like) appearance and serves as a stress-raiser in the matrix, while $\alpha$-Phase morphology is like polyhedral crystals and sometimes like Chinese script. The detrimental effects of intermetallic need to be removed or reduced; some of the techniques that are exploited include thermal treatment, chemical solutions and microstructural control by co-injecting inoculated intermetallic particles [54–56].

**Thermal treatment**—Heat treatment is a normal alternative to be considered. However, the dissolved phase possibly precipitated by thermal homogenisation process during artificial or natural ageing. This is not very effective because thermodynamically, stable phases are not influenced by heat treatment.

**Chemical solutions**—Conventional metallurgical chemical processes are used to eliminate the deleterious effects of Fe in Al alloys by limiting the amount of Fe to prevent the formation of Al-Fe-Si compounds.

**Microstructural control**—Co-injecting inoculated intermetallic particles is used to manipulate the microstructure. The particles, which vaporised during spray-forming, act as a substrate for heterogeneous nucleation, promoting nucleation and grow into the cubic. This principle involves the alteration of the type, size, morphology and the dispersion of the intermetallics in these alloys. Hosseinifar and Malakhov reported that the addition of 0.2% wt lanthanum (La) decreased the fraction of deleterious plate-like β-AlFeSi phase and increased the amount of a lesser harmful, $\alpha$-AlFeSi phase [57]. It was explained that La covers the surface of the Chinese script particles ($\alpha$-AlFeSi), a behaviour inferred to be like that of Strontium (Sr) addition. SEM images of Chinese script-shaped intermetallic compounds and the morphology of the β-AlFeSi phase are shown in **Figure 10**.

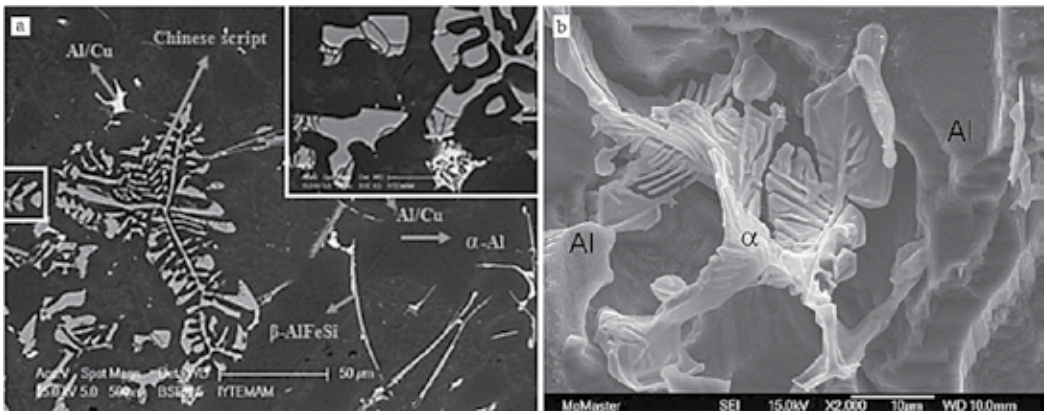


**Figure 10.** SEM images showing the (a) presence of the Chinese script-shaped intermetallic compounds [58]; (b) morphology of the b-AlFeSi phase [57].

The addition of a sufficient amount of Mn to Fe-rich intermetallics can defuse its brittleness and alter the platelet morphology to a less deleterious intermetallic compound [43, 59]. However, the addition of Mn to a melt containing Fe leads to another problem, as this increases the volume fraction of intermetallics and the mean diameter size of Fe solute. This development deteriorates the alloy's mechanical properties [60]. **Table 5** shows examples of intermetallics and their corresponding ductility improving alloying elements.

The thixoforming process has been described as an effective technique to modify the morphology of the primary phases. Gencalp and Saklakoglu used this method to improve the formability property of A390 alloy with excess levels of Fe and Mn [58]. The intermetallic compounds observed in A380 fabricated by thixoforming are $\alpha$-$Al_{15}Si_2(Fe,Mn)_3$ with polyhedral morphology, different from the Chinese script morphology observed in the traditional gravity casting. Also, in A380 alloy by thixoforming, the very harmful β-Al5FeSi particle morphology was small-plate and θ-Al2Cu phase in the form of particle. These phases, Al5FeSi and θ-Al2Cu phase morphology are needle-like and thin plate respectively in gravity casting. SEM images of the varied intermetallics between thixoforming and gravity casting are shown in **Figure 11**. The A380 by thixoforming alloys had better mechanical properties compared to A380 by traditional gravity casting method.

The solidification paths of 6xxx series Al alloys with and without La were established using careful calorimetric and microstructural investigations. Studies have shown that the addition of Sr. to Al-Si-Fe alloys prevents the formation β-phase intermetallic but promotes the production of a

| **Intermetallic** | ***β*-AlFeSi** | **$Ni_3Al$** | **TiAl** | **$Ti_3Al$** |
|---|---|---|---|---|
| Alloying element for ductility | Lanthanum (La) | Boron (B) | Manganese (Mn) | Niobium (Nb) |

**Table 5.** Intermetallics with ductility improving alloying elements [39].

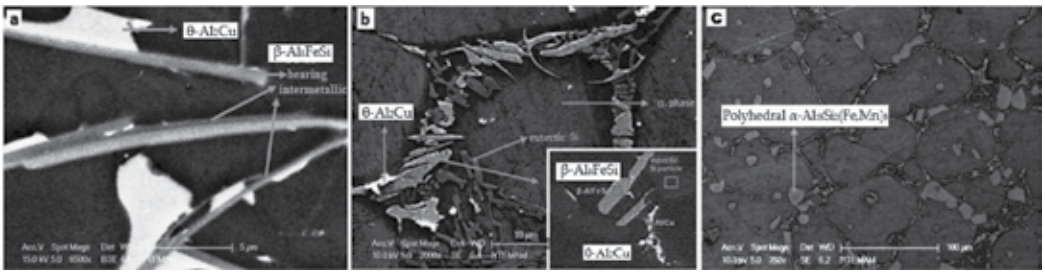


**Figure 11.** SEM images of (a) β-Al5FeSi needle-like intermetallics present in the gravity casting (b) particle small plate intermetallics, β-Al5FeSi found in thixoforming (c) $\alpha$-$Al_{15}Si_2(Fe,Mn)_3$ with polyhedral morphology found in thixoforming [58].

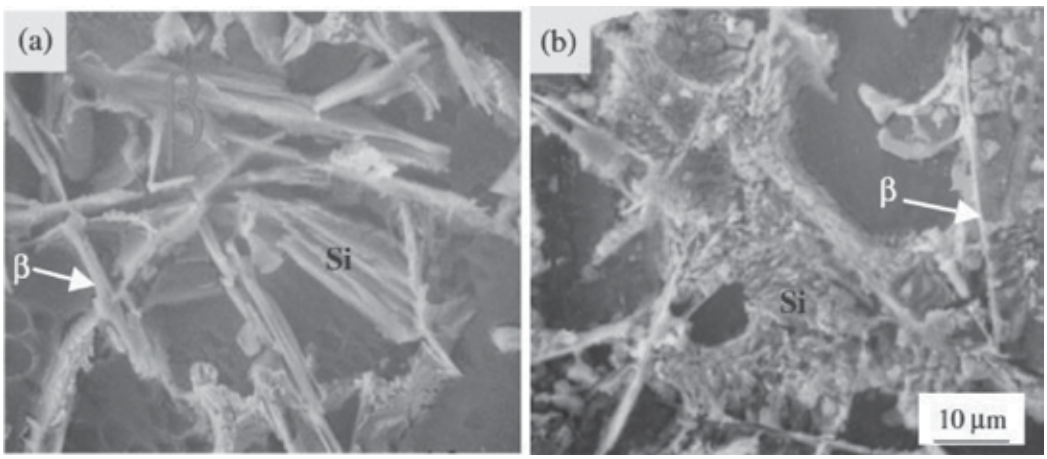


**Figure 12.** SEM images show the effect of adding Sr. on the microstructure of Al-6.5Si-3.5Cu-1.0Fe cast alloys (a) Sr. without; (b) with about 0.015% mass Sr [61].

less harmful phase, $\alpha$-AlFeSi, in as-cast alloys [48, 61]. Adding Sr to Al alloys under a fast cooling is an effective way of altering the amount, size and morphology of needle-like of $Al_5FeSi$ intermetallic compound. Chinese script or sludge are not formed in Al alloy without Mn. Addition of the combination of Fe and Mn at a high cooling rate was reported to be the most efficient technique of modifying intermetallic compounds [61]. SEM images in **Figure 12** show the Sr. unmodified and modified microstructure of Al-6.5Si-3.5Cu-1.0Fe (in mass %) alloy.

Apart from Sr., the less expensive rare-earth metal, lanthanum (La), was found to decrease the fraction of plate-like β-AlFeSi particles and increase the fraction of $\alpha$-AlFeSi particles with Chinese script morphology.

## 5. Conclusion

The influences of ternary alloying elements (Fe, Cu, Mn, and Mg) additions to Al-Si alloys (binary alloys) were discussed in this paper. The chapter observed that:

**i.** The equilibrium and non-equilibrium reactions that occur during the casting of Al alloy account for intermetallic phases.

**ii.** Primary alloying elements are not completely soluble in the $\alpha$-Al matrix and sometimes combine with impurities and matrix to form intermediate (intermetallics) phases.

**iii.** Intermetallics are products of incomplete solid solubility by alloy systems.

**iv.** Fe-based intermetallics are the most common. Fe-phases can be grouped into $\alpha$- phase, $\beta$-phases, Pi-phase, and $\delta$- phase, with $\alpha$- and $\beta$-phases the most common. The most harmful intermetallics in Al-Si-Fe alloys is $\beta$-phase ($\beta$-$Al_5SiFe$).

**v.** Iron is deliberately added to the alloy to prevent soldering in die casting mould.

**vi.** Addition of Mn and Sr reduces the negative effect of $\beta$-phase of Fe intermetallics by improving the ductility. However, the addition of Mn weakens the strength of Al-7Si-Mg alloy.

**vii.** Microstructural examination is one of the primary ways of evaluating the evolution of phases in materials.

## Author details

Williams S. Ebhota* and Tien-Chien Jen

*Address all correspondence to: willymoon2001@yahoo.com

Mechanical Engineering Department, University of Johannesburg, Johannesburg, South Africa

## References

[1] Ceschini L, Boromei I, Morri A, Seifeddine S, Svensson IL. Microstructure, tensile and fatigue properties of the al–10%Si–2%cu alloy with different Fe and Mn content cast under controlled conditions. Journal of Materials Processing Technology, Vol. 209, pp. 5669-5679, 2009/08/01/ 2009

[2] Baldan R, Malavazi J, Couto AA. Microstructure and mechanical behavior of Al9si0.8fe alloy with different Mn contents. Materials Science and Technology;**33**:1192-1199 2017/07/03 2017

[3] Aker A, Kaya H. Measurements of electrical and thermal properties with growth rate, alloying elements and temperature in the al–Si–X alloys. International Journal of Cast Metals Research;**30**:293-300 2017/09/03 2017

[4] Kuchariková L, Tillová E, Matvija M, Belan J, Chalupová M. Study of the precipitation hardening process in recycled Al-Si-cu cast alloys. Archives of Metallurgy and Materials. 2017;**62**:397

[5] Das S, Yegneswaran AH, Rohatgi PK. Characterization of rapidly solidified Aluminium-silicon alloy. Journal of Materials Science. 1987;**22**:3173-3177

[6] Uzun O, Karaaslan T, Keskin M. Production and structure of rapidly solidied Al-Si alloys. Turkish Journal Physics. 2001;**25**:455-466

[7] Zeren M, Karakulak E. Influence of Ti addition on the microstructure and hardness properties of near-eutectic Al–Si alloys. Journal of Alloys and Compounds, Vol. 450, pp. 255-259, 2008/02/14/ 2008

[8] Panagos P, Wang Y, McCartney DG, Li M, Ghaffari B, Zindel JW, et al. Characterising precipitate evolution in multi-component cast Aluminium alloys using small-angle X-ray scattering. Journal of Alloys and Compounds, Vol. 703, pp. 344-353, 2017/05/05/ 2017

[9] Barter S, Burchill M, Jones M. Fatigue crack growth calculations versus measurements of short increments of crack growth in 7XXX Aluminium alloys. International Journal of Fatigue. 2017/07/20/ 2017

[10] Yasakau KA, Zheludkevich ML, Ferreira MGS. Role of Intermetallics in corrosion of aluminum alloys. Smart corrosion protection. In: Intermetallic Matrix Composites. Sawston, Cambridge, England: Woodhead Publishing; 2018. pp. 425-462

[11] Gupta R, Sharma A, Pandel U, Ratke L. Effect of heat treatment on microstructures and mechanical properties of A356 alloy cast through rapid slurry formation (RSF) process. International Journal of Cast Metals Research, Vol. 30, pp. 283-292, 2017/09/03 2017

[12] Liao H, Sun Y, Sun G. Correlation between mechanical properties and amount of dendritic $\alpha$-Al phase in as-cast near-eutectic Al–11.6% Si alloys modified with strontium. Materials Science and Engineering: A, Vol. 335, pp. 62-66, 2002/09/25/ 2002

[13] Lasa L, Rodriguez-Ibabe JM. Wear behaviour of eutectic and hypereutectic Al–Si–cu–mg casting alloys tested against a composite brake pad. Materials Science and Engineering: A, Vol. 363, pp. 193-202, 2003/12/20/ 2003

[14] Roy RK. Recrystallization behavior of commercial purity Aluminium alloys. In: Monteiro WA, editor. Light Metal Alloys Applications. Rijeka: InTech; 2014 p. Ch. 04

[15] Smolej A, Slacek E, Turk R. State and development of some wrought aluminum alloys for special and general applications. Meta. 2002;**41**:149-155

[16] Mitra R. Intermetallic Matrix Composites: Properties and applications. Elsevier Science. 2017

[17] Phillips HWL, Annotated Equilibrium Diagrams of some Aluminium Alloy Systems. London Institute of Metals.; 1959

[18] Cáceres CH, Svensson IL, Taylor JA. Strength-ductility behaviour of al-Si-cu-mg casting alloys in T6 temper. International Journal of Cast Metals Research, Vol. 15, pp. 531-543, 2003/05/01 2003

[19] Smith R, Caceres CH, St-John D. The microstructure of Al-Si-Cu-Mg alloys. In: Materials Research 96, Brisbane, Australia. 1996. pp. 140-143

[20] Kral MV. A crystallographic identification of intermetallic phases in al–Si alloys. Materials Letters, Vol. 59, pp. 2271-2276, 2005/08/01/ 2005

[21] Mondolfo LF. Aluminium Alloys: Structure and Properties. England: Butterworths; 1976

[22] Salleh MS, Omar MZ, Syarif J. The effects of mg addition on the microstructure and mechanical properties of Thixoformed al–5%Si–cu alloys. Journal of Alloys and Compounds, Vol. 621, pp. 121-130, 2015/02/05/ 2015

[23] Liu Y, Huang G, Sun Y, Zhang L, Huang Z, Wang J, et al. Effect of Mn and Fe on the formation of Fe- and Mn-rich Intermetallics in al–5Mg–Mn alloys solidified under near-rapid cooling. Materials. 2016;**9**:88

[24] Taylor JA. The effect of iron in al-Si casting alloys. In: 35th Australian Foundry Institute National Conference, Adelaide, South Australia. 2004. p. 148

[25] Tillová E, Chalupová M, Hurtalová L. Evolution of phases in a recycled Al-Si cast alloy during solution treatment. In: Kazmiruk V, editor. Scanning Electron Microscopy. Rijeka: InTech; 2012 p. Ch. 21

[26] Chumak I, Richter KW, Ehrenberg H. Redetermination of iron Dialuminide, $FeAl_2$. Acta Crystallographica Section C. 2010;**66**:i87-i88

[27] Maximov B, Bolotina N, Simonov V, Petricek V, Schulz H. Structure of a modulated monoclinic phase of Na4TiP2O9. Acta Crystallographica Section B. 1994;**50**:261-268

[28] Stein F, Vogel SC, Eumann M, Palm M. Determination of the crystal structure of the ε phase in the Fe–al system by high-temperature neutron diffraction. Intermetallics, Vol. 18, pp. 150-156, 2010/01/01/ 2010

[29] Watanabe H, Yamamoto H, Ito K-i. Neutron diffraction study of the intermetallic compound FeSi. Journal of the Physical Society of Japan, Vol. 18, pp. 995-999, 1963/07/15 1963

[30] Marker MCJ, Skolyszewska-Kühberger B, Effenberger HS, Schmetterer C, Richter KW. Phase Equilibria and structural investigations in the system al–Fe–Si. Intermetallics, Vol. 19, 1919-1929, 2011/12/01/ 2011

[31] Ghosh G. Phase diagrams, crystallographic and thermodynamic data. In: Aluminium-Iron-Silicon, Light Metal Systems. Vol. 11A2. LandolteBörnstein, Berlin: Springer Verlag; 2005. pp. 359-409

[32] Du Y, Schuster JC, Liu Z-K, Hu R, Nash P, Sun W, et al. A thermodynamic description of the al–Fe–Si system over the whole composition and temperature ranges via a hybrid approach of CALPHAD and key experiments. Intermetallics, Vol. 18, pp. 150-156, 2008/04/01/ 2008

[33] Samuel E, Samuel AM, Doty HW, Valtierra S, Samuel FH. Intermetallic phases in Al–Si based cast alloys: New perspective. International Journal of Cast Metals Research, Vol. 27, pp. 107-114, 2014/01/01 2014

[34] Crepeau PN. Effect of iron in Al-Si casting alloys: A critical review. AFS Transactions. 1995;**103**:361-366

[35] Pearson WB. Handbook of Lattice Spacings and Structure of Metals and Alloys. London: Pergamon Press; 1967

[36] Khalifa W, Samuel FH, Gruzleski JE. Iron intermetallic phases in the Al corner of the Al-Si-Fe system. Metallurgical and Materials Transactions A. March 01 2003;**34**:807-825

[37] Backerud L, Krol E, Tamminen J. Solidification Characteristics of Aluminum Alloys: Wrought Alloys. Vol. 1. SkanAluminum: Sweden; 1986

[38] Hurtalová L, Tillová E, Chalupová M, Ďuriníková E. Effect of Chemical Composition of Secondary Al-Si Cast Alloy on Intermetallic Phases. 25/08/2017. Available: https://www.researchgate.net/profile/Lenka_Hurtalova/publication/313072818_Effect_of_chemical_composition_of_secondary_Al-Si_cast_alloy_on_intermetallic_phases/links/595b981ba6fdcc36b4dc327f/Effect-of-chemical-composition-of-secondary-Al-Si-cast-alloy-on-intermetallic-phases.pdf

[39] Smallman RE, Bishop RJ. Modern Physical Metallurgy and Materials Engineering. 6th ed. Linacre House, Jordan Hill, Oxford OX2 8DP: Butterworth-Heinemann; 1999

[40] Lievers WB, Pilkey AK, Lloyd DJ. The influence of iron content on the bendability of AA6111 sheet. Materials Science and Engineering: A, Vol. 361, pp. 312-320, 2003/11/25/ 2003

[41] Darvishi A, Maleki A, Atabaki MM, Zargami M. The mutual effect of iron and manganese on microstructure and mechanical properties of aluminium-silicon alloy. Association of Metallurgical Engineers of Serbia. 2010;**16**:pp. 11-24

[42] Shankar S, Apelian D. Die soldering: Mechanism of the Interface reaction between molten aluminum alloy and tool steel. Metallurgical and Materials Transactions B-Process Metallurgy and Materials Processing Science. 2002;**33**:465-476

[43] Shabestari SG, Shahri F. Influence of modification, solidification conditions and heat treatment on the microstructure and mechanical properties of A356 aluminum alloy. Journal of Materials Science. March 01 2004;**39**:2023-2032

[44] Hosseinifar M, Malakhov DV. The sequence of intermetallics formation during the solidification of an Al-Mg-Si alloy containing La. Metallurgical and Materials Transactions A. 2011;**42A**:825-833

[45] Spencer K, Corbin SF, Lloyd DJ. The influence of iron content on the plane strain fracture behaviour of AA 5754 Al–Mg sheet alloys. Materials Science and Engineering: A;**325**:pp. 394-404. 2002/02/28/ 2002

[46] Sarkar J, Kutty TRG, Wilkinson DS, Embury JD, Lloyd DJ. Tensile properties and bendability of T4 treated AA6111 aluminum alloys. Materials Science and Engineering: A, Vol. 369, pp. 258-266, 2004/03/25/ 2004

[47] Podprocká R, Bolibruchová D, Chalupová M. Reducing the negative of the iron in the alloy based on al-Si-mg by manganese. Archives of Foundry Engineering. 2017;**17**:212

[48] Shabestari S, Mahmudi M, Emamy M, Campbell J. Effect of Mn and Sr on Intermetallics in Fe-rich eutectic al-Si alloy. International Journal of Cast Metals Research. 2002;**15**:17-24

[49] Kashyap KT, Murali S, Raman KS, Murthy KSS. Casting and heat treatment variables of Al-7%Si-mg alloy. Materials Science and Technology. 1993;**9**:189-203

[50] Garrett GG, Knott JF. The influence of compositional and microstructural variations on the mechanism of static fracture in aluminum alloys. Metallurgical Transactions A. 1978;**9**:1187-1201

[51] Santner JS. A study of fracture in high purity 7075 aluminum alloys. Metallurgical Transactions A. 1978;**9**:769-779

[52] Park DS, Nam SW. Effects of manganese Dispersoid on the mechanical properties in al-Zn-mg alloys. Journal of Materials Science. 1995;**30**:1313-1320

[53] Das P, Kumar M, Samanta SK, Dutta P, Ghosh D. Semisolid processing of A380 Al alloy using cooling slope. Materials and Manufacturing Processes. 2014;**29**:422-428. 2014/04/03 2014

[54] Borba EC, Andrade MS. Thermodynamic calculations in the AlMnSi system. Presented at the 17° CBECIMat - Congresso Brasileiro de Engenharia e Ciência dos Materiais, Foz do Iguaçu, PR, Brasil, 2006

[55] Warmuzek M, Mrówka G, Sieniawski J. Influence of the heat treatment on the precipitation of the intermetallic phases in commercial AlMn1FeSi Alloy. Journal of Materials Processing Technology;**157**:pp. 624-632. 2004/12/20/ 2004

[56] Dang B, Jian Z-y, Xu J-f, Chang F-e, Zhu M. Effect of phosphorus and heat treatment on microstructure of al-25%Si alloy. China Foundry. January 01 2017;**14**:10-15

[57] Hosseinifar M, Malakhov DV. Effect of Ce and la on microstructure and properties of a 6xxx series type aluminum alloy. Journal of Materials Science. October 23 2008;**43**:7157

[58] Gencalp Irizalp S, Saklakoglu N. Effect of Fe-rich intermetallics on the microstructure and mechanical properties of thixoformed A380 aluminum alloy. Engineering Science and Technology, An International Journal;**17**:pp. 58-62. 2014/06/01/ 2014

[59] Apelian D, Shivkumar S, Sigworth G. Fundamental aspects of heat treatment of cast Al-Si-mg alloys. AFS Transactions. 1989;**97**:727-742

[60] Emamy GM. Casting Properties of Metal Matrix Composites. Ph.D Thesis. The University of Birmingham; 1995

[61] Ashtari P, Tezuka H, Sato T. Influence of Sr and Mn additions on intermetallic compound morphologies in Al-Si-Cu-Fe cast alloys. Materials Transactions. 2003;**44**:2611-2616

Chapter 3

# Intermetallic Bonding for High-Temperature Microelectronics and Microsystems: Solid-Liquid Interdiffusion Bonding

Knut E. Aasmundtveit, Thi-Thuy Luu,
Hoang-Vu Nguyen, Andreas Larsson and
Torleif A. Tollefsen

Additional information is available at the end of the chapter

http://dx.doi.org/10.5772/intechopen.75139

**Abstract**

Solid-liquid interdiffusion (SLID) bonding for microelectronics and microsystems is a bonding technique relying on intermetallics. The high-melting temperature of intermetallics allows for system operation at far higher temperatures than what solder-bonded systems can do, while still using similar process temperatures as in common solder processes. Additional benefits of SLID bonding are possibilities of fine-pitch bonding, as well as thin-layer metallurgical bonding. Our group has worked on a number of SLID metal systems. We have optimized wafer-level Cu-Sn SLID bonding to become an industrially feasible process, and we have verified the reliability of Au-Sn SLID bonding in a thermally mismatched system, as well as determined the actual phases present in an Au-Sn SLID bond. We have demonstrated SLID bonding for very high temperatures (Ni-Sn, having intermetallics with melting points up to 1280°C), as well as SLID with low process temperatures (Au-In, processed at 180°C, and Au-In-Bi, processed at 90–115°C). We have verified experimentally the high-temperature stability for our systems, with quantified strength at temperatures up to 300°C for three of the systems: Cu-Sn, Au-Sn and Au-In.

**Keywords:** microelectronics/microsystem assembly, bonding technology, harsh environments, wafer processing, reliability, transient liquid phase

# 1. Motivation for SLID

## 1.1. The challenge of die attach and interconnection

For all electronic systems, the attachment of components to substrates and their electrical connection is a crucial part of the system. Traditionally, the processes for attachment and interconnection have been considered more a craft than a science. The historical focus of electronics and microtechnology has been on the design, manufacturing and testing of components, circuits and devices, rather than on the system integration and the processes needed for actually building the system.

The 'electronic revolution' has given ever-increasing performance of devices at ever-decreasing prices for more than half a century. Initial milestones were the invention of the transistor (1947) and the integrated circuit (IC) (1958). The driving factor has been a continuous decrease in size (of components and on features of components) and cost, made possible through batch processing of silicon wafers. Single-crystal silicon is a very well-defined material with extremely well-characterized properties, allowing process technology that yields extremely small features (10 nm by 2017, with a further decrease expected). Miniaturization of components and the use of large Si wafers give a huge number of components manufactured in every batch, lowering the cost. Furthermore, miniaturization allows an increase in operating frequency (or a decrease in response time), as well as lower losses. The miniaturization and the high-frequency performance of the attachment and electrical interconnect technology has not maintained the same pace as the integrated circuit technology. The need for a more scientific approach for the system-integration technologies has become evident and has gradually evolved over the last decades [1]. The scientific approach is typically termed 'packaging technology', 'system-integration technology' or 'assembly, interconnect and packaging'.

Today, it is generally acknowledged that system-integration technologies often are the limiting factor for the success of an electronic system, in particular, in four different aspects: size, performance, price and reliability.

1. Size: the dimensions needed for electrical interconnections are far larger than the dimensions possible in Si technology. Also, a complex integrated circuit will typically need a high number of interconnects. Hence, the actual size of the component will typically be defined by the space needed to create the interconnects, rather than by the complexity of the IC itself.
2. Performance: a larger feature size implies a larger parasitic inductance and capacitance, as well as a longer signal path. This will limit the high-frequency/high-speed performance of the device. Typically, the packaged device therefore shows a lower operating frequency than what the naked chip would allow.
3. Price: the low price of Si chips is enabled by the parallel processing of a large number of components, in batch processes using large wafers. System-integration technologies such as die attach and electrical interconnection are traditionally processes treating single components, thus being serial processing rather than parallel processing. When the number of devices is high, these serial processes will be more expensive than the parallel Si processing.

http://dx.doi.org/10.5772/intechopen.75139

4. Reliability: the most common reason for failure of a system is broken interconnects. There are various reasons for this, some examples are stress caused by different thermal expansions of chip and substrate, uncontrolled growth of intermetallic layers where two metals are joined and galvanic corrosion. Understanding the behaviour of the materials that make up the integrated system is therefore crucial for reducing the failure rate of a device.

In summary, there is a strong need to continue research on interconnect technology, with the aim to construct reliable interconnects in a manufacturing-friendly process. The actual requirements will vary greatly depending on the application, but the possibility to miniaturize the interconnect, as well as to have low electric resistance and high mechanical strength, is an important requirement in many applications.

### 1.2. Soldering: the standard interconnection technique

The most commonly used interconnection technique is soldering. Any new technology is therefore naturally compared with soldering. Soldering is used in a number of different technologies, with a range of solder materials and on different dimensions of the joints. The common nature for any solder process is the use of a solder material that melts upon heating (wetting the two surfaces that are to be joined), and solidifies upon cooling (forming a solid joint). Typical solder materials are eutectic compounds, chosen because of their low and well-defined melting points. Historically, the standard solder material has been eutectic Sn-Pb, with a melting/solidification temperature of 183°C. Upon the ban of Pb in electronics (RoHS initiative) in 2002, a variety of lead-free solders have emerged, such as Sn-Ag-Cu compounds. The most common is 'SAC305', composed of 3.0% Ag, 0.5% Cu and 96.5% Sn, with a melting point of 220°C (as comparison, pure Sn melts at 232°C).

The advantages of soldering include the following:

1. Short process time: the melting and re-solidification in a eutectic-soldering process are both instantaneous processes. The soldering process does not depend on time-consuming process like chemical reactions, solid-state plastic deformation, stress relaxation or curing.
2. Self-alignment: a certain, initial misalignment of chip and substrate is compensated. While the solder is liquid during the bonding process, the chip can self-align because there is a driving force to minimize the surface tension of a liquid solder. Self-alignment relaxes the requirement to assembly precision, which can lower the cost substantially for fine-pitch systems.
3. Compensation of geometric imperfections: due to the liquid state during bonding, a solder process will create contact also if there is a variation in pad height, surface roughness or non-parallel contact surfaces.
4. Easy reworkability: the solder process is reversible, remelting at the same temperature as the original melting/solidification. Rework may be performed simply by re-heating the solder joint.
5. High conductance of joint: because of the metallic nature of the solder.

### 1.3. Shortcomings of soldering

Although soldering is a very versatile process, considered to render high reliability, it has certain shortcomings.

Solder joints will not withstand temperatures approaching the melting point of the solder. The joint will fail if the melting point is reached, but will also be susceptible of severe degradation, for example, by creep, at temperatures significantly below the melting temperature. A number of high-temperature applications, such as engine control, oil and gas down-hole instrumentation, geothermal energy and thermoelectric generators, require bonding that can withstand higher temperatures than the solder can. High temperatures may also be an issue during manufacturing: if chips are stacked in three dimensions (3D), more than one bonding process is required. For sequential bonding, soldering with the same solder alloy will jeopardize the earlier made connections. This may to a certain degree be solved by choosing different solder compounds with different melting points. However, there are a limited number of relevant solder alloys, and the corresponding span in melting temperatures is limited, also taking into account that high-temperature solders require high process temperatures and low-temperature solders limit the useful application of temperatures.

If the solder joint is subject to elevated temperature for a prolonged time, the intermetallic layer at the component/pad interface will increase in thickness in an uncontrolled way. Hence, the properties of the joint will change with time. The intermetallic compounds (IMCs) are typically harder and more brittle than the pure metals, particularly compared with Sn-based solder. The interface between the soft solder and the hard intermetallics is a typical fracture site when the joint is subject to mechanical load.

The liquid nature of solder bonding gives rise to a risk of short circuits between neighboring interconnects, if the liquid solder flows between. This dictates a minimum isolation distance between interconnects and is thus a limiting factor for miniaturization, particularly for devices with many interconnects, such as digital circuits.

### 1.4. The principle of SLID

Solid-liquid interdiffusion (SLID) bonding is a technique based on intermetallics as the bonding medium, receiving increasing attention as an alternative to processes such as solder bonding [2, 3]. While resembling solder bonding in terms of process temperature and materials in use, SLID bonding has an excellent thermal stability: the bond survives temperatures far surpassing the bonding temperature. This makes SLID bonding a promising candidate for high-temperature applications, where solder bonding is not applicable.

The SLID process (also known as transient liquid phase bonding [4–6], isothermal solidification [7] or 'off-eutectic bonding' [8]) uses a system of two metals, where one melts at a high temperature (such as Cu, Au, Ag and Ni) and the other melts at a low temperature (such as Sn and In). The bonding process takes place at a temperature somewhat above the lower melting temperature, assuring interdiffusion of the two metals reacting to intermetallic compounds (IMCs) with high-melting points [9] (see Cu-Sn phase diagram in **Figure 1** as an example). To obtain the high-temperature stability, a complete conversion of the low-temperature melting metal to IMC is needed. Excess of high-temperature metal is normally

http://dx.doi.org/10.5772/intechopen.75139

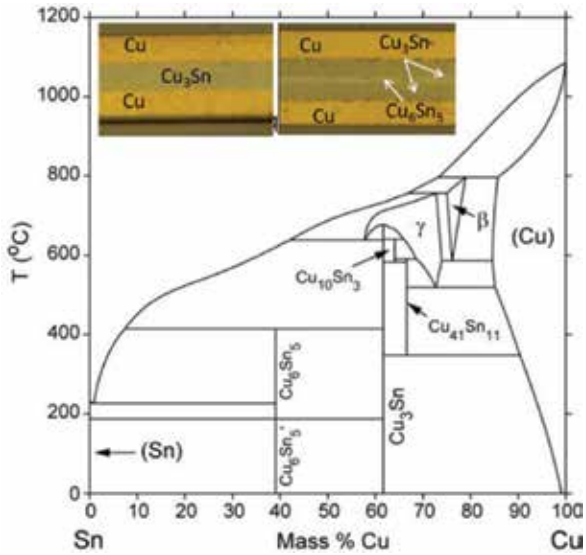


**Figure 1.** Cu-Sn phase diagram. The insets show a cross section of SLID bonds: complete conversion to $Cu_3Sn$ (left), and incomplete conversion with the remaining $Cu_6Sn_5$ layer (right).

desired, to allow for process variations such as deviations in the initial layer thickness and any inhomogeneous diffusion during bonding, and to ensure that no reaction takes place between the low-temperature metal and the thin metal layers that serve as adhesion/barrier layers between the two-metal system and the substrate/chip. Such reactions might result in new IMCs with less predictable properties. Importantly, an excess of high-temperature metal also gives ductility to the final bond (the pure metal normally being more ductile than the IMCs).

The Cu-Sn SLID system is the one that has received the most attention. As seen from the phase diagram in **Figure 1**, two IMCs are stable at room temperature: $Cu_6Sn_5$ and $Cu_3Sn$. The goal of a Cu-Sn SLID process will be a system in thermal equilibrium with remaining Cu on both sides of the IMC bond-line, implying $Cu_3Sn$ as being the desired phase.

The initial layers of Cu and Sn are typically in the range of micrometres. The bonding process temperature is above the melting point of Sn (232°C), typically in the range of 250–300°C. Cu diffuses into the liquid Sn, and the IMC $Cu_6Sn_5$ solidifies isothermally. At the $Cu/Cu_6Sn_5$ boundary, Cu and Sn react to form $Cu_3Sn$. $Cu_3Sn$ formation is much slower than $Cu_6Sn_5$ formation, since solid-state diffusion through the $Cu_6Sn_5$ layer is required. The bonding temperature is kept for sufficiently long time (typically ~30 min) for the reaction to $Cu_3Sn$ to be completed; the final bond consisting of a $Cu/Cu_3Sn/Cu$ layer structure. The bond is then in thermal equilibrium, and no material change is expected upon annealing or aging. The melting temperature of this completed bond-line is ~700°C.

Although the high-temperature stability was the original motivation for developing SLID for interconnections [9, 10], it also has good promise for creating fine-pitch interconnection [3]. Also, the ability to form thin, well-defined bond-lines with metallurgical bond is a specific advantage of SLID [11].

In this book chapter, we detail some of the main results from the SLID research at University of Southeast Norway (USN), which is ongoing during the last decade.

## 2. SLID bonding

### 2.1. Test vehicles and substrates

Much of the SLID work done in our group, as well as in other research groups, is carried out by bonding pairs of silicon chips. Si is the standard material for electronics as well as for MEMS (Micro-Electro-Mechanical Systems). Stacking multiple chips on top of each other is increasingly important, to increase integration density by also using the third dimension. By bonding identical materials, the challenge of a thermal mismatch is minimized: during temperature variation, the two bonding partners will experience the same dimensional change, thus minimizing thermomechanical stress.

For the typical bonding process where a chip is bonded to a substrate, the challenge of dissimilar thermal expansion of a chip and a substrate arises. Thermomechanical stress is the result when dissimilar materials are joined together and experience temperature variations. Solder bonding is suitable to handle this, since solder is soft and the solder thickness typically is >100 μm. SLID bonding typically uses thin bond-lines, in the micrometre range. Since the SLID process relies on diffusion, thin layers ensures that the bonds can be manufactured in a reasonable time. Furthermore, the IMC bonding layers are much harder than a solder and will therefore not absorb much of the thermomechanical stress. The remaining layers of a high-melting point metal (such as Cu or Au) may be utilized as the stress-absorbing layer. In our work, we have also bonded SiC chips to ceramic substrates with a significant thermal mismatch using Au-Sn SLID, obtaining excellent reliability in thermal cycling, as will be detailed subsequently.

### 2.2. Metal layers: design and manufacturing

The layer thicknesses of our initial two-metal system (such as Cu and Sn in the case of Cu-Sn SLID) are typically in the range of micrometres, produced by electroplating. The process is therefore well suited for wafer-level processing with additive patterning, opening for cost-effective solutions and for fine-pitch applications. The layer thicknesses should be designed so that there remains a high-temperature metal after the bond is finalized. Using Cu-Sn SLID as the example, a thickness ratio (Cu to Sn) of 1.3 is needed in order to obtain a final $Cu/Cu_3Sn/Cu$ structure, as seen by

$$\frac{t_{Cu}}{t_{Sn}} > \frac{3\,M_{Cu}\,\rho_{Sn}}{M_{Sn}\,\rho_{Cu}} = 1.3 \tag{1}$$

(where $t_{Cu}$ and $t_{Sn}$ signify the initial total thickness on the two bonding partners, $M_x$ and $\rho_x$ signify the atomic weight and the mass density of element $x$). Note that this Sn layer may be deposited on one of the bonding partners, or half the thickness on each of the bonding partners. Whereas Eq. (1) dictates the maximum relative Sn thickness, the overall roughness of Cu layers dictates a minimum Sn thickness: since Cu is solid during the entire bonding process, the highest protrusions of the Cu layer will define the standoff height between the two bonding partners. Such

http://dx.doi.org/10.5772/intechopen.75139

protrusions may be present, for example, at the edges of electroplated layers. As a rule of thumb, the Sn layer should be thicker than the variation in the surface height of the Cu layer, to ensure that liquid Sn fills the volume between the two Cu pads and thus minimizes void formation.

Alternative metal deposition techniques are evaporation, sputtering, printing or the use of preforms. With the exception of preforms, all are compatible with wafer-level processing and patterning. Preforms can be used for die bonding where fine-pitch patterning is not required and for proof-of-concept experiments. Evaporation and sputtering are restricted to thin films (not much more than 1 μm). Printing (of metal pastes) is a low-cost and versatile process, typically giving thicker (tens to hundreds of micrometres) metal layers, with somewhat lower precision in the lateral feature size than the photolithography-defined techniques (evaporation, sputtering, electroplating). Pastes may be formulated with a small particle size to allow fast reactions, but the availability of relevant pastes is presently limited.

### 2.3. Bonding profiles

The bonding profile (temperature and pressure as a function of time) chosen is crucial in order to obtain optimal results within a reasonable time frame. To obtain a uniform growth of the IMC layers, a short holding time slightly below the melting temperature is typically used [12]. This ensures a thin IMC layer formed at the material interfaces while all materials are solid. This controls diffusion through the solid IMC also when the low-melting point metal is melted. If the temperature is raised to the melting point without this interface IMC formed, the system is prone to scallop growth of IMCs, with voids in the bond-line as a result [13, 14].

### 2.4. Wafer-level versus chip-level bonding: atmosphere during bonding

We perform bonding at a chip level as well as at a wafer level. Wafer-level processing is the preferred option for high-volume industry, since the parallel processing increases throughput greatly and has the potential for lowering the unit cost. Chip-level processing is the relevant choice for low-volume industry. In a research setting, chip-level bonding also allows for more variation of process parameters to be optimized.

For Sn-based solder on Cu pads, the use of flux is essential for avoiding oxides during soldering. However, remaining flux is a challenge, particularly for vacuum cavities in MEMS devices. Also, the cleaning of flux residues is more difficult for thin SLID bonds than for solder bonds with a higher chip-to-substrate separation. All the SLID bonding in this work (Cu-Sn as well as other systems) is therefore flux-free. For Cu-Sn SLID, this is obtained by using equal Sn thickness on both bonding partners, Sn oxides being thinner and more readily absorbable in the bond-line than Cu oxides [15].

### 2.5. Characterization

The performance of the bonds is evaluated by shear testing. Usually, shear testing is performed at room temperature. In addition, we performed shear testing while the bonded sample was heated, to verify the applicability of the SLID bonds at elevated temperatures. The fracture surfaces after die shear are inspected in order to identify the fraction sites, showing up at the weaker parts of the SLID bonds.

The bond-line morphology and the phases present are investigated by cross-section microscopy. Cross-sections are made either by mechanical grinding and polishing or by Ar ion milling. Samples are inspected by using optical microscopy and scanning electron microscope (SEM) with EDX (energy-dispersive X-ray spectroscopy). For Au-Sn, we also used X-ray diffraction in order to more clearly identify the phases in the bond-line.

## 3. Cu-Sn bonding

### 3.1. Rationale for Cu-Sn

Cu-Sn is by far the most investigated SLID bonding system and also the one used as an example in the previous section. It is the natural choice in applications sensitive to cost, and the material system is quite similar to what is common in soldering, where an Sn-based solder applied to Cu pads is the most common configuration. The fundamental understanding of the process is well established. Our group has experimentally verified the high-temperature stability that has long been predicted from the phase diagram, as detailed in Section 8.1. The main part of our work on Cu-Sn SLID has focused on manufacturing aspects: how to make a flux-free wafer-level process with optimized manufacturing parameters and a predictable result possible. This has led to the industrial implementation of our Cu-Sn SLID process [15–17].

### 3.2. Fabrication process

Our Cu-Sn SLID work has aimed for wafer-level bonding, with initial experiments carried out at chip level. All our work has been on Si substrates with electroplated layers, typically 5 μm Cu and 1–2 μm Sn. For wafer-level bonding, equal layer thicknesses on both bonding partners have been used, and the bonding profile (temperature and pressure vs. time) has been carefully selected to allow flux-free bonding [2, 18]. For the initial chip-bonding, Sn has been electroplated only on the chip side, in order to allow maintaining the substrate hot (no Cu-Sn interdiffusion prior to bonding) while mounting successive Sn-coated chips.

### 3.3. Wafer-level process optimization

In order to optimize the bonding profile for a Cu-Sn SLID bond, we developed a model for the kinetics of the reactions from Cu and Sn to IMCs [19]. We annealed Cu-Sn bi-layered test structures, at different times and temperatures. The samples were cross-sectioned and layer thicknesses measured in optical microscopy, the different phases having been verified by SEM and EDX. The layer thickness of pure, unreacted Sn was obtained by etching with 30% HCl (selectively etching Sn and not IMCs), measuring the $Cu_3Sn$ and $Cu_6Sn_5$ thicknesses and thus calculating the Sn thickness. The evolution of the IMC thickness is then modeled by a quasi-diffusion equation:

$$y_t^2 - y_0^2 = k_0 \, exp\left(\frac{-Q}{RT}\right) t^{2n} \tag{2}$$

http://dx.doi.org/10.5772/intechopen.75139

where $y_t$ is the IMC thickness, alternatively Sn thickness reacting to form IMCs; T is the absolute temperature; $t$ is the annealing duration, $y_0$ is the initial IMC thickness, or Sn thickness already reacted with Cu at $t = 0$; $n$ is an empirical exponent, where $n = 0.5$ signifies diffusion as the mechanism; $Q$ is the activation energy; $k_0$ is the diffusion coefficient.

Values for $Q$, $k_0$ and $n$ (shown in **Table 1**) are extracted through linear fitting using appropriate logarithmic plots, and a Matlab model is constructed, predicting the IMC evolution for any given bonding temperature profile [19]. Note that the change in the empirical exponent $n$ reflects the different physical processes occurring: $n = 0.5$ corresponds to the reaction kinetics being limited by diffusion, implying that the reaction to IMCs is fast. Below the melting point of Sn, the reactions are slower, implying that diffusion does not alone contribute to the kinetics.

**Figure 2** shows the experimentally observed thicknesses, together with curves for the model given by Eq. (2) and **Table 1**.

**Figure 3** shows two different bonding profiles: one where the simulation predicts that a layer of $Cu_6Sn_5$ remains after bonding and one where the bond is predicted to be fully converted to a $Cu/Cu_3Sn/Cu$ structure. The lower part of the figures shows cross-section micrographs of samples bonded with the corresponding bonding profile, showing a good correspondence to the predicted values. Important parameters from a manufacturing point of view are as follows:

| | **$Cu_3Sn$** | **Reacted Sn** |
|---|---|---|
| $k_0\left[\frac{\mu m^2}{min^{2n}}\right]$ | $7.9 \times 10^6$ | $2.8 \times 10^4$ |
| $Q\left[\frac{kJ}{mol}K\right]$ | 78 | 52 |
| Empirical exponent $n$ | 0.5 ($T \geq 232^\circ C$) | 0.45 ($T \geq 180^\circ C$) |
| | 0.4 ($180^\circ C \leq T \leq 232^\circ C$) | 0.3 ($T < 180^\circ C$) |

**Table 1.** Kinetics coefficients for Cu-Sn SLID. Reprinted with permission from Springer Nature [19].

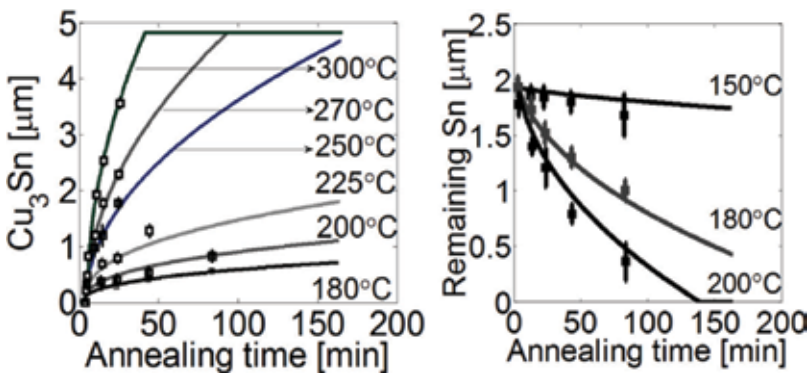


**Figure 2.** Comparison between simulation results (lines) and measured values (discrete points) for both $Cu_3Sn$ thickness and remaining Sn. Reprinted with permission from Springer Nature [19].

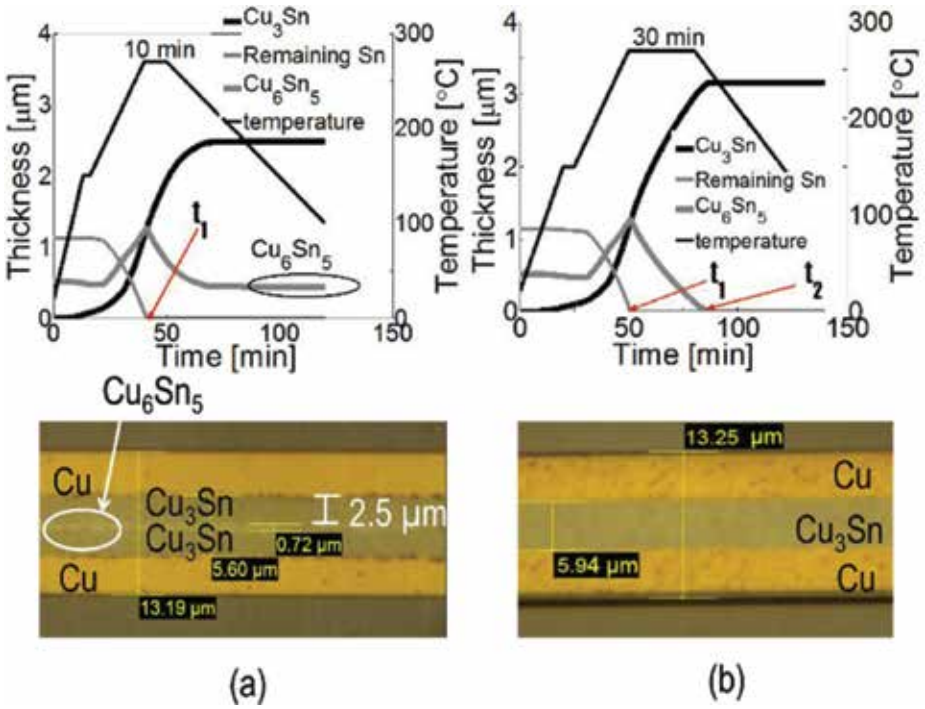


**Figure 3.** Different bond profiles for Cu-Sn SLID wafer-level bonding and the corresponding cross sections. Reprinted with permission from Springer Nature [19].

1. $t_1$: the time from the start of the bonding process until all Sn is consumed and the bond has solidified: 41 min for profile (a), 50 min for profile (b).
2. $t_2$: the time from the start of the bonding process until the final $Cu/Cu_3Sn/Cu$ structure is obtained: 85 min for profile (b), not achieved for profile (a).

$t_2$ gives the total bonding process time, whereas $t_1$ gives the minimum time where the wafer bonder should be used (the remaining time to $t_2$ may be performed as batch annealing).

## 4. Au-Sn bonding

### 4.1. Rationale for Au-Sn

Au-Sn is the system of choice for high reliability systems, for example, when chemical inertness and ductility are desired [20]. As a consequence, our work on Au-Sn SLID bonding has included verification of reliability. The Au-Sn phase diagram (see **Figure 4**) is quite more complex than Cu-Sn, and the fundamentals of Au-Sn SLID bonds have previously been less explored than those of Cu-Sn SLID. Hence, our work has included an investigation of the phases present in Au-Sn SLID bonding and the properties of the resulting bond. We have experimentally verified the expected high-temperature stability, as will be detailed in Section 8.1 subsequently.

http://dx.doi.org/10.5772/intechopen.75139

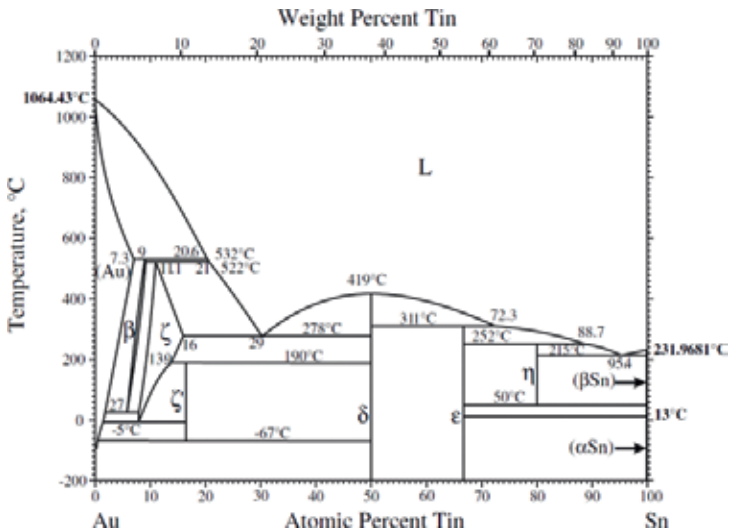


**Figure 4.** Au-Sn phase diagram, reprinted with permission from Springer Nature [21].

### 4.2. Fabrication process and testing

For the reliability test and the investigations of the phases present in an Au-Sn SLID bond, a chip/substrate system relevant for use at high temperatures was used: an SiC dummy transistor (BJT) from Fairchild Semiconductor was bonded to an $Si_3N_4$ substrate with symmetric active metal-bonded (AMB) Cu (150 μm) metallization. This system has a significant mismatch in coefficients of thermal expansion (CTE): SiC and $Si_3N_4$ having similar CTE of 4.2 ppm/K while the thick Cu layers have a CTE of 17 ppm/K giving a realistic substrate-to-chip thermal mismatch.

The Au-Sn SLID bonding was performed by electroplating 10 μm Au layers on both the chip and the substrate, sandwiching a 7.5 μm thick eutectic $Au_{80}Sn_{20}$ preform between the bonding partners and the bond, varying bonding temperature in the range of 290–350°C and the bonding time in the range of 4–14 min.

The quality of the bonds was probed by die shear testing.

Reliability tests were performed by thermal cycling (1000 cycles, 0–200°C) and high-temperature storage (HTS) at 250°C up to 6 months. Die shear strength was performed after thermal cycling and/or HTS.

Cross-section microscopy was performed on as-bonded and high-temperature-stored samples. The phases were identified by a combination of optical microscopy, SEM/EDX and X-ray diffraction, the latter technique being used both on cross-sectioned samples and on fracture surfaces.

### 4.3. Main results

The die shear strength of Au-Sn SLID bonds is found to be excellent, in the order of 140 MPa. Such high bonding strengths are obtained for bonding temperatures down to 300°C and bonding times down to 6 min, as shown in **Figures 5** and **6**. A lower bonding time

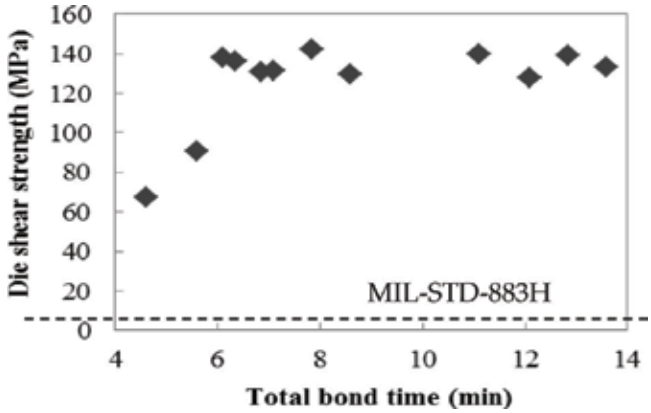


**Figure 5.** The die shear strength of an Au-Sn SLID bond as a function of the bonding time (time above the melting point of eutectic Au-Sn (278°C)) [22] (© 2012 IEEE).

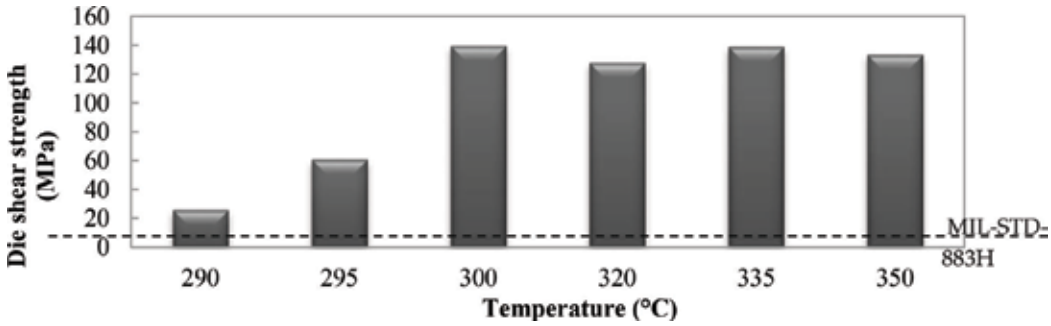


**Figure 6.** The die shear strength of an Au-Sn SLID bond as a function of the bonding temperature [22] (© 2012 IEEE).

(tested down to 4 min) and temperature (tested down to 290°C) give significantly lower shear strength, but still well above the requirements of MIL-STD-883H [22].

*4.3.1. Phases obtained*

**Figure 7** shows cross-sectional micrographs of a sample bonded at 300°C for 6 min. The IMC layer has been identified by EDX and X-ray diffraction to be the ζ-phase.

Cross-section microscopy (optical and SEM) shows that high-temperature-stored samples have thicker IMC layers compared to the as-bonded. Using X-ray diffraction on cross sections and on fractured bonding surfaces, the IMC layer of these high-temperature-stored samples is identified as the β-phase [23]. This shows that the as-bonded samples with an Au/ζ/Au bond layer structure are not yet in thermal equilibrium. The Au/β/Au structure obtained after our high-temperature storage represents a thermal equilibrium situation, since the Au-Sn phase diagram (**Figure 4**) does not contain phases between Au and β. When designing a layer structure for Au-Sn SLID bonds for high-temperature applications, the overall Au-Sn system should therefore have an Sn content below 8 at%. The evolution of the layer structure upon bonding and aging is sketched in **Figure 8**.

http://dx.doi.org/10.5772/intechopen.75139

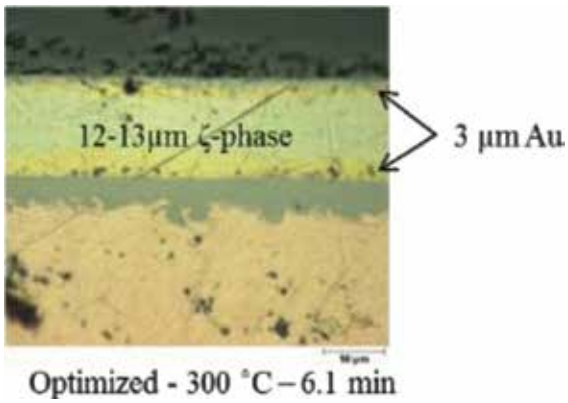


**Figure 7.** Cross section of an optimized Au-Sn SLID bond [22] (© 2012 IEEE).

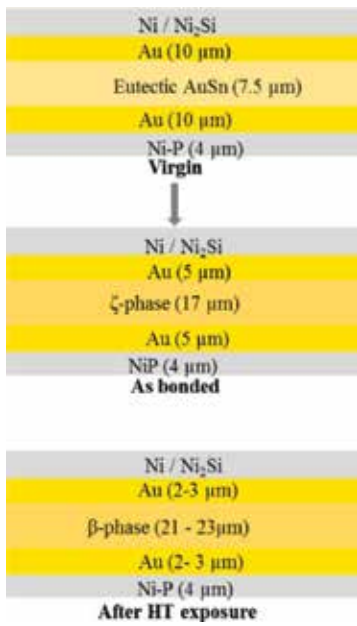


**Figure 8.** A schematic overview of the layered structure of an optimized Au-Sn SLID bond at different life stages. The different material phases were identified with energy-dispersive X-ray spectroscopy (EDX) and X-ray diffraction. Reprinted with permission from Springer Nature [23].

### *4.3.2. Thermal cycling survival*

Even after combined high-temperature storage and thermal cycling, the shear strength of an Au-Sn SLID-bonded sample is very high, around 70 MPa (see **Figure 9**). This clearly shows that Au-Sn SLID bonding is a suitable choice for high-temperature applications, also with thermally mismatched substrate-chip pairs. The demonstrated reliability is excellent.

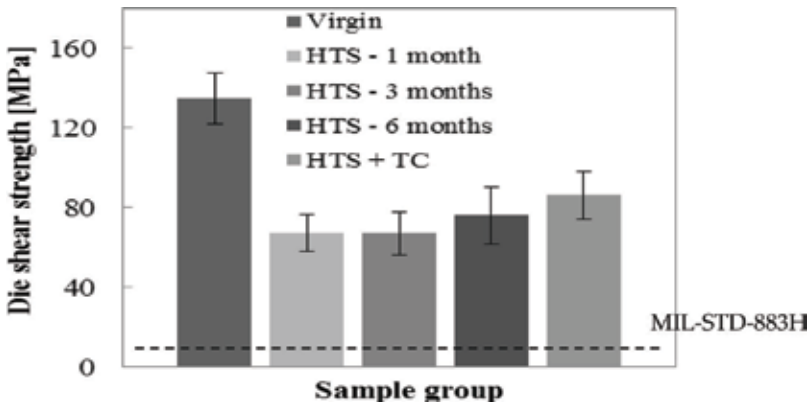


**Figure 9.** Die shear strength for virgin Au-Sn SLID samples, high-temperature-stored (HTS) samples—at 250°C for 1, 3 and 6 months—and samples exposed for 3 months HTS + 1000 thermal cycles (TC) between 0 and 200°C. Reprinted with permission from Springer Nature [23].

## 5. Ni-Sn bonding

### 5.1. Rationale for Ni-Sn

The Ni-Sn material system comprises three IMCs which all have a high-melting point ranging from 798 to 1280°C [24], see **Figure 10**. The high-temperature compatibility is the most frequent reason for investigating the Ni-Sn system [25–27]. In addition, Nickel and tin are relatively low-cost materials which make them attractive for more cost-sensitive applications [26, 28]. The formed IMCs may also have matching thermomechanical material properties which may be critical in applications with very high operation temperatures [29]. Residual Ni can be used as a diffusion barrier for other materials in joint structures, such as Au and Cu, preventing them from contaminating attached devices [30]. The relatively low melting point of Sn, 232°C, also allows similar process temperatures as the Cu-Sn system. In addition, the excellent corrosion resistance of Ni [28] makes the Ni-Sn system attractive for forming SLID joints. Still, information on Ni-Sn SLID joints is sparse.

### 5.2. Fabrication process

To be able to complete the homogenization process forming Ni-$Ni_3Sn$ joints, the pre-joint structure requires a volumetric ratio, Ni:Sn, of not less than 1.22:1. We have used a symmetric pre-joint structure of 3.0 μm Ni/2.0 μm Sn/2.0 μm Sn/3.0 μm Ni. The layers were built by sputtering a thin Ni layer onto metallized (TiW) Si wafers. The required thickness was achieved by electroplating additional Ni. The top layer of Sn was then electroplated. Samples were pressed together with a contact pressure of about 3 MPa and the temperature was raised above the melting point of Sn and then held there for a period of time until the liquid Sn reacted with the adjoining Ni substrate. The joint was then cooled down. The joint morphology and evolution as a function of process parameters were investigated by changing the

http://dx.doi.org/10.5772/intechopen.75139

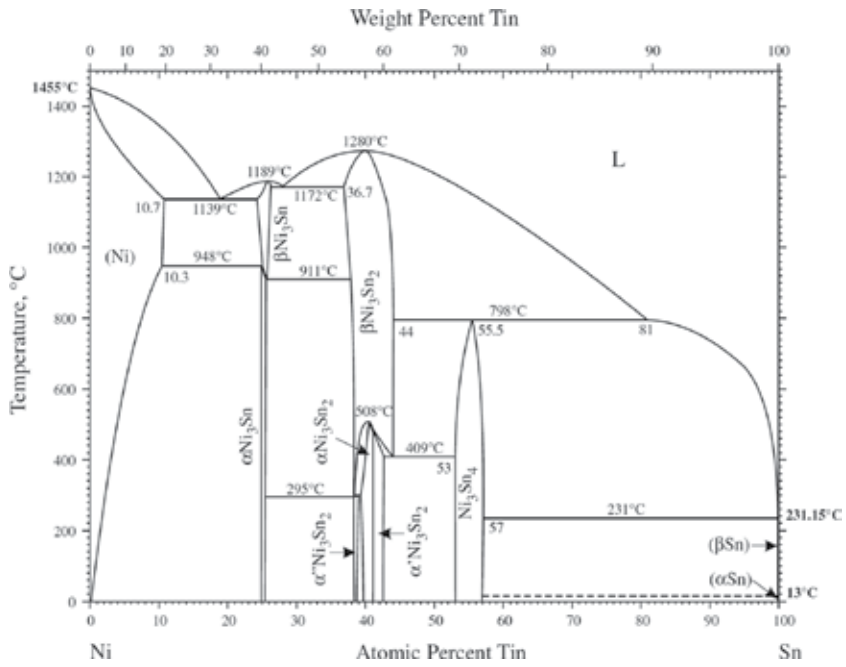


**Figure 10.** Ni-Sn phase diagram. Reprinted with permission from Springer Nature [24].

process temperature and duration. The maximum temperature was varied between 250 and 360°C, and the hold time was varied between 1 and 20 min. The ramp rate was 120°C/min and the process was carried out in vacuum.

### 5.3. Main results

Our studies have shown that 5 min at 300°C is insufficient to complete the isothermal solidification process step for our configuration, showing unreacted Sn in the joint centre, see **Figure 11(a)**; 20 min at 300°C or 5 min at 360°C created a developed $Ni_3Sn/Ni_3Sn_2/Ni_3Sn$ joint structure, see **Figure 11(b)** and **(c)**. Bader et al. [25] have reported that 105 h at 400°C was necessary to completely homogenize a 2.6-μm thick Sn layer on Ni into an $Ni/Ni_3Sn/Ni$ structure. The intermetallic formation evolves by forming idiomorphic $Ni_3Sn_4$ crystals at the Ni/Sn interface. These crystals grow anisotropically into columnar structures extending across the joint. They have a significant impact on the mechanical compliancy of the joint, restricting its ability to conform to volumetric changes as the joint evolves. The phase transformation from liquid to the solid intermetallic phases causes a volumetric shrinkage of about 14–17%. The inability to conform causes a high intrinsic stress state within the joint. This may result in significant voiding as depicted in **Figure 11**. One way to overcome the problem of forming the large idiomorphic crystals restricting the joint compliancy would be to fabricate joints with an Ni-Sn paste. This would also significantly reduce the necessary process time to homogenize the bond [31]. Unfortunately, such pastes are per now not commercially available. The nominal

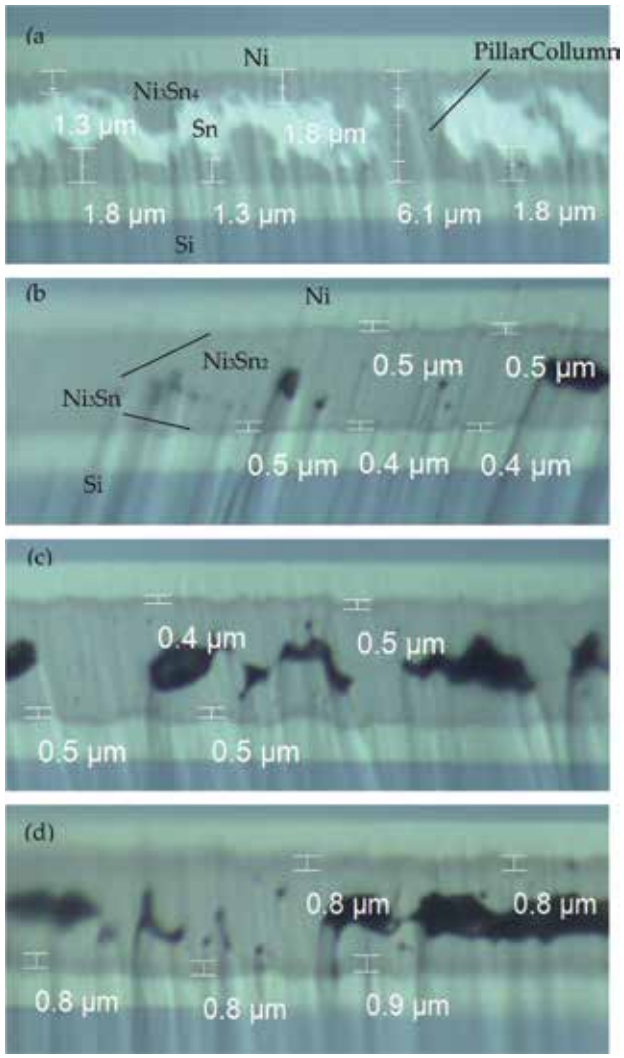


**Figure 11.** Optical micrographs of cross sections illustrating solidification and homogenization process for four different processes: (a) 1–300°C, 5 min, (b) 2–300°C, 20 min, (c) 3–360°C, 5 min, and (d) 4–360°C, 20 min [27] (© 2016 IEEE).

shear strength was measured to be at least 40 MPa according to the normal shear testing procedure. Greve et al. have demonstrated a shear strength capacity above 10 MPa at 600°C [31]. Fractography revealed that the strength was limited by a poor adhesion layer. Despite severe voiding in the joints themselves, they showed a significant shear strength exceeding 200 MPa when the actual bonded area was considered.

The pertinent literature has studied layered structures, either Ni/Sn/Ni or Ni/Sn. Both Sn preforms [26] and deposited layers have been used. The deposited layers have been electroplated [27, 28, 30], e-beam [32], thermally evaporated, sputtered [25, 32] or a combination of the abovementioned methods.

http://dx.doi.org/10.5772/intechopen.75139

# 6. Au-In bonding

## 6.1. Rationale for Au-In

The Au-In system (**Figure 12**) has a high number of IMCs. Whereas In has a low melting point of 156°C, all IMCs are solid at 450°C and higher. This opens for the possibility of a low-temperature bonding process with the capability of high-temperature stability. A low-temperature bonding is important for temperature-sensitive materials and also to minimize thermomechanical stress generated in the bonding process. Au-In SLID bonding will allow applications in an extended temperature range, defined by the tolerance of the bonded materials, whereas In-based soldering can only be used for applications well below the melting point of In. Our work in Au-In SLID bonding is a feasibility work, demonstrating that wafer-level bonding with good strength is achievable and that the bonds survive temperatures much higher than the melting point of In.

## 6.2. Fabrication process

Au-In interdiffusion is significant already at room temperature, converting In to $AuIn_2$ [34, 35]. If a system is designed with metal layer thicknesses aiming for an Au/IMC/Au bond-line, similar to Sn-based SLID systems, all In may have been converted to $AuIn_2$ before bonding, leaving no liquid phase available during bonding. Therefore, we have used thin Au layers in our Au-In bonding. In was deposited by evaporation, allowing only thin-layer deposition. We selected Au-In thickness on one bonding partner as 0.16 μm/1.25 μm and the other bonding partner as 0.8 μm Au, as shown in **Figure 13**. Bonding was performed at wafer level.

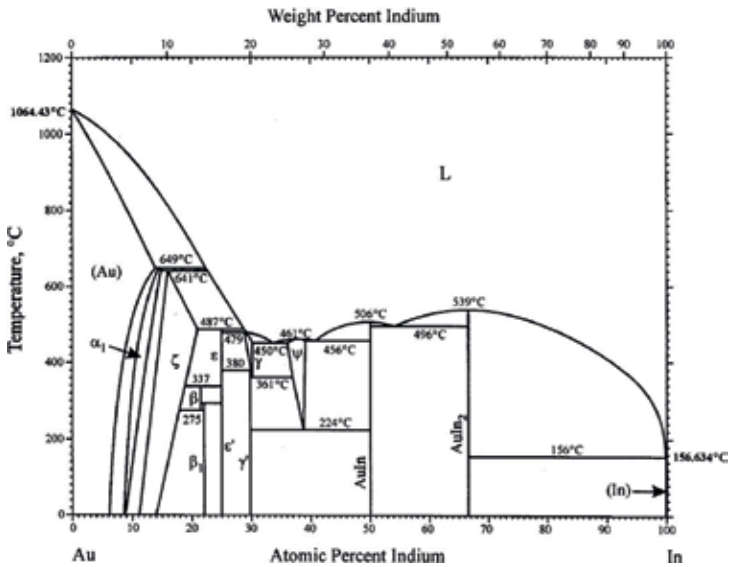


**Figure 12.** Au-In phase diagram. Reprinted with permission from Springer Nature [33].

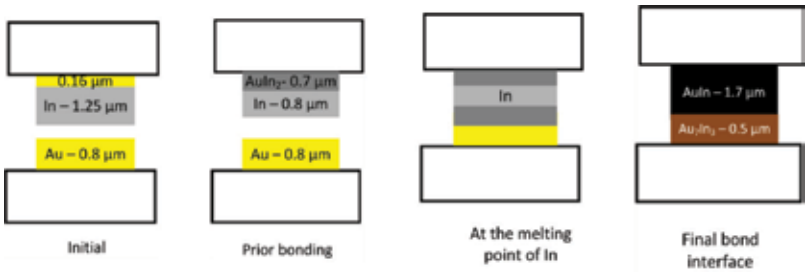


**Figure 13.** Design principle for Au-In SLID bonding.

### 6.3. Main results

Wafer bonding of Au-In was successful, with shear strengths in the range of 30 MPa [36]. **Figure 14** shows the microstructure of the final Au-In bond interface, where two IMC phases, AuIn and $Au_7In_3$, are present.

Shear testing at elevated temperatures, up to 300°C, confirms the high-temperature stability predicted from the phase diagram. **Figure 15** shows that the bond is solid at temperatures much higher than the In melting temperature of 156°C. Actually, the bond-line has a higher shear strength at 300°C than at room temperature. Inspection of the fracture surfaces reveals that die shear at temperatures from room temperature up to 200°C results in brittle fracture, with well-defined fracture surfaces: along the original bond interface, as well as in the adhesion layers. At 300°C, the fracture inside the IMC is very different. It has a ductile nature and no longer follows the original bond interface nor any other well-defined plane. The higher shear strength and change in fracture mode is explained from the phase diagram: a solid-state phase transition to the Ψ phase occurs at temperatures above 224°C. For our layer thicknesses, this phase transition involves interdiffusion of Au and In across the original bond interface, giving an annealing effect at this interface. When the weakest part of the bond-line is strengthened, an overall increase in strength is observed [36].

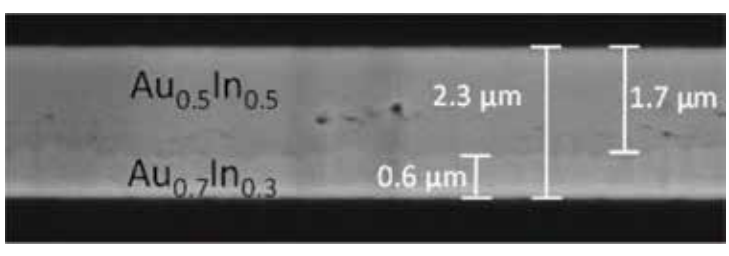


**Figure 14.** Cross section of the bonded sample. Two Au-In intermetallic compounds (IMCs) are present in the final bond-line. Reprinted with permission from Springer Nature [36].

http://dx.doi.org/10.5772/intechopen.75139

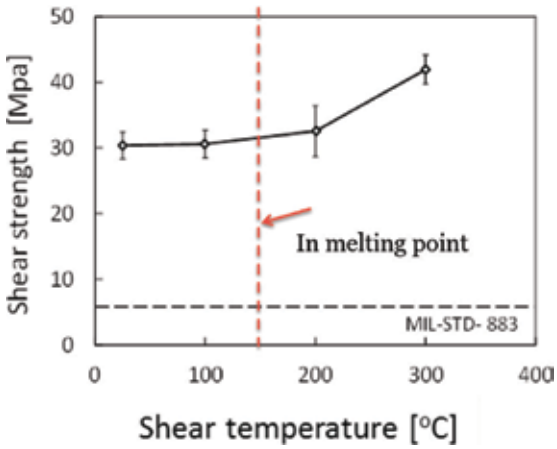


**Figure 15.** Au-In strength versus temperature.

## 7. Au-In-Bi bonding

### 7.1. Rationale for Au-In-Bi

While the use of In as a low-melting point material allows bonding at lower temperatures than ordinary solder temperatures, a number of applications and materials will require even lower bonding temperatures. Examples of temperature-sensitive materials are poled piezoelectric materials (that should not approach or exceed the Curie temperature, which can be ~150°C for a typical piezoelectric material such as PZT, lead zirconate titanate), ferromagnetic materials and polymers.

In-Bi is a metal system with particularly low melting points (see **Figure 16**): 72.7°C for the eutectic composition (78.5 at% In), and with all In-Bi intermetallic compounds having melting points within the range of 89–110°C. Ternary phase diagrams of the Au-In-Bi system are not readily available. However, Au and Bi are not miscible and have no IMCs that are stable at ambient temperatures. The lowest melting point of the Au-Bi system is a Bi-rich eutecticum (241.1°C). A suitable low-temperature bonding process may therefore be expected to result in Au-In IMCs, together with Bi, in the bond-line. The remelting temperature of such a bond will then be that of Bi (271°C). This will allow for a low-temperature bonding process without a severe restriction on the allowed temperature span in application.

### 7.2. Fabrication process

Most of our Au-In-Bi SLID bonds were carried out by sandwiching a eutectic In-Bi (78.5 at% In to 21.5 at% Bi) preform (thickness about 140 μm) between Au-coated dies and substrates. Bonding was performed with a bonding pressure ranging from 5 to 8 MPa, bonding temperatures ranging from 90 to 130°C and bonding times ranging from minutes up to 15 h [38]. Initial

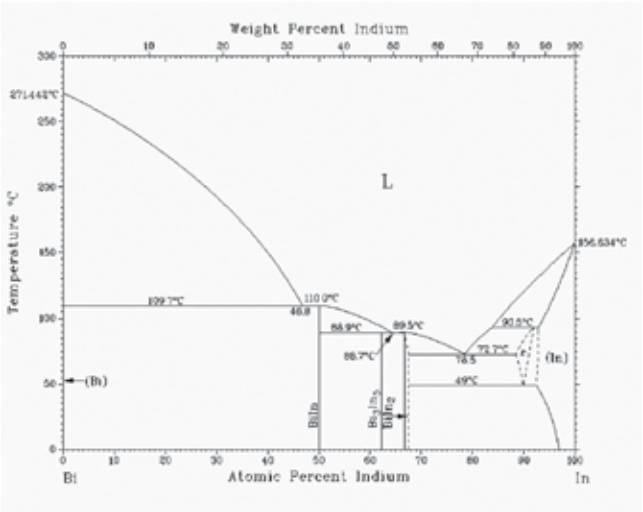


**Figure 16.** The Bi-In phase diagram. Reprinted with permission from ASM International [37].

experiments using a fast temperature ramp of 20°C/min gave a bond morphology with large scallops. All our main experiments are therefore carried out with a slow temperature ramp of 2°C/min, giving the desired layered SLID bond-line structure where the interdiffusion is controlled by IMC layers formed at the Au-to-preform interface already at temperatures below the melting temperature of the eutectic preform.

Au-In-Bi SLID bonding using thin-film (2.5–3 μm) thermally evaporated eutectic In-Bi on Au surfaces was also demonstrated [39]. This approach opens up for a much shorter process time, as well as being compatible with photolithographic patterning.

### 7.3. Main results

#### *7.3.1. Phases obtained*

##### *7.3.1.1. Bonding at 90°C*

Bonding at a low temperature of 90°C is indeed successful, as shown in **Figure 17**. The bond-line is much thinner than the original thickness of the In-Bi foil, showing that the material has been squeezed out while in liquid phase. The bond-line shows a layered structure of various Au-In IMCs, as well as inclusions of the $BiIn_2$ phase. No remaining In phase, no Au-Bi IMCs nor ternary Au-Bi-In phases are observed. $BiIn_2$ has a melting temperature of 89.5°C; hence, a higher process temperature is needed to obtain the desired, higher remelting temperatures.

##### *7.3.1.2. Bonding at 110°C*

**Figure 18** shows cross-section micrographs of the bonding performed at 110°C.

The cross-sections show a layered morphology similar to **Figure 17** (bonding at 90°C), but with thicker layers of the more Au-rich IMCs AuIn and $Au_7In_3$. No In-Bi IMCs are observed,

http://dx.doi.org/10.5772/intechopen.75139

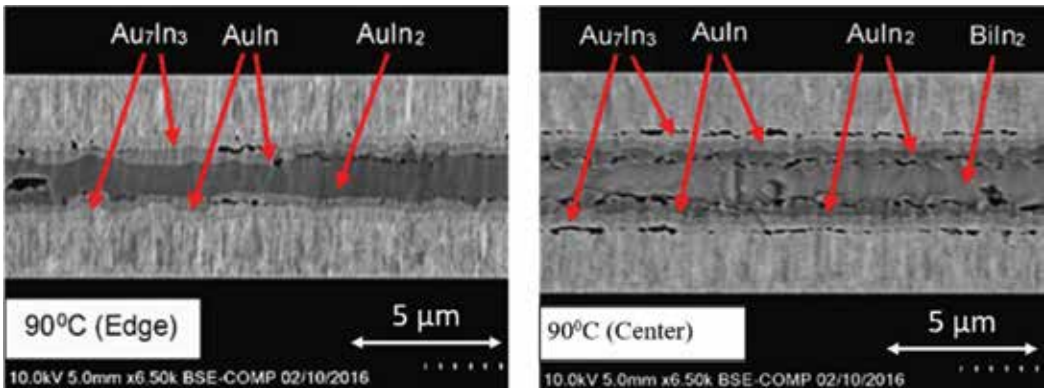


**Figure 17.** Cross-section micrograph of In-Bi SLID bond on Au pads, bonding temperature of 90°C, temperature ramping rate of 2°C/min and bonding time of 4.5 h. The phases are identified by EDX [38] (© 2016 IEEE).

but inclusions of Bi. This indicates that this bond would have a remelting temperature of 271°C. The existence of Bi as opposed to $BiIn_2$ (which appears in the 90°C-bonded samples) is explained from the Bi-In phase diagram: as the Au-In IMCs grow during the bonding process, the liquid Bi-In is gradually depleted of In and the Bi content rises. If the temperature of the liquid is below 89.5°C, $BiIn_2$ will solidify isothermally as the Bi content in the liquid approaches 33 at%. If the temperature of the liquid is between 89.5 and 110°C, $BiIn_2$ is not stable, and BiIn will solidify isothermally as the Bi content in the liquid approaches 50 at%. For temperatures above 110°C, no Bi-In IMCs are stable, and Bi will solidify isothermally as the In content in the liquid is depleted. The bonding temperature has a finite precision, so a bonding temperature set to 90°C may easily be consistent with a liquid temperature below 89.5°C, and similarly a bonding temperature set to 110°C may easily be consistent with a liquid temperature above the melting point of BiIn.

A bonding temperature of 110°C is marginal if one wishes to avoid the presence of the low-melting Bi-In IMCs. In our later work, we have therefore bonded at 115°C.

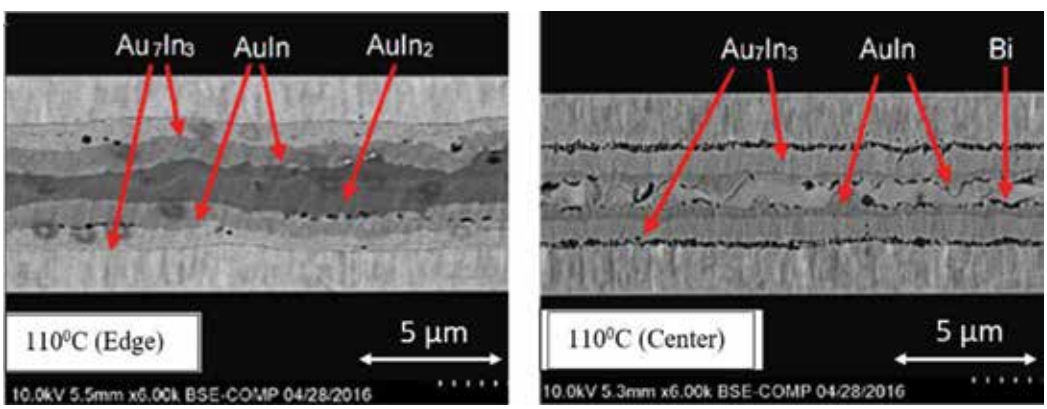


**Figure 18.** Cross-section micrograph of In-Bi SLID bond on Au pads, bonding temperature of 110°C, temperature ramping rate of 2°C/min and bonding time of 4.5 h. The phases are identified by EDX [38] (© 2016 IEEE).

*7.3.1.3. Bonding at higher temperatures and/or longer bonding times*

For samples bonded at a higher temperature (120 and 130°C) and/or bonding times longer than 4.5 h, the bond-line morphology is similar to that of the sample bonded at 110°C (**Figure 18**), except that the $Au_7In_3$ layer is significantly thicker and the $AuIn_2$ layer thickness is much reduced. This is as expected, with increased Au-In interdiffusion.

For extended bonding/annealing times, we expect an entire conversion to $Au_7In_3$, in an Au/$Au_7In_3$/Au configuration, when the Au:In ratio allows for that. Further reactions to even more Au-rich IMCs can be expected in order to reach thermal equilibrium, but the kinetics of these reactions is not known.

*7.3.1.4. Bonding using thin-film deposited In-Bi*

The Au-In-Bi preform SLID bonding discussed earlier requires long bonding times, due to slow diffusion through Au-In IMCs at these low bonding temperatures. Our preliminary experiments with thin-film-deposited In-Bi show that similar bond morphologies can be obtained, with decreased bonding times [39].

*7.3.2. Characterization*

Solid bond strengths, up to 50 MPa, are recorded. Bonded, acoustically active materials are tested with electrical impedance spectroscopy, confirming a very limited amount of voiding, compatible with ultrasonic applications [39].

## 8. Conclusion

### 8.1. Summary of USN results on different SLID systems

**Table 2** compares the different SLID systems that our group has worked with and what has been our group's research focus for each system. The obtained bond strength is a good indication of the quality of the bond. For all SLID systems, we obtain shear strength at the level of or higher than when using Sn-based solder (typically around 30–40 MPa [40, 41]). The highest bond strength is obtained by Au-Sn. This system will not show significant oxidation of the metal layers prior to bonding. This assures good wetting of the bonding partners, and a bond with very limited voiding has been the result.

**Figure 19** shows the shear strength versus temperature of Au-Sn, Cu-Sn and Au-In bonding systems. All systems show solid bonds at temperatures higher than the melting temperatures of In (156°C) and Sn (232°C), experimentally verifying the predicted high-temperature stability [42]. For Au-Sn, a solid bond at 400°C is also shown [43], without quantification. For Au-In-Bi SLID, a solid bond at 115°C is demonstrated, although a destructive test to quantify the bond strength has not been performed.

All SLID systems survived the highest tested temperature; we have not quantified the actual remelting temperature for any of these.

http://dx.doi.org/10.5772/intechopen.75139

| | Cu-Sn | Au-Sn | Ni-Sn | Au-In | Au-In-Bi |
|---|---|---|---|---|---|
| USN contributions | Flux-free, wafer-level bonding for hermetic sealing<br>Simulation model for IMC kinetics<br>Industrial implementation<br>Strength versus temperature | Composition determined<br>Excellent reliability (HTS and TC, also with CTE mismatch)<br>Strength versus temperature | Bond demonstrated and characterized | Bond demonstrated and characterized<br>Strength versus temperature | Bond demonstrated and characterized (mechanically and acoustically) |
| Process temperature | >232°C | >278°C | >232°C | >156°C | >73°C |
| Obtained bond strength | 70 MPa | 140 MPa | >40 MPa (nominally)<br>> 200 MPa in the actually bonded areas | 30 MPa (breaking at bond interface)<br>40 MPa at 300°C | 50 MPa |

**Table 2.** Different SLID material systems.

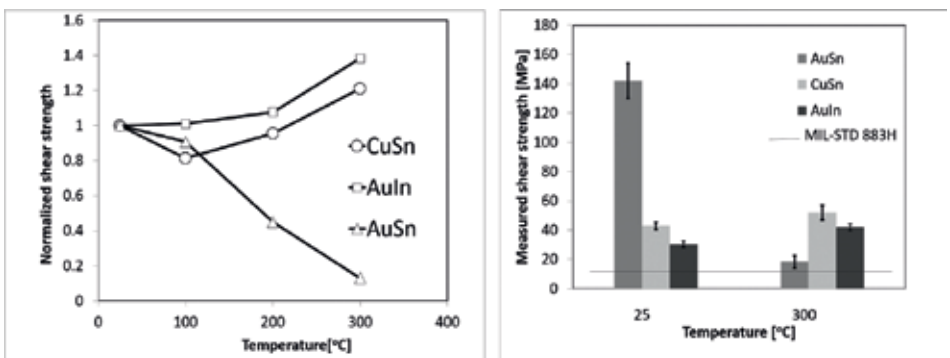


**Figure 19.** Normalized shear strength versus die shear temperature and actual shear strength at RT and 300°C [42] (© 2014 IEEE).

The temperature behaviour of the three SLID systems shown in **Figure 19** is rather different. For Cu-Sn, the variations in the shear strength with temperature are rather small, as might be expected since the phase diagram shows no phase transitions occurring in the $Cu/Cu_3Sn$ system below 350°C. Au-In shows a remarkable increase in strength at 300°C, explained earlier by a solid-state phase transformation occurring above 224°C. With the layer thicknesses in our design, this gives rise to interdiffusion across the initial bond interface, which was the weakest point in the bond-line at room temperature [36]. Au-Sn shows decreasing strength with temperature, but is solid at temperatures above the eutectic temperature in the Au-Sn system (278°C). The IMC in our Au-Sn SLID bonds is the non-stoichiometric ζ phase, which has a very composition-dependent melting temperature (ranging from 278 to 522°C, see **Figure 4**). We propose that more Au-rich Au-Sn SLID bonds with a longer bonding time, where the β

phase is the resulting IMC, will have the potential of even better high-temperature performance [44]. Note, however, that even though the relative decrease in Au-Sn shear strength is significant, the room temperature strength is extraordinarily high. Even though the strength of this system is reduced at 300°C to a level lower than the two other material systems, it is still at an acceptable level (~3× MIL-STD).

### 8.2. Related work

Many groups have contributed to research in SLID (**Table 3**). Most work has been on the Cu-Sn system, with Au-Sn as the second-most studied system.

Huebner et al. [3] demonstrated in 2006 that Cu-Sn SLID was capable of producing fine-pitch interconnections, down to 30 μm. This is significantly finer pitch than what can be obtained by a standard solder process. Lannon et al. [45] in 2012 showed the applicability of Cu-Sn SLID for high-density bonding with a very high number of interconnections (>22,000). In recent years, the industry in need of fine-pitch interconnection has implemented 'Cu pillar technology', where the pitch can be less than 10 μm [46], by electroplating fine-pitch Cu pillars (with diameters down to 1 μm [47]) and restricting the solder applied to a small volume

| Author(s) | Ref. | Main contribution |
|---|---|---|
| Bernstein (and Bartholomew) | [9, 10] | First introduction of SLID, for bonding in microelectronics, in 1966 |
| Huebner et al. | [3] | Cu-Sn SLID for early (2006) fine-pitch (<30 μm) interconnection |
| Lannon et al. | [45] | Cu-Sn SLID (2012) high-density interconnections (>22,000 interconnects) |
| Huang et al. | [46] | Solder-capped Cu pillars (fine-pitch technology where the material composition is similar to Cu-Sn SLID) |
| Liu et al. | [47] | Solder-capped Cu pillars with extreme fine-pitch (down to 1 μm) |
| Huang et al. | [48] | Metastable SLID: Cu-Sn SLID process not reaching thermal equilibrium, faster process time |
| Syed-Khaja and Franke | [49] | Solder paste used for Cu-Sn SLID |
| Vuorinen et al. | [50–52] | Au-Sn and Cu-Sn SLID, dynamics of bonding and of void formation |
| Ross et al. | | |
| Nga et al. | [53, 54] | Cu-Sn SLID, hermetic sealing of MEMS devices and for through-silicon vias (TSVs) |
| Yuhan Cao et al. | | |
| Marauska et al. | [55, 56] | Cu-Sn and Au-Sn SLID |
| Xu et al. | | Wafer-level hermetic encapsulation |
| Chang et al. | [57–60] | Cu-Sn SLID for 3D integration |
| Civale et al. | | |
| Chang et al. | | |
| Ko et al. | | |
| Cook and Sorensen | [5] | Overview article (2011) |

**Table 3.** SLID and related work, examples from various groups.

on top of the Cu pillars. Although usually referred to as a solder process, the process is very similar to a SLID process because of the small Sn volume applied and a resulting bond-line dominated by intermetallics.

Huang et al. [48] have developed 'Metastable SLID', where an Ni barrier layer restricts the amount of Cu to be used for the reaction with Sn, resulting in a SLID bond with $Cu_6Sn_5$ as the IMC. This allows for a much faster processing time, while a number of the desired properties of SLID are intact.

Alternative methods for depositing Sn in the Cu-Sn SLID/ TLP system are explored, for example, by using Sn-based solder paste [49].

Vuorinen et al. [50] have investigated Au-Sn and Cu-Sn SLID, with a special focus on the mechanisms of the dynamic evolution during bonding and the corresponding void formation [51, 52].

Although solder bonding is likely to be the most used bonding method also in the future, SLID bonding is likely to be increasingly important for industrial applications where high-temperature performance or fine-pitch metallurgical bonding is important.

## Author details

Knut E. Aasmundtveit[1]*, Thi-Thuy Luu[2], Hoang-Vu Nguyen[1], Andreas Larsson[1,3] and Torleif A. Tollefsen[4]

*Address all correspondence to: knut.aasmundtveit@usn.no

1 University of Southeast Norway, Borre, Norway

2 Zimmer and Peacock AS, Horten, Norway

3 TECHNI AS, Borre, Norway

4 TEGma AS, Kristiansand, Norway

## References

[1] Tummala RR. Fundamentals of Microsystems Packaging. New York, USA: McGraw-Hill; 2000

[2] Hoivik N, Aasmundtveit K. Wafer-level solid–liquid interdiffusion bonding. In: Handbook of Wafer Bonding. Weinheim, Germany: Wiley-VCH Verlag GmbH & Co. KGaA; 2012. pp. 181-214

[3] Huebner H, Penka S, Barchmann B, Eigner M, Gruber W, Nobis M, et al. Microcontacts with sub-30 μm pitch for 3D chip-on-chip integration. Microelectronic Engineering. 2006;**83**:2155-2162

[4] Duvall DS, Owczarski WA, Paulonis DF. TLP Bonding: A New Method for Joining Heat Resisant Alloys. 1974. p. 203

[5] Cook GO, Sorensen CD. Overview of transient liquid phase and partial transient liquid phase bonding. Journal of Materials Science. 2011;**46**:5305-5323

[6] Macdonald WD, Eagar TW. Transient liquid-phase bonding. Annual Review of Materials Science. 1992;**22**:23-46

[7] Schmid-Fetzer R. Design fundamentals of high-temperature composites. In: Lin RY, editor. Intermetallics and Metal-ceramic Systems. Warrendale, PA: TMS; 1995. pp. 75-97

[8] Johnson WR, Wang CQ, Liu Y, Scofield JD. Power device packaging technologies for extreme environments. IEEE Transactions on Electronics Packaging Manufacturing. 2007;**30**:182-193

[9] Bernstein L. Semiconductor joining by solid-liquid-interdiffusion (SLID) process. Journal of the Electrochemical Society. 1966;**113**:1282-1288

[10] Bernstein L, Bartholomew H. Applications of solid-liquid interdiffusion (SLID) bonding in integrated-circuit Fabricatoin. Transactions of the Metallurgical Society of AIME. 1966;**236**:405-411

[11] Aasmundtveit KE, Tollefsen TA, Luu TT, Duan A, Wang K, Hoivik N. Solid-liquid interdiffusion (SLID) bonding—Intermetallic bonding for high temperature applications. In: 19th European Microelectronics and Packaging Conference, EMPC 2013, Grenoble; France; 9 September 2013 through 12 September 2013, ed: IEEE Conference Proceedings. 2013. p. 6

[12] Luu T-T, Duan A, Wang K, Aasmundtveit K, Hoivik N. Cu/Sn SLID wafer-level bonding optimization. In: Electronic Components and Technology Conference (ECTC), 2013 IEEE 63rd. 2013. pp. 1531-1537

[13] Peng W, Monlevade E, Marques ME. Effect of thermal aging on the interfacial structure of SnAgCu solder joints on Cu. Microelectronics Reliability. 2007;**47**:2161-2168

[14] Etschmaier H, Torwesten H, Eder H, Hadley P. Suppression of Interdiffusion in copper/tin thin films. Journal of Materials Engineering and Performance. 2012;**21**:1724-1727

[15] Hoivik N, Wang K, Aasmundtveit K, Salomonsen G, Lapadatu A, Kittilsland G, et al. Fluxless wafer-level Cu-Sn bonding for micro- and nanosystems packaging. In: Electronic System-Integration Technology Conference (ESTC), 2010 3rd. 2010. pp. 1-5

[16] Forsberg F, Lapadatu A, Kittilsland G, Martinsen S, Roxhed N, Fischer AC, et al. CMOS-integrated Si/SiGe quantum-well infrared microbolometer focal plane arrays manufactured with very large-scale heterogeneous 3-D integration. IEEE Journal of Selected Topics in Quantum Electronics. 2015;**21**:1-11

[17] Forsberg F, Roxhed N, Fischer AC, Samel B, Ericsson P, Hoivik N, et al. Very large scale heterogeneous integration (VLSHI) and wafer-level vacuum packaging for infrared bolometer focal plane arrays. Infrared Physics & Technology. 2013;**60**:251-259

[18] Lapadatu A, Kittilsland G, Elfving A, Hohler E, Kvisterøy T, Bakke T, et al. High-performance long wave infrared bolometer fabricated by wafer bonding. In: SPIE Defense, Security, and Sensing. 2010. p. 12

[19] Luu TT, Duan A, Aasmundtveit KE, Hoivik N. Optimized Cu-Sn wafer-level bonding using intermetallic phase characterization. Journal of Electronic Materials. 2013;**42**:3582-3592

[20] Tollefsen TA, Larsson A, Lovvik OM, Aasmundtveit K. Au-Sn SLID bonding-properties and possibilities. Metallurgical and Materials Transactions B-Process Metallurgy and Materials Processing Science. 2012;**43**:397-405

[21] Okamoto H. Au-Sn (gold-tin). Journal of Phase Equilibria and Diffusion. 2007;**28**:490-490

[22] Tollefsen TA, Taklo MMV, Aasmundtveit K, Larsson A. Reliable HT electronic packaging—Optimization of an Au-Sn SLID joint. In: Presented at the Electronic System-Integration Technology Conference (ESTC); 2012 4th; Amsterdam, Netherlands. 2012

[23] Tollefsen TA, Larsson A, Taklo MMV, Neels A, Maeder X, Hoydalsvik K, et al. Au-Sn SLID bonding: A reliable HT interconnect and die attach technology. Metallurgical and Materials Transactions B-Process Metallurgy and Materials Processing Science. 2013;**44**:406-413

[24] Okamoto H. Ni-Sn (nickel-tin). Journal of Phase Equilibria and Diffusion. 2008;**29**:297-298

[25] Bader S, Gust W, Hieber H. Rapid formation of intermetallic compounds by interdiffusion in the Cu-Sn and Ni-Sn systems. Acta Metallurgica et Materialia. 1995;**43**:329-337

[26] Yoon SW, Glover MD, Shiozaki K. Nickel-tin transient liquid phase bonding toward high-temperature operational power electronics in electrified vehicles. IEEE Transactions on Power Electronics. 2013;**28**:2448-2456

[27] Larsson A, Tollefsen TA, Aasmundtveit KE. Ni-Sn solid liquid interdiffusion (SLID) bonding—Process, bond characteristics and strength. In: 2016 6th Electronic System-Integration Technology Conference (ESTC). 2016. pp. 1-6

[28] Lis A, Kenel C, Leinenbach C. Characteristics of reactive $Ni_3Sn_4$ formation and growth in Ni-Sn interlayer systems. Metallurgical and Materials Transactions A-Physical Metallurgy and Materials Science. 2016;**47A**:2596-2608

[29] Larsson A,Tollefsen TA, Løvvik OM, Aasmundtveit KE. Aasmundtveit, "Ni-Sn solid-liquid interdiffusion (SLID) bonding for thermo-electric elements in extreme environments—FEA of the joint stress," in 2015 European Microelectronics Packaging Conference (EMPC), 2015, pp. 1-6

[30] Yu CC, Su PC, Bai SJ, Chuang TH. Nickel-tin solid-liquid inter-diffusion bonding. International Journal of Precision Engineering and Manufacturing. 2014;**15**:143-147

[31] Greve H, Moeini SA, McCluskey FP. Reliability of paste based transient liquid phase sintered interconnects. In: 2014 IEEE 64th Electronic Components and Technology Conference (ECTC). 2014. pp. 1314-1320

[32] Chu K, Sohn Y, Moon C. A comparative study of Cn/Sn/Cu and Ni/Sn/Ni solder joints for low temperature stable transient liquid phase bonding. Scripta Materialia. 2015;**109**:113-117

[33] Okamoto H. Au-In (gold-indium). Journal of Phase Equilibria and Diffusion. 2004;**25**: 197-198

[34] Zhang W, Ruythooren W. Study of the Au/In reaction for transient liquid-phase bonding and 3D chip stacking. Journal of Electronic Materials. 2008;**37**:1095-1101

[35] Liu YM, Chuang TH. Interfacial reactions between liquid indium and Au-deposited substrates. Journal of Electronic Materials. 2000;**29**:405-410

[36] Luu T-T, Hoivik N, Wang K, Aasmundtveit KE, Vardoy A-SB. Characterization of wafer-level Au-In-bonded samples at elevated temperatures. Metallurgical and Materials Transactions A—Physical Metallurgy and Materials Science. 2015;**46A**:2637-2645

[37] Okamoto H. Bi-In (bismuth-indium). In: Massalski TB, editor. Binary Alloy Phase Diagrams. Vol. 1. ASM International; 1990. pp. 748-751

[38] Aasmundtveit KE, Nguyen TAV, Nguyen HV. In-bi low-temperature SLID bonding. In: 2016 6th Electronic System-Integration Technology Conference (ESTC). 2016. pp. 1-5

[39] Aasmundtveit KE, Eggen T, Manh T, Nguyen H-V. In–Bi low-temperature SLID bonding for piezoelectric materials. In: The 21st European Microelectronics and Packaging Conference (EMPC); Warsaw, Poland. 2017. pp. 1-6

[40] Kang SK. Development of lead (Pb)-free interconnection materials for microelectronics. Metals and Materials International. 1999;**5**(6):545-549

[41] Siewert T, Liu S, Smith DR, Madeni JC. Properties of Lead-Free Solders [Online]. Available: http://www.boulder.nist.gov/div853/lead_free/solders.html

[42] Aasmundtveit KE, Luu TT, Vardøy ASB, Tollefsen TA, Wang K, Hoivik N. High-temperature shear strength of solid-liquid interdiffusion (SLID) bonding: Cu-Sn, Au-Sn and Au-In. In: Electronics System-Integration Technology Conference (ESTC); 2014. 2014. pp. 1-6

[43] Aasmundtveit K, Luu TT, Nguyrn H, Johannessen R, Hoivik N, Wang K. Au-Sn fluxless SLID bonding: Effect of bonding temperature for stability at high temperature, above 400°C. In: Electronics System Integration Technology Conference. 2010

[44] Tollefsen TA, Lovvik OM, Aasmundtveit K, Larsson A. Effect of temperature on the die shear strength of a au-Sn SLID bond. Metallurgical and Materials Transactions A—Physical Metallurgy and Materials Science. 2013;**44A**:2914-2916

[45] Lannon JM, Gregory C, Lueck M, Reed JD, Huffman CA, Temple D. High density metal-metal interconnect bonding for 3-D integration. IEEE Transactions on Components, Packaging and Manufacturing Technology. 2012;**2**:71-78

[46] Huang TC, Smet V, Raj PM, Tummala RR, Ramos G, Kilian A, et al. Demonstration of next-generation Au-Pd surface finish with solder-capped Cu pillars for ultra-fine pitch

applications. In: 2016 IEEE 66th Electronic Components and Technology Conference (ECTC). 2016. pp. 2553-2560

[47] Liu YX, Chu YC, Tu KN. Scaling effect of interfacial reaction on intermetallic compound formation in Sn/Cu pillar down to 1 μm diameter. Acta Materialia. Sep 2016;**117**:146-152

[48] Huang TC, Smet V, Kawamoto S, Sundaram V, Raj PM, Tummala RR. Modeling, design and demonstration of ultra-short and ultra-fine pitch metastable Cu-Sn interconnections with high-throughput SLID assembly. In: 2015 IEEE 65th Electronic Components and Technology Conference (ECTC). 2015. pp. 1377-1384

[49] Syed-Khaja A, Franke J. Investigations on advanced soldering mechanisms for transient liquid phase soldering (TLPS) in power electronics. In: Proceedings of the 5th Electronics System-integration Technology Conference (ESTC). 2014. pp. 1-7

[50] Vuorinen V, Rautiainen A, Heikkinen H, Paulasto-Krockel M. Optimization of contact metallizations for reliable wafer level Au-Sn bonds. Microelectronics Reliability. 2016;**64**:676-680

[51] Ross G, Vuorinen V, Paulasto-Krockel M. Void formation and its impact on Cu-Sn intermetallic compound formation. Journal of Alloys and Compounds. 2016;**677**:127-138

[52] Ross G, Vuorinen V, Petzold M, Paulasto-Krockel M, Brand S. Gigahertz scanning acoustic microscopy analysis of voids in Cu-Sn micro-connects. Applied Physics Letters. 2017;**110**(5)

[53] Pham NP, Cherman V, Vandevelde B, Limaye P, Tutunjyan N, Jansen R, et al. Zero-level packaging for (RF-)MEMS implementing TSVs and metal bonding. In: 2011 IEEE 61st Electronic Components and Technology Conference (ECTC). 2011. pp. 1588-1595

[54] Cao Y, Ning W, Luo L. Wafer-level package with simultaneous TSV connection and cavity hermetic sealing by solder bonding for MEMS device. IEEE Transactions on Electronics Packaging Manufacturing. 2009;**32**:125-132

[55] Marauska S, Claus M, Lisec T, Wagner B. Low temperature transient liquid phase bonding of Au/Sn and Cu/Sn electroplated material systems for MEMS wafer-level packaging. Microsystem Technologies. 2013;**19**:1119-1130

[56] Xu H, Broas M, Dong H, Vuorinen V, Suni T, Vähänen S, et al. Reliability of wafer-level SLID bonds for MEMS encapsulation. In: 2013 Eurpoean Microelectronics Packaging Conference (EMPC). 2013. pp. 1-6

[57] Chang YJ, Ko CT, Hsiao ZC, Chiang CH, Fu HC, Yu TH, et al. Electrical investigation and reliability of 3D integration platform using Cu TSVs and micro-bumps with Cu/Sn-BCB hybrid bonding. In: 2013 IEEE 63rd Electronic Components and Technology Conference. 2013. pp. 64-70

[58] Civale Y, Tezcan DS, Philipsen HGG, Jaenen P, Agarwal R, Duval F, et al. Die stacking using 3D-wafer level packaging copper/polymer through-si via technology and Cu/Sn interconnect bumping. In 2009 IEEE International Conference on 3D System Integration. 2009. pp. 1-4

[59] Chang YJ, Ko CT, Chen KN. Electrical and reliability investigation of Cu TSVs with low-temperature Cu/Sn and BCB hybrid bond scheme. IEEE Electron Device Letters. 2013;**34**:102-104

[60] Ko CT, Hsiao ZC, Chang YJ, Chen PS, Huang JH, Fu HC, et al. Wafer-level 3D integration with Cu TSV and micro-bump/adhesive hybrid bonding technologies. In: 2011 IEEE International 3D Systems Integration Conference (3DIC), 2011 IEEE International. 2012. pp. 1-4

Chapter 4

# The Importance of the Fluorine Effect on the Oxidation of Intermetallic Titanium Aluminides

Alexander Georg Donchev and
Mathias Christian Galetz

Additional information is available at the end of the chapter

http://dx.doi.org/10.5772/intechopen.75696

**Abstract**

Due to the low Al activity within technical titanium aluminides and the similar thermodynamic stabilities of Al- and Ti-oxide these alloys always form a mixed oxide scale at elevated temperatures consisting of $TiO_2$, $Al_2O_3$ and also nitrides if the exposure takes place in air. This mixed scale does not provide any oxidation protection especially under thermocyclic load or in water vapor containing environments. Thus accelerated oxidation occurs. Alloying of additional elements such as Nb improves the oxidation behavior if the additions stay within a certain concentration range but such additions cannot suppress non-protective mixed scale formation. Coatings are another way to protect these materials but several obstacles and new degradation mechanisms exist such as delamination e.g. due to CTE mismatch or development of brittle intermetallic phases due to interdiffusion. Therefore, other suitable protective measures have to be undertaken to make sure a protective oxide scale will develop. The so called halogen effect is a very promising way to change the oxidation mechanism from mixed scale formation to alumina formation. After optimized halogen treatment the alumina layer is very protective up to several thousand hours even under thermocyclic load and in atmospheres containing water vapor or $SO_2$.

**Keywords:** titanium aluminides, oxidation, halogen effect

## 1. Introduction

Intermetallics possess very interesting properties due to their unique ordered crystal structure, which differs from those of the constituting elements. Bonding includes metallic and covalent portions so that they combine metallic and ceramic properties such as high strength and decent corrosion resistance but on the other hand usually low ductility at room temperature

(RT). Some of these materials are promising candidates to replace conventional heavy nickel-based alloys in several high-temperature (HT) applications. In particular, alloys based on titanium and aluminum, so-called titanium aluminides, consisting predominantly of the γ-TiAl phase have a high service potential (**Figure 1**). Their density is only about 4 g/cm$^3$, which is about half that of conventional Ni-based superalloys. The specific strength of this new class of materials is even higher than that of Ni alloys [1]. Technical TiAl alloys have an Al content of about 40–50 at.% and consist of at least two phases, i.e., γ-TiAl and $\alpha_2$-$Ti_3Al$. Recent developments have led to alloys with an Al content below 45 at.% and additions of β-stabilizing elements such as Nb or Mo, which solidify via the β-phase to have three phases $\alpha_2$, γ, and $\beta_0$ present at service temperature [2]. All in all the average composition of such technical TiAl alloys can be written as Ti (42–48), Al (2–8), Nb (0.5–3), other metals such as Cr or Mo (0.1–1), and nonmetals as B, C, and Si (0.1–0.5) [3].

Still, there are some drawbacks to the widespread distribution of titanium aluminides, i.e., low room temperature ductility [4] and low oxidation resistance at temperatures above ca. 750°C [5], which are major topics in research all over the world. Alloying of additional elements can improve the oxidation resistance [6] but is usually not sufficient to lift the application temperature far above the current range of application up to 750°C.

Due to the similar thermodynamic stabilities of Al and Ti oxide and an Al activity too low to form $Al_2O_3$, these alloys always develop a mixed oxide scale at elevated temperatures in oxidizing environments [7]. The scale consists of $TiO_2$, $Al_2O_3$, and also nitrides if the exposure

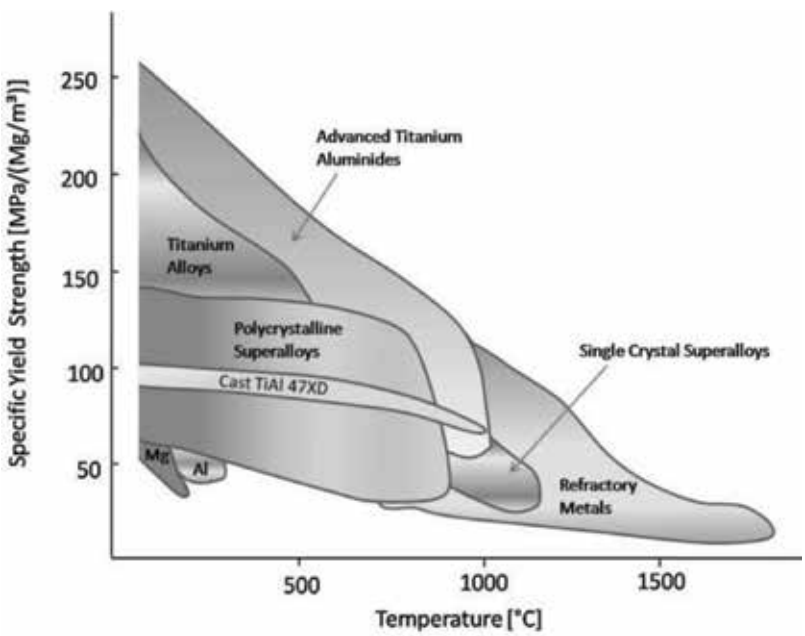


**Figure 1.** Comparison of the specific yield strength of engineering materials, which are used in automotive engines and in aeroengines. The figure shows that advanced titanium aluminide alloys are capable to bear higher application temperatures and loads than Ti alloys. It is evident that TiAl alloys have an advantage over Ti-based materials [1].

takes place in air [8]. $TiO_2$ grows very fast at temperatures above 600°C so that the mixed scales can get very thick within rather short exposure times. The mixed scale does not provide oxidation protection especially under thermal cyclic load. Due to the different coefficient of thermal expansion (CTE) of the substrate and the oxides, stresses arise which can lead to spallation of the scale if a certain stress level is reached [9]. This can happen especially during cooling down from service temperature. Thus, accelerated oxidation will occur. Alloying of additional elements such as Nb improves the oxidation behavior if the additions stay within a certain concentration range, but all these additions cannot suppress the mixed scale formation [6]. Coatings are another way to protect these materials, but several obstacles and new degradation mechanisms exist such as delamination, e.g., due to CTE mismatch or development of brittle intermetallic phases due to interdiffusion [5]. Therefore, other suitable protective measures have to be undertaken to make sure a protective oxide scale will develop. The so-called halogen effect is a very promising way to change the oxidation mechanism from mixed scale formation to alumina formation. After optimized halogen treatment, the alumina layer is very protective up to several thousand hours even under thermolcyclic load and in atmospheres containing water vapor or $SO_2$ [10].

## 2. Mechanism

Due to alumina formation by the halogen effect, the oxidation kinetics of halogenated specimens is reduced compared to that of untreated TiAl. In **Figure 2** the mass change data derived from thermogravimetric analysis, i.e., mass change measuring during isothermal oxidation, are shown. The mass change curve of the fluorinated sample reveals the beneficial fluorine

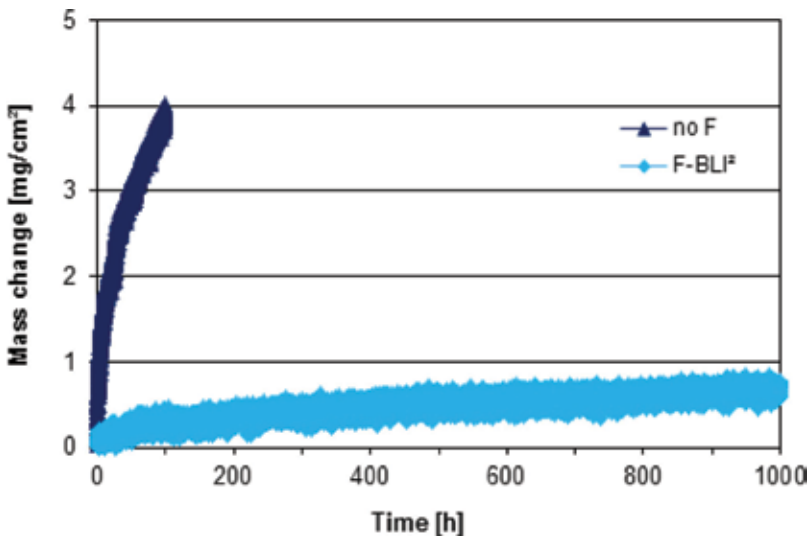


**Figure 2.** Thermogravimetric results of an untreated TiAl sample and a beamline fluorine-implanted TiAl sample during isothermal oxidation at 900°C in air.

effect. This positive result was achieved by applying the accurate amount of fluorine to the surface of the material [11]. In this case an optimized beamline implantation of fluorine was applied (F-BLI$^2$). This resulted in a rather low mass gain of less than 1 mg/cm$^2$ after 1000 h of oxidation at 900°C in air, while the final mass gain of the untreated specimen is almost four times higher, ca. 4 mg/cm$^2$, after a much shorter period of time (100 h).

The beneficial effect of fluorine on the oxide scale formation is shown in **Figure 3**. Only one side of the specimen was beamline implanted with fluorine prior to oxidation at 900°C in air, while the other side was not treated. It can be seen that the implanted side (**Figure 3a**) developed a thin oxide layer (1–2 μm) rich in alumina, while on the non-implanted side (**Figure 3b**), a thicker mixed scale (>20 μm) of $Al_2O_3$ + $TiO_2$ and nitrides was formed. The mixed scale consists of an outer layer of coarse rutile crystals, followed by a darker alumina-rich zone and a yellowish mixed oxide zone with nitrides. The Ni plating was applied prior to metallographic preparation to protect the oxide scales during preparation of the metallographic cross sections.

Alumina formation is promoted by optimized additions of the halogens fluorine, chlorine, bromine, and iodine to the surface of TiAl alloys. However, large amounts of halogens in the surface zone are very detrimental. They induce accelerated high-temperature corrosion [12, 13]. On the other hand, if the amounts of halogens are too low, there is no impact on the oxidation behavior of TiAl alloys, i.e., mixed scale formation.

This so-called halogen effect was first reported in [14–16]. Several models have been proposed in the literature to explain the positive effect of the halogens. One model is based on doping of titanium oxide by negatively charged halogen ions. By this negative charge, the rate of oxygen diffusion and hence $TiO_2$ growth is reduced [14]. A second model claims aluminum enrichment in the subsurface zone of the alloy due to formation of gaseous titanium halides and their evaporation which reduces the Ti content. This leads to an increased Al activity at the alloy/scale interface, which promotes the $Al_2O_3$ scale growth [15]. Contrarily, experimental results by Donchev et al. [17] have clearly shown that these two proposed models can be neglected to

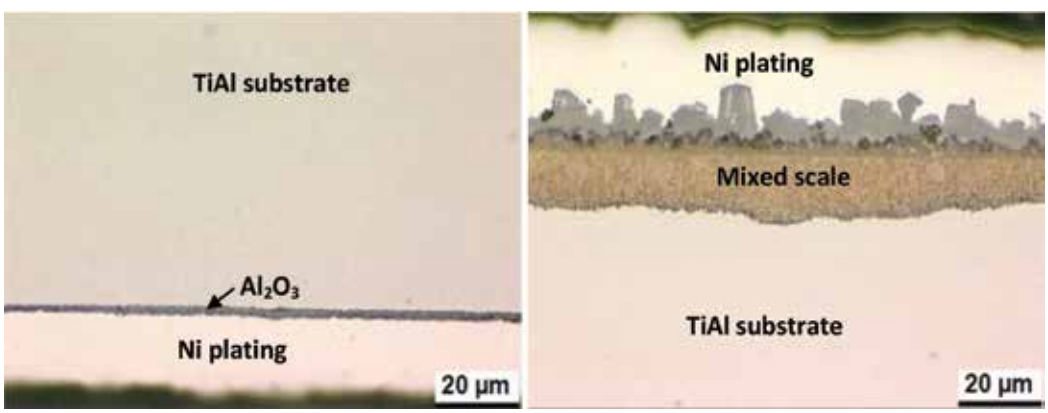


**Figure 3.** Cross-sectional LOM images showing the effect of beamline implantation of fluorine on one side (a) compared to the untreated side (b) after oxidation of a TiAl sample at 900°C for 100 h in air.

http://dx.doi.org/10.5772/intechopen.75696

describe the halogen effect. Their third model is based on the transport of aluminum via selective formation of gaseous Al halides. They diffuse outward from the substrate to the inner region of the naturally grown oxide scale where they are then oxidized to $Al_2O_3$ due to the steep increasing oxygen partial pressure. After an incubation period, the amount of $Al_2O_3$ formed in the inner region reaches a sufficient volume fraction to result in a pronounced reduction in the scale-growing kinetics [18]. In [17] the underlying thermodynamic mechanisms were mostly described for a chlorine beamline implantation. In a similar approach, the following data and equations are described for fluorine, which has shown to be more effective than chlorine during thermocyclic exposure [18]. Since AlF is the predominant carrier molecule for the aluminum transport, the reactions leading to $Al_2O_3$ formation can be signified as follows:

$$Al_{(s,TiAl)} + F \rightarrow AlF_{(g)} \Delta G_{900^\circ C} = -3.63 \times 10^5 \text{ J/mol} \tag{1}$$

$$4\ AlF_{(g)} + 3\ O_2 \rightarrow 2\ Al_2O_{3(s,\text{oxide scale})} + 2\ F_2 \Delta\ G_{900^\circ C} = -1.19 \times 10^6 \text{ J/mol} \tag{2}$$

where Al is from the TiAl alloy and fluorine from different fluorine treatments (see below). Fluorine is released by Eq. (2) so that it can react again with Al from the substrate according to Eq. (1). The enthalpies of formation for both reactions are negative. Thus, they tend to react to the proposed products.

The minimum aluminum flux required via gaseous Al fluorides to sustain the growth of $Al_2O_3$ is determined by its growth kinetics, which follows the parabolic rate equation:

$$\Delta w = \left(k_p t\right)^{\frac{1}{2}} \tag{3}$$

where $k_p$ is the parabolic rate constant ($g^2/cm^4 s$), $\Delta w$ is the mass gain (g), and t is time (s). The flux of aluminum in the growing $Al_2O_3$ scale, $J_{Al}^{ox}$, is connected with the mass gain, i.e.,

$$J_{Al}^{ox} \propto \frac{d\Delta w}{dt} \tag{4}$$

and in the case of $Al_2O_3$ growth, it is found that

$$J_{Al}^{ox} = \frac{1}{48}\left(\frac{k_p}{t}\right)^{\frac{1}{2}} \qquad \frac{\text{mol Al}}{\text{cm}^2 \cdot \text{s}} \tag{5}$$

The $k_p$ for $Al_2O_3$ scale growth at 900°C equals $5 \times 10^{-13}$ $g^2/cm^4$ s [19]. Therefore, the flux $J_{Al}^{ox}$ = $2 \times 10^{-9}$ mol/$cm^2$ s after 60 s of oxidation. This value represents the minimum amount of aluminum which is necessary to maintain parabolic $Al_2O_3$ scale growth after this time. The flux, $J_{Al}$, of the gaseous Al fluorides within the nano−/micro-channels and cracks can be derived from the Hertz-Langmuir equation (kinetic theory of gases [20]). In the case of an aluminum mono-fluoride AlF, the equation is as follows

$$J_{AlF} = J_{Al} = 44.3\frac{P_{AlF}}{\left(M_{AlF} T\right)^{\frac{1}{2}}} \qquad \frac{\text{mol Al}}{\text{cm}^2 \cdot \text{s}} \tag{6}$$

where $P_{AlF}$ is the partial pressure of AlF in bar, $M_{AlF}$ is the molecular weight of AlF (45.98 g/mol), and T is the absolute temperature (K). For AlF at 900°C (1173 K), Eq. 6 can be transformed to.

$$J_{Al} = 0.191 P_{AlF} \quad \frac{\text{mol Al}}{\text{cm}^2 \cdot \text{s}} \tag{7}$$

Therefore, by equalizing the two fluxes given by Eqs. (5) and (6), the minimum pressure $P_{AlF}^{min}$ needed to sustain parabolic $Al_2O_3$ scale growth at 900°C and 60 s of oxidation can be calculated:

$$J_{Al}^{ox} = J_{Al} \tag{8}$$

$$2x10^{-9} = 0.191 P_{AlCl} \tag{9}$$

$$P_{AlF}^{min} = 1 \times 10^{-8}\ \text{bar} \tag{10}$$

There is a clear time and temperature dependency of $P_{AlF}^{min}$, decreasing with increasing time and/or decreasing temperature. The variation of $P_{AlF}^{min}$ within the relevant calculated temperature range 700–1100°C for an oxidation time of 60 s is shown in **Table 1**. Obviously, the real partial pressure of the reacting halide has to be greater than the minimum predicted by the above-derived method. This has to be the case during the early stages of the oxidation process. Furthermore, it has to be taken into account that not all aluminum halide species will contribute to the positive effect.

According to thermodynamic equilibrium calculations, AlF is the most volatile species of the gaseous metallic fluorides within a certain $F_2$ pressure range. Consequently, Eqs. (1) and (2) are the principal reactions of concern from the standpoint of the beneficial fluorine effect. This also shows that at least two AlF molecules are required to react with each other to form $Al_2O_3$. Therefore, adsorption and nucleation on a surface are favored, because a direct reaction by gas collision is not likely.

With these assumptions kept in mind, thermodynamic calculations are useful to determine the minimum partial pressure of fluorine, $P_{F_2}^{min}$, necessary in reaction (1) to obtain $P_{AlF}^{min}$. The results from those calculations are presented in **Table 1**.

| T/°C | $k_p(Al_2O_3)/g^2/cm^4s$ | $P_{AlF}^{min}$/bar | $P_{F_2}^{min}$/bar |
|---|---|---|---|
| 700 | $1 \times 10^{-15}$ | $4.3 \times 10^{-10}$ | $8.6 \times 10^{-10}$ |
| 800 | $5 \times 10^{-14}$ | $3.0 \times 10^{-9}$ | $6.0 \times 10^{-9}$ |
| 900 | $5 \times 10^{-13}$ | $1.0 \times 10^{-8}$ | $5.0 \times 10^{-7}$ |
| 1000 | $1 \times 10^{-12}$ | $1.6 \times 10^{-8}$ | $3.2 \times 10^{-8}$ |
| 1100 | $8 \times 10^{-12}$ | $4.5 \times 10^{-8}$ | $9.0 \times 10^{-8}$ |

The $k_p(Al_2O_3)$ values were obtained from the literature [19].

**Table 1.** Calculated minimum partial pressures of gaseous AlF and resulting pressures of $F_2$ which are necessary to sustain parabolic $Al_2O_3$ growth after 60 s of oxidation.

http://dx.doi.org/10.5772/intechopen.75696

As indicated by Eq. (1), it is required that fluorine is somehow present in the surface zone to react with the aluminum from the alloy to form gaseous Al fluorides. The implanted or "alloyed" fluorine has to develop a certain activity or partial pressure. Since the thermodynamic data for the fluorine activity in solid solution is not available, data for the $F_2$ partial pressure which can be calculated are taken into account for the following discussion. The partial pressure of elemental fluorine, $P_{F2}$, can be derived from the following equation:

$$P_{F_2} = a_F^2 \exp\left(\frac{-\Delta G}{RT}\right) \tag{11}$$

where $\Delta G$ is the Gibbs free enthalpy for the formation of $F_2$ and $a_F$ is the chemical activity of F in the TiAl substrate. Unfortunately, no data exist for both of these parameters. In addition it has to be kept in mind that the system is not closed. During high-temperature exposure, fluorine can be released by outward diffusion of gaseous species without reacting with Al before a closed alumina scale can block this [18]. Hence, the $P_{F2}$ at the alloy/scale interface can only be approximated to be within a certain range. However, it will be shown that meaningful results can be obtained by making such an approximation.

Also, an upper limiting $P_{F2}$ value for the beneficial fluorine effect ($P_{F_2}^{max}$) has to be approximated. This approximation is based on the competition of Al and Ti oxide formation. As discussed earlier, the formation and subsequent growth of the $Al_2O_3$-rich scale requires the adsorption of the aluminum fluoride species onto the surfaces of pores and micro-cracks within the oxide. The extent of aluminum adsorption would be expected to increase with an increase in the summed partial pressure of the reactive Al fluoride species, $\sum P_{AlFx}$, up to the point where the rate of aluminum supply is sufficient to sustain parabolic $Al_2O_3$ growth kinetics, i.e., when $\sum P_{AlFx} = P_{\Sigma AlF_x}{}^{min}$. Beyond this point the rate of $Al_2O_3$ growth would be solid-state diffusion controlled and therefore independent of $P_{AlFx}$. The extent of titanium adsorption and subsequent $TiO_2$ growth would be equally expected to increase with increasing partial pressure of the volatile Ti halide species, $\sum P_{TiXy}$. However, the rate of $TiO_2$ growth is significantly greater than that of $Al_2O_3$ [21]. Therefore, if it is assumed that the probability for oxidation is the same for all chemisorbed species and that non-protective inner-scale formation occurs when the rate of $TiO_2$ growth exceeds that of $Al_2O_3$; then, it can be approximated that the beneficial fluorine effect can only occur if $\sum P_{TiFy} < \sum P_{\Sigma AlF_x}{}^{min}$ (stoichiometry and molar volume of the oxides are being neglected in this approximation since no significant changes in the results would occur). As will be shown in the following, this essentially equates to $P_{F_2}^{max}$ being set by $P_{TiF3} = P_{AlF}^{min}$. When $P_{F_2} > P_{F_2}^{max}$, the predominance of aluminum oxidation is not possible, and the formation of a non-protective $TiO_2$-$Al_2O_3$ or $TiO_2$-rich scale occurs instead.

$P_{F_2}^{min}$ and $P_{F_2}^{max}$ can be obtained from thermodynamic calculations. The main aim of the thermodynamic calculations is to quantify the $P_{X2}$ "corridor" (and by this the level of the necessary halogen reservoir) in which the beneficial halogen effect can operate. The potential reactions considered in these calculations are given in the following for fluorine. The calculations were conducted using the thermodynamic software packages ChemSage and FactSage [22].

Apart from the formation and oxidation of $AlF_{(g)}$ given by reactions (1) and (2), the following reactions must also be considered because their enthalpy is negative:

$$Al_{(TiAl)} + F_2 \rightarrow AlF_{2(g)}; \Delta G = -6.64 \times 10^5 \quad (12)$$

$$Al_{(TiAl)} + 1.5\ F_2 \rightarrow AlF_{3(g)}; \Delta G = -1.14 \times 10^6 \quad (13)$$

$$Ti_{(TiAl)} + 0.5\ F_2 \rightarrow TiF_{(g)}; \Delta G = -1.92 \times 10^5 \quad (14)$$

$$Ti_{(TiAl)} + F_2 \rightarrow TiF_{2(g)}; \Delta G = -6.57 \times 10^5 \quad (15)$$

$$Ti_{(TiAl)} + 1.5\ F_2 \rightarrow TiF_{3(g)}; \Delta G = -1.11 \times 10^6 \quad (16)$$

$$Ti_{(TiAl)} + 2\ F_2 \rightarrow TiF_{4(g)}; \Delta G = -1.41 \times 10^6 \quad (17)$$

$$2\ TiF_{(g)} + 2\ O_2 \rightarrow 2\ TiO_{2(s)} + F_2; \Delta G = -1.09 \times 10^6 \quad (18)$$

$$TiF_{2(g)} + O_2 \rightarrow TiO_{2(s)} + F_2; \Delta G = -7.93 \times 10^4 \quad (19)$$

Unlike other halogens [19], the enthalpies of the oxidation of the fluorides with a high oxygen state of the cation are positive for both metals Al and Ti:

$$4\ AlF_{3(g)} + 3\ O_2 \rightarrow 2\ Al_2O_{3(s)} + 6\ F_2; \Delta G = +1.94 \times 10^6 \quad (20)$$

$$4\ AlF_{2(g)} + 3\ O_2 \rightarrow 2\ Al_2O_{3(s)} + 4\ F_2; \Delta G = +3.66 \times 10^4 \quad (21)$$

$$TiF_{3(g)} + O_2 \rightarrow TiO_{2(s)} + 1.5\ F_2; \Delta G = +3.76 \times 10^5 \quad (22)$$

$$TiF_{4(g)} + O_2 \rightarrow TiO_{2(s)} + 2\ F_2; \Delta G = +6.79 \times 10^5 \quad (23)$$

From the enthalpies of the reactions (10), (18), and (19), it can be concluded that only AlF leads to the fluorine effect, i.e., there is no thermodynamic driving force for the oxidation of the stable molecules $AlF_2$ or $AlF_3$. As a consequence of this, all the thermodynamic calculations for $P^{min}_{Al_xF_y}$ and $P^{max}_{Al_xF_y}$ are based on the assumption that $Al_2O_3$ growth is sustained only via AlF transport. The maximum pressure $P^{max}_{F_2}$ is reached if the titanium fluorides start to get relevant, i.e., $P_{Ti_xF_y}$ equals $P^{min}_{AlF}$ . In **Figure 4** the pressures of the gaseous fluorides at 900°C are presented. It can be clearly seen that $AlF_{(g)}$ is the predominant species.

In the envisaged temperature range above 700°C where oxidation protection of TiAl components is needed, a positive fluorine effect is established (**Figure 5**). The corridor for the so-called fluorine effect widens with increasing temperature and spans several orders of magnitude of the fluorine pressure. The values for $P^{min}_{F_2}$ rise steadily with increasing temperature, while for $P^{max}_{F_2}$ a type of plateau is reached at about 1000°C. The values of $P^{max}_{F_2}$ at 900 and 1100°C are slightly lower than the one at 1000°C. The limits for the other halogens are similar (see Appendix **Figures A1**, **A2**, **A3**).

http://dx.doi.org/10.5772/intechopen.75696

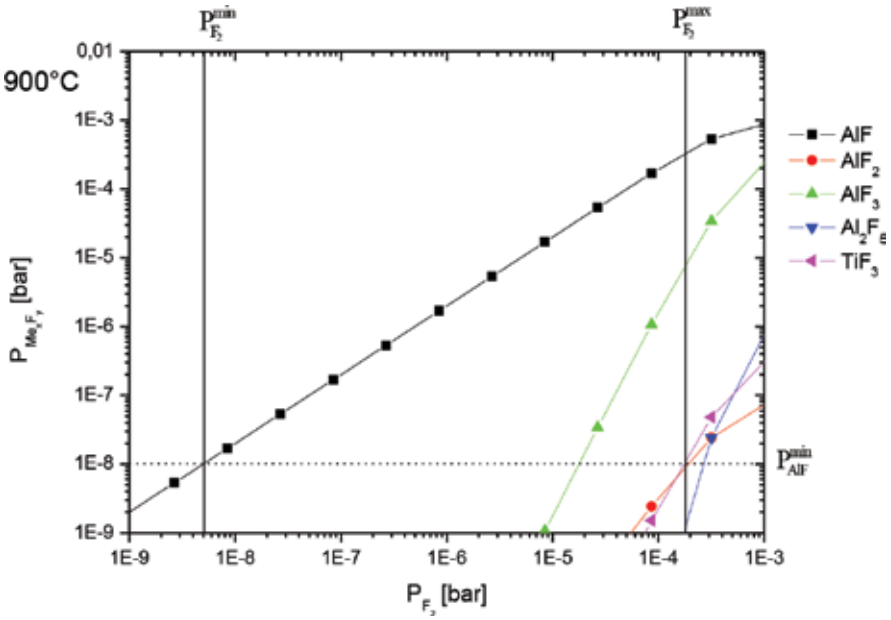


**Figure 4.** Calculated partial pressures of the gaseous metal fluorides versus elemental fluorine partial pressure at 900°C.

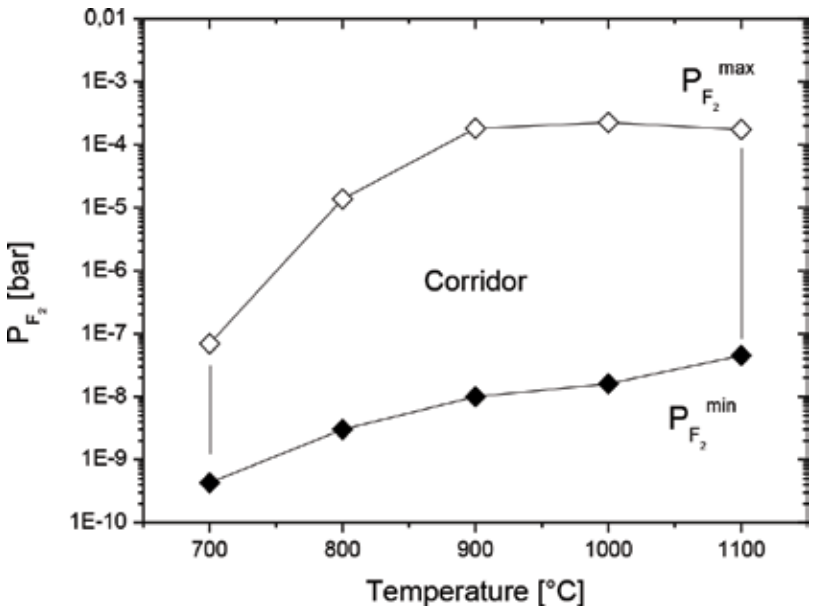


**Figure 5.** $P_{F2}$ limits of the fluorine effect.

Furthermore, evaporation of stable titanium fluorides during heating up has to be considered (s. **Table 2**) because the higher-valence titanium fluorides are very stable and do not show much tendency to form titanium oxide (see reactions (20) and (21)). This leads to a fluorine loss

| Temperature/°C | $p(TiF_{4(g)})$/bar |
|---|---|
| 100 | $5.10 \times 10^{-5}$ |
| 200 | $3.08 \times 10^{-3}$ |
| 300 | $1.70 \times 10^{-0}$ |
| 400 | $8.40 \times 10^{-0}$ |
| 500 | $6.36 \times 10^{-6}$ |
| 600 | $1.20 \times 10^{-10}$ |

**Table 2.** Calculated partial pressures of $TiF_{4(g)}$ during heating up.

which has to be overcome by an "over-doping." On the other hand, this can have a certain buffering effect if too much fluorine is applied locally.

The calculations and consideration confirm the positive fluorine effect if the oxidation temperature is sufficiently high, the heating-up period is kept short, and if an overdose of fluorine (but not so high to induce corrosion) is applied in order to account for fluorine losses during heating to oxidation temperature.

## 3. Fluorination

The positive results of the optimized F-BLI[2] shown in **Figure 1** were achieved during isothermal exposure at 900°C in air. For the technical use of TiAl components, protection under thermocyclic conditions for much longer exposure times is an obligatory requirement. Additionally, different fluorination techniques had to be developed because beamline implantation can only be used for laboratory-scale samples with flat surfaces and not for technical components with complex structures, e.g., turbo charger rotors. Therefore, several attempts have been undertaken to apply a fluorine treatment which is independent of any sample geometry. First, a liquid-phase treatment by dipping in aqueous $HF_{(aq.)}$ was utilized [23]. The concentration of the acid, the temperature, and the dipping time had to be adjusted. The concentration is very relevant because the etching of the metallic surface must be limited. After optimization the best results were achieved by the following set of parameters, dipping in 0.1 mol% $HF_{(aq)}$ for 2 h at room temperature (RT) which can be seen in **Figure 6**.

A second liquid-phase treatment was performed by spraying halogen-containing polymers uniformly over the whole surface of different TiAl samples at RT and simple drying in air afterward. Depending on the polymer and it's amount used, a mass loss is observed after the beginning of oxidation which levels off to alumina kinetics during further exposure (**Figure 7**). This mass loss is caused by the decomposition of the polymer and evaporation of the organic residues. The released fluorine reacts with the metal surface, thus activating the fluorine effect. Samples of the technical second-generation alloy γ-MET (Ti-46.5Al-4(Cr, Nb, Ta, B)) were exposed thermocyclically at 900°C in air. The samples were placed in the hot furnace, kept at temperature for 24 h, removed from the hot furnace, cooled to RT within about 15 min,

http://dx.doi.org/10.5772/intechopen.75696

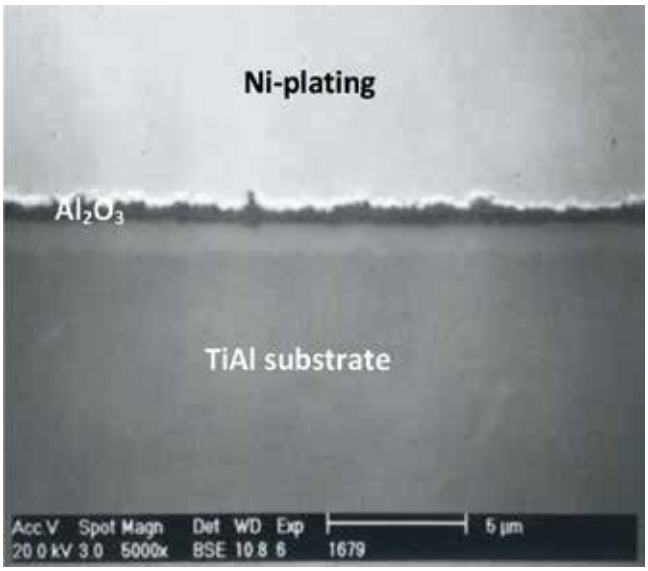


**Figure 6.** SEM/BSE image of a TiAl specimen treated with 0.1 mol% HF for 2 h at RT and oxidized for 100 h at 900°C in air.

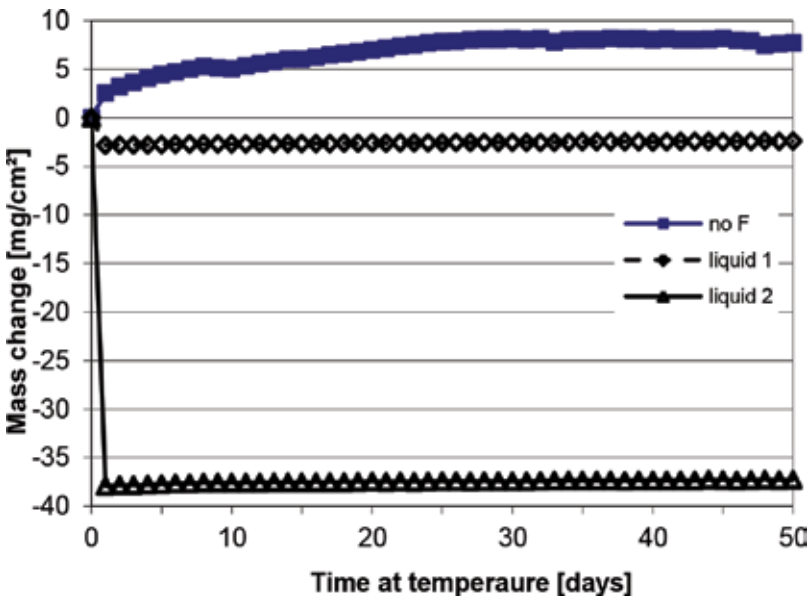


**Figure 7.** Mass change data of three TiAl specimens exposed thermocyclically at 900°C in air. One sample is untreated, and the two other samples are liquid-phase F-treated.

weighed, and put back into the hot furnace after 1 hour, thus resulting a 25 h cycle test. The untreated sample reveals a mass gain which is interrupted several times by minor mass losses due to spallation of parts of the oxide scale. Spallation can occur if the stresses caused by the

CTE mismatch between ceramic oxide and metallic substrate exceed a certain level. The final mass gain after 50 days of exposure (= 1200 h) is about 8 mg/cm$^2$. The mass change behavior of the two treated specimens is characterized by a mass loss during the first day of exposure due to evaporation of the organic residues of the polymer. Depending on the polymer, this mass loss can vary between 1 and almost 40 mg/cm$^2$. After this mass loss, a very slow-growing scale and absolutely no spallation of any parts of the scale were observed. The mass gain during the 49 remaining days of exposure was less than 2 mg/cm$^2$ for both F-polymer-treated samples.

Besides the described liquid-phase treatments, fluorination via the gas-phase directly at elevated temperatures has also been proven to be successful. The first attempt has been made by the decomposition of solid fluorine-containing polymers. TiAl samples were placed in a hot furnace together with small amounts of a solid fluorine-containing polymer. During the initial hours of exposure, the polymer decomposes and fluorine is released. The fluorine reacts with the specimen to allow the fluorine effect to operate. The whole process is performed under laboratory air. No protective gas is needed. In **Figure 8** results of the same thermocyclic 25 h cycle test are presented. The F-treated sample showed a pronounced mass gain during the first day due to uptake of fluorine and oxygen, but during the second day, the mass gain rate has dropped, and the total mass gain during the next 49 days of exposure stayed below 1 mg/cm$^2$.

Beamline ion implantation (BLI$^2$) cannot provide total protection for technical TiAl compounds. Therefore, a different implantation technique has to be used. The plasma immersion ion implantation (PI$^3$) allows implantation of specimens with more complex geometries [24]. During this treatment the samples are placed in a vacuum chamber and a negative charge is applied. The fluorine-containing gas is led into the chamber and the plasma is ignited. Due to the high voltage, the fluorine cations are accelerated to the surface of the specimen so that this is implanted

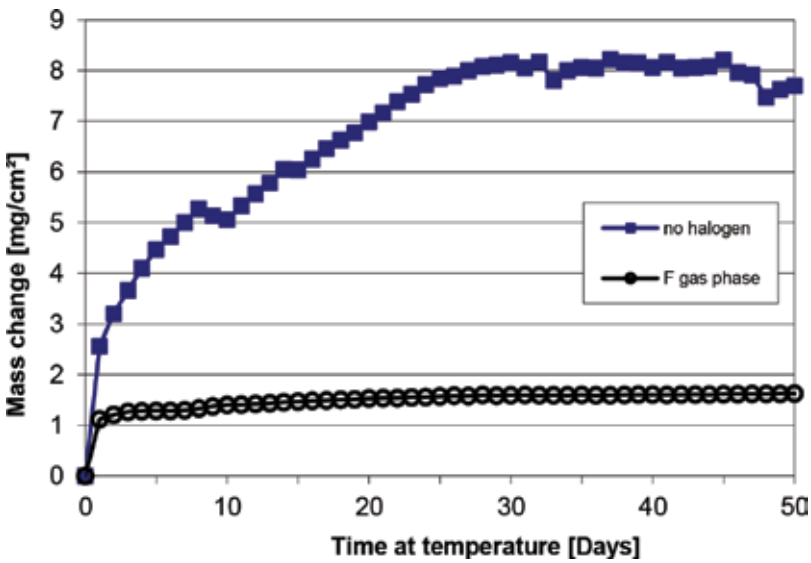


**Figure 8.** Mass change data of two TiAl specimens exposed thermocyclically at 900°C in air. One sample is untreated and the second is gas-phase F-treated.

http://dx.doi.org/10.5772/intechopen.75696

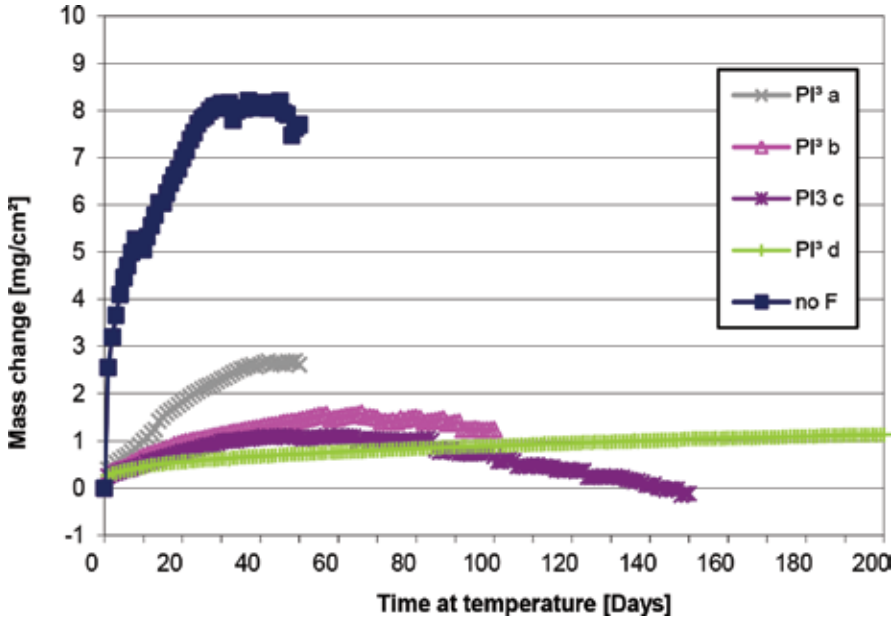


**Figure 9.** Mass change data of an untreated and four F-PI$^3$-treated TiAl specimens exposed thermocyclically at 900°C in air.

completely. Elemental $F_2$ gas or other fluorine-containing gases such as $CH_2F_2$ can be used. After optimization of this technique, thermocyclic long-term oxidation protection of TiAl samples for 4800 h at 900°C in air was achieved (**Figure 9**). Only the sample named PI$^3$-d showed slow-growing alumina kinetics over the whole period of exposure (200 days = 4800 h), while the three other F-PI$^3$ implanted specimens revealed at better behavior than the untreated sample, but further optimization was needed. Their mass gains are higher than the one of the sample PI$^3$-d, and some mass losses due to partial spallation of the oxide scale can be seen even leading to a final negative mass change value of the sample PI$^3$-c after 150 days of exposure. It can be said that the process was finally optimized to result in stable oxidation protection of TiAl specimens.

An evaluation of the mass changes of several samples after each day during thermocyclic exposure can be seen in **Figure 10**. The differences of the masses of the specimens treated with fluorine by different techniques are almost zero from day 2 of exposure to the end, while the untreated sample reveals a much larger scatter. During the first days of exposure, the difference gets smaller. The observable mass losses were caused by spallation. The higher mass gains directly afterward were due to formation of a new mixed oxide scale at the spalled areas. Even during the last days of exposure, the variation of the mass of the untreated sample is always higher than the ones of the F-treated specimens.

### 3.1. Long-term protection

The 24 h cycle test was prolonged for 1 year, i.e., 365 days (= 8760 h), to investigate the long-term stability of the fluorine effect. In **Figure 11** the mass change data of the exposed samples

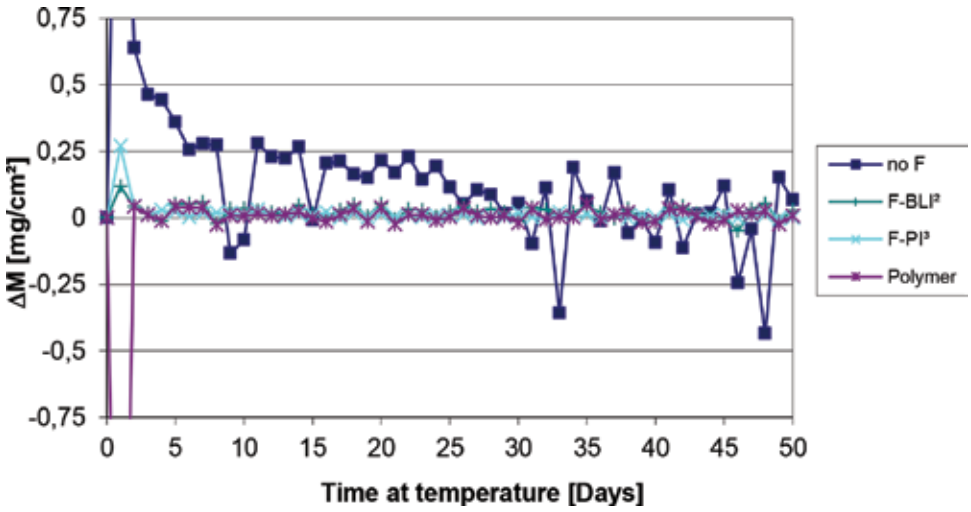


**Figure 10.** Mass change between each day of an untreated and three different F-treated TiAl specimens exposed thermocyclically at 900°C in air for 50 days.

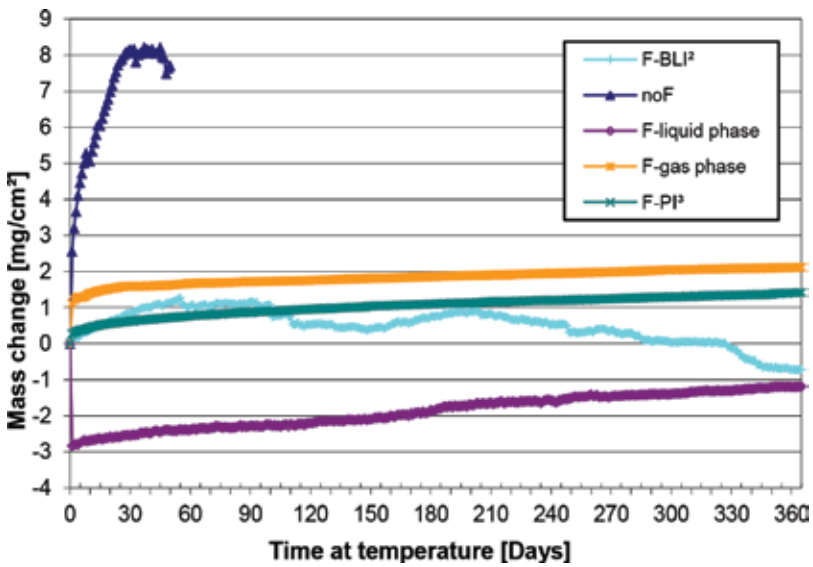


**Figure 11.** Mass change data of an untreated and four different F-treated specimens exposed thermocyclically at 900°C in air.

are depicted. The F-BLI$^2$ implanted sample had a negative mass change at the end of the test. This was caused by spallation of parts of the oxide at areas of the specimen where a mixed scale has formed. This sample was not protected at the edges due the limitation of the BLI$^2$ process so that ordinary mixed scale formation took place at these spots. During the fast cooling to RT, parts of this mixed scale spalled off. The other three F-treated specimens did

http://dx.doi.org/10.5772/intechopen.75696

not show any tendency to spallation. The mass gain was slow and steady. The reasons for the mass loss of the sprayed specimen and the mass gain of the gas-phase-treated specimen after the first day are described above. The PI$^3$ also provides total coverage. The F-treated samples do not show any weakness in the protective fluorine effect. This effect is expected to the last much longer. Post-experimental investigations illustrate the nature of the scales formed during exposure. The appearance of the specimens reflects their mass change data. The untreated sample is covered with a yellowish scale which has partly spalled (**Figure 12a**). The edges of the F-BLI$^2$ sample are covered with a yellow/brown mixed scale, while the faces are gray, which indicates the protective alumina layer (**Figure 12b**). The faces were implanted, but the edges could not be treated due to the limits of the beam process. The PI$^3$ process on the other hand is also capable of implanting the edges; hence, the sample appears totally gray (**Figure 12c**). The sprayed sample looks white (**Figure 12d**). This is caused by the residues of the spray which were oxidized above the protective alumina layer. This will be subsequently shown in detail in the metallographic cross sections.

The metallographic cross sections reveal the nature of the oxide scales. The light optical microscope (LOM) images show the differences of the scales formed during oxidation on the surfaces of the exposed samples. The mixed scale on the untreated sample after 50 days of exposure is roughly 100 μm thick and exhibits a lot of cracks (**Figure 13a**). The mixed scale consists of an outer rutile layer, followed by an alumina layer and a mixed oxide nitride scale

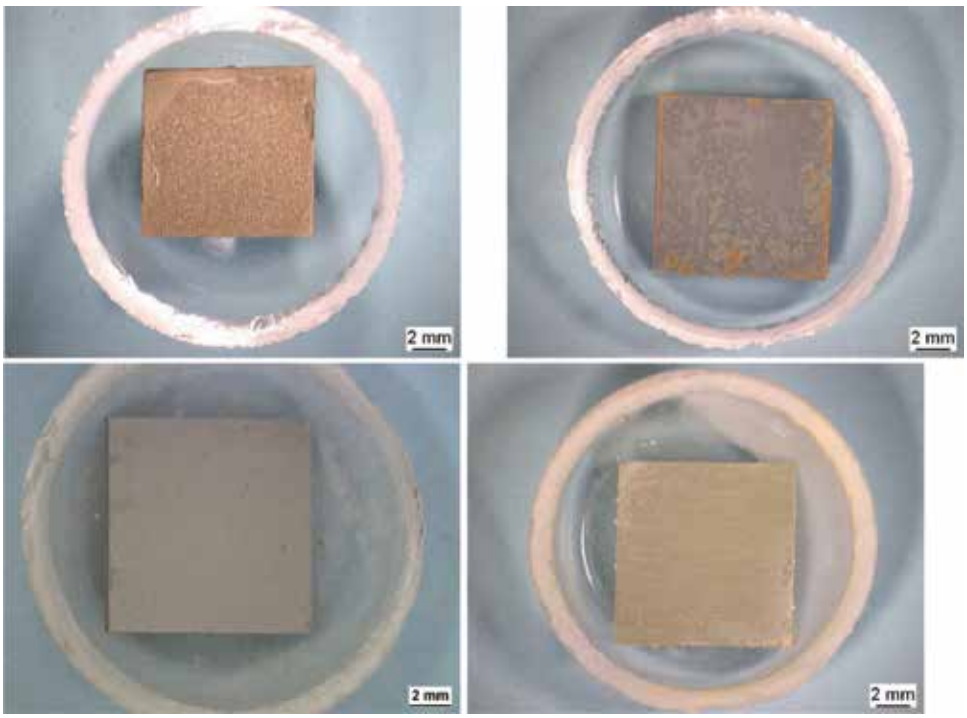


**Figure 12.** Optical appearance of the exposed TiAl samples after thermocyclic oxidation at 900°C in air: (a) untreated sample after 50 days, (b) F-BLI$^2$, (c) F-PI$^3$, and (d) F-sprayed all three after 365 days.

above the substrate. The LOM images of the treated specimens indicate the thin layers where the fluorine effect had functioned (**Figure 13b–d**).Accelerated oxidation occurred at the unimplanted edges of the F-BLI$^2$ sample (**Figure 14a**, **b**). The metallic cross section is reduced due to spallation and renewed oxidation (**Figure 14 a**). The transition of the thick mixed scale to the areas with the thin alumina layer can be seen. Here, the fluorine effect via the BLI$^2$ is still working. The mixed scale is undulated and roughly 50–100 μm thick (**Figure 14b**).

Scanning electron microscopic investigations coupled with energy dispersive X-ray spectroscopy (SEM/EDX) provide a better grasp of the microstructure and composition of the scales. The images of the F-treated specimens look similar; hence, only one sample is presented here. The F-spayed sample is covered with a thin protective alumina layer on all faces (**Figure 15a**). This layer is approximately 2–3 μm thick (**Figure 15b**). Underneath this layer some fluorine was detected locally in some spots at the metal/oxide interface (**Figure 16a**). This was proven by EDX (**Figure 16b**). The scale is very thin (1–2 μm), thus Ni from the Ni plating and Ti, Cr, and Nb from the substrate were detected next to Al, O, and F from the scale.

Electron probe microanalysis (EPMA) provides the elemental distributions within the scales. Fluorine was found at two spots underneath the thin alumina layer (**Figure 17a**). The oxide layer consists predominantly of Al and O (**Figure 17b**, **c**) with some titanium oxide on the outer surface (**Figure 17d**), which was formed during the incubation period. The metallic subsurface

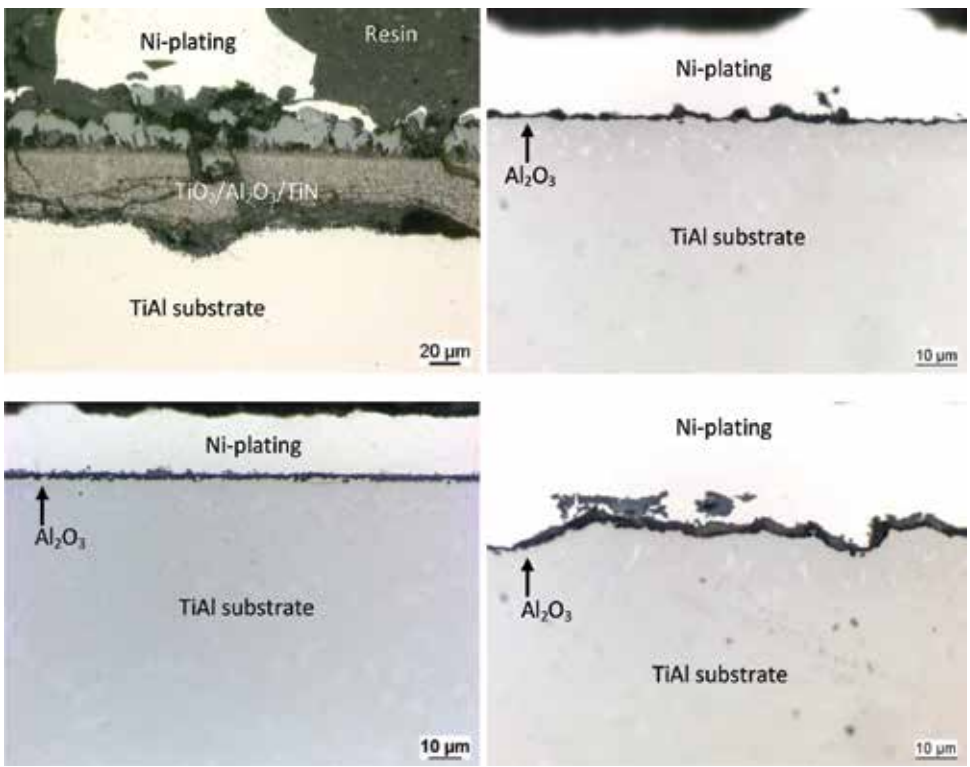


**Figure 13.** LOM images of the exposed TiAl samples after thermocyclic oxidation at 900°C in air: (a) untreated sample after 50 days, (b) F-BLI$^2$, (c) F-PI$^3$, and (d) F-sprayed all three after 365 days.

http://dx.doi.org/10.5772/intechopen.75696

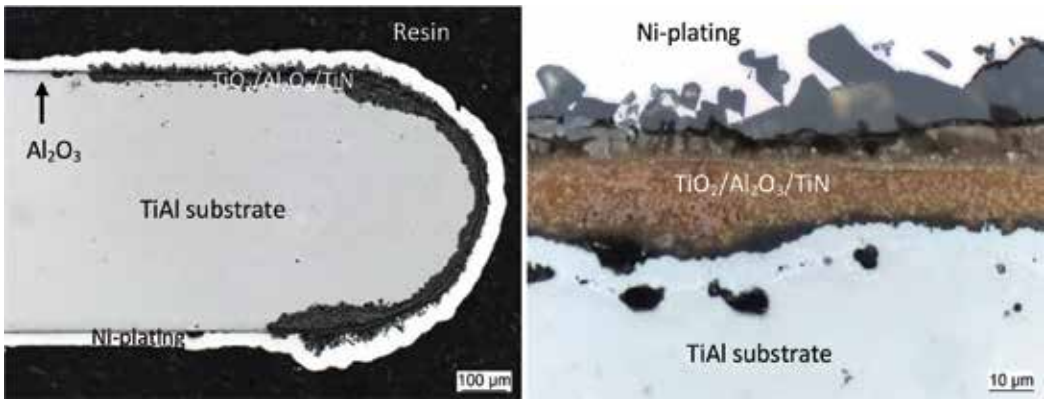


**Figure 14.** LOM images of the exposed F-BLI$^2$ sample after thermocyclic oxidation at 900°C for 365 days in air: (a) overview and (b) detailed image of the mixed scale.

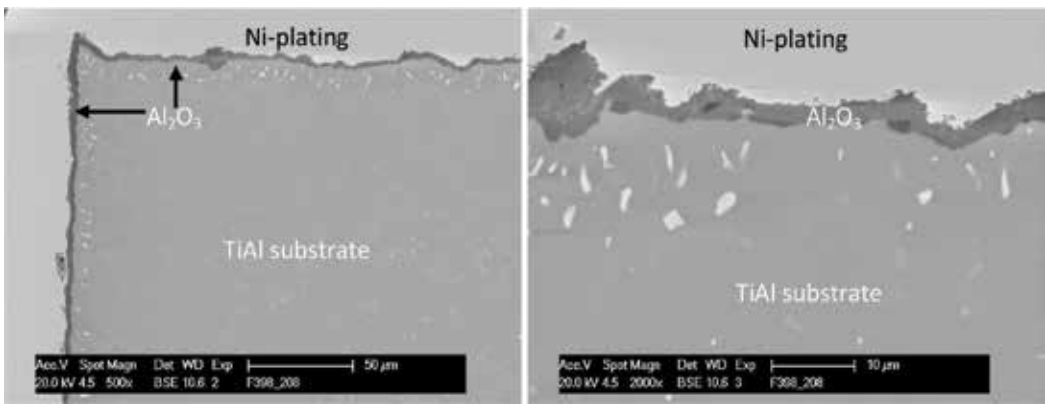


**Figure 15.** SEM images of the F-sprayed sample after thermocyclic oxidation at 900°C for 365 days in air: (a) overview of an edge and (b) detailed image of the thin alumina layer.

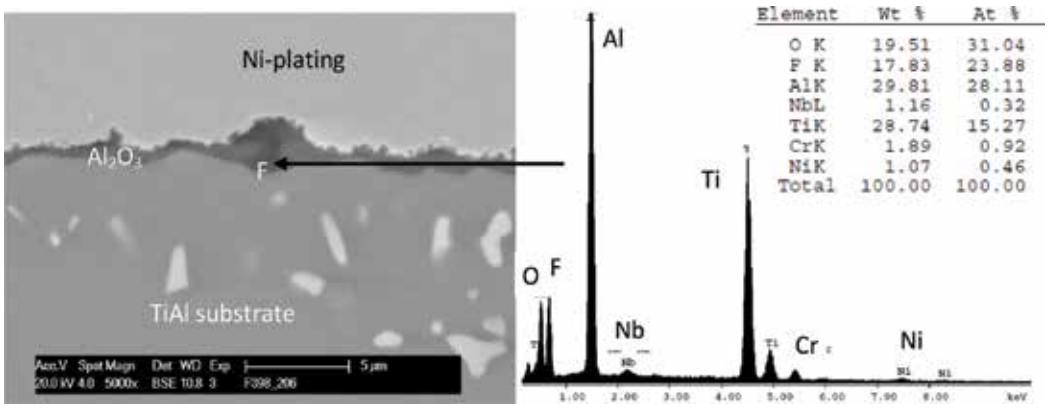


**Figure 16.** SEM/BSE image (a) and EDX spectrum (b) of the F-BLI$^2$ sample after thermocyclic oxidation at 900°C for 365 days in air.

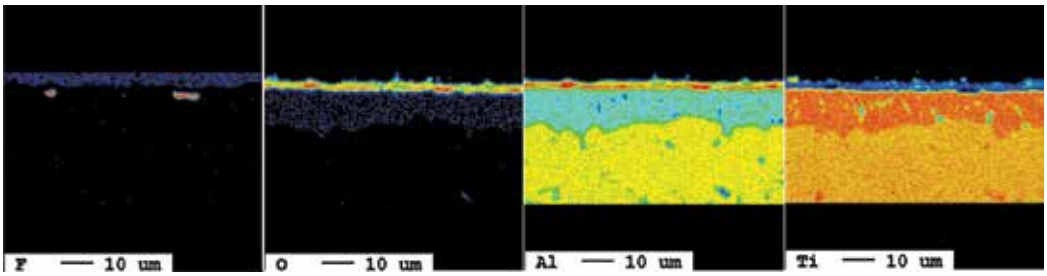


**Figure 17.** EPMA elemental distribution images of F (a), O (b), Al (c), and Ti (d) of the F-PI[3] sample after thermocyclic oxidation at 900°C for 365 days in air.

zone is depleted in Al due to alumina formation via the fluorine effect. This can be seen in the elemental distributions (**Figure 17c,d**), while it is hard to see this feature in the corresponding SEM/BSE image (**Figure 18**). The additional elements such as Nb or Cr are enriched in precipitates also in the subsurface zone. Those can be correlated to the bright spots in **Figure 18**. The fluorine spots underneath the alumina layer can be seen in this figure, too.

### 3.2. TiAl components

Turbocharger rotors as examples for technical TiAl components have been tested as well. The components were used in the as-received state. Fluorination was performed by spraying. The samples were exposed at 1050°C for up to 1200 h in laboratory air. In every 100 h the samples were taken out of the hot furnace cooled to RT outside the furnace, images were made, and

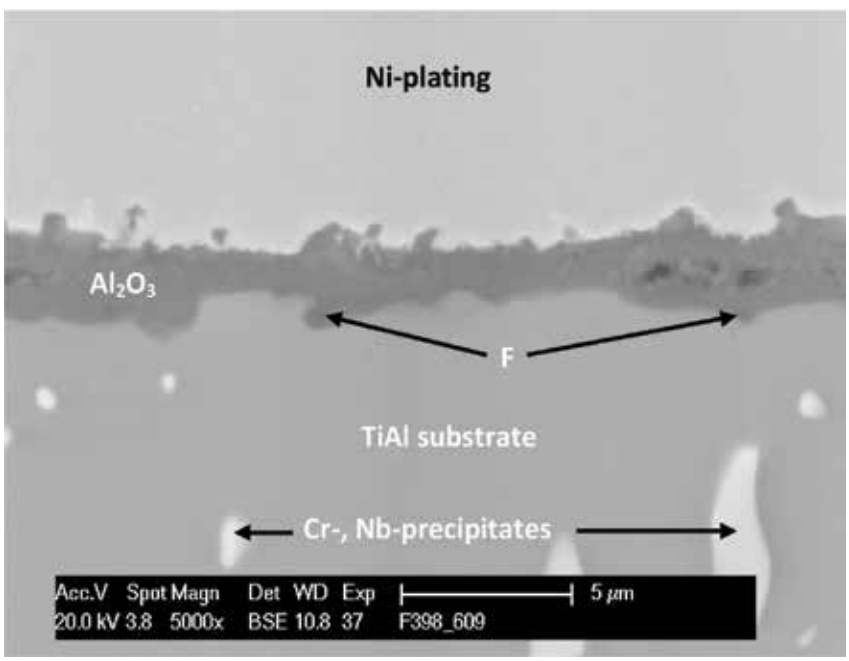


**Figure 18.** Corresponding SEM/BSE image of the F-PI[3] sample after thermocyclic oxidation at 900°C for 365 days in air.


**Figure 19.** Macroscopic images of an untreated turbocharger rotor before (a), after 100 h (b), and 1200 h (c) of oxidation at 1050°C in laboratory air.

after 1 hour, the samples were put back in the hot furnace. The untreated specimens show severe spallation of the oxide scale (**Figures 19**, **20b–c**). This happened during each cooling down very shortly after removing from the furnace, while the sample was still hot. The load-bearing cross section of the blades is reduced due to this attack. Exposure at 1050°C can even lead to the total destruction of the component only by oxidation itself if the material is more sensitive to oxidation, i.e., due to changes in the chemical composition (**Figure 20a–c**). In contrast the fluorine treatment protected the rotors for the whole period of exposure. The treated samples only change color. The shown sample appears yellowish after 100 h and only became a bit darker (**Figure 21a–c**). No sign of any spallation is visible.


**Figure 20.** Macroscopic images of the second untreated TiAl rotor with a different chemical composition before (a), after 100 h (b), and totally destroyed after 1200 h (c) of oxidation at 1050°C in laboratory air.


**Figure 21.** Macroscopic images of an F-treated turbocharger rotor after spraying (a), after 100 h (b), and 1200 h (c) of oxidation at 1050°C in laboratory air.

## 4. Conclusions

The results show the remarkable effect of several optimized fluorine treatments by improving the oxidation resistance of TiAl alloys. The oxidation mechanism of the TiAl alloys is changed from non-protective mixed scale formation to alumina formation via the halogen effect if a defined amount of halogen is applied at the surface. Fluorine is the best doping element. Its effect lasts as long as 1 year under thermocyclic conditions without any signs of weakness, e.g., spallation. If only oxidation is taken into account, the temperature capability of TiAl alloys can be raised up to at least 1050°C. The fluorine content has to reach a certain minimum level to obtain the effect to operate, but an upper level must not be exceeded. Otherwise, negative fluorine corrosion occurs which would lead to accelerated oxidation. After optimized fluorine treatment, i.e., $PI^3$; liquid-phase treatment, e.g., by spraying; or a gas-phase treatment, total coverage of the surface can be achieved. With such a treatment, the use of TiAl components at elevated temperatures could be possible with all the advantages of this lightweight material regarding the efficiency of, e.g., jet engines or automotive engines.

## Acknowledgements

The work was funded by the German Federal Ministry for Economic Affairs and Energy via the German Federation of Industrial Research Associations which is gratefully acknowledged by the authors. The fruitful discussions with Prof. B. Gleeson and Prof. M. Schütze concerning the mechanism of the halogen effect are also acknowledged.

## A. Appendix

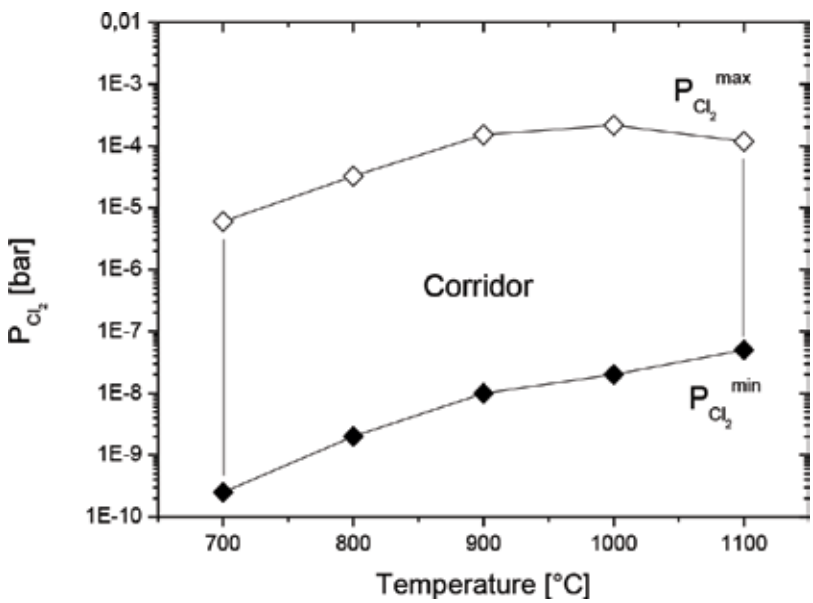


**Figure A1.** $P_{Cl2}$ limits for the chlorine effect.

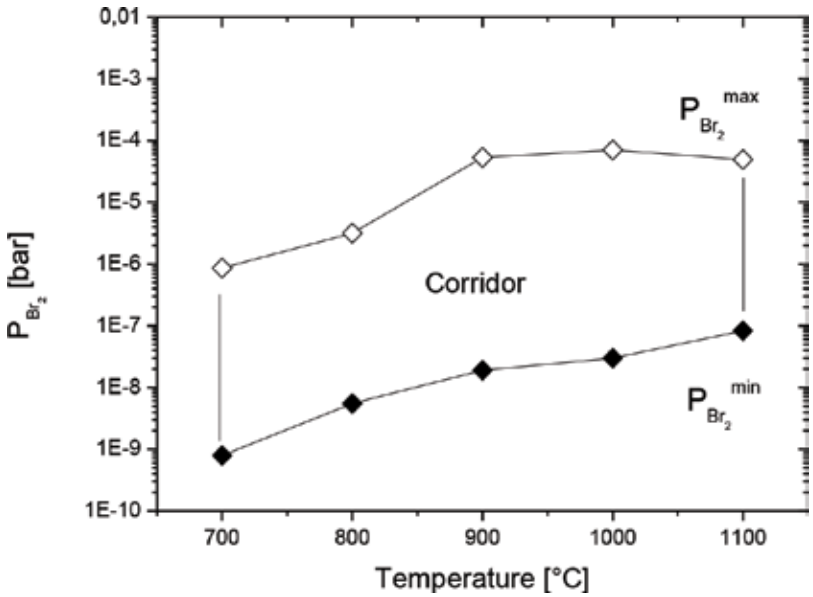


**Figure A2.** $P_{Br2}$ limits for the bromine effect.

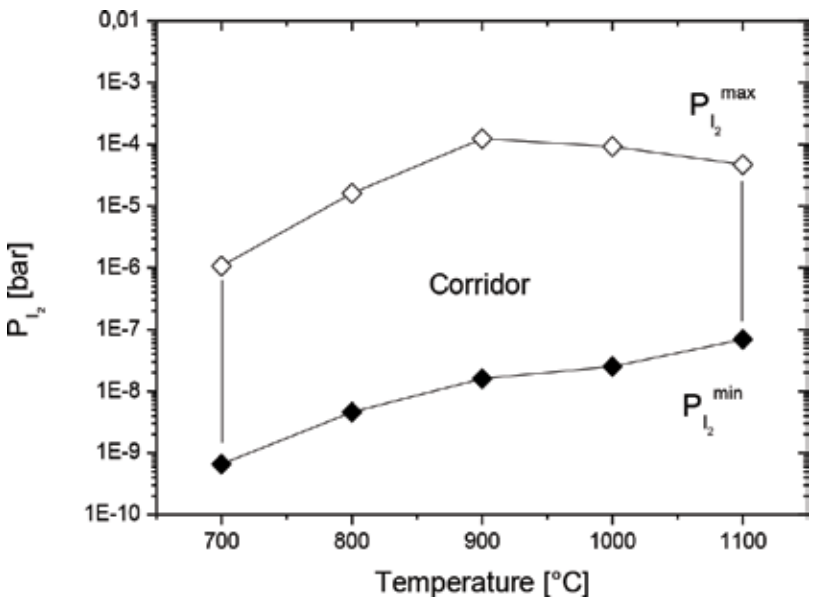


**Figure A3.** $P_{I2}$ limits for the iodine effect.

## Author details

Alexander Georg Donchev and Mathias Christian Galetz*

*Address all correspondence to: galetz@dechema.de

DECHEMA-Forschungsinstitut, Frankfurt am Main, Germany

## References


[1] Clemens H, Mayer S. Advanced Engineering Materials. 2013;**15**:191

[2] Schwaighofer E, Clemens H, Mayer S, Lindemann J, Klose J, Smarsly W, Güther V. Intermetallics. 2014;**44**:128

[3] Appel F, Oehring M, Paul J. Gamma Titanium Aluminide Alloys. Weinheim, Germany: WILEY-VCH; 2011

[4] Appel F, Oehringe M. In: Leyens C, Peters M, editors. Titanium and Titanium Alloys. Weinheim, Germany: WILEY-VCH; 2003. p. 89

[5] Leyens C. In: Leyens C, Peters M, editors. Titanium and Titanium Alloys. Weinheim, Germany: WILEY-VCH; 2003. p. 187

[6] Shida Y, Anada H. Corros. Science. 1993;**35**:945

[7] Luthra KL. Oxidation of Metals. 1991;**36**:475

[8] Dettenwanger F, Schumann E, Rakowski J, Meier GH, Rühle M. Material Science Forum. 1997;**211**:251-254

[9] Schütze M. In: Holmes DR, editor. Protective Oxide Scales and their Breakdown. Chichester, UK: WILEY-Chichester; 1997

[10] Donchev A, Schütze M, Kolitsch A, Yankov R. Material Science Forum. 2012;**1061**:706-709

[11] Donchev A, Zschau H-E. M. Schütze. In: Brillas E, Cabot P-L, editors. Trends in Electrochemistry and Corrosion at the Beginning of the 21st Century. Barcelona, Spain: Universitat Barcelona; 2004. p. 1061

[12] Bender R, Schütze M. Materials and Corrosion. 2003;**54**:652

[13] Fähsing D, Rudolphi M, Konrad L, Galetz MC. Oxidation of Metals. 2017;**88**:155

[14] Kumagai M, Shibue K, Kim M-S, Yonemitsu M. Intermetallics. 1996;**4**:557

[15] Taniguchi S. Materials and Corrosion. 1997;**48**:1

[16] Schütze M, Hald M. Material Science Engineering A. 1997;**239-240**:847

[17] Donchev A, Gleeson B, Schütze M. Intermetallics. 2003;**11**:387

[18] Donchev A, Zschau H-E, Schütze M. Mat. High Temperature. 2005;**22**:309

[19] Hindam H, Whittle DP. Oxidation of Metals. 1982;**18**:245

[20] Poirier DR, Geiger GH. Transport Phenomena in Materials Processing. Warrendale, USA: TMS; 1994

[21] Kofstad P. High Temperature Corrosion. London, UK: Elsevier; 1988

[22] Computer Software Packages ChemSage and FactSage by GTT-Technologies GmbH, Herzogenrath, Germany

[23] Zschau H-E, Gauthier V, Schumacher G, Dettenwanger F, Schütze M, Baumann H, Bethge K, Graham M. Oxidation of Metals. 2003;**59**:183

[24] Anders A. Handbook of Plasma Immersion Ion Implantation and Deposition. New York, USA: John Wiley & Sons; 2000

Chapter 5

# Structural and Mechanical Behaviour of Al-Fe Intermetallics

Mohammed Ishaq Raviathul Basariya and
Nilay Krishna Mukhopadhyay

Additional information is available at the end of the chapter

http://dx.doi.org/10.5772/intechopen.73944

**Abstract**

In this chapter, results of our recent investigations on Al-25%Fe (at.%), Al-30%Fe and Al-34.5%Fe alloys close to $Al_3Fe$, $Al_5Fe_2$ and $Al_2Fe$ intermetallic phases have been discussed. The effect of process parameters on structural aspects and mechanical behaviour of Al-Fe intermetallics has been studied. The high melting intermetallics that are difficult to prepare by conventional processing technique are easily synthesized in nanocrystalline state with a homogeneous structure by mechanical means. In this process, we have come out with a single orthorhombic $Al_5Fe_2$ nanocrystalline intermetallic phase. Hardness measurements of intermetallic revealed an increase in hardness with a decreasing grain size up to a critical grain size, followed by a decrease. A decrease in hardness with a grain size refinement, an indication of softening behaviour, demonstrating the Inverse Hall-Petch (IHP)-like phenomenon has been observed in intermetallic compounds. The deviation from the regular Hall-Petch (HP) behaviour has been discussed using various deformation models based on the dislocations and grain boundary-mediated processes. The study is focused on investigations of Al-rich iron aluminide intermetallics to understand the structure property correlations.

**Keywords:** high-energy ball milling, intermetallics, $Al_5Fe_2$, $Al_3Fe$, inverse Hall-Petch, nanostructured materials, mechanical properties, deformation mechanisms, grain boundary sliding

## 1. Introduction

Intermetallics represent a manifold class of materials that possess intermediate properties between metallic and non-metallic materials. Intermetallic phases and compounds are formed by a combination of two or more metals falling at or near a fixed stoichiometric ratio

and exhibit different crystal structure and properties than their constituent elements. The composition of an intermetallic may vary within a restricted composition range known as homogeneity range. Since 2500 BC, metallurgists have used intermetallics, and its phases have attracted significant interests during the last few decades since they offer new prospects for developing structural materials for high-temperature applications.

### 1.1. Intermetallics

An increased need for new and novel materials with specified properties and particular application has attracted greater attention of metallurgists and material scientists in recent years. Intermetallics are one such material with a vast potential for application in a wide range of technologically important areas [1]. The first observation of an intermetallic was made in 1839 by Karl Karsten, when he observed a discontinuity in the action of acids on alloys of copper and zinc at the equi-atomic composition and suggested the formation of a compound. The compound is now popularly called as β-brass (CuZn). Intermetallics are already indispensable in many applications and offer the possibility of providing additional breakthrough in performance in, for example, high-temperature structural materials, magnetic materials and hydrogen storage materials. As a by-product of amorphization studies or alloying development, nanocrystalline intermetallic compounds can be synthesized. Nanocrystalline intermetallics possess improved mechanical properties at an ambient temperature. Bohn et al. [2] have suggested that nanocrystalline intermetallic compounds may have improved mechanical properties. Their study concludes several possible ways of improving strength and ductility. However, the strength of elemental nanocrystalline metals can be increased by factors of 4–5 over conventional grain size materials [3], strengthening effects in some hard intermetallics that are more modest of the order of 10–20% [4]. The brittle nature of most intermetallics requires powder metallurgical processing route. Amorphization of intermetallic compounds by mechanical alloying (MA) was first reported by Ermakov et al. [5, 6] in Y-Co and Gd-Co systems. Amorphous phases from elemental powder mixtures or powders of intermetallics synthesized by high-energy ball milling have attained an unprecedented interest. A polymorphous phase transformation from crystalline phase to amorphous phase can occur when the free energy of an intermetallic compound is raised by severe mechanical deformation above that of the amorphous phase. The observed transformation could be ascribed to an increased volume fraction of grain boundaries and simultaneous disordering [7]. Zou et al. [8] reported the formation of amorphous phase in Al-Fe alloy at early stages of MA. It has also been reported that during prolonged milling, amorphous phase undergoes crystallization to form intermetallics.

### 1.2. Al-Fe intermetallics

Considering all excellent physical and mechanical properties of aluminium, it has become an important element in intermetallics. Iron (Fe) and aluminium (Al) alloys rank among the most important engineering materials because they provide good properties at a low material cost in many applications [9]. Iron aluminide compounds are solid examples of the use of aluminium in intermetallics industry. Changing the aluminium content in iron-aluminium system leads to different iron aluminide compounds. Al-rich iron aluminides are characterized by low density, but also by lower strength and hardness than $Fe_3Al$ or FeAl ones. However, the strength and

| Phases | Symbol | Crystal structure | Stability range (at.%) | Vickers hardness (9.8 N) |
|---|---|---|---|---|
| AlFe | β″ | BCC (Order) | 23–55 | 491–667 |
| $AlFe_3$ | β′ | $DO_3$ | 23–34 | 344–368 |
| $Al_2Fe$ | ζ | Triclinic | 66–67 | 1058–1070 |
| $Al_5Fe_2$ | η | Orthorhombic | 70–73 | 1000–1158 |
| $Al_3Fe$ | θ | Monoclinic | 74.5–76.5 | 772–1017 |

**Table 1.** Crystal structure, stability range and hardness of intermetallic phases formed in Al-Fe binary systems at room temperature [10].

hardness can be improved by grain size refinement, especially to nanometric scale. Having their strength increased, Al-based intermetallics possess a high specific strength. **Table 1** indicates the crystal structure, stability range and hardness for the Al-Fe intermetallic phases. Studies on Al-Fe system have been concentrated mainly on mechanical alloying (MA) with individual elements [11–14]. Moreover, similar structures have been evidenced for a range of Al content. In Al-Fe intermetallic, $Al_2Fe$ compound retains the lowest possible symmetry crystal structure, triclinic (Pearson symbol aP19) [15]. Due to its lowest symmetry, the triclinic phase transforms to a high-symmetry $Al_5Fe_2$ orthorhombic (Pearson symbol oC24) in the nearby composition. Stability calculations utilizing first principles total energy envisage that oC24 structure has a much lower atomic density than aP19 structure, resulting in a high vibrational entropy and hence aP19 structure loses stability to the oC24 structure at elevated temperatures [16].

### 1.3. Al-Fe intermetallics by mechanical alloying/mechanical milling

Nanocrystalline intermetallic compounds are said to have enhanced properties as compared to conventional grain-sized materials. MA/mechanical milling (MM) has been considered a suitable processing method capable of attaining this goal of producing nanostructured materials [9]. The synthesis of intermetallics through MA/MM has emerged as a valuable method for the following reasons: (1) the synthesis of intermetallics which are difficult to prepare by conventional methods, (2) to obtain enhanced properties through microstructural modifications and (3) the synthesis of nonequilibrium microstructures, such as amorphous alloys at intermetallic compositions. The formation of amorphous phase in Al-20 at.%Fe alloy was reported by Zhou et al. after 240 h of MA [17]. Almost complete amorphous phase in Al-(17–33) at.%Fe system was observed by Huang et al. [18]. In a similar study, for Al-34 at.%Fe, Al-25 at.%Fe, Al-25 at.%Fe and Al-20 at.%Fe system, respectively, crystalline phases were evidenced by Enzo et al. and Cardellini et al. [19, 20]. For a composition range of Al-34.7–35.3 at.%Fe intermetallic phase, $Al_5Fe_2$ along with $Al_2Fe$ was observed by Gasior et al. [21]. A comparison of the phases formed in Al-Fe alloys as analysed from the X-ray diffraction (XRD) traces is given in **Table 2**. In addition to MA experiments, Romero et al. [22] reported the effect of mechanical milling (MM) on the structural evolution of as-cast $Al_2Fe$ and $Al_5Fe_2$ intermetallic systems at different short milling times. Apart from this study, no other reports on systematic investigation on the structural evolution of as-cast Al-rich iron aluminide intermetallics are available. The possibility of nanostructured and amorphous phases and their stability by MM can

| Alloy | Phases formed | References |
|---|---|---|
| Al-34.7–35.3 at.%Fe | $Al_5Fe_2$ + $Al_2Fe$ | Gasior et al. [21] |
| Al-28.45 at.%Fe | $Al_5Fe_2$ + $Al_2Fe$ | Romero et al. [22] |
| Al-25 at.%Fe | $Al_5Fe_2$ | Cardellini et al. [20] |
| Al-20 at.%Fe | Amorphous | Zhou et al. [17] |
| Al-20 at.%Fe | $Al_5Fe_2$ | Cardellini et al. [20] |
| Al-34 at.%Fe | $\alpha$-Al | Enzo et al. [19] |
| Al-17–33 at.%Fe | Amorphous | Huang et al. [18] |
| Al-25 at.%Fe | $\alpha$-Al | Enzo et al. [19] |
| Al-33.28 at.%Fe | $Al_5Fe_2$ + $Al_2Fe$ | Romero et al. [22] |

**Table 2.** List of phases formed in Al-Fe alloy.

be explored from the thermodynamic explanation based on a semi-experimental theory of improved Miedema's model (Zhang model) [23] by calculating the Gibbs free energy of the phases from their enthalpy of formation.

### 1.4. Nanostructured materials

Nanostructured materials are an important class of metastable materials that are produced by ball milling. Materials are considered as nanostructured if the crystallite size is of the order of few nanometres (typically 1–100 nm). A novel way of transforming a material to a metastable state is to reduce its grain size from micrometres to nanometres, when the proportion of atoms at the grain boundaries is equal to or higher than those inside the grains. The fine grain-sized materials are structurally characterized by a large volume fraction of atoms in or near the grain boundaries, which significantly alter the material properties that are often superior or sometimes completely new in comparison with conventional coarse-grained polycrystalline materials. In 1987, Thompson and Politis first reported the formation of a nanostructured material synthesized by MA [24]. A mechanism for the formation of nanostructures by MA/MM has been reported [25]. In 1992, Li et al. proposed a relation between grain size and the time of milling by a model for the refinement of grain size during ball milling [26].

It is given by

$$d = K t^{-2/3} \tag{1}$$

where $d$ is the grain size, $t$ is the time and $K$ is a constant.

The balance between defect/dislocation structure introduced by the plastic deformation of milling and its recovery processes forms the main criteria to decide on the minimum grain size that can be achieved by mechanical milling. This process will result in a lower bound for the grain size of pure metals and alloys and reveals that a small grain size itself provides a limit for further grain refinement on milling. On the whole, when the material exhibits a nanocrystalline

http://dx.doi.org/10.5772/intechopen.73944

structure, hence microstructural refinement cannot be observed and further deformation can only be accomplished by grain boundary sliding (GBS). It has been suggested that the minimum grain size that can be achieved by milling is determined by the balance between defect/dislocation structure introduced by the plastic deformation of milling and its recovery by thermal processes. This contributes to a lower bound for the grain size of pure metals and alloys and reveals that a small grain size itself provides a limit for further grain refinement on milling. Once the whole material exhibits a nanocrystalline structure, further deformation can only be accomplished by grain boundary sliding, and hence microstructural refinement cannot be observed. The limiting grain size is normally determined by the minimum grain size that can sustain a dislocation pile-up within a grain and by the rate of recovery [27]. Earlier researchers have proposed that hardness decreases at small grain sizes as it becomes impossible to accommodate the high density of dislocations required to form a pile-up at a grain boundary [28, 29].

## 2. Effect of process parameters on mechanical properties

Despite the same composition of initial powder mixture, various structures can evolve depending on the parameters of the milling process. In this section, the effect of mechanical milling (MM) on the structural evolution of as-cast Al-rich iron aluminide intermetallics through different stages of milling and its mechanical behaviour has been discussed. The mechanical properties of intermetallics are closely related to their structure and its stability [30]. Grain boundaries are the most important microstructural elements of materials, and their strengthening effect is phenomenologically quantified by a classical HP relationship. However, deviations from HP relation contributing to a softening behaviour are also observed after a critical grain size ($d_c$). Due to the difference in the mechanical properties, which is greatly influenced by the microstructure [31, 32] of the intermetallic phases and its transformation during milling, a significant difference in the force displacement curves manifested not only by the shapes of the load-penetration depth but also by the maximum penetration depth attained under the same conditions was observed when evaluated using Oliver and Pharr method [33] (Oliver et al. (2004)). For intermetallics that are concerned, the effort has been directed mainly towards the development of high strength materials, and reports that address softening behaviour in nanoscale microstructures or composite microstructures are very rare. Al-25 at.%Fe, Al-30 at.%Fe and Al-34.5 at.% Fe close to $Al_3Fe$, $Al_5Fe_2$ and $Al_2Fe$ intermetallic phases have been prepared in an arc-melting furnace under argon atmosphere. The pre-alloyed ingots were brittle and therefore repeatedly crushed and mechanically sieved to powders. Mechanical milling of the crushed powders was then carried out using high-energy planetary ball mill. This study provides some insights to understand the correlation between the process parameters and the mechanical behaviour of Al-Fe intermetallics.

### 2.1. Microstructural and structural features

**Figure 1** shows X-ray diffraction pattern of crushed as-cast powders of Al-25 at.%Fe alloy. Diffraction peaks confirm mostly single-phase complex monoclinic $Al_3Fe$ ($\theta$) structure. **Figure 2** shows the structural evolution of $Al_3Fe$ intermetallic subjected to varying hours of MM. A relatively broad peak was observed because of the fine crystallite size and the presence of strain in

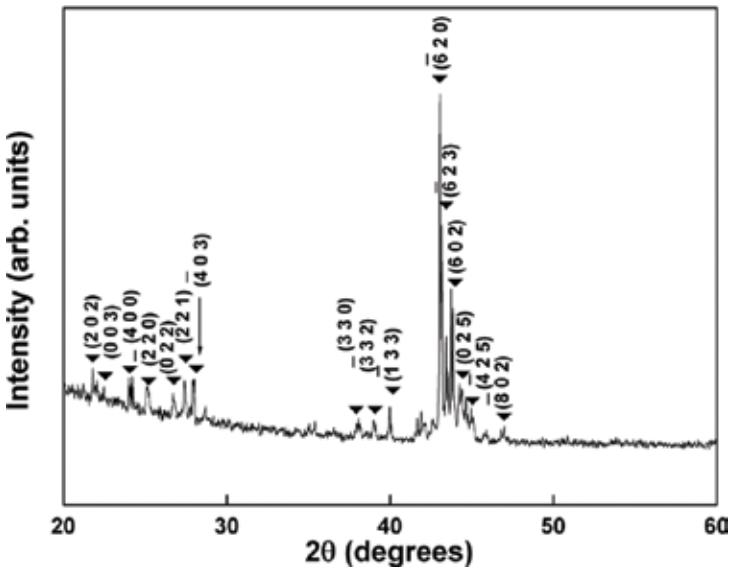


**Figure 1.** XRD pattern of Al-25 at.%Fe as-cast alloy showing single θ-$Al_3Fe$ intermetallic phase (reprinted with kind permission from reference [34], copyright 2015, Elsevier).

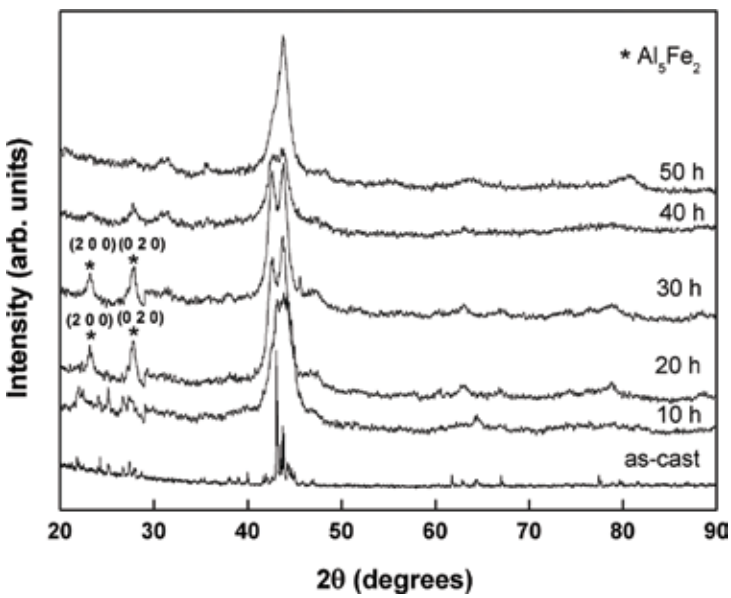


**Figure 2.** XRD patterns showing structural evolution of θ-$Al_3Fe$ intermetallic phase (reprinted with kind permission from reference [34], copyright 2015, Elsevier).

the powder at early stages of milling. After 10–20 h of milling, the formation of η-$Al_5Fe_2$ was evidenced as an intermediate phase. The presence of η-$Al_5Fe_2$ prevailed till 30 h of milling, but a further increase in the milling time led to the broadening of these peaks too. The intermetallic $Al_3Fe$ phase was completely transformed into the amorphous state after 50 h of milling. A broad

halo at 2θ = 40–47° suggests that the formation of an amorphous phase was seen from the XRD patterns shown in **Figure 2**. Eventually, the phase transformations during MM for Al–25 at.%Fe alloy powders are expressed as follows:

$$\theta - Al_3Fe \rightarrow (\theta - Al_3Fe + \eta - Al_5Fe_2) \rightarrow (\eta - Al_5Fe_2 + \text{Amorphous}) \rightarrow \text{Amorphous}. \quad (2)$$

Transmission electron microscope (TEM) image of Al-25 at.%Fe alloy milled for 50 h is shown in **Figure 3**. The micrograph showed the co-existence of nanocrystalline, η-$Al_5Fe_2$ and amorphous phases, and a diffuse ring along with diffraction spots was evidenced in a selected area diffraction (SAD) pattern. However, complete amorphization after 50 h of milling was observed in its corresponding XRD pattern. The broadening of the peak observed in XRD corresponds not only to the formation of amorphous structure but also to the refinement of the nanocrystalline structure induced by mechanical milling, and hence residual crystalline phase is present along with amorphous phase. The characteristic X-ray diffraction pattern of as-cast powders of Al-30 at.% Fe alloy is shown in **Figure 4**. The most intense diffraction peaks (2 2 1) and (3 1 1) at $2\theta$ = 42.55 and 43.79 were found in the as-cast alloy. JCPDS data suggest that this compound is representative of a single $Al_5Fe_2$ orthorhombic phase (JCPDS reference code: 00-047-1435) [36] with lattice parameters of a = 0.7648 nm, b = 0.6413 nm and c = 0.4216 nm. Results of XRD patterns showing the structural evolution of $Al_5Fe_2$ intermetallic subjected to MM for different ranges of milling time are shown in **Figure 5**. It is apparent that milling up to 30-h disappearance of all peaks except for major peaks of (2 2 1) and (3 1 1) was observed. The broadening observed in the diffraction peak can be attributed to the major peaks overlapping from the intermetallic phase. The results obtained are in contrary to $Al_5Fe_2$ obtained by MA route [11], where complete formation of intermetallic phase was achieved in Al-25%Fe

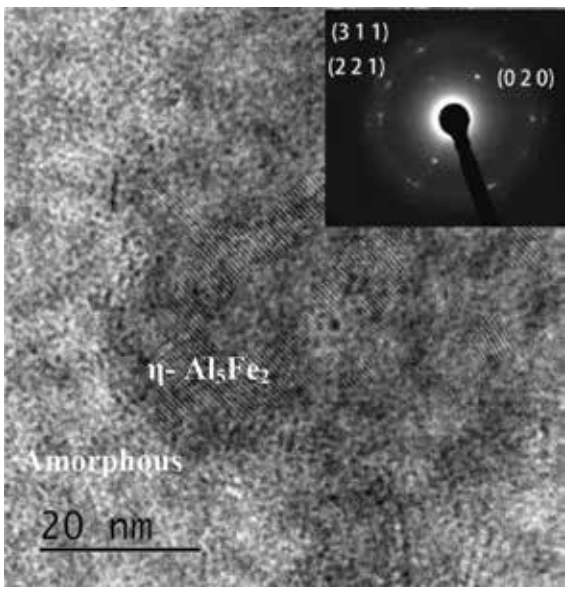


**Figure 3.** TEM image of 50 h milled product of Al-25 at.%Fe alloy showing crystalline η- $Al_5Fe_2$ and amorphous phase and its corresponding SAD pattern (reprinted with kind permission from reference [34], copyright 2015, Elsevier).

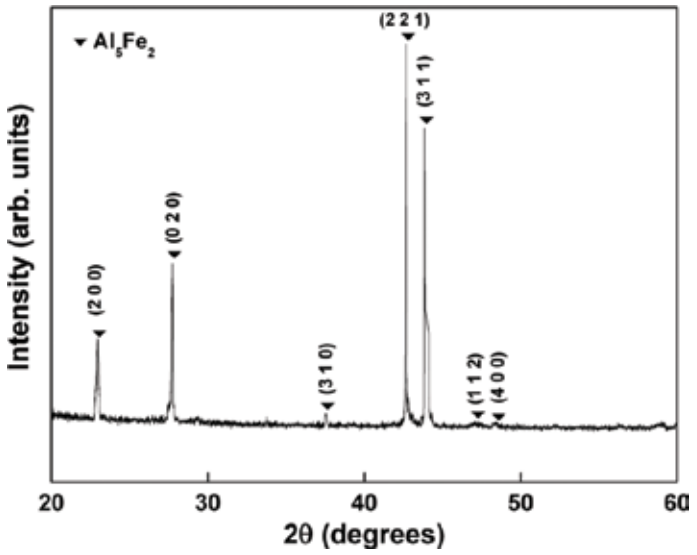


**Figure 4.** XRD pattern of as-cast Al-30 at.% Fe alloy (reprinted with kind permission from reference [35], copyright 2016, Taylor & Francis).

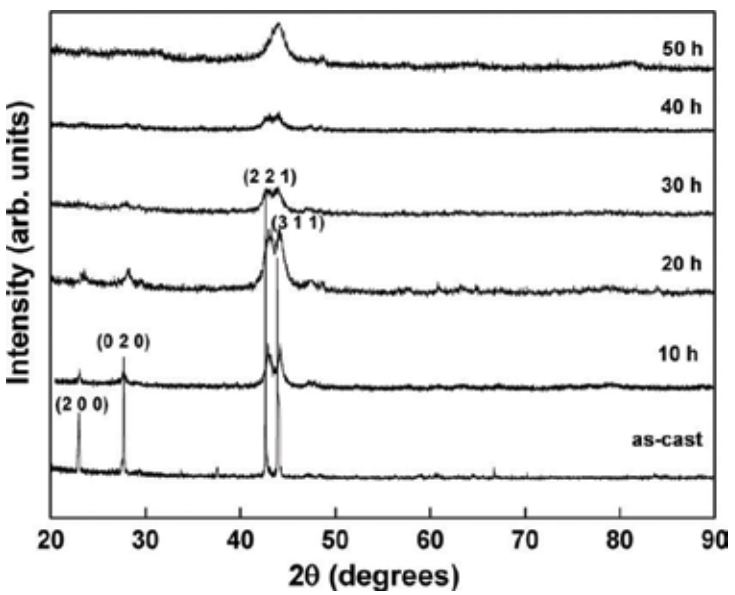


**Figure 5.** XRD patterns showing structural evolution of $Al_5Fe_2$ intermetallic during MM (reprinted with kind permission from reference [35], copyright 2016, Taylor & Francis).

after 30 h of MA, and the formation of amorphous phase was seen after 50 h of MA. Further in a similar work, Hunag et al. [18] observed the formation of the $Al_5Fe_2$ intermetallic in Al-24.4%Fe powder heat-treated at 500°C after MA for 180 h. It is interesting to note that the XRD peaks undergo broadening in the course of mechanical milling up to 50 h mainly due to cumulative effects of grain refinement and lattice strain. A bright field and dark-filed

http://dx.doi.org/10.5772/intechopen.73944

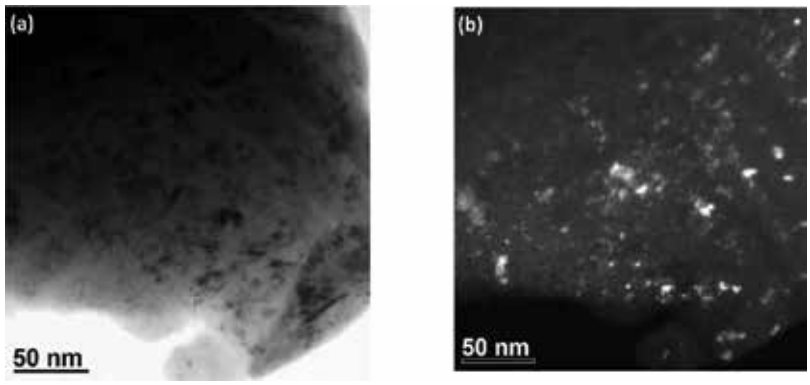


**Figure 6.** (a) Bright field image and (b) dark field image of 50 h milled powder of Al-30 at.% Fe alloy (reprinted with kind permission from reference [35], copyright 2016, Taylor & Francis).

image of 50 h-milled Al-30 at.% Fe alloy (**Figure 6a** and **b**) reveals the presence of a nano-crystalline structure suggesting the presence of a nanostructured $Al_5Fe_2$ intermetallic phase which agrees well with the structural evolution observed from the XRD pattern.

**Figure 7** shows the XRD pattern of as-cast Al-34.5 at.%Fe alloy. Diffraction peak confirms a mixture of intermetallic phases namely ζ-$Al_2Fe$ and η-$Al_5Fe_2$. For a compositional range of 34.7–35.3 at.%Fe in Al alloy, the observed intermetallic phase $Al_5Fe_2$ along with $Al_2Fe$ was observed by Gasior et al. [21]. Phase transformation from crystalline triclinic $Al_2Fe$ and orthorhombic $Al_5Fe_2$ to the partial formation of amorphous phase at 10 h of MM resulted in Al-34.5 at.%Fe alloy. Due to the peak overlapping from the mixture of intermetallic phases, a width was observed in the most, intense diffraction peak. With continued milling, a decrease

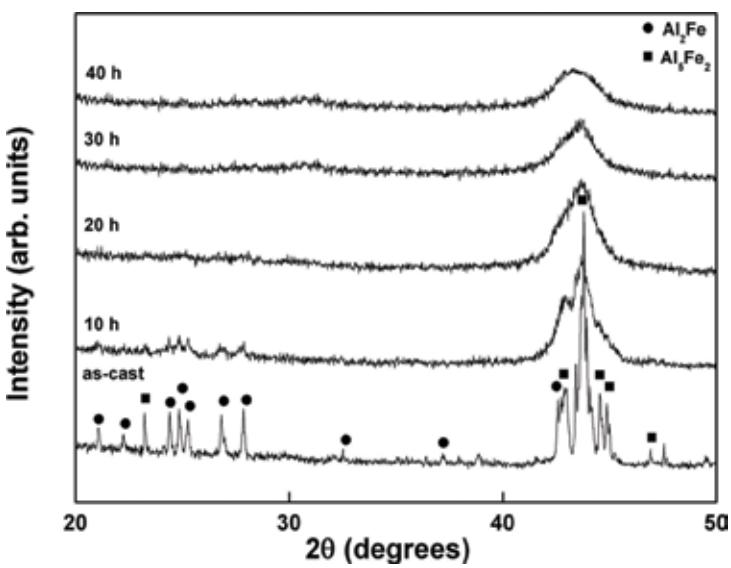


**Figure 7.** XRD patterns Al-35.4 at.%Fe as-cast alloy and after mechanically milled for various intervals showing structural evolution with milling time (reprinted with kind permission from reference [34], copyright 2015, Elsevier).

in the width of Bragg peaks and an increase in peak resolution were noted, indicating that $Al_2Fe$ intermetallic phase becomes unstable as a result of MM. The detected phase transition that occurred during milling process is suggestive of the accumulation of structural defects which increases the stored energy in the intermetallic material.

As evidenced in **Figure 7**, complete amorphization after 40 h of milling was achieved in this particular composition with prolonged milling time. The fine grain size and consequently large surface area induced by MM make the powders of this particular composition pyrophoric in nature after 40 h of milling. The same was observed even when milling experiments were paused periodically at regular intervals of every 30 min. Phase transformations achieved as a result of MM for Al-34.5 at.%Fe alloy powders are expressed as.

$$\left(\zeta - Al_2Fe + \eta - Al_5Fe_2\right) \rightarrow \eta - Al_5Fe_2 \rightarrow \text{Amorphous.} \tag{3}$$

The orthorhombic structure of $Al_5Fe_2$ phase features a rigid framework of fully occupied Al and Fe sites as well as partially occupied Al sites confined within channels [37]. This kind of structure makes it unstable when subjected to a severe plastic deformation leading to an amorphous phase. Further, for the present milling conditions, $Al_5Fe_2$ phase was also found to be stable with respect to its competing phases. Due to lattice defects introduced by MM which promote spontaneous transformation to the amorphous phase, the intermetallic compounds with narrow homogeneity ranges tend to become amorphous [38]. A high-resolution TEM micrograph corresponding to Al-34.5 at.%Fe alloy milled for 40 h is shown in **Figure 8**. The micrograph reveals a single amorphous phase and is corroborated by the fast Fourier transformation-selected area diffraction (FFT-SAD) pattern.

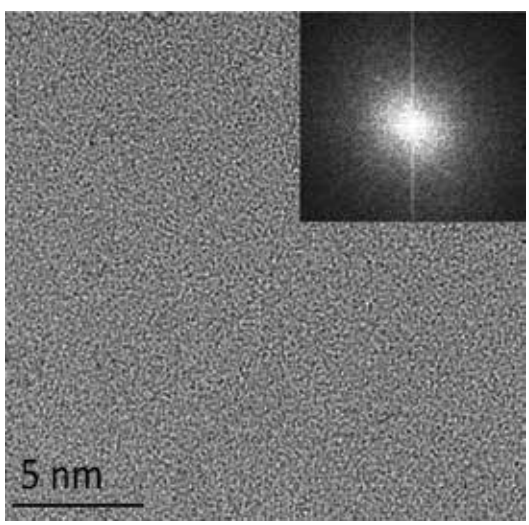


**Figure 8.** HRTEM image and the corresponding FFT-SAD of Al-35.4 at.%Fe showing a complete amorphous phase after 40 h of milling (reprinted with kind permission from reference [34], copyright 2015, Elsevier).

http://dx.doi.org/10.5772/intechopen.73944

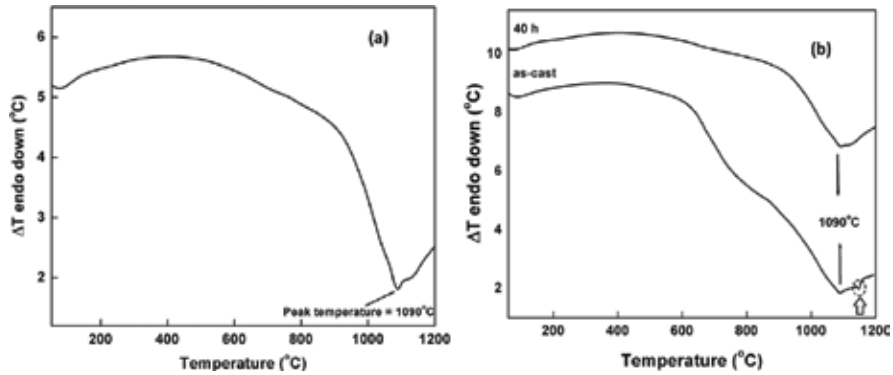


**Figure 9.** DTA traces of milled powders for (a) Al-25 at.%Fe and (b) Al-34.5 at.%Fe alloy (reprinted with kind permission from reference [34], copyright 2015, Elsevier).

Differential thermal analysis (DTA) trace of 50 h-milled Al-25 at.%Fe intermetallic powders is shown in **Figure 9a**. Upon heating the as-milled powders at a constant rate of 10°C/min, one exothermic peak at around 1090°C was revealed. An equilibrium diagram of Al-Fe [10] confirms that this peak corresponds to the melting point of the $Al_5Fe_2$ intermetallic phase, formed as a result of phase transformation of monoclinic $Al_3Fe$ after high-energy ball milling. DTA curves of as-cast Al-34.5 at.%Fe alloy and ball-milled powder obtained after 40 h of milling are shown in **Figure 9b**. As marked by arrows, the thermal curves indicated the presence of two endothermic peaks for the as-cast alloy. According to the equilibrium phase diagram, the first peak at 1090°C corresponds to the melting point of $Al_5Fe_2$ intermetallic compound, and the second peak at a higher temperature (1149°C) as marked by an arrow is due to the melting of $Al_2Fe$. A single exothermic peak around 1090°C corresponding to $Al_5Fe_2$ phase formed as a result of transformation of an $Al_2Fe$ intermetallic phase to a high-symmetry phase $Al_5Fe_2$ after high-energy milling was evidenced from DTA trace of 40 h milled powders. Thermal analysis results agree well with the XRD results as shown in **Figure 7**, where the pattern corresponds to both $Al_5Fe_2$ and $Al_2Fe$ phases for as-cast alloy and a single $Al_5Fe_2$ phase for 40 h milled powders. The calculation of free energy of equilibrium phases was carried out based on the improved Miedema's model (Zhang model). **Table 3** gives the data of Al and Fe necessary for the calculation of Gibbs free energy. The variation of $\Delta G$ (for amorphous, two intermetallic compounds and crystalline solid solutions) as a function of composition for different values of $d_c$ is shown in **Figure 10**. It is observed that the free energy of crystalline phase of a large crystallite size is lower compared to that of amorphous phase. Henceforth, for the entire compositional range, the crystalline phase is expected to be more stable than the amorphous phase. As the Gibbs free energy is minimum at the corresponding composition, the intermetallic thus found is considered as a most stable phase. The two intermetallic phases ($Al_3Fe$ and $Al_2Fe$) corresponding to the compositions Al-25 at.% Fe and Al-34.5 at.% Fe are the most stable phases compared to the solid solution phase. $Al_3Fe$ phase can transform to the amorphous phase at $d_c < 20$ nm, and to convert $Al_2Fe$ phase into the amorphous state, the phase grain size should be below 30 nm. The results obtained from XRD and TEM analysis of the milled powder support that

| Element | $n^{1/3}$ ($cm^{-1}$) | Φ (V) | K (GPa) | $\mu$ (GPa) | $T_m$ (K) | $V^{2/3}$ ($cm^2$) | γ (erg/$cm^2$) | $\Delta H_f$ (kJ/mole) |
|---|---|---|---|---|---|---|---|---|
| Al | 1.39 | 4.2 | 75.83 | 26 | 933 | 4.6 | 340 | 10.83 |
| Fe | 1.77 | 4.93 | 164.78 | 82 | 1812 | 3.7 | 756 | 13.86 |

**Table 3.** Data of Al and Fe taken for thermodynamic calculation.

the phases are intermetallic prior to milling and amorphous after milling at the composition of Al-25 at.% Fe and Al-34.5 at.% Fe.

### 2.2. Mechanical properties

**Figure 11a** shows the milling time dependence of Vickers hardness for Al-25 at.%Fe alloy for various milled powders. The hardness increases with an increase in the milling time and reaches its maximum value between 20 and 30 h of milling and then decreased. A higher hardness value of about 8.6 GPa resulted at 30 h of milling. Thus, the optimum milling time for the studied composition is 30 h. The formation of intermetallic phase, η-$Al_5Fe_2$, and its co-existence with amorphous phase could be the reason for the observed peak in hardness values. However, for Al-20 at.%Fe alloy, the microhardness of 12.4 GPa was reported for 20 h of MA followed by cold consolidation and subsequent annealing at 673 K for 2 h [39]. **Figure 11b** shows the change in microhardness as a function of reciprocal square root of the grain size. It is evident that up to a grain size of about 42 nm, the values of hardness increase linearly with the reciprocal square root of the grain size. Over the range of grain sizes from 132 to 42 nm, the Hall-Petch (HP) behaviour is established. Further, the HP slope, which describes grain size

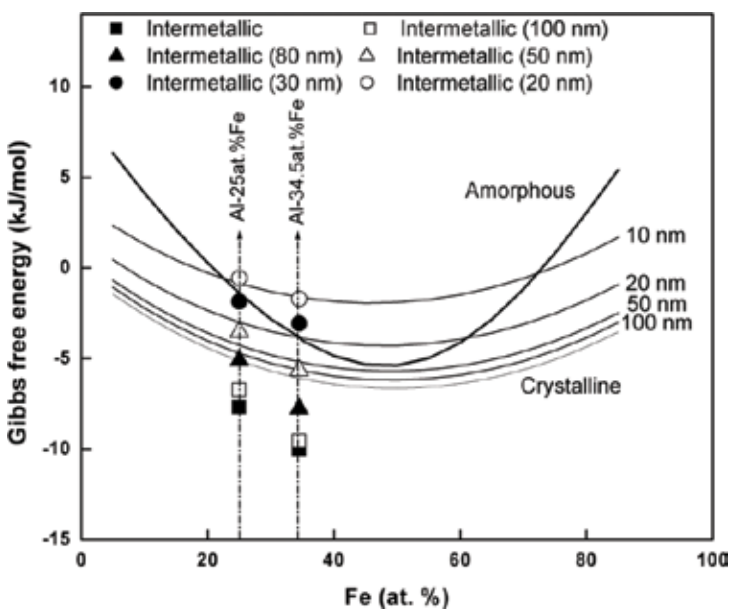


**Figure 10.** Gibbs free energy of the amorphous, solid solution and intermetallic phases of Al-Fe system as a function of composition and grain size.

http://dx.doi.org/10.5772/intechopen.73944

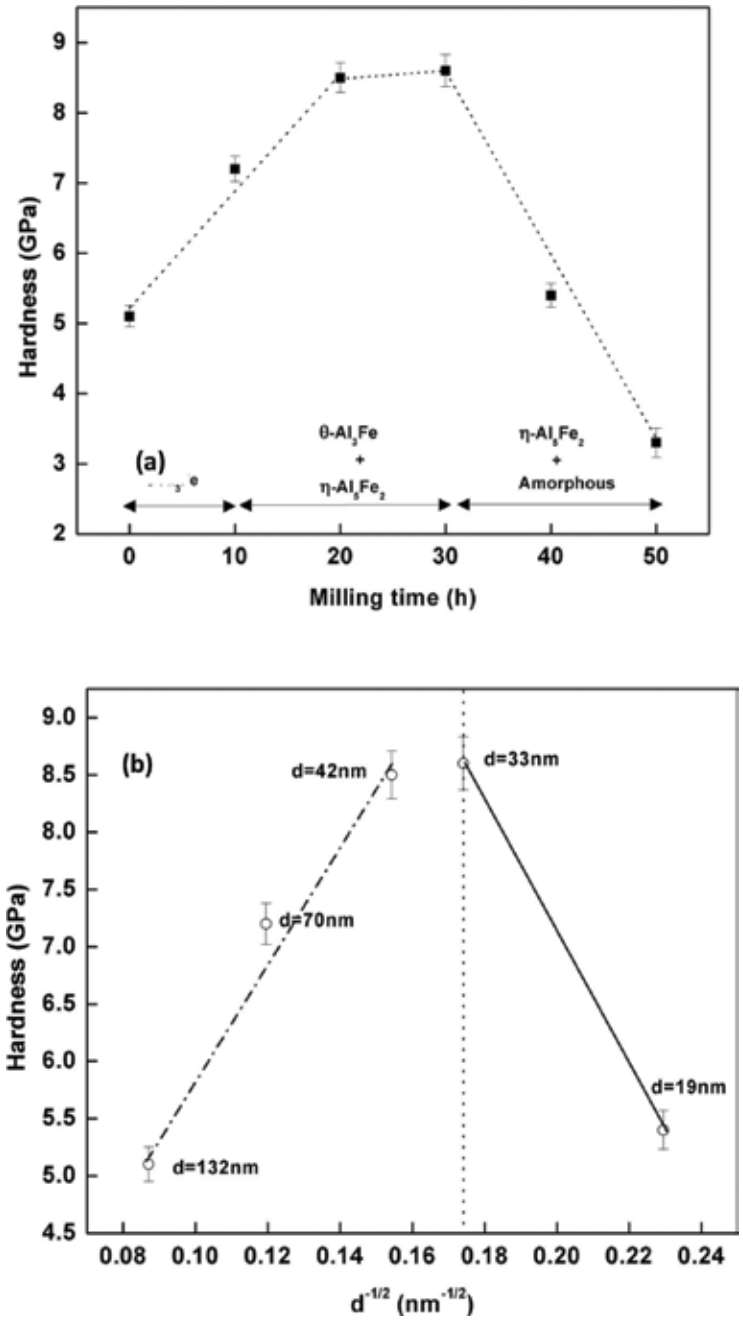


**Figure 11.** (a) Variation of microhardness as a function of milling time for Al-25 at.%Fe alloy showing the phase sequence and softening behaviour, (b) variation of microhardness as a function of square root of the grain size to test the Hall-Petch relationship for Al-25 at.%Fe alloy (reprinted with kind permission from reference [34], copyright 2015, Elsevier).

sensitivity, also have a similar value to that found for conventional grain sizes. This behaviour is ascribed to the refinement in the grain size produced as a result of MM. However, it is worth noting that when the crystallite sizes drop below 42 nm, the slope of the Hall-Petch plot

becomes negative. The evidenced effect could be due to a softening behaviour, an attribute described as an inverse H-P phenomenon [28, 29]. Theoretically, the critical value of the grain size below which the plot becomes negative can be calculated from Eq. (4)

$$\sigma = \sigma_0 + k\, d^{-\frac{1}{2}} \tag{4}$$

To examine the discrepancy involved in a dislocation pile-up mechanism related to a softening behaviour, the critical grain size was calculated and found that the theoretical value obtained was about 8 nm in comparison to the experimental value of 42 nm. It can be concluded that the presence of competing/contributing effects of nanocrystalline and amorphous phase could be the reason for the differences observed. Though the critical grain size for nanocrystalline materials where softening occurs can be predicted by a dislocation pile-up model, it fails for composite structure involving nanocrystalline and amorphous phase. **Figure 12** shows the microhardness variation with a milling time for Al-30 at.% Fe alloy. It is apparent from the plot that a single $Al_5Fe_2$ intermetallic phase subjected to MM resulted in Hall-Petch (HP) break-down and showed two distinct behaviours. The break-down of Hall-Petch for the averaged hardness can be attributed to the deformation mechanism and structure that occur due to mechanical milling. The HP slope decreases below a critical grain size and becomes negative, indicating an inverse Hall-Petch (IHP) behaviour. The HP strengthening has been ascribed to the pile-up of dislocations and their resistance to slip transfer. However, HP behaviour for grain size ranging from

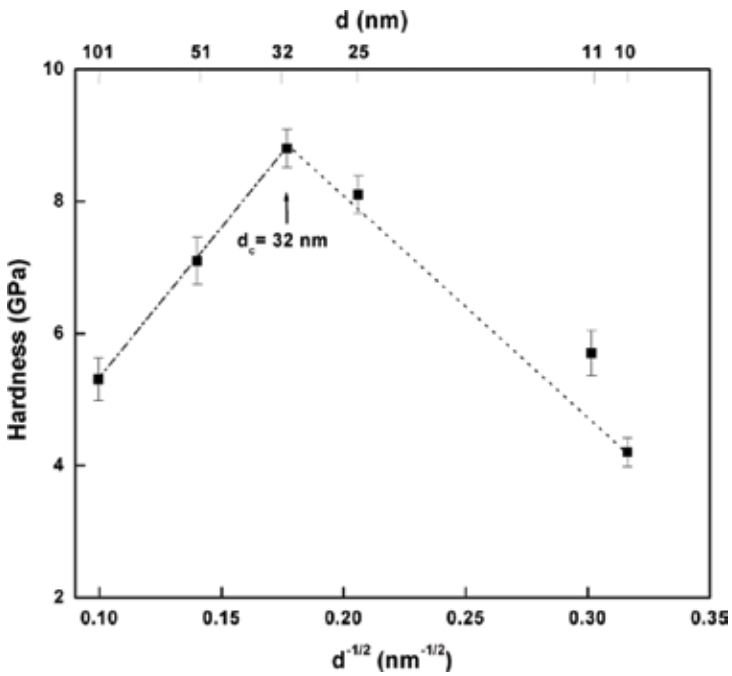


**Figure 12.** Hall-Petch plot of hardness of $Al_5Fe_2$ intermetallic against inverse square root of grain size showing transition from conventional Hall-Petch behaviour to inverse Hall-Petch behaviour (reprinted with kind permission from reference [35], copyright 2016, Taylor & Francis).

http://dx.doi.org/10.5772/intechopen.73944

101 to 32 nm and an IHP behaviour for grain sizes less than 32 nm was observed. The variation of microhardness as a function of milling time for Al-34.5 at.%Fe alloy is shown in **Figure 13**. The figure clearly demonstrates that the hardness of the alloy increased with increasing the milling time at the early stage and after prolonged milling reveals softening during the formation of amorphous phase. The hardness values increase with an increase in the milling time, which is an indicative of the formation of amorphous phase along with crystalline intermetallic phase. A softening behaviour observed at higher milling durations can be attributed to the high volume fraction of grain boundaries resulting in an increased triple junction leading to a grain boundary sliding [40]. The transition from hardening to softening behaviours that occurs in an amorphous phase could be ascribed to mechanisms such as a decrease in the interfacial excess volume and free volume model [29]. However, detailed investigation regarding this issue is needed to understand the softening behaviour. The typical load-displacement curves showing elastic-plastic material response for intermetallic phases milled for various durations, for indentations made to peak loads of 20 mN at room temperature, are presented in **Figure 14a** and **b**. Under the same conditions, the force displacement curves showed significant differences manifested not only by the shapes of the load-penetration depth but also by the maximum penetration depth attained. The microstructure of the intermetallic phases and its transformation during milling causes difference in the mechanical properties [29, 40] as evidenced in curves. The standard procedure according to Oliver and Pharr [33] (Oliver et al. (2004)) was employed to calculate the elastic modulus and hardness values. These parameters, estimated from the curve, are given in **Table 4**. The evolution of elastic modulus with a milling time indicates a relative complex effect of the phase formation/transformation in Al-Fe alloys.

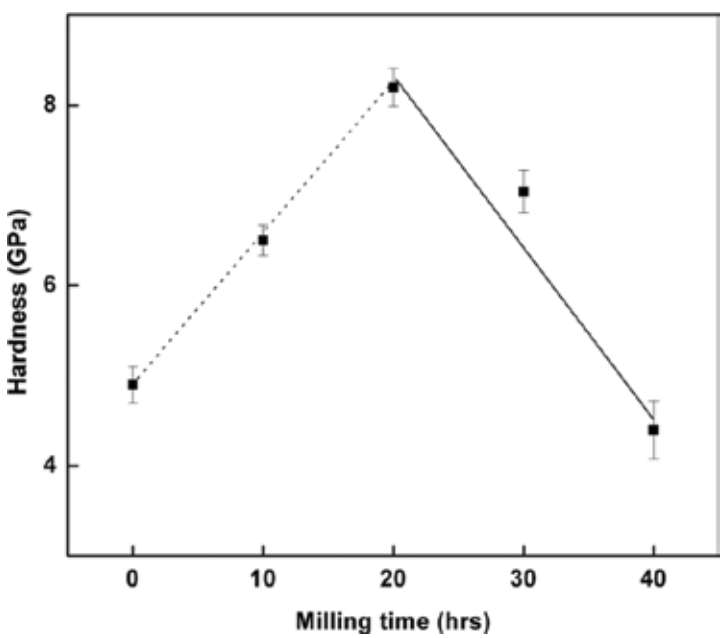


**Figure 13.** Microhardness variation as a function of milling time for Al-34.5 at.%Fe alloy showing transition from hardening to softening behaviour (reprinted with kind permission from reference [34], copyright 2015, Elsevier).

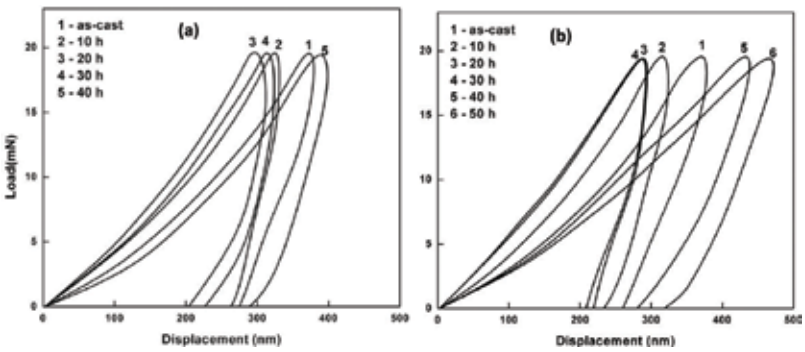


**Figure 14.** Nanoindentation load-displacement curves for (a) Al-25 at.%Fe and (b) Al-34.5 at.%Fe alloy at varying milling times (reprinted with kind permission from reference [34], copyright 2015, Elsevier).

| Material | Hardness (GPa) | | | | | | Elastic modulus (GPa) | | | | | |
|---|---|---|---|---|---|---|---|---|---|---|---|---|
| | Milling time (h) | | | | | | | | | | | |
| | 0 | 10 | 20 | 30 | 40 | 50 | 0 | 10 | 20 | 30 | 40 | 50 |
| Al-25 at.%Fe | 7.2 | 7.8 | 9.3 | 8.2 | 6.5 | 5.0 | 121 | 139 | 168 | 146 | 116 | 89 |
| Al-35.4 at.%Fe | 6.1 | 7.0 | 8.8 | 7.6 | 4.9 | — | 100 | 129 | 157 | 138 | 88 | — |

**Table 4.** Hardness and elastic modulus of alloy powders of as-cast and for various durations of milling measured by nanoindentation (reprinted with kind permission from reference [34], copyright 2015, Elsevier).

The interatomic distance and the bonding strength between atoms, which is a representation of elastic modulus, are greatly influenced by the severe plastic deformation induced by mechanical milling. The increased hardness and elastic modulus resulted at the early stages of milling are due to the refinement in grain size which resists grain boundary motion. The maximum elastic modulus of 168 and 157 GPa and the peak hardness of about 9.3 and 8.8 GPa at 20 h were observed for Al-25 at.%Fe and Al-34.5 at.%Fe alloys, respectively. After a longer milling time where amorphous phase formation was evidenced, the hardness and elastic modulus values decreased to a factor of about two. The differences in the average values of 0.6 GPa between microhardness and nanohardness observed were ascribed to indentation size effect (ISE) [41].

## 3. Effect of grain size on mechanical properties

Mechanical property is an important consideration for the application of materials and depends fundamentally upon their microstructure on a variety of length scales and the nature of bonding among their constituent atoms. Mechanical deformation can be either elastic or plastic. Elastic deformation is effected through reversible changes in the interatomic spacing or the bending and stretching of bonds between atoms; it is governed by the elastic constants or moduli of a material. For metals, such deformation is in general relatively easy owing to the

non-local nature of metallic bonding, but for materials with a strong covalent or ionic bonding such as intermetallic compounds, it is difficult. Mechanical properties of nanocrystalline materials display an increasing interest. Reducing the grain sizes not only creates a big impact on the microstructures of the nanocrystalline materials but also alters their mechanical properties significantly. The most important mechanical properties of nanocrystalline metals and alloys include significantly increased hardness, strength and ductility, and so on with respect to the decreasing grain sizes [42]. The mechanical properties of NC materials not only depend on the average grain size but also depend on the grain size distribution and the microstructure, such as the grain boundary structures have a critical effect on their mechanical properties.

### 3.1. Inverse Hall-Petch effect in nanocrystalline materials

As suggested by the well-known Hall-Petch relationship, the mechanical properties of the material increase with the inverse square root of the grain size. However, as the grain size decreases to the submicrometre range, the $k$ value (material-dependent constant) often referred to as the HP slope tends to decrease and when the grain size is decreased to less than 100 nm; the $k$ value often becomes negative. The relationship between the strength of the nanostructured material and the grain size is very complicated. Since dislocation activity is almost absent in these materials, below a critical grain size, the HP relation becomes invalid. Deviations from the Hall-Petch relation were first reported by Chokshi et al. [43] on nanocrystalline copper and palladium, and this softening behaviour for nanocrystalline materials is the so-called inverse Hall-Petch effect, that is, hardness and strength decrease with a decrease in the grain size. At the nanoscale grain size where the dislocation activity is believed to be absent [44], below a critical grain size, k, the HP slope becomes negative, implying that the materials get softened. The break-down in the Hall-Petch trend has been attributed to different deformation mechanisms that become dominant once the grain size is reduced down to below a critical value [45]. The major interest involving the studies of strength has been to see if the HP relation holds at the smallest grain sizes. In this section, we present the results of recently observed IHP in the intermetallic $Al_5Fe_2$, and various deformation models in the present context of grain size softening will be discussed.

### 3.2. Deformation mechanisms

The expansion of the understanding of deformation of conventional polycrystalline materials to materials with grain sizes on the scale of nanometre is, at present, an evolving process. The experimental finding on inverse Hall-Petch has prompted various researches to propose models pertaining to their mechanism of deformation. Of the proposed models, different deformation mechanisms for nanocrystalline $Al_5Fe_2$ intermetallic are discussed subsequently.

#### *3.2.1. Dislocation pile-up model*

It is pertinent to point out that dislocation activities [46] have been shown to exist in some nanocrystalline materials. Nevertheless, the dislocation activity can be considered virtually absent in nanostructured materials where the grain size is lower than the minimum required distance to be maintained between the two dislocations. Therefore, the HP relation is expected to witness

a transition below a critical grain size, $d_c$. TEM and molecular dynamics (MD) simulation have also demonstrated that the grain boundaries can act as a source and a sink for dislocations. In nanomaterials, Hall-Petch behaviour breaks down because the grain is too small for dislocations to pile-up. In a polycrystalline sample, each individual grain will no longer be able to support more than one dislocation [48]. Using the concept proposed by Nieh and Wadsworth, Farghalli and co-workers [47, 48] developed a relationship between the critical grain size and hardness for the critical grain size below which softening occurs. Assuming that the stress field of a dislocation is valid at the nanoscale, and on the suggestion that fine grain sizes affect dislocation self-energy, a mathematical analysis was proposed and it leads to Eq. (5):

$$\frac{b}{d_{min}} = -\frac{2\beta H_i}{3G} + \frac{2}{3}\beta\left(\frac{H}{G}\right) \tag{5}$$

where $b$ is the Burgers vector, $H$ the measured hardness, $H_0$ the hardness equivalent of the applied stress at the moment of load application, $G$ the shear modulus and $\beta$ is a constant ranging equals 0.6 [47]. By using the material parameters for $Al_5Fe_2$ ($b$ = 0.422 nm [49], $G$ = 55 GPa $\beta$ = 0.6, $H$ = 8.8 GPa and $H_0$ = 0.45GPa [50] in the above equation, $d_{min}$ is estimated as 3.3 nm. Similarly, the critical grain size, after Nieh and Wadsworth [48] model, was calculated based on the following equation: $d_{min} \leq \frac{3Gb}{\pi(1-\nu)H}$, and it was found to be 3.58 nm. The calculated critical grain size (32 nm) was nearly eight times more than the values predicted based on dislocation pile-up models. Therefore, it is clear that dislocation-mediated process is not operative in these nanocrystalline intermetallics.

*3.2.2. Grain boundary shearing/sliding model*

It is clearly evident that the models based on dislocation pile-up could not account for grain size softening. For such fine grains, the deformation based on dislocation mechanisms becomes less dominant, and the mode of deformation based on grain boundary phase (via grain boundary shearing) comes into picture [51]. This would lead to a decrease in hardness and strength, since strain hardening due to dislocation will be absent and the grain boundary will be softer [52]. The deformation in nanocrystalline materials below a critical grain size has been analysed as a thermally activated process, determining the parameters such as activation energy (ΔF) and activation volume (ΔV). Conrad and Narayan [29] considered the thermally activated deformation and proposed a rate-controlling equation, which is given as

$$\dot{\gamma} = \frac{6\,b^*\,\nu_D}{d}\sinh\left(\frac{\nu\tau_e}{kT}\right)\exp\left(-\frac{\Delta F}{kT}\right) \tag{6}$$

The parameters in Eq. (6) are the Debye frequency, $\nu_D$($10^{13}$ $s^{-1}$); the grain boundary width taken to be $3b^*$, where $b^*$ the atomic diameter; the effective stress, $\tau_e$ equals $\tau$-$\tau_c$ where $\tau$ is the applied stress and $\tau_c$ is the threshold stress; v, the activation volume taken to be $b^{*3}$; $\Delta F$ the Helmholtz free energy; $k$ the Boltzmann constant; and T is the temperature on absolute scale. For analysis, the shear rate $\dot{\gamma}$ is taken to be $10^{-3}\,s^{-1}$. By assuming threshold stress, $\tau_c$ to be zero, the effective stress, $\tau_e$, then equals the applied stress, $\tau$, where $\tau = H/3\sqrt{3}$. The values of activation volume can

be obtained from the slope of the best fit straight line from plot of $H$ versus $ln\ d$. Eq. (6) can be rewritten in terms of hardness, by assuming *sinh* stress function to be exponential in one form and $\tau_c = 0$ in the other form. In view of the above and by taking logarithm, Eq. (6) can be modified as

$$H = 3\sqrt{3}\left\{\frac{kT}{v}\left[\ln\left(\frac{\dot{\gamma}}{3\,b^{*}\,v_D}\right)+\frac{\Delta F}{kT}\right]+\left(\frac{kT}{v}\right)\ln d\right\} \tag{7}$$

$$H = 3\sqrt{3}\left\{\frac{kT}{v}\left[\left(\frac{\dot{\gamma}}{6\,b^{*}\,v_D}\right)\exp\frac{\Delta F}{kT}\right]\right\}d \tag{8}$$

The model was validated for IHP regime of the current experimental data, and the experimentally observed and calculated hardness values of this system are shown in **Figure 15**. The degree of fit, as described by coefficient of correlation, for all the three expressions $H_v$ versus ln(L), $H_v$ versus L (these two describe the rigorous and approximate forms of the relationship in the model by Conrad and Narayan [29]) and $H_v$ versus $(L\text{-}L_0)^{0.5}/L$ [53], is very similar, and the findings are presented in **Table 5**. On this basis, both the models are acceptable. The preceding discussion shows that although the model proposed by Conard and Narayan explains the IHP effect, the parameters used for validation is quite unreasonable: (1) the effective stress is taken to be equal to the applied stress, that is, the strain-rate sensitivity index, m = 1.0. However, in nanocrystalline materials at room temperature, the value of m is in the range of 0.02–0.08 [54, 55] and (2) further, the strain rate was assumed as $10^{-3}\ s^{-1}$, but according to [56, 57], the strain rate lies in the range of $5 \times 10^{-2}$ to $5 \times 10^{-4}\ s^{-1}$. Thus, the experimental data were analysed using both the strain rate values and the free energy of activation, $\Delta F_0$, for the rate-controlling process (mesoscopic GBS), and refined values of $\gamma_0$ were determined as a function of strain rate and the results are presented in **Table 6**. The following observations are interesting: the relative change in hardness as one goes from the HP to the IHP region is much less in intermetallics than in nanocrystalline materials. This aspect needs further study. However, it is clear that the observed IHP effect in intermetallics also could be explained in terms of the mesoscopic grain boundary sliding controlled flow process, as with the other classes of materials. Finally, as the value of N for the system (**Table 6**) is less than one, it follows from the model [58–60] that the plane interface formation in these intermetallics of the studied grain size ranges is the result of dislocations/partial dislocations being emitted from the deforming boundary, which then traverse the grain and get absorbed at the opposite boundary [58, 59]. The value of $\Delta F$ equals 70 kJ/mol and $v$ equals $(1.887 \times 10^{-10})^3\ nm^3$ was obtained by plotting experimental hardness against ln d. A plot of $H$ versus $ln\ d$ for the IHP data is presented in **Figure 16**. In addition, $\Delta F$ values obtained by linear fit of both experimental hardness values against $ln\ d$ and $d$ resulted in a reasonable agreement. The activation energy for grain boundary diffusion of this type of intermetallics [29] was found to be slightly higher compared to the present activation energy obtained from this analysis. The results are somewhat in accordance with the previous work on nano-quasicrystalline materials, which proposed a similar approach for the observed softening related to inverse Hall-Petch behaviour [51]. Using this model, the predicted and

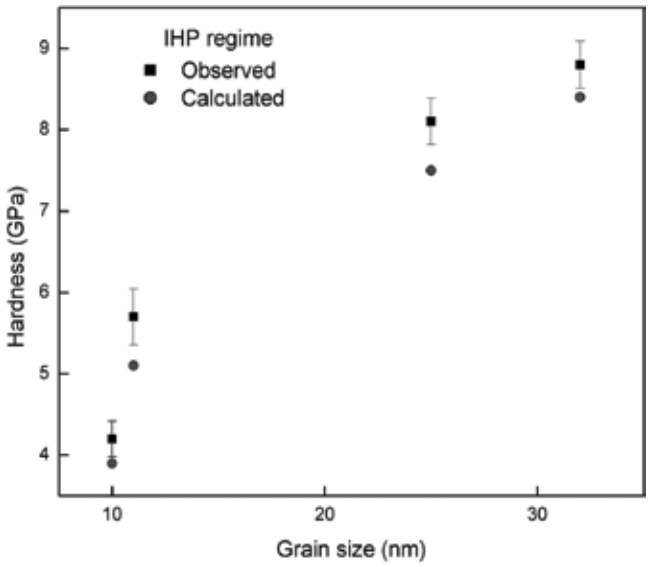


**Figure 15.** Hardness versus grain size in IHP regime observed values and calculated values obtained using Eq. (8) (reprinted with kind permission from reference [35], copyright 2016, Taylor & Francis).

| System | L, nm | H, GPa | Correlation coefficient of H and | | |
|---|---|---|---|---|---|
| | | | ln(L) | L | $(L-L)^{0.5}/L$ |
| $Al_5Fe_2$ | 32.0 | 8.8 | 0.970 | 0.949 | 0.968 |
| | 23.6 | 8.1 | | | |
| | 11.0 | 5.7 | | | |
| | 10.0 | 4.2 | | | |

**Table 5.** Degree of fit for the three relations: $H \upsilon \alpha \ln(L)$, $H \upsilon \alpha L$ and H v α(L − L) 0.5/L (reprinted with kind permission from reference [53], copyright 2016, Elsevier).

the current experimental data were plotted, and it was shown that qualitatively the fit is acceptable (**Figure 15**). The detailed examination showed that the correlation coefficient calculated based on grain boundary sliding using $H_v$ versus $d^{0.5}$ plot and grain boundary shearing calculated based on $H_v$ versus $d$ and $H_v$ versus $ln\ (d)$ resulted in identical values, proposing that both the models can describe the so-called inverse Hall-Petch effect. Despite the abovementioned similarity, manifest difference exists in the activation energy for the rate-controlling process due to their atomistic approach in the rate-controlling process. In case of grain boundary shearing approach, the effective stress is considered as the applied stress, that is, the strain-rate sensitivity index, m, equals 1.0. Nevertheless, in nanocrystalline materials, "m" ranges between 0.02 and 0.08 at room temperature. In general, it was pointed out that some of the approximations made in atomistic grain boundary shearing model to explain are questionable [34].

| System | N | L, nm | $\tau_o$, GPa | $\gamma_0$, refined* | $\Delta F_0$, kJ/mol | |
|---|---|---|---|---|---|---|
| | | | | | $\dot{\gamma} = 5 \times 10^{-2}, s^{-1}$ | $\dot{\gamma} = 5 \times 10^{-4}, s^{-1}$ |
| $Al_5Fe_2$ | 0.8458 | 32.0 | 1.52 | 0.0711 | 157.73 | 170.37 |
| | | 23.6 | 1.74 | | | |
| | | 11.0 | 2.27 | | | |
| | | 10.0 | 2.33 | | | |

G = 61.8 GPa.*As the strain rates in the indentation tests are assumed to be in the range of $5 \times 10^{-2}$ $s^{-1}$ to $5 \times 10^{-4}$ $s^{-1}$ [56], refined $\gamma_0$ values were obtained for the mean values of $\Delta F_0$ for this range.

**Table 6.** The average shear strain in the basic unit of sliding, the number of grain boundaries that align to form a plane interface during mesoscopic boundary sliding and the free energy of activation for the rate-controlling GBS process (reprinted with kind permission from reference [53], copyright 2015, Elsevier).

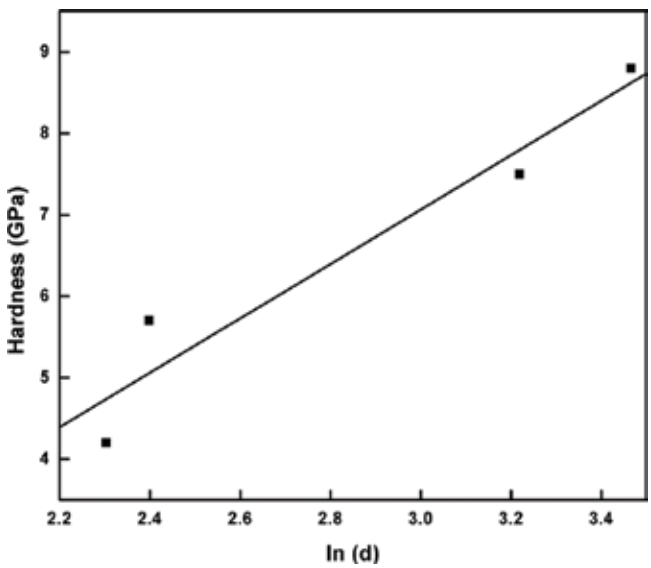


**Figure 16.** Plot of hardness *H*versus ln*d* for IHP regime (reprinted with kind permission from reference [35], copyright 2016, Taylor & Francis).

## 4. Conclusion

In this section, the recent progress in the synthesis of Al-Fe intermetallics and their softening behaviour using various deformation mechanisms is discussed. In this process, Al-25 at.%Fe and Al-34.5 at.%Fe alloys resulted in $Al_3Fe$ and $Al_2Fe$ intermetallic phases after normal casting and annealing routes. Monoclinic $Al_3Fe$ and triclinic $Al_2Fe$ phase was found to be unstable under high-energy milling condition and transformed to orthorhombic $Al_5Fe_2$ phase. Nanocrystalline and amorphous phase co-exist for 30 h of milling where the maximum hardness was observed. A microhardness of Al-25 at.%Fe alloy showed strengthening down to a

grain size of 42 nm, and Hall-Petch behaviour was thus established over the range of grain sizes from 132 to 42 nm. At the smallest grain size (33 nm), the slope of HP plot becomes negative indicating IHP behaviour.

In addition, $Al_5Fe_2$ resulted from Al-30%Fe alloy resulting in the formation of nanocrystalline intermetallic and was found to be quite stable under the present experimental conditions, and the crystallite size of it decreases up to 10 nm with an increase in the milling time. Microhardness measurements of single $Al_5Fe_2$ nanocrystalline intermetallic phase produced by mechanical milling resulted in Hall-Petch (HP) break-down and showed two distinct behaviours. The break-down of HP for the averaged microhardness measurements was found to be due to the transition of deformation mechanism from dislocation activity to grain boundary sliding. Dislocation models could not intend the critical grain size at which the HP relation breaks down, and so models based on grain boundaries were considered. Detailed analysis showed that models based on grain boundaries namely grain boundary sliding and thermally activated grain boundary shearing seem to be reasonable in explaining the IHP effect. Grain boundary sliding is ascribed to be a viable deformation mechanism resulting in a softening behaviour observed in this system.

## Acknowledgements

The authors are thankful to Dr. V.C. Srivastava and Prof. K.A. Padmanabhan for many stimulating discussions. One of the authors (Raviathul Basariya) gratefully acknowledges the financial support by L.S. Ameer Dheen, Chennai, India, in the form of Research Fellowship. Sections 2 and 3 of this chapter are reproduced with permission from References [34, 35] (©2015, 2016 Elsevier).

## Author details

Mohammed Ishaq Raviathul Basariya[1]* and Nilay Krishna Mukhopadhyay[2]

*Address all correspondence to: ravia80@gmail.com

1 College of Engineering, Guindy Campus, Anna University, Chennai, Tamil Nadu, India

2 Department of Metallurgical Engineering, Indian Institute of Technology, Banaras Hindu University, Varanasi, Uttar Pradesh, India

## References

[1] Darolia R. NiAl alloys for high temperature structure applications. The Journal of The Minerals, Metals & Materials Society. 1991;**43**(3):44

[2] Bohn R, Hanbold T, Birringer R, Gleiter H. Nanocrystalline intermetallic compounds-an approach to ductility? Scripta Metallurgica et Materialia. 1991;**25**:81

[3] Jang JS, Koch CC. The Hall-Petch relationship in nanocrystalline iron produced by ball milling. Scripta Metallurgica et Materialia. 1990;**24**:1599

[4] Koch CC, Cho YS. Nanocrystals by high energy ball milling. Nanostructured Materials. 1992;**1**:207

[5] Ermakov A, Yurchikov E, Barinov V. The magnetic properties of amorphous Y-Co alloy powders obtained by mechanical comminution. Physics of Metals and Metallography. 1981;**52**:50

[6] Yermakov AY, Yurchikov YY, Barinov VA. Magnetic properties of amorphous powders prepared by the mechanical grinding of Y-Co alloys. Fizika Metallov I Metallovedenie. 1981;**52**:1184

[7] Koch CC, Whittenberger JD. Review: Mechanical milling/alloying of intermetallics. Intermetallics. 1996;**4**:339

[8] Zou Y, Saji S, Kusabiraki T. Fast amorphization and crystallization in Al-Fe binary system by high-energy ball milling. Materials Research Bulletin. 2002; 37:123

[9] Ashby MF. Materials Selection in Mechanical Design. Butterworth-Heinemann: Burlington, MA; 2005

[10] Massalski TB. Binary Phase Diagram. OH, USA: American Society for Metals, Metals Park; 1986: 1 & 2

[11] Mukhopadhyay DK, Suryanarayana C, Froes FH. Structural evolution in mechanically alloyed Al-Fe powders. Metallurgical and Materials Transactions. 1995;**26**A:1939

[12] Krasnowski M, Kulik T. Nanocrystalline Al–Fe intermetallics—Lightweight alloys with high hardness. Intermetallics. 2010;**18**:47

[13] Mhadhbi M, Khitouni M, Escoda L, Sunol JJ, Dammak M. Microstructure evolution and mechanical properties of nanocrystalline FeAl obtained by mechanical alloying and cold consolidation. Journal of Alloys and Compounds. 2011;**509**:3293

[14] Krasnowski M, Kulik T. Nanocrystalline and amorphous Al–Fe alloys containing 60-85% of Al synthesised by mechanical alloying and phase transformations induced by heating of milling products. Materials Chemistry and Physics. 2009;**116**:631

[15] Corby RN, Black PJ. The structure of $FeAl_2$ by anomalous dispersion methods. Acta Crystallographica B. 1973;**29**:2669

[16] Mihalkovic M, Wisdom M. Structure and stability of $Al_2Fe$ and $Al_5Fe_2$: First principles total energy and phonon calculations. Physical Review B. 2012;**85**:014113

[17] Zhou F, Luck R, Scheffer M, Lang D, Lu K. The crystallization process of amorphous Al80Fe20 alloy powders prepared by ball milling. Journal of Non-Crystalline Solids. 1999;**250**-25:704

[18] Huang B, Ishihara KN, Shingu PH. Metastable phases of Al–Fe system by mechanical alloying. Materials Science and Engineering: A. 1997;**231**:72

[19] Enzo S, Mulas G, Frattini R. The structure of mechanically alloyed AlxFe(1-x) end-products after annealing. Materials Science Forum. 1998;**269**-272:385

[20] Cardellini F, Contini V, Gupta R, Mazzone G, Montone A, Perin A, Principi G. Microstructural evolution of Al–Fe powder mixtures during high energy ball milling. Journal of Materials Science. 1998;**33**:2519

[21] Gasior W, Debski A, Moser Z. Formation enthalpy of intermetallic phases from Al-Fe system measured with solution calorimetric method. Intermetallics. 2012;**24**:99

[22] Romero-Romero JR, Luis Lopez-Miranda J, Esparza R, Espinosa-Medina MA, Rosas G. High-energy ball-milling of $FeAl_2$ and $Fe_2Al_5$ intermetallic systems. Materials Science Forum. 2013;**755**:47

[23] Zhang RF, Liu BX. Proposed model for calculating the standard formation enthalpy of binary transition-metal systems. Applied Physics Letters. 2002;**81**:1219

[24] Thompson JR, Politis C. Formation of amorphous Ti-Pd Alloys by mechanical alloying methods. Europhysics Letters. 1987;**3**:199

[25] Hellstern E, Fecht HJ, Garland C, Johnson WL. Multicomponent ultrafine microstructure. Materials Research Society. 1989;**132**:137

[26] Li S, Wang K, Sun L, Wang Z. A simple model for the refinement of nanocrystalline grain size during ball milling. Scripta Metallurgica et Materialia. 1992;**27**:437

[27] Eckert J, Holzer JC, Kill CE III, Johnson WL. Structural and thermodynamic properties of nanocrystalline fcc metals prepared by mechanical attrition. Journal of Materials Research. 1992;**7**:1751

[28] Padmanabhan KA, Dinda GP, Hahn H, Gleiter H. Inverse Hall-Petch and grain boundary sliding controlled flow in nanocrystalline materials. Materials science and Engineering: A. 2007;**452**-453:462

[29] Conrad H, Narayan J. On the grain size softening in nanocrystalline materials. Scripta Materialia. 2000;**42**:1025

[30] Zhu J, Miao Y, Guo JT. The effect of boron on charge density distribution in $Ni_3Al$. Acta Materialia. 1997;**45**:1989

[31] Xu S, Prasitthipayaong A, Pickel AD, Habib AH, McHenry ME. Mechanical properties of FeCo magnetic particles–based Sn-Ag-Cu solder composites. Applied Physics Letters. 2013;**102**:251909

[32] Chromik RR, Vinci RP, Allen SL, Notis MR. Nanoindentation measurements on Cu-Sn and Ag-Sn intermetallic formed in Pb-free solder joints. Journal of Materials Research. 2003;**18**:2251

[33] Oliver WC, Pharr GM. Measurement of hardness and elastic modulus by instrumented indentation: Advances in understanding and refinements to methodology. Journal of Materials Research. 2004;**19**:3

[34] Raviathul Basariya M, Roy RK, Pramanick AK, Srivastava VC, Mukhopadhyay NK. Structural transition and softening in Al-Fe intermetallic compounds induced by high energy ball milling. Materials Science and Engineering: A. 2015;**638**:282

[35] Raviathul Basariya M, Srivastava VC, Mukhopadhyay NK. Inverse Hall-Petch like behaviour in a mechanically milled nanocrystalline $Al_5Fe_2$ intermetallic phase. Philosophical Magazine. 2016;**96**:2445

[36] Burkhardt U, Yu G, Ellner M, Peters K. Structure refinement of the iron-aluminium phase with the approximate composition $Fe_2Al_5$. Acta Crystallographica. 1994;B50:313

[37] Gu N, Henley CL, Mihalkovic M. Co-rich decagonal Al-co-Ni: Predicting structure, orientation order and puckering. Philosophical Magazine. 2006;**86**:593

[38] Schwarz RB, Petrich RR, Saw CK. The synthesis of amorphous Ni-Ti alloy powders by mechanical alloying. Journal of Non-Crystalline Solids. 1985;**76**:281

[39] Nayak SS, Wollgarten M, Banhart J, Pabi SK, Murty BS. Nanocomposites and an extremely hard nanocrystalline intermetallic of Al-Fe alloys prepared by mechanical alloying. Materials Science Engineering: A. 2010;**527**:2370

[40] Carlton CE, Ferreira PJ. What is behind the inverse hall-Petch effect in nanocrystalline materials? Acta Materialia. 2007;**55**:3749

[41] Mukhopadhyay NK, Paufler P. Micro- and nanoindentation techniques for mechanical characterization of materials. International Materials Reviews. 2006;**51**:209

[42] Siegel RW, Fougere GE. Mechanical properties of nanophase metals. Nanostructured Materials. 1995;**6**:205

[43] Chokshi AH, Rosen A, Karch J, Gleiter H. On the validity of the Hall-petch relationship in nanocrystalline materials. Scripta Metallurgica. 1989;**23**:1679

[44] Koch CC, Narayan J. The inverse Hall-Petch effect—fact or artifact. Materials Research Society Symposia Proceedings. 2001;**634**:B5.1.1

[45] Koch CC. Optimization of strength and ductility in nanocrystalline and ultrafine grained metals. Scripta Materialia. 2003;**49**:657

[46] Froseth AG, Derlet PM, Van Swygenhoven H. Dislocations emitted from nanocrystalline grain boundaries: Nucleation and splitting distance. Acta Materialia. 2004;**52**:5863

[47] Mohamed FA, Yuwei Xun. Correlations between the minimum grain size produced by milling and material parameters. Materials Science and Engineering R: Reports. 2003;**354**:133

[48] Nieh TG, Wadsworth. Hall Petch relation in nanocrystalline solids. Scripta Metallurgica et Materialia. 1991;**25**:955

[49] Hirose S, Itoh T, Makita M, Fujii S, Arai S, Sasaki K, Saka H. Defect structure of deformed $Fe_2Al_5$ intermetallic compound. Intermetallics. 2003;**11**:633

[50] Weertman JR, Averback RS. Mechanical properties. In: Edelstein AS, Cammarata RC, editors. Nanocrystalline Materials: Synthesis, Properties and Applications. Bristol: Institute of Metals Publishing; 1996: 13

[51] Padmanabhan KA, Sripathi S, Hahn H, Gleiter H. Inverse Hall–Petch effect in quasi-and nanocrystalline materials. Materials Letters. 2014;**133**:151

[52] Jiang B, Weng GJ. A composite model for the grain-size dependence of yield stress of nanograined materials. Metallurgical and Materials Transactions A: Physical Metallurgy and Materials Science. 2003;**34**:765

[53] Raviathul Basariya M, Mukhopadhyay NK, Sripathi S, Padmanabhan KA. Grain size softening effect in intermetallics. Journal of Alloys and Compounds. 2016;**673**:199

[54] Padmanabhan KA. Mechanical properties of nanostructured materials. Materials Science and Engineering A. 2001;**304**:200

[55] Varam S, Rajulapati KV, BhanuSankaraRao K. Strain rate sensitivity studies on bulk nanocrystalline aluminium by nanoindentation. Journal of Alloys and Compounds. 2014;**585**:795

[56] Maier V, Durst K, Mueller J, Backes B, Hoppel HW, Goken M. Nanoindentation strain-rate jump tests for determining the local strain-rate sensitivity in nanocrystalline Ni and ultrafine-grained Al. Journal of Materials Research. 2011;**26**:1421

[57] Padmanabhan KA, Schlipf J. Model for grain boundary sliding and its relevance to optimal structural superplasticity: Part 1 e theory. Materials Science and Technology. 1996;**12**:391

[58] Padmanabhan KA, Gleiter H. Optimal structural superplasticity in metals and ceramics of microcrystalline- and nanocrystalline-grain sizes. Materials Science and Engineering A. 2004;**381**:28

[59] Venkatesh TA, Bhattacharya SS, Padmanabhan KA, Schlipf J. Model for grain boundary sliding and its relevance to optimal structural superplasticity. Materials Science and Technology. 1996;**12**:635

[60] Ali MNK, Scudino S, Samadi Khoshkhoo M, Stoica M, Srivastava VC, Uhlenwinkel V, Vaughan G, Suryanarayana C, Eckert J. Grain size softening effect in $Al_{62.5}Cu_{25}Fe_{12.5}$ nano-quasicrystals. Applied Physics Letters. 2013;**103**:201914

Chapter 6

# Technological Aspects of Production and Processing of Functional Materials Based on Intermetallic Fe-Al

Magdalena Jabłońska, Iwona Bednarczyk,
Anna Śmiglewicz and Tomasz Mikuszewski

Additional information is available at the end of the chapter

http://dx.doi.org/10.5772/intechopen.76701

**Abstract**

The problems of this paper relate to a possibility to affect the structure and properties of new alloys with an intermetallic phase matrix of the Fe-Al system by improvements in casting and hot plastic working processes. The studies were focused on selection of an optimum chemical composition and parameters of the casting and heat treatment processes for further hot plastic working process. The primary goal was to obtain semi-finished products in the forms of sheets and bars with specified set of mechanical and physical properties. The works included several selected alloys with various Al content and variable contents of alloying elements influencing the formation of intermetallic phases. A series of characteristics of mechanical, physical, and chemical properties of alloys containing 28 and 38% of Al were developed. The result of the work consists in the development of a technology for hot forming of flat and round products.

**Keywords:** Fe-Al intermetallics, structure ordering, vacancy hardening, plastic working, microstructure

## 1. Introduction

Fe-Al alloys with an ordered solid solution structure belong to the group of modern heat-resistant engineering materials with favorable physicochemical and mechanical properties at elevated and high temperature [1, 2]. The properties of Fe-Al alloys, such as low density, high melting point, high strength, and good oxidation resistance, combined with fracture toughness, create broad perspectives for industrial applications [3, 4]. These properties are the result of the existing ordering of the crystal structure, which reduces the free energy of the ordered alloys

and thus their greater durability. In addition, alloys from the Fe-Al system are characterized by high fatigue strength [5]. Particular properties of alloys from the Fe-Al system make them a favorable material used for construction, as an alternative for stainless steels containing expensive alloying elements and for superalloys, as a coating material, as a material for elements operating under high-temperature corrosion, and as a starting material for complex alloys and composites [1–7]. Their application options are oriented toward filling the gap between the currently used conventional steels having particular properties and nickel superalloys in manufacturing of products for aircraft, automotive, and power industries. Despite many advantages of the Fe-Al alloys, their practical use is limited by their low creep strength at high-temperature, insufficient plasticity at moderate and low temperatures, as well as susceptibility to brittle cracking at room temperature [2–6, 8–15]. In some cases long-range ordering occurring in these alloys, on the one hand, limits the use of typical processing technologies such as cold plastic working and, on the other hand, provides a set of unique mechanical, physical, and chemical properties. According to the Fe-Al phase equilibrium system (**Figure 1**) [14], aluminum dissolves with iron $\alpha$ up to 54 at.% at 1102°C and 48 at.% at a temperature of about 200°C. During cooling, the constant limit solution Al in Fe is changed to the order Fe-Al. Further cooling affects to replace superstructure Fe-Al into the superstructure of $Fe_3Al$.

For alloys from the Fe-Al system, the most important factors affecting their properties are aluminum content and the content of alloy microadditions. Fe-Al alloys show an increase in the yield stress with an increase of Al content. Two groups of alloying additives can be distinguished in Fe-Al alloys due to their effect:

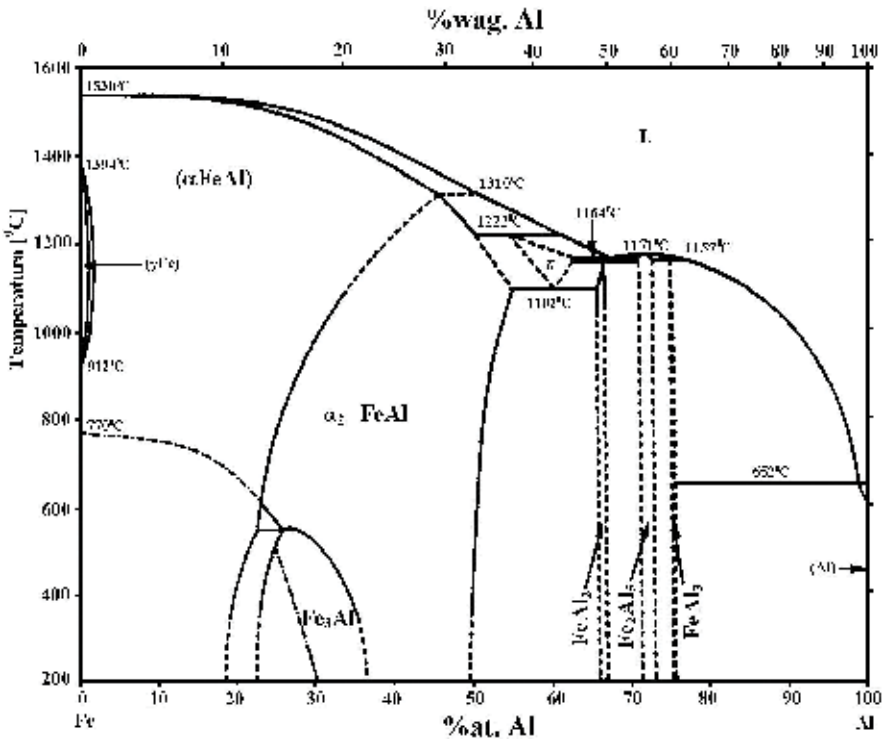


**Figure 1.** Fe-Al system.

1. Additives forming separations that affect the increase of strength. These include Nb, Zr, B, C, Cu and Ta.
2. Alloy additions affecting the strengthening of the solid solution, which may include Cr, Ti, Mn, Si, Mo, V, and Ni.

Fe-Al-based alloys have the highest concentration of thermal vacancies as the only of the long-range intermetallic alloy group. Their presence exerts influence on mechanical properties and, as a result, on the possibilities of industrial-scale application. The concentration of vacancies in Fe-Al alloys increases with the increase of Al content. Alloy additions, such as Cu, Ni, Mn, Cr, V, and Ti, which increase the hardness, affect the slight increase in the concentration of thermal vacancies; however, the addition of B is significant here because it affects the acceleration of the elimination of vacancies. At low temperatures, triple defects and their diffusion dominate by jumping the Fe atoms to the Al subnet. Then, the process of pushing back the anti-position Fe atoms from the Al subnet to the Fe network takes place. At a higher temperature, double vacancies are formed, and their movement is made by double jumps. The increase in the concentration of vacancies causes the increase of the yield stress [16–18].

Time perspective of application of this group of materials depends particularly on thorough understanding of the dependence between, on the one hand, the production processes and the microstructure, and on the other hand, physical properties, such as thermal conductivity and thermal expansion, phase transition temperatures, and defecting and structural ordering of these compounds [18–28]. Such an approach will provide a range of information which allows for anticipating ways of influencing the process plasticity of these alloys.

## 2. Characteristics of the material for studies

Binary and complex alloys from the Fe-Al system (**Table 1**) were the materials for studies. An analysis of available Fe-Al and Fe-Al-Me equilibrium systems and literature research indicate that the chemical composition of alloys for plastic working should be in the range of 25% at. Al to 60% at. Al, and it may contain additives such as molybdenum, zirconium, carbon, and boron, with contents in the following ranges (at.%): Mo (0.2 ± 0.1), Zr (0.1 ± 0.05), C (0.1 ± 0.1),

| Alloy | Al | Mo | Zr | C | B | Cr | Fe | HV2 |
|---|---|---|---|---|---|---|---|---|
| Fe-28Al | 28.0 | – | – | – | – | – | 72.0 | 299 |
| Fe-28Al-5Cr | 28.0 | – | – | – | – | 5.0 | 67.0 | 240 |
| Fe-38Al | 38.0 | – | – | – | – | – | 62.0 | 287 |
| Fe-38Al-5Cr | 38.0 | – | – | – | – | 5.0 | 57.0 | 213 |
| Fe-28Al+microadd. | 28.0 | 0.2 | 0.05 | 0.10 | 0.01 | – | 71.64 | 303 |
| Fe-28Al-5Cr+microadd. | 28.0 | 0.2 | 0.05 | 0.10 | 0.01 | 5.0 | 66.64 | 266 |
| Fe-38Al+microadd. | 38.0 | 0.2 | 0.05 | 0.10 | 0.01 | – | 61.64 | 281 |

**Table 1.** Chemical composition of the obtained alloys (at.%) and their hardness after heat treatment at 1000°C/24 h and furnace-cooling.

and B (0.02 ± 0.01). Most of all, the indicated microadditions serve the purpose of strengthening of grain boundaries, as well as grain refining.

An analysis of chemical composition carried out by optical emission spectrometry (OES) confirmed obtaining chemical compositions assumed for melting.

## 3. Results of experiments

### 3.1. Preparation of alloys with varied contents of Al, Fe, alloying elements, and microadditions

Currently, the alloys from the Fe-Al system used as casting materials do not pose major technological problems during melting and casting. However, the requirements set for these alloys increase if semifinished products intended for a further processing are manufactured from them. Such alloys must exhibit a set of features ensuring their technological plasticity, including high-purity, uniform, and fine-grained structure with a minimal level of casting defects such as shrinkage porosities, cracks, and microporosity. Melting was carried out using a conventional melting technique in an IS5/III induction vacuum furnace from Leybold-Heraeus, using a compacted magnesia crucible (from $MgO{\cdot}Al_2O_3$ spinel) with a granulation of 0.05–2 mm, under a vacuum of 13.5 Pa. Melting of alloys under vacuum allows for avoiding the use of protective covers and refiners and enables to use pure metals instead of master alloys as charges. It also promotes alloy degassing and protects from oxidation, but it requires taking into account the melting loss of the components in the result of their evaporation. The following constituents were used during the melting process: as charge components (ARMCO iron, aluminum of 99.98 wt.% purity, electrolytic chromium) and as microadditions (technically pure molybdenum in the form of a compressed powder, technically pure iodine zirconium, crystalline boron, carbon in the form of anthracite). Due to the form of the charge materials, the melting loss was assumed for molybdenum, zirconium, carbon, and boron. Mechanically, purified and dried pieces of the main alloy components, i.e., iron and aluminum, were placed together in the crucible. After melting and homogenization, the charge was overheated to a temperature of approx. 1600°C, and the following microadditions were added to the melt: zirconium, molybdenum, carbon, and boron. After reducing the temperature to approx. 1530÷1550°C and maintaining it for homogenization and degassing, the alloy was cast. After melting, the alloys were remelted once. Preparation of casts both having circular (the so-called bars) and rectangular (the so-called flats) cross sections was planned. The alloys were cast under the same conditions into cold graphite molds (**Figure 2**). In the upper sections of the mold, double insulating felt with a thickness of 3÷4 cm was used, serving the purpose of protection from rapid solidification of the liquid metal. **Figures 1–4** show the applied graphite molds and dimensions of the obtained ingots.

The alloys after casting were characterized by a coarse-grained structure. In the case of the alloys without microadditions, occurrence of grains with diversified dimensions was observed, while in the alloys containing microadditions, the shape of the grains is typical for a primary dendritic structure. In **Figure 3**, selected microstructures of the studied alloys after homogenizing at 1000°C for 24 h and furnace-cooling are shown. In the alloys not containing

http://dx.doi.org/10.5772/intechopen.76701

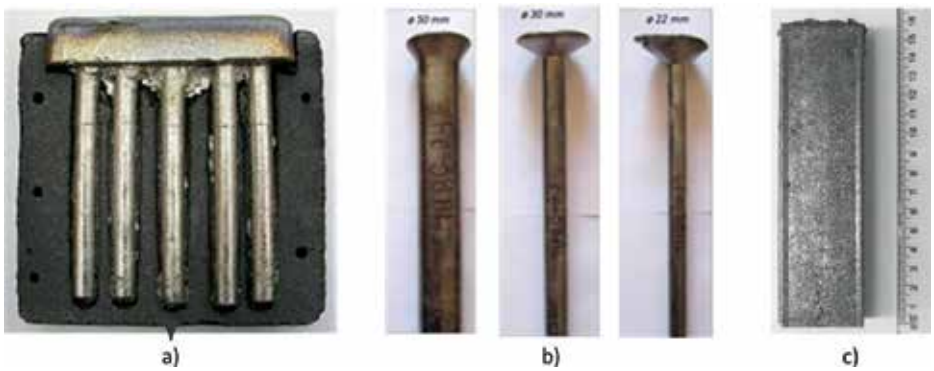


**Figure 2.** Graphite mold for ingots having dimensions (a) Ø12 mm, l = 120 mm, (b) l = 45 mm and diameters (a) Ø50 mm, (b) Ø30 mm, and (c) Ø22 mm, (c) of approx. 160 mm × 30 mm × 20 mm.

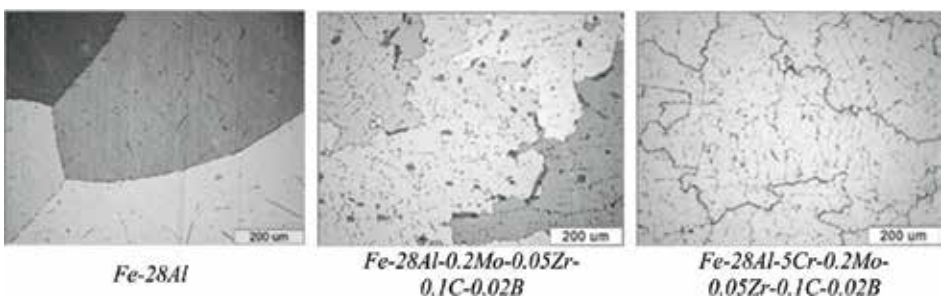


**Figure 3.** Microstructures of the alloys after annealing 1000°C/24 h/furnace.

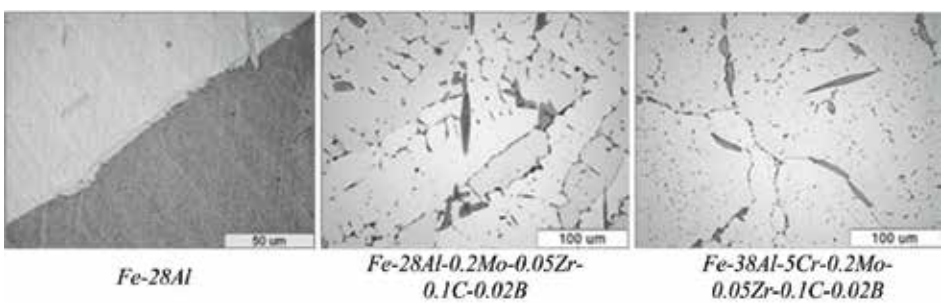


**Figure 4.** Microstructures of the alloys after annealing 1000°C/24 h/furnace. The presence of phases inside the grains and at their boundaries.

the Cr alloying element, both binary (Fe-28Al, Fe-38Al) and complex (Fe-28Al-0.2Mo-0.05Zr-0.1C-0.02B, Fe-38Al-0.2Mo-0.05Zr-0.1C-0.02B) occurrence of precipitations both at the grain boundaries and inside the grains was found (**Figure 3**).

To identify the precipitations found in the studied alloys, investigations using scanning electron microscopy (SEM), scanning transmission electron microscopy (STEM), and transmission electron microscopy (TEM) were carried out. Non-etched and etched samples were

examined. Due to the fact that phases of the same type were found in the Fe-28Al, Fe-28Al-0.2Mo-0.05Zr-0.1C-0.02B, Fe-38Al, and Fe-38Al-5Cr-0.2Mo-0.05Zr-0.1C alloys, the phase identification results are presented for the Fe-28Al alloy only. The results of qualitative and quantitative analyses of chemical composition for the Fe-28Al alloy are presented in **Figure 5**.

The results of studies of chemical composition microanalysis obtained by scanning electron microscopy (analysis in microzones and surface distribution of the elements) indicate

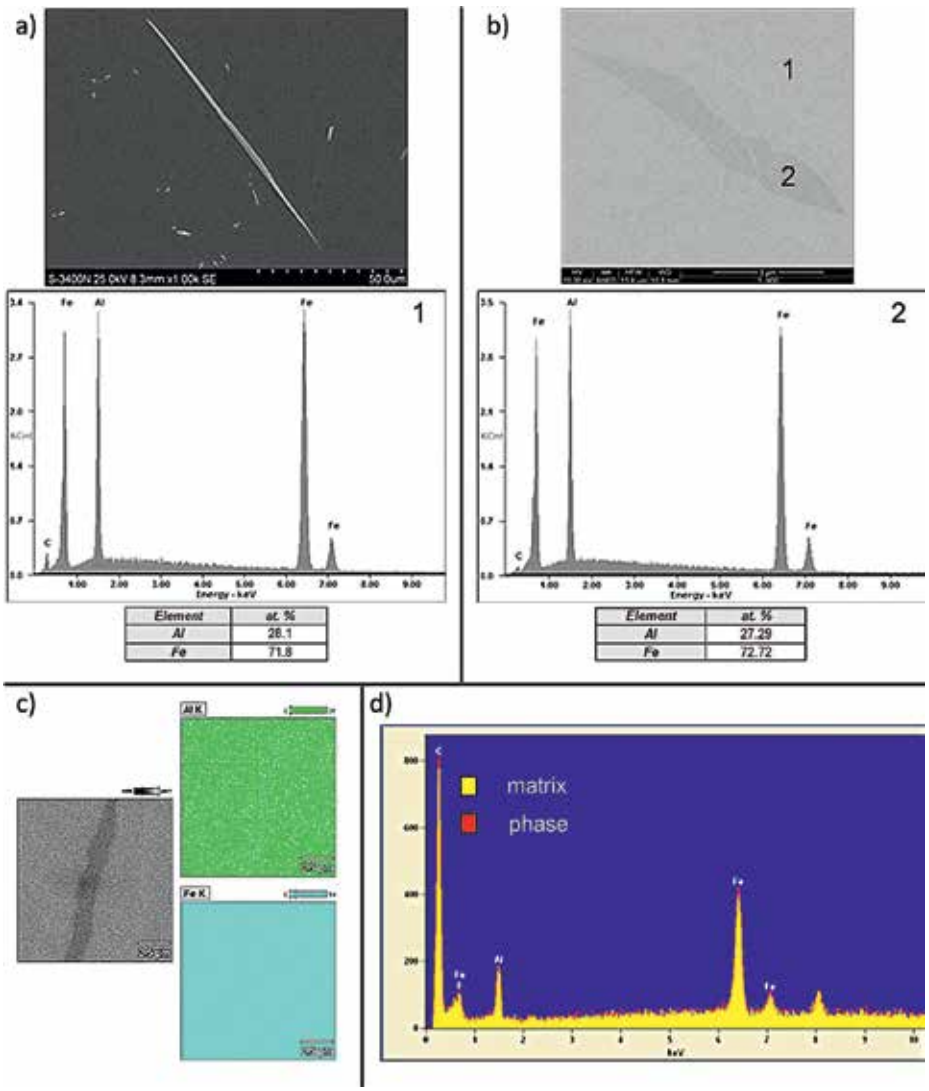


**Figure 5.** Results of microstructure studies (SEM, STEM) and analysis of chemical composition together with the X-ray spectra (EDS) of the Fe-28Al alloy after annealing at 1000°C for 24 h and furnace-cooling: (a) etched microsection, (b) non-etched microsection, (c) surface distribution of the elements, and (d) collation of characteristic radiation spectra for the matrix and the phase.

existence of phases with chemical composition close to that of the matrix. The obtained results (SEM) are confirmed by qualitative analysis of chemical composition, carried out by scanning transmission electron microscopy, where also the presence of iron and aluminum only was found in the identified phases. **Figure 5** presents a collation of X-ray spectra obtained by STEM for the matrix and for the investigated phase. No differences in characteristic radiation spectra for the matrix and for the phase were found, which proves comparable concentrations of elements in both studied microzones.

Then, studies using electron backscatter diffraction were carried out. The obtained pattern of Kikuchi lines of the disclosed phase is shown in **Figure 6**. An analysis of geometry of the line pattern indicated occurrence of a $Fe_3Al$ phase in the Fe-28Al alloy. This fact was confirmed by studies of electron diffraction on a transmission electron microscope. Its results are depicted in **Figure 7**.

The results are consistent with the phase equilibrium system, because in both studied systems, the $Fe_3Al$ phase may form during slow cooling at a temperature from approx. 500°C (for Fe-28Al) and from approx. 300°C (for Fe-38Al).

Due to the hot plastic working process planned in further steps, a structural analysis in the state after the high-temperature annealing was carried out, using rapid cooling in oil for vacancy freezing. In the case of the studied alloys, rapid cooling eliminates the formation of phase in the microstructure, exemplified in **Figure 8**. It suggests a lack of influence of the $Fe_3Al$ phase disclosed in the heat treatment process on the planned course of the hot plastic working process in the studied alloys.

### 3.2. Characteristics of the selected thermal properties of alloys intended for further plastic working

Thermomechanical behavior of intermetallic alloys at a high temperature is connected with the existing state of structural ordering and with the complex defect structure, including the characteristic phenomenon of supersaturation with vacancies [1, 2]. Both the structure ordering and the presence of multiple defect types affect the properties of the studied alloys

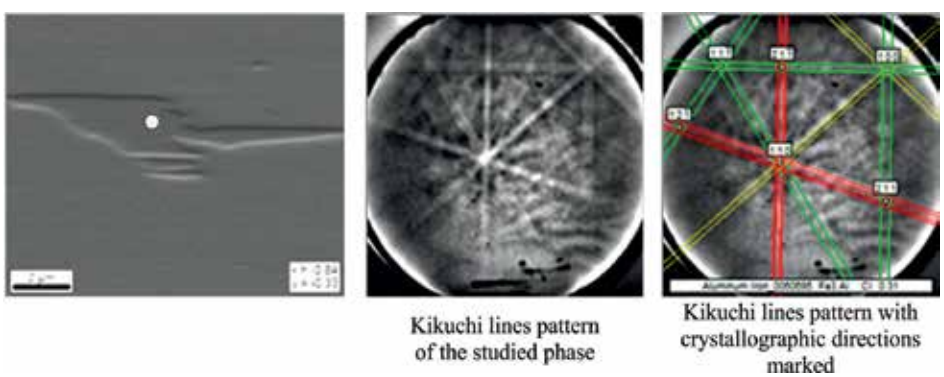


**Figure 6.** Results of studies of the microstructure (EBSD) of the Fe-28Al alloy after annealing at 1000°C for 24 h and furnace-cooling.

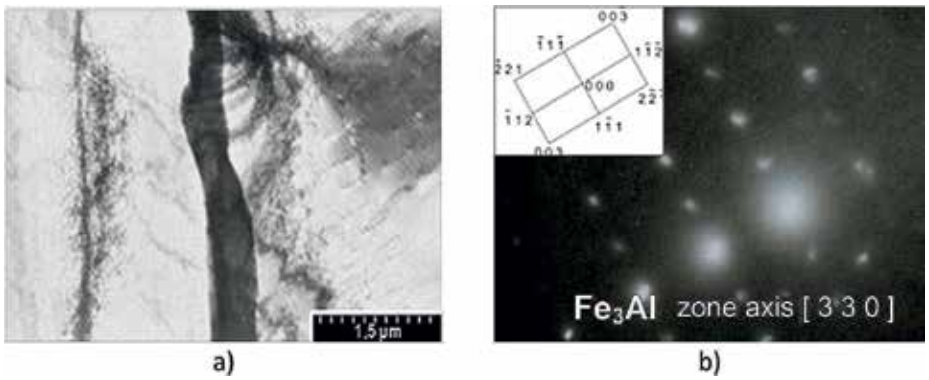


**Figure 7.** Microstructure of the Fe-28Al alloy after annealing at 1000°C for 24 h and furnace-cooling (TEM): (a) experimental zone (white area) and (b) diffraction pattern from the analyzed phase and diffraction solution.


**Figure 8.** Microstructures of the studied alloys after the high-temperature annealing for 24 h and oil cooling.

significantly. From the point of view of the plastic working process, it is necessary to determine the characteristic temperatures in relation to changes in the ordering type and the temperature of transition into a disordered state, in which the plastic working process may be realized. Characteristic transition temperatures were determined by dilatometric method and confirmed by DTA. The results obtained for the selected alloys are gathered in **Figure 9**. Critical temperature of the change in the ordering type in the alloys with 28 at.% Al was identified, connected with the transition from the B2 ordering-type state into $DO_3$ at a temperature of approx. 550°C. For alloys with 38 at.% Al, a thermal effect was observed at a temperature of approx. 1260°C, which may be connected with the process of transition from a disordered (A2) into an ordered (B2) solid solution, and another one at a temperature of approx. 1060°C, which is probably a result of changes in physical properties within the phase B2 occurrence area, and precisely, with the B2(h) → B2′ transition, the changes being connected with a rebuilding of the defect structure [6].

### 3.3. Plastometric studies and their verification

Technological plasticity and thus the deformabilities of the studied alloys are significantly affected by the value of flow stress. In the case of the Fe-Al alloys, the more important

http://dx.doi.org/10.5772/intechopen.76701

**Dilatometric analysis**

| | Transition temperatures | | | | Transition temperatures | |
|---|---|---|---|---|---|---|
| Fe-28Al | N [°C] | 573 | 1279 | Fe-38Al | N [°C] | 1310 |
| | description | $DO_3 \leftrightarrow B2$ | end of the disordering process $B2 \leftrightarrow A2$ | | description | end of the disordering process $B2 \leftrightarrow A2$ |
| | CH [°C] | 1163 | 522 | | CH [°C] | 1286 |
| | description | beginning of the ordering process $A2 \leftrightarrow B2$ | $B2 \leftrightarrow DO_3$ | | description | beginning of the ordering process $A2 \leftrightarrow B2$ |

N – heating; CH – cooling

**DTA analysis**

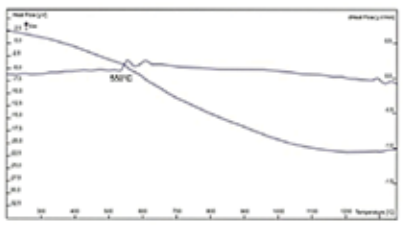

DTA curve for cooling of the Fe-28Al alloy after annealing at 1000°C/24h and furnace-cooling

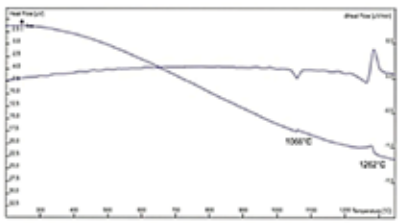

DTA curve for cooling of the Fe-38Al alloy after annealing at 1000°C/24h and furnace-cooling

**Figure 9.** Transition temperatures for the Fe-28Al and Fe-38Al alloys recorded by dilatometric method and differential thermal analysis method.

factors affecting their behavior during deformation at a given temperature include Al content and, consequently, the obtainable different structure types of the alloy matrix, i.e., a matrix with an ordered structure of $DO_3$ or B2 type. The type of the alloy matrix should be related to phase transitions, occurring with the given chemical composition, which may be used while selecting the parameters of the plastic working so as to decrease the value of flow stress at the given value of deformation. Also, the different deformation mechanism, depending on the Al content in this case, should be taken into account.

The obtained results of plastometric examinations indicate that at a temperature below 900°C, the discussed alloys undergo a strong hardening. Deformation at a higher temperature affects a decrease of the flow stress value (**Figure 10**). A tendency to increase the hardening with the increasing Al content was found in the plastometric tests. The highest $\sigma_p$ values among the studied alloys are exhibited by the Fe-38Al alloy.

Analysis of the shape of the flow curves and evaluation of the structure of the studied alloys indicated that the prevailing rebuilding mechanism of the defected structure changes depends on the Al content. In alloys containing 28 at.% Al, a phenomenon of grain defragmentation is

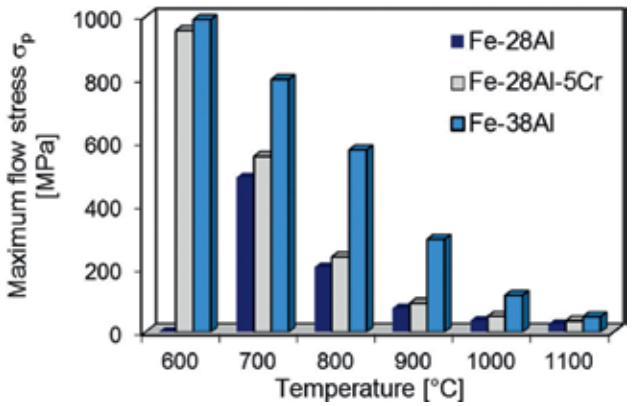


**Figure 10.** Influence of the deformation temperature on maximum flow stress of the studied alloys (deformation rate 1 $s^{-1}$).

observed in the microstructure (**Figure 11**). Inside the primary grains, new grains nucleate. In the substructure, climb of dislocation, polygonization, and subgrain coalescence prevail phenomena characteristics for dynamic recovery process (**Figure 12**). In alloy with a higher Al content, prevalence of the wide-angle migration process of the grain boundaries and formation of new grains and phenomena accompanying the process of stricture rebuilding in the result of dynamic recrystallization were observed (**Figures 11** and **13**).

After plastometric studies, rolling tests under laboratory conditions were carried out. Ingots of Fe-28Al, Fe-28Al-5Cr, and Fe-38Al alloys having dimensions of approx. 160 × 30 × 20 mm (**Figure 2**) after homogenizing annealing constituted charge materials. Hot rolling was carried out on a two-high reversed rolling mill with roller diameter of 65 mm at VSB-TU Ostrava. The samples were heated to a temperature of 1150°C and then rolled in three roll passes. The following percentage reductions were applied: 15, 15, and 15%. Rotational speed of the rollers was 80 rpm. After rolling, the samples were cooled in air. The process was carried out for ingots without covers and using covers made of ferritic steel (AISI 430) in order to protect the alloy surface from oxidation and cracking in the result of contact with cold rollers. In **Figure 13**, views of obtained profiles are collated. It was observed that in the case of binary alloys, it was necessary to use covers during hot rolling. A particularly evident net of deep cracks was observed after

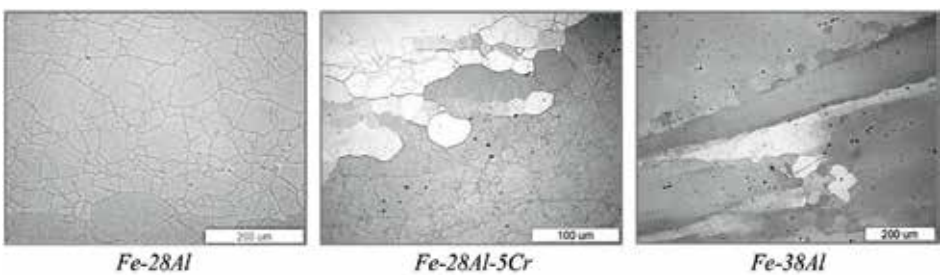


**Figure 11.** Microstructures of the alloys after deformation with a rate of 0.1 $s^{-1}$ at T = 1000°C.

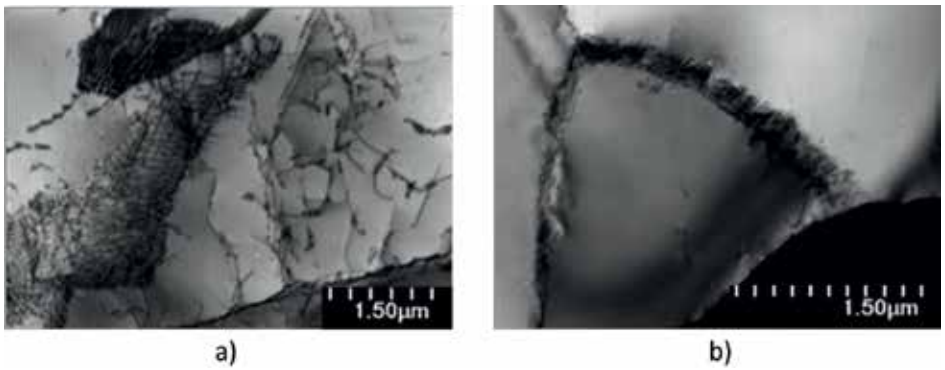


**Figure 12.** Substructure of the Fe-28Al alloy after deformation with a rate of 0.1 $s^{-1}$ at T = 1000°C: (a) subgrain structure and (b) dislocation rearrangement-polygonization effect.

rolling without covers in the Fe-38Al alloy. In the case of the Fe-28Al-5Cr alloy, a qualitatively good surface was obtained even after rolling without covers (**Figure 14**).

For selected flats, a further rolling process was carried out using percentage reductions 15, 15, and 15% to a thickness of 6 mm, obtaining semifinished products (**Figure 15**) of satisfactory quality.

Then, tests of corrosion resistance in the "acid rain" environment – pH = 3.5 and 3% NaCl aqueous solution, for samples after homogenizing annealing and rolling was carried out. The scope of the tests included potentiostatic, galvanostatic, and potentiodynamic examinations as well as investigation of the condition of the sample surface after corrosion. It was proven that, in most cases, the tested alloys are characterized by a tendency for activation (depassivation) of the surface under the aforementioned conditions. The best corrosion resistance was exhibited by samples of the Fe-38Al alloy. For the samples of this alloy, the lowest values of current density for a potential both of $E = E_{kor} + 300$ mV and $E = E_{kor} + 500$ mV were recorded. A significant increase in the current density from the value of the corrosion current density to the value of the current density for the potential of $E = E_{kor} + 300$ mV was characterized here. Comparing the tests results for the samples

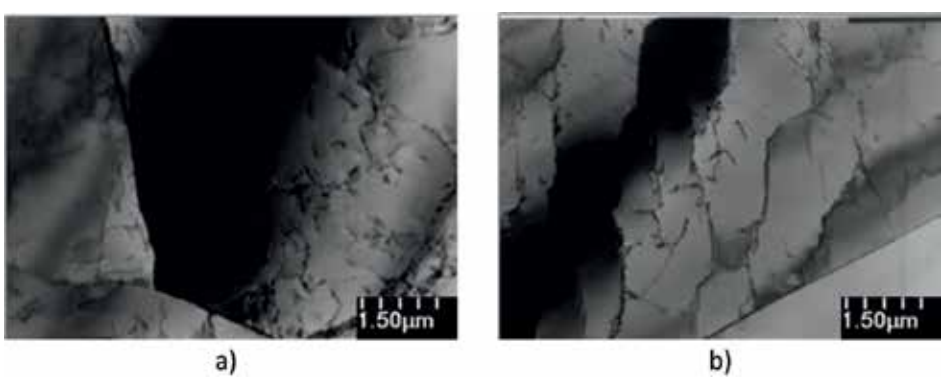


**Figure 13.** Substructure of the Fe-38Al alloy after deformation with a rate of 1 $s^{-1}$ at T = 1000°C: (a) wide-angle boundaries migration and (b) subgrain structure with a diversified dislocation density.

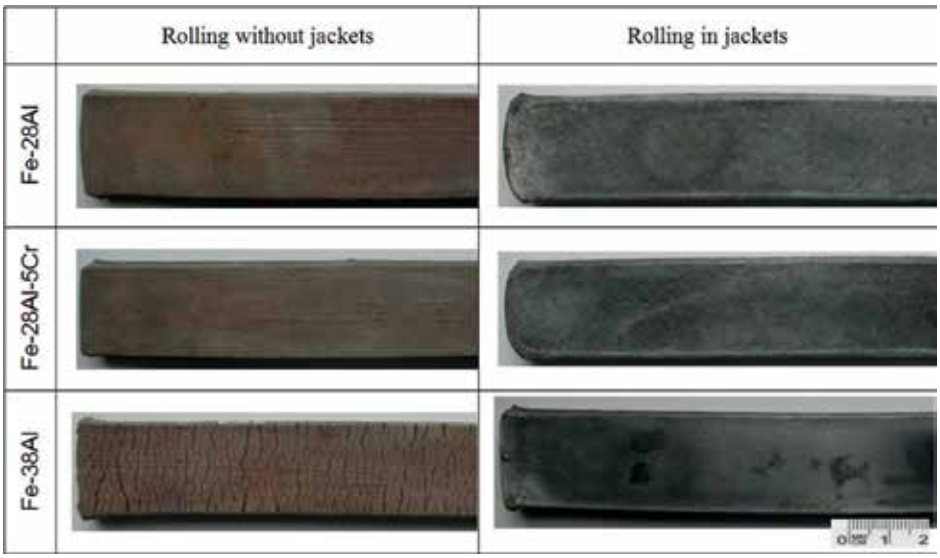


**Figure 14.** Photographs of surfaces of the flats obtained after hot rolling.


**Figure 15.** Views of the profiles after rolling with total reduction of ~70% to a thickness of 6 mm.

with various degrees of deformation, one may see that a higher deformation degree under nonstationary conditions, or those closer to the actual corrosion conditions, does not cause an acceleration of the corrosion but, unlike under stationary conditions, a slowdown. For all studied alloys, the corrosion has a local character and leads to the formation of small point pits (**Figure 16**).

The studies carried out hitherto allowed for ascertaining that further technological tests should be carried out for the alloy with 38 at.% Al content. However, realization of tests for the alloy with such aluminum content with microadditions was planned at this stage. It was imposed, most of all, by the role of microadditions in the hardening process of grain boundaries.

Realizing the planned research program intended for obtaining semifinished products in the form of thin sheets, a sheet production process from the Fe-38Al-0.2Mo-0.05Zr-0.1C-0.02B alloy was applied, consisting of heat treatment and plastic working. A semifinished product with a thickness of ~2 mm (**Figure 17**) was obtained.

http://dx.doi.org/10.5772/intechopen.76701

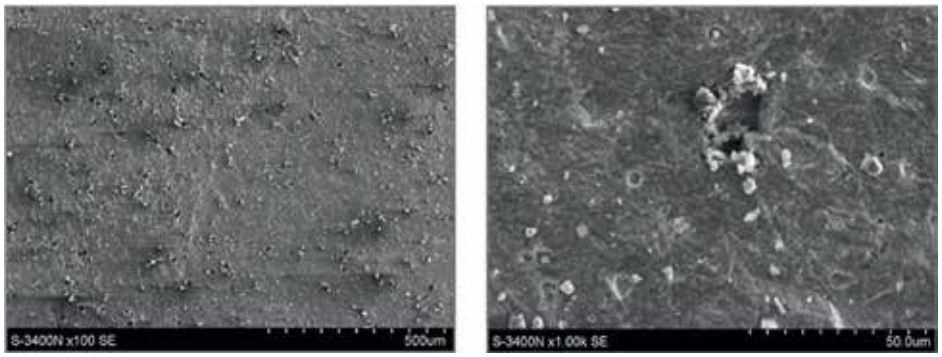


**Figure 16.** Surface of the Fe-38Al alloy (condition after rolling with a total reduction of ~70% to a thickness of 6 mm) after corrosion tests.

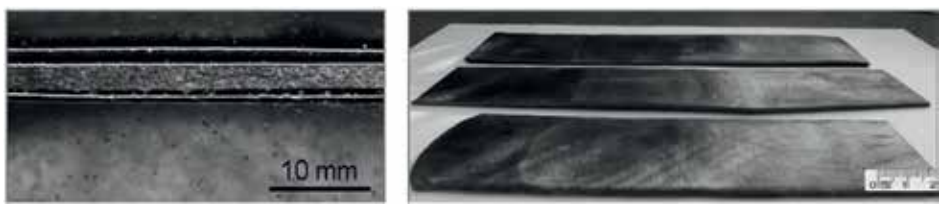


**Figure 17.** Flats made of the Fe-38Al-0.2Mo-0.05Zr-0.1C-0.02B alloy.

Successful results of the realized rolling tests induced realization of further planned goals, i.e., preparation of bars from the tested alloy by two techniques: rolling and hydrostatic extrusion. Execution of these tests was planned using metal covers.

Rolling of ingots from the Fe-38Al-0.2Mo-0.05Zr-0.1C-0.02B alloy with initial diameters of Ø30 mm and Ø22 mm (**Figure 2**) was carried out on a three-high mill. Before the rolling, the ingots were heated for approx. 45 min; the heating temperature was higher by 30°C than the planned initial rolling temperature, i.e., 1250°C. The rolling was carried out without reheating. In the first step, rolling of the ingots to a diameter of Ø12 mm was planned. **Figure 18**


**Figure 18.** Cross sections of the bars formed in the hot rolling process (uncontrolled material flow).

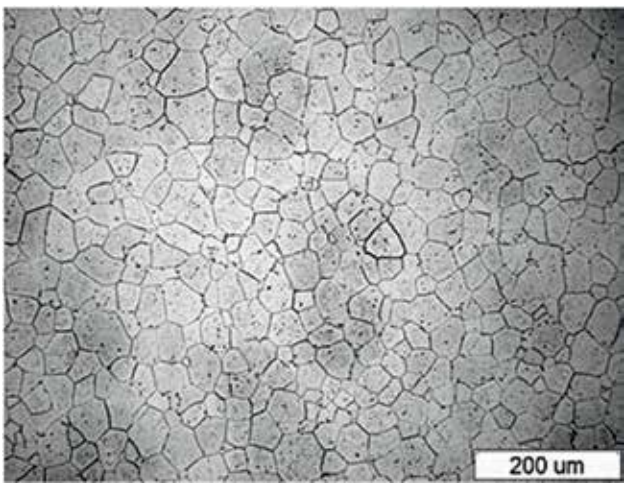


**Figure 19.** Microstructure of the Fe-38Al-0.2Mo-0.05Zr-0.1C-0.02B alloy after the hot rolling process.


**Figure 20.** Cross sections of the bars formed in the hot hydrostatic extrusion process.

shows cross sections of the produced bars. Considering the occurrence of an uncontrolled material flow, further reduction of the cross section was canceled. However, it should be emphasized that in spite of the technological difficulties, a homogeneous and fine-grained structure was obtained (**Figure 19**).

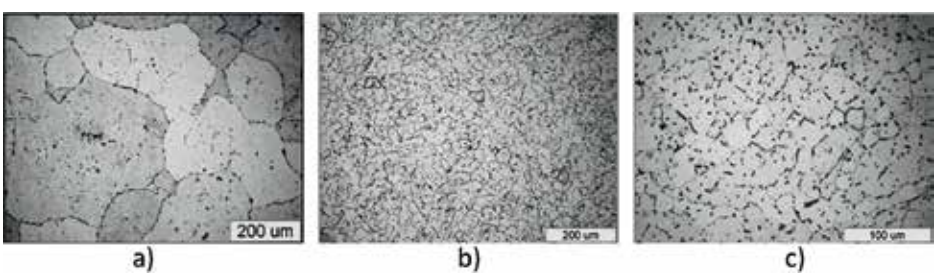


**Figure 21.** Microstructure of the Fe-38Al-0.2Mo-0.05Zr-0.1C-0.02B alloy: (a) after casting and heat treatment and (b–c) after the hot hydrostatic extrusion process (diameter 2 mm).

http://dx.doi.org/10.5772/intechopen.76701

The hot hydrostatic extrusion process was carried out for an ingot of the Fe-38Al-0.2Mo-0.05Zr-0.1C-0.02B alloy, having a diameter of 30 mm after homogenization at a temperature of 1000°C. Cross sections of the prepared bars are shown in **Figure 20**.

An effective structure refinement was obtained after the hydrostatic extrusion process. **Figure 21** presents the alloy microstructure after the homogenization process and after the extrusion process.

## 4. Summary and conclusions

The tests carried out proved that melting of the studied alloys in induction vacuum furnaces is technically possible while maintaining the given process parameters. In the results of the application of the charge in the form of very pure components, melting and single refinement remelting, alloys with an assumed chemical composition, and a very low total content of gaseous impurities of the order of several ppm are obtained. It was found that the produced alloys are characterized by a very low castability and a high casting shrinkage (from 3.30 to 3.40%), leading to a coarse-grained primary structure and occurrence of shrink-type defects being deposited in the ingots.

In the process of heat treatment, during cooling, $Fe_3Al$ phase forms in the studied alloys. According to the phase equilibrium system, the $Fe_3Al$ phase may form during slow cooling at a temperature from approx. 500°C (for Fe-28Al) and from approx. 300°C (for Fe-38Al). In order to eliminate the influence of the $Fe_3Al$ phase disclosed in the heat treatment process on the planned hot plastic working process, a heat treatment operation with oil cooling was used for the studied alloys to freeze the structure. Therefore, lack of influence of the aforementioned phase on the deformation process was confirmed.

From the point of view of the plastic working process, it was necessary to determine the characteristic temperatures in the studied alloys, particularly in relation to the changes in the ordering type and the temperature of transition into a disordered state, in which the plastic working process could be realized. Critical temperature of the change in the ordering type in the alloys with 28 at.% Al was identified, connected with a transition from the ordered state of B2 type into $DO_3$ type at a temperature of approx. 550°C. For alloys containing 38 at.% Al, a temperature of transition from a disordered (A2) into an ordered (B2) solid solution was identified, and temperatures of transitions are connected with a rebuilding of the defect structure within the B2 phase.

The obtained results of the plastometric studies indicated possibilities of technological forming of the studied alloys in the temperature range from 900 to 1200°C. At a lower temperature, strong hardening renders the deformation process more difficult. The technological hot plastic forming tests proved a possibility to obtain flat hot-rolled products consistent with the assumptions while maintaining the final rolling temperature not lower than 950°C, using metal covers. A proper method for production of bars consistent with the assumptions is the high-temperature hydrostatic extrusion process. A product obtained by this method warrants meeting the dimensional requirements, which has not been obtainable by rolling. In the case of both technologies applied, manufacturing of products in the form of bars requires an additional operation for jacket removal.

## 5. Possible applications

Potentially, the use of the developed flat products in heating systems of heat exchangers as substitutes for stainless steels used hitherto may be planned. Moreover, application of the developed products in the form of bars as elements of operational systems of motor vehicles may be envisaged, including particularly the use for roller axles of the supercharging pressure system of turbo.

## Author details

Magdalena Jabłońska*, Iwona Bednarczyk, Anna Śmiglewicz and Tomasz Mikuszewski

*Address all correspondence to: magdalena.jablonska@polsl.pl

Silesian University of Technology, Faculty Materials Engineering, Institute of Materials Engineering, Katowice, Poland

## References

[1] Wolff J, Franz M, Broska A, Kerl R, Weinhagen M, Köhler B, Brauer M, Faupel F, Hehenkamp T. Intermetallics. 1999;**7**:289-300. DOI: 10.1016/S0966-9795(98)00105-8

[2] De Diego N, Plazaola F, Jiménez JA, Serna J, del Río J. Acta Materialia. 2005;**53**:163-172. DOI: 10.1016/j.actamat.2004.09.013

[3] Stoloff NS. Materials Science and Engineering. 1998;**A258**:1-14. DOI: 10.1016/S0921-5093(98)00909-5

[4] Kratochvil P, Schindler I. Intermetalics. 2007;**15**:436-438. DOI: 10.1016/j.intermet.2006.06.005

[5] Schindler I, Kratochvil P, Prokopcakova P, Kozelsky P. Intermetallics. 2010;**18**:745-747. DOI: 10.1016/j.intermet.2009.11.005

[6] Kerl R, Wolff J, Th H. Intermetallics. 1999;**7**:301-308. DOI: 10.1016/S0966-9795(98)00118-6

[7] Pike LM, Liu CT. Intermetallics. 2000;**8**:1413-1416. DOI: 10.1016/S0966-9795(00)00095-9

[8] Baligidad RG, Radhakrishna A. Materials Science and Engineering. 2001;**A308**:136-142. DOI: 10.1016/S0921-5093(00)02026-8

[9] Cizek J, Lukac F, Melikhova O, Prochazka I, Kuzel R. Acta Materialia. 2011;**59**:4068-4078. DOI: 10.1016/j.actamat.2011.03.031

[10] Salazar M, Albiter A, Rosas G, Pérez R. Materials Science and Engineering. 2003;**A351**:154-159. DOI: 10.1016/S0921-5093(02)00825-0

[11] Jabłońska MB, Mikuśkiewicz M, Śmiglewicz A, Bernstock-Kopaczyńska E. Defect and Diffusion Forum. 2012;**326-328**:573-577. DOI: 10.4028/www.scientific.net/DDF.326-328.573

[12] Jabłońska M, Hanc A, Szostak A. Solid State Phenomena. 2010;**163**:299-302. DOI: 10.4028/www.scientific.net/SSP.163.299

[13] Jabłońska M, Jasik A, Hanc A. Archives of Metallurgy and Materials. 2009;**54**:731-739

[14] Massalski TB editor. ASMM, Metals Park, O. 1986. p. 234

[15] Anton DL, Shah DM. High temperature ordered intermetallic alloys IV. In: Johnson LA, Pope DP, Stiegler JO, editors. Mater. Res. Soc. Proc. 213. Pittsburgh, PA; 1991. p. 733

[16] Fraczkiewicz A, Gay AS, Biscondi M. Materials Science and Engineering. 1998;**A258**:108. DOI: 10.1016/S0921-5093(98)00923

[17] Morris MA, Morris DG. Scripta Materialia. 1998;**38**:509. DOI: 10.1016/S1359-6462(97)00468-5

[18] Konrad J, Zaefferer S, Schneider A, Raabe G, Frommeyer G. Intermetallics. 2005;**13**: 1304-1312. DOI: 10.1016/j.intermet.2004.10.01

[19] Kobayashia S, Zambaldib C, Raabe D. Acta Materialia. 2010;6672-6684. DOI: 10.1016/j.intermet.2004.10.017

[20] Schindler I, Kopeček J, Kawulok P, Jabłońska M, Hadasik E, Jóźwik P, Opěla P, Hanus P, Polkowski W, Bojar Z. Archives of Civil and Mechanical Engineering. 2017;**17**(4): 816-826. DOI: 10.1016/j.acme.2017.03.004

[21] Li D, Lin D, Liu Y. Materials Science and Engineering. 1998;**A249**:206-216. DOI: 10.1016/S0921-5093(98)00507-3

[22] Łyszkowski R, Bystrzycki J. Intermetallics. 2006;**14**:1231-1236. DOI: 10.1016/j.intermet.2005.12.014

[23] Reimann U, Sauthoff G. Intermetallics. 1999;**7**:437-441. DOI: 10.1016/S0966-9795(98)00104-6

[24] Łyszkowski R, Bystrzycki J, Płociński T. Intermetallics. 2010;**18**:1344-1349. DOI: 10.1016/j.intermet.2009.12.026

[25] Dolata A, Śleziona J, Formanek B. Journal of Materials Processing Technology. 2006;**175** (1-3):192-197. DOI: 10.1016/j.jmatprotec.2005.04.015

[26] Karczewski K, Jóźwiak S, Bojar Z. Archives of Metallurgy and Materials. 2007;**52**:361-365

[27] Cebulski J, Basa J, Pasek D. Solid State Phenomena. 2014;**212**:49-52. DOI: 10.4028/www.scientific.net/SSP.212.49

[28] Łyszkowski R, Bystrzycki J. Materials Characterization. 2014;**96**:196-205. DOI: 10.1016/j.matchar.2014.07.004

Chapter 7

# Inter-Diffusion of Nickel and Palladium with Germanium

Adrian Habanyama and Craig M. Comrie

Additional information is available at the end of the chapter

http://dx.doi.org/10.5772/intechopen.73190

**Abstract**

Nickel and palladium germanides are the most promising candidates for nano-electronic contact materials to active areas of germanium-based devices. Solid-state reactions were thermally induced in conventional thin film couples of the Ni/Ge and Pd/Ge systems in order to study the sequence of phase formation. By embedding a thin layer of tantalum or tungsten as an inert marker between coupling thin film layers and observing its movement during phase formation, the dominant diffusing species were identified and monitored. In the Ni/Ge system, $Ni_5Ge_3$ was the first phase to form followed by NiGe. The results showed that during $Ni_5Ge_3$ formation, Ni was the sole diffusing species. During NiGe formation, both Ni and Ge diffused with the Ge diffusion prominent during the early stages, while the later stage of growth was dominated by Ni diffusion. The only phases observed to form in the Pd/Ge system were PdGe and $Pd_2Ge$, the latter being the first. Palladium was the dominant diffusing species during both phase formations. Lateral diffusion couples were also prepared by the deposition of thick rectangular islands of germanium on to thin films of nickel and palladium. Several aspects of thermally induced lateral (as opposed to vertical) growth of phases were studied.

**Keywords:** thin film, inter-diffusion, ion beam analysis

## 1. Introduction

Silicon-based materials used in nano-electronics have been pushed to their physical limits because of the downscaling of devices to ever smaller dimensions and greater performance. Charge carriers have a greater mobility in germanium than in silicon; therefore, research work is being carried out to see if Ge can be used in place of Si in some niche metal-oxide semiconductor (MOS) applications [1, 2] for high performance.

The implementation of Ge-based technology in the nano-electronics industry requires the identification of appropriate materials for ohmic contacts to the active areas of a Ge-based device. Metal-silicides are used as ohmic contacts in silicon technology; metal-germanides are therefore being investigated so that they may be used in a similar way in Ge-based technology. A systematic study of the thermally induced reaction of a large number of transition metals with germanium substrates revealed that NiGe and PdGe are the most promising candidates for ohmic contacts in germanium-based technology [2, 3].

Some electronic properties of Ni/Ge and Pd/Ge junctions have been studied in previous work. Schottky barrier diodes have been used in many applications such as gates for metal-semiconductor field-effect transistors, opto-electronics as in solar cells and solid-state detectors [4–7]. Some of the previous research on the electronic properties of Ni/Ge junctions is the work reported by Peng et al. [8] on the I-V characteristics of Ni/Ge(100) Schottky barrier-based diodes. Peng et al. [8] also reported on some work in which Schottky contacts were rapidly anneal treated at 300–600°C, resulting in nickel germanide-induced strain. Differences in lattice parameters caused the orthorhombic structure of NiGe to induce some epitaxial tensile strain on substrates of Ge. This strain was explained to be a possible cause for an observed increase in Schottky barrier height as the temperature of annealing was raised. Hallstedt et al. [9] studied the phase transformation and sheet resistance of Ni on single crystalline SiGe(C) layer after annealing treatments at 360–900°C. The formation of crystalline Ni(SiGe) was completed at 400–450°C but the thermal stability decreased rapidly with increased Ge amount due to agglomeration (binding of primary particles leading to phase formation). This thermal behavior was shifted to higher annealing temperatures when carbon was incorporated, Ni (SiGeC) layers formed at 500–550°C after which there was Ge segregation to the underlying layer and carbon accumulation at the interface. Thanailakis et al. [10] were able to demonstrate how the Schottky barrier heights of as-deposited Ni/Ge(111) and Pd/Ge(111) are related to the Ge substrate density of surface states and the Ni or Pd work functions, respectively.

Apart from electrical properties, a thorough understanding of the solid-state interactions in metal-germanium systems is required in order to foresee and avoid problems that may be encountered during integration [the process of producing an integrated circuit (I.C.)]. Solid-state interactions in the Ni/Ge system have been extensively studied in the past [1, 2, 11–13], while the Pd/Ge system has received less attention [14–16]. The available reports agree on the second and final phase, NiGe for the Ni/Ge system but there is some disagreement on the first phase. A few researchers report hexagonal $Ni_3Ge_2$ as the first phase [11] but monoclinic $Ni_5Ge_3$ is generally agreed upon by most researchers as the first phase to form [1, 2, 12, 13] and it forms around 150°C. There is an agreement that $Pd_2Ge$ is the first phase to be formed in the Pd/Ge system, the second and final phase to be formed is PdGe. The formation of these phases is generally reported to be sequential [4, 15] but PdGe has been reported to form before the end of $Pd_2Ge$ formation [16]. **Table 1** summarizes the sample preparation, observed phase-formation sequences and some formation temperatures (where available) of the phases in the Ni/Ge and Pd/Ge systems, as reported by some previous researchers.

What is lacking in the previous research done in this area is a quantitative determination of the dominant diffusing species (DDS) during NiGe and PdGe formation and a comprehensive lateral diffusion study of the Ni/Ge and Pd/Ge systems. The DDS during first phase formation,

| Sample preparation | Characterization techniques used | Phase formation | Refs. |
|---|---|---|---|
| Ge(111) wafers were cleaned by piranha ($H_2O_2/H_2SO_4$ = 1:3) before a Ni sputter deposition. Prior to the Ni deposition, the samples were dipped into dilute HF to remove any residual native oxide. A Ni film of about 100 Å thick was deposited onto the wafers at room temperature by sputtering. The base pressure was below $5 \times 10^{-7}$ Torr and the deposition pressure was about $3 \times 10^{-3}$ Torr. | Two annealing methods were used. The first method was rapid thermal annealing (RTA) at 400°C for 60 s in an $N_2$ ambient with a ramp rate of 30°C/s, while the other method was an in situ annealing process at 400°C for 30 min in the Ni sputtering chamber. Samples were characterized by 2D area X-ray diffraction (XRD) with Cu *Kα* radiation and micro-Raman spectroscopy techniques. Cross-sectional transmission electron microscopy (TEM) was employed to study the surface morphology and the interfacial structure of the annealed films. Corresponding elemental information was determined using the energy dispersive X-ray spectrometry (EDS) technique in TEM. | According to the EDS analysis in TEM, two phases, NiGe and $Ni_3Ge_2$, were detected in the RTA method, whereas only the NiGe phase was observed at 400°C in the in situ annealing method. | Jin et al. [11] |
| Several substrate options were overviewed. Ge wet etch behavior was reported in a variety of acidic, basic, oxidizing, and organic solutions, widely used in the microelectronics industry. Modifications of the cleaning procedure suitable for Ge are discussed. The electrical data analyzed was from pMOS devices of 1–2 μm thick Ge on Si wafers. | This work provided an overview of some of the key processing issues for the fabrication of Ge pMOS devices and their impact on performance. Junction leakage behavior as a function of n-type doping, temperature, and electric field for Ge pMOS devices was analyzed. | NiGe germanide voids were reported to form in the active areas of the devices but the use of a two-step rapid thermal anneal (two-RTA) process was shown to suppress these defects. | Brunco et al. [1] |
| Metal films, nominally 30 nm thick, were deposited at room temperature by magnetron sputtering on substrates of crystalline Ge(001) and 200 nm amorphous germanium (*α*-Ge) over 100 nm $SiO_2$ on Si(001) wafers. The Ge substrates were cleaned with dilute HF (100:1). The base vacuum of the magnetron sputtering system was $1.3 \times 10^{-7}$ Pa and the Ar pressure during deposition was maintained at 0.53 Pa. | Metal-Ge reactions were monitored in situ during ramp anneals at 3°C $s^{-1}$ in a purified He atmosphere using time-resolved XRD, diffuse light scattering, and resistance measurements. | NiGe and PdGe phases appeared especially interesting: they exhibited the lowest sheet resistance, formed at low temperature, had limited sensitivity to oxidation and remained morphologically stable over a wide temperature range. The morphological degradation began at 580 and 550°C for NiGe and PdGe, respectively. | Gaudet et al. [2] |
| Thin films of 50 nm polycrystalline Ni were deposited by e-beam evaporation on 500 nm amorphous or polycrystalline germanium (*α*-Ge or *p*-Ge). The reactions were characterized by *ex situ* and in situ XRD using the Bragg–Brentano geometry and a Cu *Kα* source. Isothermal heat treatments were performed in situ | The first phase was carefully investigated by XRD and TEM. Samples at selected stages of reaction were taken out and analyzed *ex situ* by long collection time XRD and examined by TEM both in plane view and cross-sectional samples. | The formation of NiGe was observed during deposition. $Ni_5Ge_3$ was then observed to form. It was shown that the growth of $Ni_5Ge_3$ and NiGe was simultaneous and not sequential, during isothermal annealing. $Ni_5Ge_3$ reached a critical thickness (around 10 nm) before NiGe was able to grow. | Nemouchi et al. [12] |

| Sample preparation | Characterization techniques used | Phase formation | Refs. |
|---|---|---|---|
| at temperatures between 150 and 190°C in vacuum in the $10^{-5}$ mbar range. | | | |
| 100 nm of Ge was evaporated onto thermally oxidized Si wafer substrates, which were 75 mm in diameter. This was followed by a 400 nm deposition of room temperature Ni. The wafers were cleaned using a standard organic solvent and acid etch sequence. | Both temperature ramping and isothermal annealing were performed. Characterization was by XRD, cross-sectional TEM, 4-point kelvin resistance measurements and X-ray photoelectron spectroscopy (XPS). | The reaction path began with the consumption of Ni and Ge to form $Ni_5Ge_3$ and continued with the consumption of $Ni_5Ge_3$ and Ge to form NiGe in the temperature range, 200–300°C. NiGe was the terminal phase with agglomeration (in this case, being the segregation of Ge to the exposed surface) occurring at around 500°C. | Patterson et al. [13] |
| Ni films, 30 nm thick, were deposited at room temperature by magnetron sputtering on substrates of Ge(111), Ge(001), and 200 nm amorphous germanium ($\alpha$-Ge) over 100 nm $SiO_2$ on Si(001) wafers. The Ge substrates were cleaned with dilute HF (100:1). The base vacuum of the magnetron sputtering system was $1.3 \times 10^{-7}$ Pa and the Ar pressure during deposition was maintained at 0.53 Pa. | Ni/Ge reactions were monitored in situ during ramp anneals in a purified He atmosphere using time-resolved XRD, diffuse light scattering, and resistance measurements. | $Ni_5$ $Ge_3$ and NiGe appeared consecutively on Ge(111) while they grow simultaneously on $\alpha$-Ge and Ge (001). Phase-formation temperatures depended strongly on the nature of the substrate being the lowest on $\alpha$-Ge and the highest on Ge(111). | Gaudet et al. [14] |
| Samples were prepared by depositing 1000–3000 Å thick Pd films on large-area Ge(111) and Ge (100) substrates by an electron beam. The Ge wafers were etched in CP4, rinsed in deionized water, and immersed in a solution of HF. Pd was also evaporated on amorphous Ge layers evaporated on silicon oxide substrates. Heat treatment was performed both in vacuum and $N_2$. | The phases were identified by X-ray diffraction and grain size measurements were performed by X-ray diffraction line broadening. Rutherford Backscattering Spectroscopy (RBS) and RBS channeling measurements were also performed to study the structural phase orientation with respect to the substrate lattice. | The hexagonal $Pd_2Ge$ phase was observed at 120°C. Orthorhombic PdGe was observed at higher temperatures and/or longer annealing times. The structure of the compounds was not significantly affected by the nature, either evaporated or single-crystal, of the germanium substrate; however, the kinetics, both for $Pd_2Ge$ and for PdGe, were three to four times faster on amorphous Ge than on single-crystal Ge. | Majni et al. [15] |
| The substrates consisted of Ge (100), Ge(111), polycrystalline Ge wafers, and a 200 nm thick amorphous Ge film that was deposited on an $SiO_2$ wafer using thermal evaporation in a vacuum of $10^{-4}$ Pa. After a short HF dip (20 s), a 30, 100, or 150 nm thick Pd film was sputter deposited in an Ar atmosphere with a pressure of $5 \times 10^{-1}$ Pa. | Samples were characterized by means of in situ XRD and laser light scattering (LLS). The kinetics of the Pd/Ge solid-state reaction was performed in which the thickness of the growing Pd germanides was monitored using in situ RBS. | The first germanide that is observed during the Pd/Ge solid-state reaction is the $Pd_2Ge$ phase at 200°C This phase grows up to 270°C at which temperature, the entire Pd film was consumed. The $Pd_2Ge$ phase then became the seeding layer for the growth of the PdGe phase which was stable up to its melting temperature of 725°C. | Knaepen [16] |

**Table 1.** Summary of the sample preparation and observed phase-formation sequence and some formation temperatures (where available) of the phases in the Ni/Ge and Pd/Ge systems, as reported by some previous researchers.

that is, formation of $Ni_3Ge_2$ and $Pd_2Ge$, has been reported. Palladium is reported to be DDS during $Pd_2Ge$ formation, contributing about two-third toward diffusion [17], while Ni appeared to be the sole moving species during the formation of the first nickel germanide phase, $Ni_3Ge_2$ [18]. The literature appears to be lacking in information regarding the diffusing species during the formation of subsequent phases in both the Pd/Ge and Ni/Ge systems. It has however been proposed that during NiGe formation in certain thin film configurations, Ge could be the DDS [19]. As mentioned earlier, NiGe and PdGe are the most promising candidates for ohmic contacts in germanium-based technology [2, 3].

The approach of our study, as presented in this chapter, is essentially twofold. Firstly, solid-state reactions were thermally induced in conventional nano-metric thin film couples of the Ni/Ge and Pd/Ge systems in order to study the sequence of phase formation in these two germanide systems. Conventional thin film couples were also used to identify and monitor the dominant diffusing species during the phase formation. By embedding a thin layer of tantalum (Ta) or tungsten (W) as an inert marker between coupling thin film Ni/Ge or Pd/Ge layers, the atomic transport across this marker layer could be monitored by observing the movement of the marker during phase formation. It is important, for device integrity, to identify the DDS during the formation of the respective germanides as this can influence their thermal stability. Excessive diffusion of the substrate element, in this case Ge, during germanide formation could result in overgrowth and bridging in devices, which would have a detrimental effect on their performance [20].

Secondly, lateral diffusion couples were prepared by the deposition of thick rectangular islands of one material on top of a much thinner film of another material. Upon annealing, the island-material would react with the underlying film through vertical diffusion. The natural phase-formation sequence of the system is followed up to the phase that has the highest proportion of island-material. At this point, the vertical diffusion gives way to lateral diffusion because there can be no further reaction between the island-material and the thin film material directly below it. The lateral diffusion may result in the phase that is most island-material rich to grow outward into the surrounding thin film. This phase would eventually reach a critical growth length where it would then give way to the lateral growth of other phases, simultaneous growth of a number of lateral phases of often observed. This multiple phase formation is not common in conventional thin film couples but is typical of bulk diffusion couples; therefore lateral diffusion couples offer a transition between these two types of behavior. The amount of material that is deposited in the island region of a lateral diffusion couple is relatively large. This allows one to carry out a more extensive investigation of phase formation and reaction kinetics than can be achieved using ordinary planar thin films. Bulk diffusion couples can be simulated using lateral diffusion structures because in the latter structures, phase formation could extend to length of around 100 μm [21]. In kinetic studies of thin film planar structures, the diffusion lengths are typically less than 0.5 μm. One can therefore study the transition from thin film to bulk diffusion couple behavior. The study of lateral diffusion couples is particularly well suited for dealing with the challenges of achieving the required lateral abruptness of semiconductor junctions. Various early techniques were developed to study lateral diffusion couples [22–31]. In later studies, microprobe-Rutherford backscattering spectrometry (μRBS) was used to study them [21, 32, 33]. The major advantage of this technique is its ability to give depth information.

## 2. Experimental summary

Conventional thin film couples for the Ni/Ge study were prepared using electron beam evaporation at a pressure of $10^{-7}$ Torr. The deposition technique used to prepare the thin film samples for the Pd/Ge study was sputtering at a pressure of $10^{-6}$ Torr. Ge(100) substrates were chemically cleaned in a procedure that ended with a 2% HF dip before being loaded for evaporation. The inert marker used for the Ni/Ge investigation was a 0.5 nm thick layer of Ta. The Pd/Ge marker study was carried out using a 0.3 nm thick layer of W. Since NiGe and PdGe phase formation takes place around 250–350°C, whereas Ta only begins to react with Ge at temperatures above 750°C and W does not appear to react with Ge at all (at least to temperatures of up to 900°C) [2], both Ta and W should remain chemically inert during the formation of the various germanide phases.

Instead of using the conventional approach, where different thermal anneals are performed on similar specimens after which the position of the marker is determined, we have performed the thermal anneal and measurement simultaneously using real-time Rutherford Backscattering Spectrometry (RBS). Using this method, only one sample can be used to monitor the position of the marker during the whole reaction process. In this way, one is able to identify the diffusing species more accurately because it eliminates the small variations that always exist between samples. Real-time RBS is able to determine any variations in the relative contributions of the diffusion of each atomic type as the reaction proceeds. RBS has the useful capacity of being able to give depth information of atomic composition thereby making it possible to monitor the position of the marker, between coupling layers, during phase formation. Real-time RBS data were collected during a ramped annealing rate of 2°C/min for the Ni/Ge system and a rate of 1°C/min for the Pd/Ge system. An ion beam of 2 MeV alpha particles was used to produce the RBS data, which were recorded in 30-s intervals during annealing. Statistical improvement of the results was achieved by grouping the data such that each group provided a statistically averaged spectrum within a temperature range of 4°C in the Ni/Ge investigation and 2°C in the Pd/Ge study. RUMP software [34] was used for the analysis of the RBS data. In a number of our figures, we use the thickness units of atoms/cm$^2$ because they are easier to work with in RBS-related studies of atomic diffusion than the conventional units of nm. The two units are interchangeable in that by dividing the values in atoms/cm$^2$ by the atomic concentration of a layer one gets a thickness in cm, which is then converted to nm.

For the Ni/Ge investigation, a single detector positioned at a backscattering angle of 165° was used and the sample was rotated by 50° with reference to the direction of the incident alpha particles, the depth resolution is improved in this way. The atomic masses of Ni and Ge are relatively close resulting in peak overlap between the Ni and Ge RBS spectra. This is more so if Ni is on the top of Ge because the atomic mass of Ni is smaller than that of Ge. Ordinarily, this would make the RBS analysis problematic but the Ni/Ge system only has two phases $Ni_5Ge_3$ and NiGe, which can be resolved using careful RUMP simulation. The Ni/Ge system, on the other hand, has the advantage that the small peak from the thin Ta marker is not close to the Ni or Ge peaks.

In the Pd/Ge system, Pd and Ge peaks do not overlap but the small peak of the W marker is close to the Pd peak. For this reason, the thickness of the Pd layer had been relatively small and it was necessary to mount a second RBS detector. The first detector was placed at a scattering angle of 165° and the sample normal rotated by 30° to the $He^+$ beam direction toward the detector. With this geometry, it was possible to separate the W marker signal from the Pd signal, but the depth resolution was compromised. A second detector was therefore placed at a scattering angle of $-135^\circ$, which produced a scattering outgoing beam angle of $75^\circ$ with respect to the normal of the surface. This geometry of the second detector improved the depth resolution for determining the thickness of various layers of phases; however, the second detector could not determine the position of the W marker because the geometry resulted in an overlap between the Pd and W peaks. The spectrum from the second detector was therefore used to determine the thicknesses of the various palladium germanide phases, while that from the first detector establish the depth of the W marker in the layers. Combining the information obtained from the two detectors in this way enabled the thickness of the various phases to be measured with reasonable confidence, while at the same time determining the depth of the marker in the sample.

The lateral diffusion couples were prepared by electron beam evaporation at a base pressure in the low $10^{-5}$ Pa range. Thermally oxidized single crystal silicon wafers with a (100) crystal orientation were used as substrates in all studies. The reaction of $SiO_2$ with Ge, Ni, or Pd was insignificant at the annealing temperatures used; hence, the substrates were "inert." A thin film of one material was deposited first. Without breaking the vacuum, an ordinary silicon wafer with an array of 390 × 780 $\mu m^2$ rectangular windows (referred to as a silicon mask) made by photolithographic techniques and selective etching, was thereafter placed close to the surface of the thin film that was deposited first. A second material was then deposited through the rectangular windows in the silicon mask to form islands of the second material on thin films of the first material. After removing the samples from the evaporation chamber, they were cleaved into 12 parts, which were later annealed and analyzed.

The samples were examined using scanning electron microscopy (SEM) to distinguish the various reaction regions and measure their diffusion lengths. Representative samples were selected for further analysis by μRBS. The distribution of elements as a function of lateral position was obtained using μRBS. This technique also provided information regarding the elemental distribution as a function of depth and the thickness of the films. 2 MeV alpha particles were focused to a beam size of about 1 × 1 μm using a nuclear microprobe and scanned across an area of the samples, which was chosen in such a way as to include all reaction regions identified using SEM. The size of the scanned area was about 400 × 400 $\mu m^2$. The samples were placed in such a way that the alpha beam scanned parallel to the edge of the original interface between the island and surrounding film. This avoided any compositional variations along the line scanned by the beam. About 128 RBS spectra were collected along each line scanned and these were summed to improve statistics. About 128 lines were scanned parallel to the original island interface, which resulted in RBS data being recorded as a function of lateral position. RUMP simulation was used to analyze the data.

## 3. Results

### 3.1. Ni/Ge system

*3.1.1. Thin film couples*

The thin film sample used to investigate the relative contributions of each atomic species to the diffusion process in the Ni/Ge system was prepared with the configuration: Ge(100)/Ta (0.5 nm)/Ni(76.5 nm). If this sample configuration is annealed, one would expect to observe the Ta marker moving toward the surface, if Ni were the dominant diffusing species during the formation of $Ni_5Ge_3$. If Ge was the dominant diffusing species, then the marker would move into the sample away from the surface. **Figure 1** shows the real-time RBS results during a ramped anneal at a rate of 2°C/min.

**Figure 1(a)** shows a stacking up of RBS spectra obtained during the annealing as a function of temperature producing a "surface" plot. The small Ta marker peak is seen around channel 405. The Ni and Ge signals are at channels below the Ta channel position. The Ta marker moves to

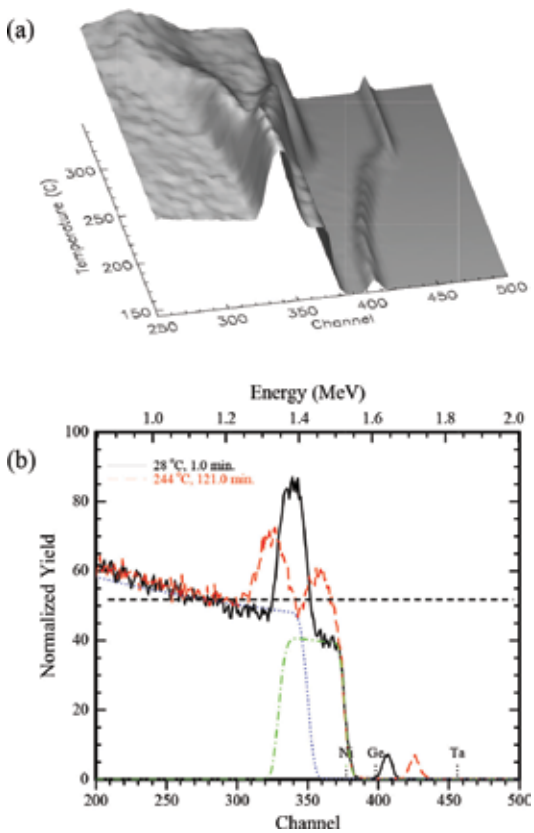


**Figure 1.** (a) Surface plot of RBS spectra obtained after the annealing of a Ge(100)/Ta/Ni sample at 2°C/min, the movement of the Ta marker to higher energies during the thermal anneal is clearly visible in the figure. (b) Individual as-deposited and 244°C RBS spectra with simulations showing the contribution of the Ni (lower dashed line) and Ge (dotted line).

higher channels as the temperature is increased indicating that Ni was the dominant diffusion species.

**Figure 1(b)** shows a spectrum from the as-deposited sample, which is similar in form to the front spectrum in **Figure 1(a)**, since there is a very little reaction below 150°C. **Figure 1(b)** also shows a spectrum, which was captured during the reaction around 244°C. The Ge, Ni, and Ta surface positions are indicated in the figure. The separate contributions of the Ge and Ni peaks to the spectrum from the as-deposited sample were simulated using RUMP and are also shown in the figure. It can be seen that the Ge and Ta signals appear at lower positions than their surface positions because there is a layer of Ni above them. The shoulder at the high energy end of the Ni signal is at the surface position as would be expected. The peak around channel 340 is due to the overlap between the back of the Ni signal and the front of the Ge signal. The Ni diffuses deeper into the sample as the reaction proceeds while the Ge diffuses toward the surface. This causes the overlap peak to split into two as seen in the spectrum collected at a temperature of 244°C.

An analysis of the individual RBS spectra indicated that the formation of $Ni_5Ge_3$ below the marker began around 155°C. As the reaction proceeded, the $Ni_5Ge_3$ phase continued to grow below the marker until around 200°C. When the $Ni_5Ge_3$ layer grew to a thickness of 14.2 nm, the NiGe phase started to appear below the marker between the Ge substrate and the $Ni_5Ge_3$ layer. As the temperature was increased, the two phases grew simultaneously. At around 265°C, about 55% of the Ni was consumed and at this point, the thickness of the layers of $Ni_5Ge_3$ and NiGe were 38.4 and 18.1 nm, respectively.

The Ta marker is observed to be at the surface position in the final spectra. Since, all the NiGe formed was below the marker, it is obvious that the marker movement was solely due to the growth of $Ni_5Ge_3$. We therefore conclude that Ni was the only diffusing species during the formation of $Ni_5Ge_3$. If there had been any Ge diffusion, then the Ta marker would not have been at the surface position after all the Ni had been consumed.

Since the growth of NiGe was below the marker, it was not possible to determine the dominant diffusing species during the formation of this phase. A sample with a different configuration was needed in order to study the relative diffusion of Ni and Ge during the formation of the phase NiGe. The configuration of the sample prepared for investigating the growth of NiGe was: Ge(100)/Ta(0.5 nm)/Ge(49 nm)/Ni(47 nm). Upon annealing this sample, there should be a reaction between Ni and Ge deposited on top of the Ta. **Figure 2** is a schematic diagram illustrating the various stages of this reaction.

As illustrated in **Figure 2(b)**, the sample was designed to make sure that after all the deposited Ge was consumed forming $Ni_5Ge_3$, there would still remain some Ni above the marker (about 7.5 nm of Ni). This $Ni_5Ge_3$ cannot be converted into NiGe while there is still some unreacted Ni above the marker. The only way that the reaction can continue is by the Ni above the marker reacting with Ge below the marker. Since we have established that Ni is the only diffusing species during the formation of $Ni_5Ge_3$, we would expect Ni to diffusing across the marker presumably to form $Ni_5Ge_3$ below, this is illustrated in **Figure 2(c)**. The abundance of Ge below the marker means that the $Ni_5Ge_3$ below would react with Ge thereby converting into the more Ge rich phase NiGe, this is illustrated in **Figure 2(d)**. One can then study the diffusing species

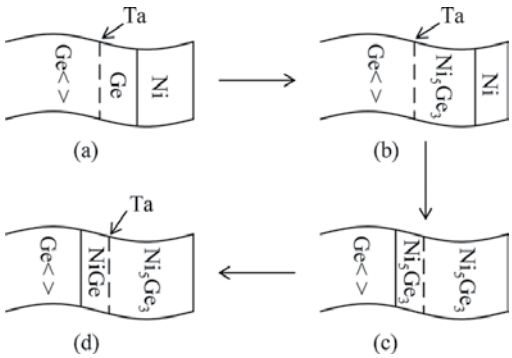


**Figure 2.** Schematic diagram showing the sample configuration used to determine the dominant diffusing species during NiGe formation. Upon heating, Ni first reacts with the Ge deposited on top of the marker and then the remaining Ni, after all the Ge on top of the marker has been consumed, diffuses past the marker [35].

during the formation of NiGe by monitoring the marker movement as $Ni_5Ge_3$ is converted into NiGe. **Figure 3** shows the ramped real-time RBS results of the thickness evolution of each layer as a function of temperature, as analyzed using RUMP.

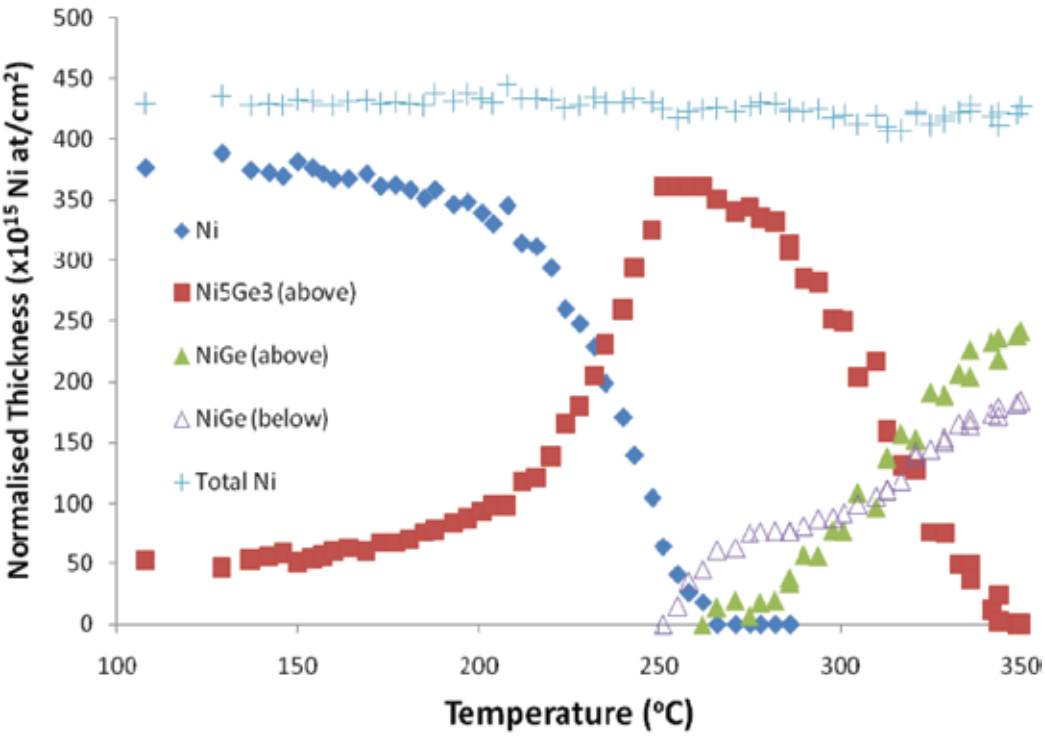


**Figure 3.** Experimental results showing the thickness of the various layers formed during the ramped annealing of the Ge(100)/Ta/Ge/Ni sample. The thickness of each layer is expressed in Ni atoms/cm$^2$ for normalization. With this format, the total Ni thickness remains constant throughout the process making it easier to determine the relative proportion of each layer formed [35].

*3.1.2. Lateral diffusion couples*

The lateral diffusion couples prepared with thick Ni islands on thin Ge films showed very limited lateral diffusion upon annealing. The reaction did not proceed beyond a certain point despite annealing at high temperatures and for long periods of times. The reaction region was too narrow to properly resolve and monitor, this is a qualitative indicator that Ni was not a DDS for lateral phase growth in the Ni/Ge system. The reverse configuration with Ge islands (200 nm thick) on Ni films (36 nm thick) showed substantial lateral diffusion indicating that Ge is the DDS during lateral phase growth in the Ni/Ge system. **Figure 4(a)** shows an optical micrograph of part of a Ge island on a sample that was annealed at 500°C for 2 h. The darkened rectangular area on the right end of the island is the area that was scanned with the nuclear microprobe. **Figure 4(b)** is an SEM micrograph covering the various reaction zones of the sample shown in **Figure 4(a)**.

There are five reaction regions observed in **Figure 4** and they are label from A to E. The region labeled A is the original Ge island region, while E is the region of the unreacted Ni film. The regions labeled from B to D are phase regions produced during the thermal annealing of the sample. There is no well-defined boundary seen in **Figure 4(b)** between the regions C and D but region D clearly appears coarser than region C.

**Figure 5(a)–(d)** shows the representative measured RBS spectra extracted from each of the four reaction regions A–D in the sample annealed at 500°C for 2 h, together with their RUMP simulations; thickness is in units of $10^{15}$ atoms/cm$^2$.

The simulations show that region A comprised of NiGe overlaid by unreacted Ge while regions B, C, and D consisted of exposed NiGe, $Ni_3Ge_2$, and $Ni_5Ge_3$, respectively. The original island interface is between the NiGe and $Ni_3Ge_2$ phases.

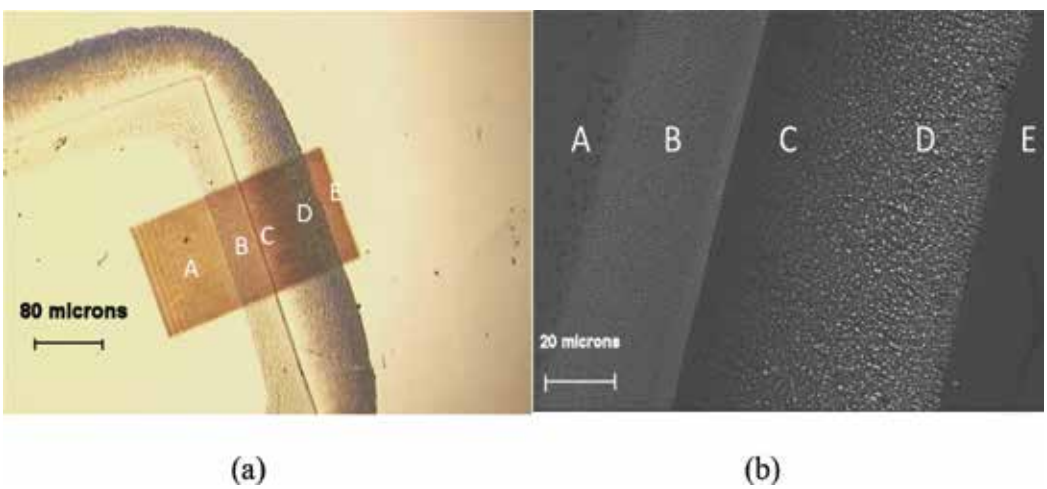


**Figure 4.** (a) An image obtained using an optical microscope showing one end of an island after annealing at 500°C for 2 h. (b) A micrograph showing five regions obtained using SEM on the same island shown in (a) [36].

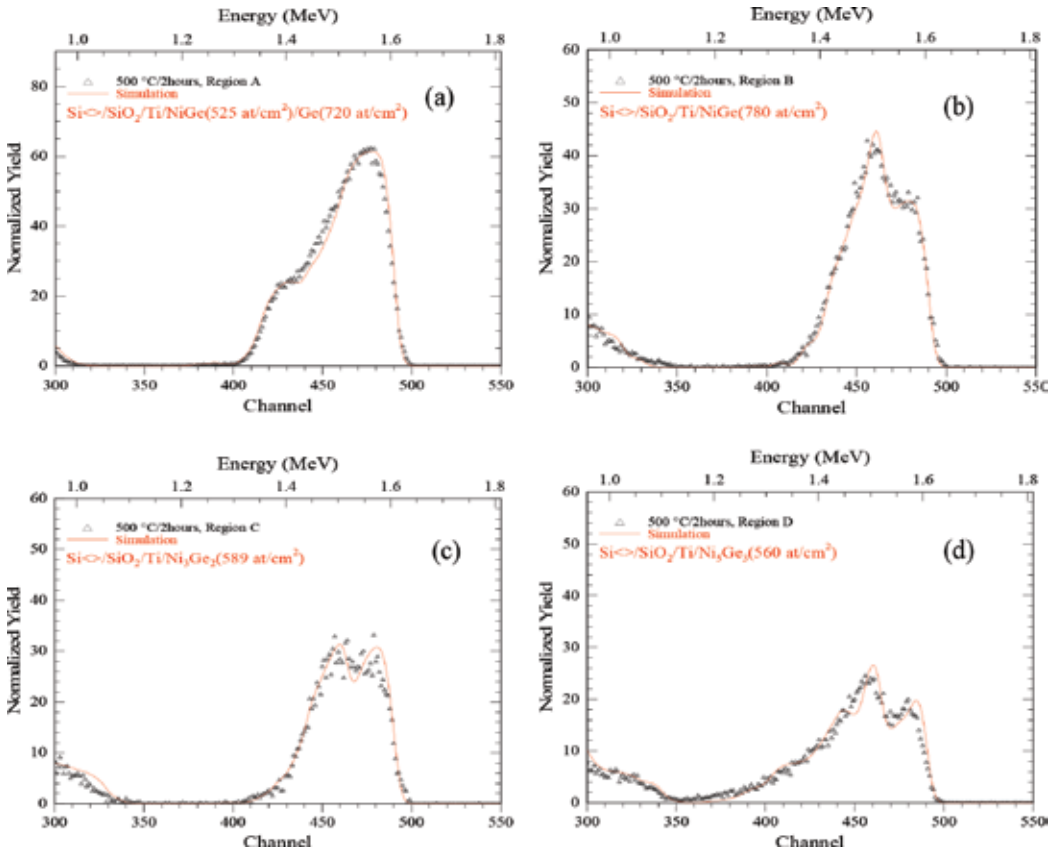


**Figure 5.** (a)–(d) show representative RBS spectra extracted from each of the four reaction regions A–D in the sample annealed at 500°C for 2 h, together with their RUMP simulations with thickness in units of $10^{15}$ atoms/cm$^2$.

### 3.2. Pd/Ge system

#### *3.2.1. Thin film couples*

The sputtered particles during the preparation of the thin film sample to investigate the relative contributions of each atomic species to the diffusion process in the Pd/Ge system had incident energies between 10 and 20 eV. This resulted in a degree of mixing of the sputtered particles with the substrate below the marker. It was detected using RBS analysis on the sample immediately after deposition (before any annealing) that some Pd atoms had penetrated through the atoms of the thin layer of W atoms into the region of the substrate Ge atoms. The configuration of the as-deposited sample was then: Ge(100)/$Pd_xGe$/W(0.3 nm)/Pd(42.5 nm). After RUMP simulation of this sample, it was found that the $Pd_xGe$ layer could have been a 4 nm layer of $Pd_2Ge$. **Figure 6** shows the real-time RBS results during a ramped anneal at a rate of 1°C/min.

A schematic diagram summarizing results obtained is shown in **Figure 7**.

As the reaction commenced at around 150°C, the phase $Pd_2Ge$ was formed on both sides of the marker as shown in **Figure 7(b)**. PdGe was formed around 180°C below the marker

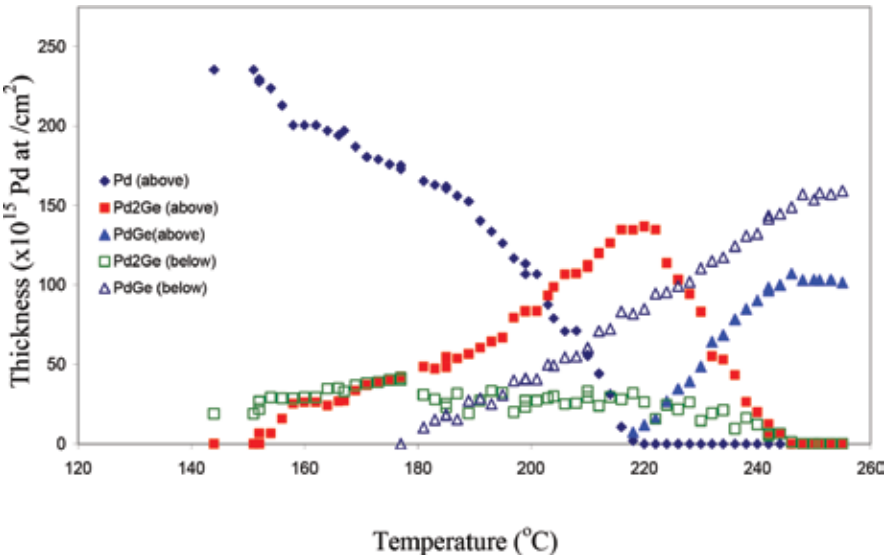


**Figure 6.** Plot showing the thickness of the various layers during the ramped thermal annealing of the Ge(100)/W/Pd sample. $Pd_2Ge$ growth above and below the marker commences around 150°C. The PdGe phase first appears below the marker at around 180°C, and it appears above the marker at around 220°C, once all the Pd has been consumed [35].

between the Ge substrate and $Pd_2Ge$ and Ge substrate, as shown in **Figure 7(c)**. It can be seen from **Figure 6** that $Pd_2Ge$ was slightly consumed during the initial growth stages of PdGe. As temperature was increased, $Pd_2Ge$ continued to grow above the marker while PdGe grew below the marker. At a temperature of around 220°C, the unreacted Pd was completely consumed and most of the phase below the marker was PdGe as shown in **Figure 7(d)**. The next stage of the reaction was the conversion of $Pd_2Ge$ above the marker into PdGe. Above 220°C, the phase PdGe was present both below and above the marker as seen in **Figure 6**. **Figure 6** also shows that the reaction ended at a temperature of around 250°C.

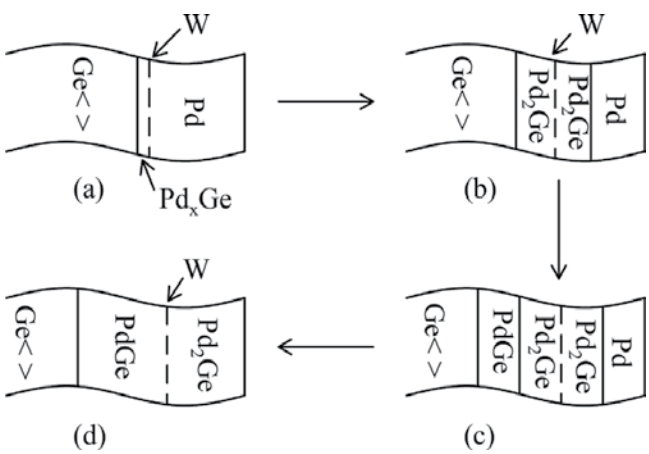


**Figure 7.** Schematic diagram summarizing the results obtained during the ramped thermal anneal of the Ge(100)/W/Pd sample.

*3.2.2. Lateral diffusion couples*

Samples for the lateral diffusion study of the Pd/Ge system were prepared by deposition of Ge islands (100 nm thick) on Pd films (20 nm thick). This configuration was chosen because the lateral diffusion couple results with Pd islands on Ge films showed little lateral diffusion upon annealing with a reaction region that was too narrow to resolve and monitor properly, indicating that Pd was not the DDS during lateral phase growth in the Pd/Ge system. Several lateral diffusion samples were annealed at various temperatures for different lengths of time. The Pd/Ge system exhibited relatively low temperature reaction. It was therefore necessary to carry out the investigation for this system at much lower temperatures than those used for the Ni/Ge systems. **Figure 8** shows an SEM micrograph of one representative sample with a 100 nm thick Ge island on a 20 nm thick Pd film, annealed at 325°C for 2 h, showing three distinct regions labeled A–C.

Areas which were chosen to include all the reaction regions observed were scanned on the nuclear microprobe for analysis by μRBS. A spectrum picked from each of the three regions of the Pd/Ge lateral diffusion sample is shown in **Figure 9**.

The spectrum from region C shows a peak of unreacted Pd and no Ge. The peak height of the spectrum taken from the region B shows the phase $Pd_2Ge$. This phase is seen at the surface position. From the solid line in the figure, it can be seen that the region A consisted of unreacted Ge and PdGe.

The solid line shows the spectrum form the original island region. This spectrum has a Pd peak at the surface position indicating that there was some Pd at the surface of the original island region. The fact that this Pd peak has what is labeled as a shoulder in **Figure 9** means that there was much less Pd at the surface of the region than deeper down. It therefore means that the region consisted of PdGe in the depth of the sample but toward the surface the PdGe phase was mixed with unreacted Ge making the Pd concentration much less.

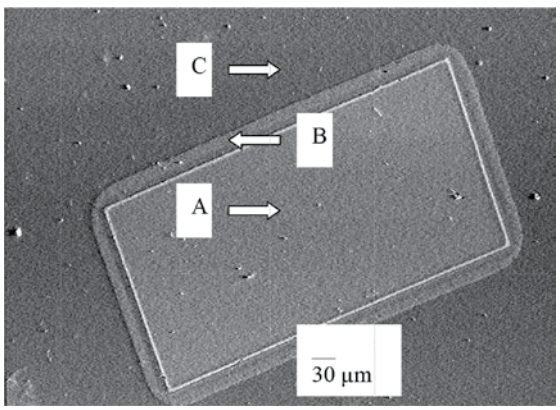


**Figure 8.** SEM micrograph of a Ge island (100 nm) on a Pd film (20 nm) annealed at 325°C for 2 h showing the different reaction regions.

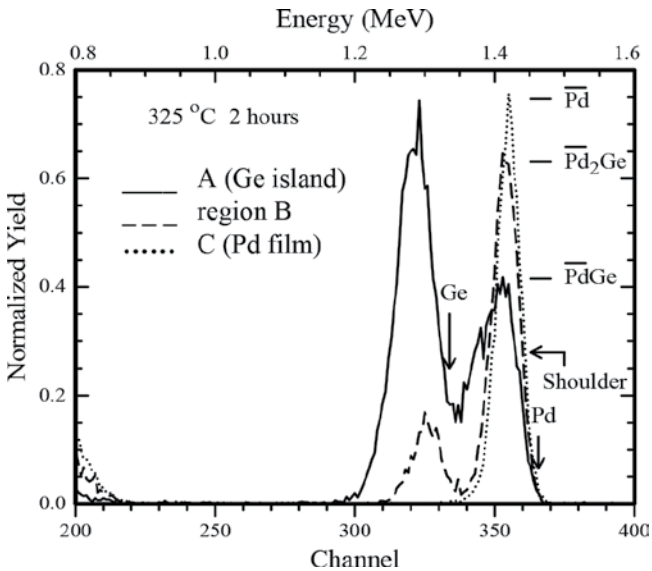


**Figure 9.** Superposition of selected RBS spectra from each of the regions of the Pd/Ge lateral diffusion sample. Pd peak heights of the various phases and surface positions of Ge and Pd are indicated.

## 4. Discussion

### 4.1. Thin film couples

The ideal case in marker studies is that the marker material should not have any effect on the formation of phases in the coupling materials. Ta and W appeared to be good choices of marker materials in that they did not react with Ge in the temperature ranges studied. An investigation was carried out during this work to see if the marker had any effect on the phase formation particularly at the beginning of the reaction. The temperature at which the reaction started in samples with a marker between the coupling layers was compared to the reaction onset temperature with no marker between the layers. It was found that the start of the reaction was delayed by a temperature of less than 10°C when the marker was present. This meant that although the marker acted as a sort of reaction barrier between coupling layers, its effect was not large enough to have any significant effect on the results of this study, in terms of the temperature of the first phase formation. Subsequent phases were expected to start forming when the supply of unreacted atoms to the growth interface reduced a level below some characteristic critical point [37]. The phase-formation sequence is not always expected to be straight forward because some cases of simultaneous phase growth have been report, as in the phases $Ni_5Ge_3$ and NiGe on Ge(100) substrates [38].

It was clear from the results of our thin film study that Ni was the only diffusing species during the formation of the first phase in the Ni/Ge system, $Ni_5Ge_3$. We now discuss the diffusing species during the formation of the second phase which is formed in the Ni/Ge system, NiGe.

It can be seen in **Figure 3** that the total amount (both reacted and unreacted) of Ni atoms/cm$^2$ remains constant throughout the reaction. One of the advantages of presenting the layer thickness in atoms/cm$^2$ units (as opposed to nm) is that this total amount remains constant for each element throughout the reaction, which provides an easy way of checking the consistency of the results at each temperature. It is seen in **Figure 3** that the reaction above the marker started at a much lower temperature than the reaction observed in the earlier marker investigation to establish the diffusing species during the formation of $Ni_5Ge_3$. It is likely that this is because in this case there is no Ta barrier between the coupling layers of Ni and Ge as was the case in the earlier investigation. In fact, room temperature reaction has been reported in the Ni/Ge system [39], in such a case where there is no barrier between the Ni and Ge layers.

The Ge above the marker was all converted in to $Ni_5Ge_3$ by the temperature of 250°C. The unreacted Ni then diffused across the marker to react with the Ge below. After the consumption of all the Ni, the $Ni_5Ge_3$ both below and above the marker both started to be converted into NiGe.

The conversion of $Ni_5Ge_3$ to NiGe above the marker could take place by either of the two reaction processes. Firstly, there is the decomposition reaction, $Ni_5Ge_3 \rightarrow 3NiGe + 2Ni$, where two Ni atoms are released, which then diffuse across the marker to react with the Ge in the substrate. If the NiGe formed below and above the marker were purely as a result of this reaction, then Ni would be the sole diffusing species during NiGe formation. This 100% Ni diffusion driven reaction would mean that three NiGe molecules would be formed above the marker for every two NiGe molecules formed below. A second possible reaction for the formation of NiGe above the marker is $Ni_5Ge_3 + 2Ge \rightarrow 5NiGe$. This would require that Ge diffuses across the marker to react with the $Ni_5Ge_3$ above. In all, we therefore see that the NiGe formed above the marker could be as a result of the diffusing of Ni, Ge, or both. The NiGe formed below the marker could only be due to Ni diffusion. In **Figure 10**, the NiGe formed above the marker is plotted against the total amount of NiGe formed.

Predicted plots for 100% Ni and 100% Ge diffusion are included as a dashed and dotted line respectively. The offset from the origin along the horizontal "total amount of NiGe" axis is

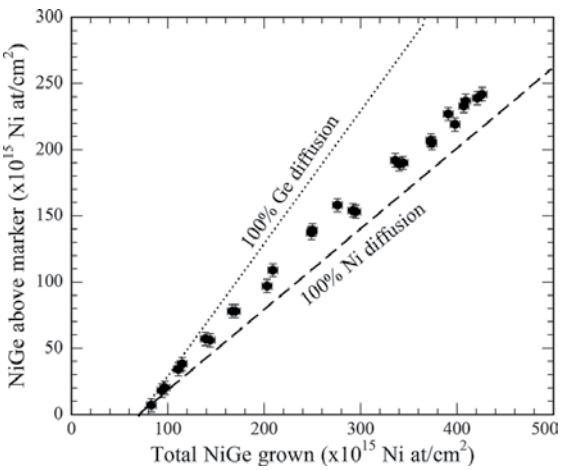


**Figure 10.** A plot of NiGe formed above the marker against the total amount of NiGe formed. Predicted plots for 100% Ni and 100% Ge diffusion are also included as a dashed and dotted line respectively [35].

because NiGe was initially formed by a reaction with unreacted Ni from the surface and not by the conversion of $Ni_5Ge_3$ into NiGe. It can be seen from **Figure 10** that both Ni and Ge diffuse during the formation of NiGe. The diffusion of Ge is dominant in the initial stages of the reaction but Ni diffusion becomes the prominent growth mechanism thereafter.

In our thin film study of the Pd/Ge system the results showed that during a large part of the reaction the W marker lay between two $Pd_2Ge$ layers as shown in **Figure 7(c)**. This was before the total consumption of the unreacted Pd. Pd and Ge diffusion during the formation of $Pd_2Ge$ can therefore be studied by monitoring the marker movement during this initial period. This part of the analysis does not include the reaction after all the Pd is consumed. Interestingly we will demonstrate later that the reaction after all Pd is consumed can be used to study the diffusing species during the formation of the second phase, PdGe.

**Figure 11** shows the growth of $Pd_2Ge$ above the maker as plotted against the $Pd_2Ge$ formed below which also took into account the $Pd_2Ge$ which had been converted into PdGe.

The three initial data points have been excluded during the plotting of the dashed line in **Figure 11**. This is because the initial stages of the reaction were complicated by the Pd which was deposited below the W marker during the sputter deposition. When one takes into account the fact that one Ge atom which diffuses across the marker forms one $Pd_2Ge$ molecule above the marker whereas it takes two Pd atoms to diffuse across the marker to form one $Pd_2Ge$ molecule below, then the best fit straight line through the data in **Figure 11** corresponds to Ge diffusion of about 40% and Pd diffusion of 60%.

If we look back at **Figure 7(d)** we see that this is the sample configuration at the point when the unreacted Pd is totally consumed. **Figure 7(d)** shows the marker at a position between PdGe and $Pd_2Ge$. There are two possible ways in which the reaction above the marker could proceed after this point. The first is for Ge atoms from the substrate below to diffuse across the marker

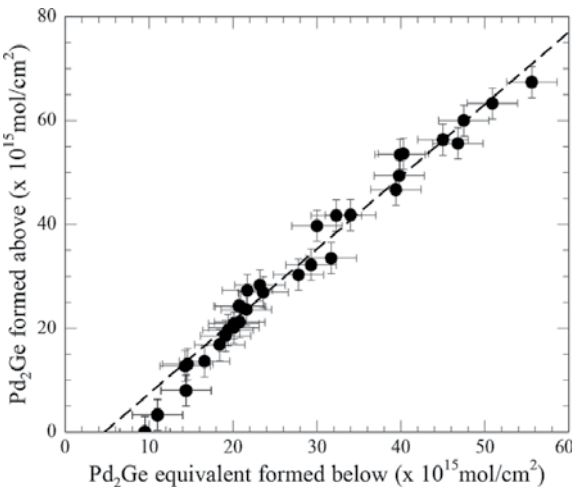


**Figure 11.** The growth of $Pd_2Ge$ above the maker plotted against the $Pd_2Ge$ formed below which also takes into account the $Pd_2Ge$ which had been converted into PdGe. The dashed line, drawn through the uniform region (i.e., the line excludes the initial three data points), indicates that Pd is the dominant diffusing species during $Pd_2Ge$ growth with a contribution of about 60%.

and react with $Pd_2Ge$ converting it into PdGe. The other reaction could be the breaking down of $Pd_2Ge$ producing PdGe and Pd. The Pd could then diffuse across the marker to react with the Ge below forming PdGe. We therefore get PdGe both below and above the marker, this is seen in **Figure 6**. The data acquired during the stage of the reaction after all Pd was consumed can therefore be used to study the diffusing species during the formation of PdGe. According to the reaction, $Pd_2Ge + Ge \rightarrow 2PdGe$, every Ge atom that diffuses across the marker from below will produce two PdGe molecules above the marker. From $Pd_2Ge \rightarrow PdGe + Pd$, we see that every Pd atom that diffuses across the maker from above will leave a PdGe molecule above and form another one below the marker. Any increase in the total amount of Ge above the marker could only be due to Ge diffusion from below. Any increase in the total amount of Pd below the marker could only be due to Pd diffusion from above. **Figure 12** is a plot of the total amount of Ge above the marker versus the total amount of Pd below the marker during the stage of the reaction after all unreacted Pd was consumed.

More scatter in found in this data set than for $Pd_2Ge$ growth, but because of the relatively large number of readings obtained during real-time growth of the final phase the uncertainty is reduced, with the plot giving $65 \pm 3\%$ Pd diffusion during PdGe growth.

### 4.2. Lateral diffusion couples

As seen in **Figure 4(a)** and **(b)**, the interface between the regions C (consisting $Ni_3Ge_2$) and D (consisting of $Ni_5Ge_3$) was not distinct in the SEM and optical micrographs. It could only be determined using microprobe RBS. The available "beam time" on the microprobe was however not sufficient to analyze all our lateral diffusion samples. The growth lengths of these two regions were therefore combined during our analysis of the growth kinetics. Plots of reaction length against annealing time for the temperatures 300, 400, and 500°C were made. **Figure 13** shows the plot for 400°C.

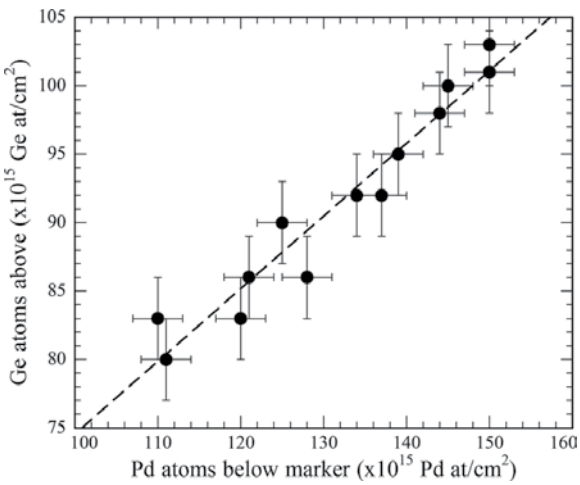


**Figure 12.** A plot of the total amount of Ge above the marker as a function of the total amount of Pd below the marker as $Pd_2Ge$ transforms into PdGe, after all unreacted Pd is consumed. The gradient of the plot indicates that around 65% Pd diffusion took place during PdGe formation.

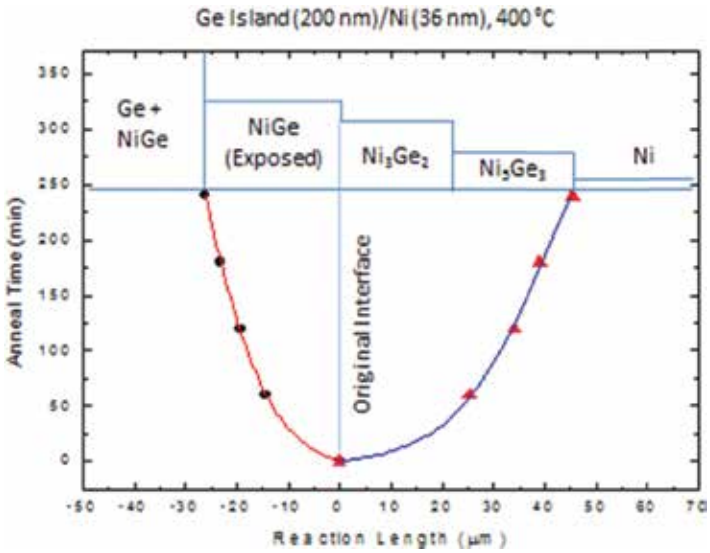


**Figure 13.** A plot of the reaction lengths of the phases against time of annealing at a temperature of 400°C. A parabolic dependence of compound growth with annealing time is observed.

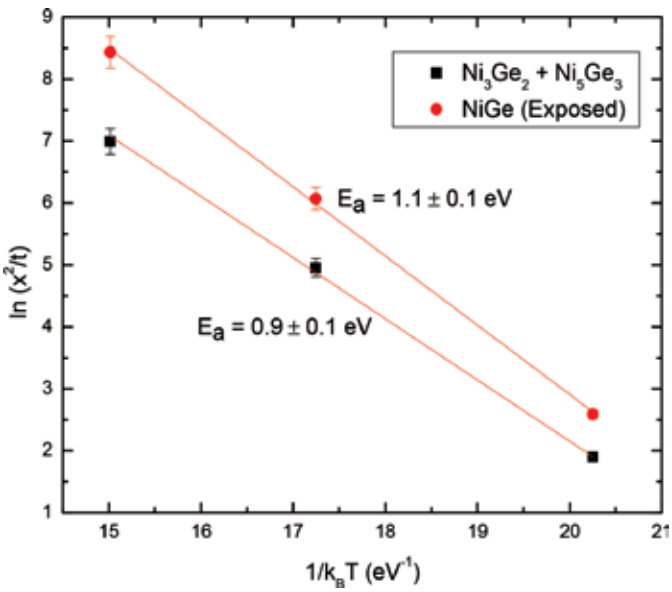


**Figure 14.** An Arrhenius plot for the combined lateral growth of $Ni_3Ge_2$ and $Ni_5Ge_3$ giving an activation energy of 0.9 ± 0.1 eV and another giving an activation energy of diffusion for Ge in NiGe as 1.1 ± 0.1 eV.

A parabolic dependence of compound growth with annealing time is observed. At every temperature, $T$ the width, $x_\beta$ of each phase region was measured. The values of the widths obtained were squared and plotted as a function of the corresponding periods of time, $t$ that the samples were annealed for at the particular temperature. The slopes of these graphs gave the diffusional

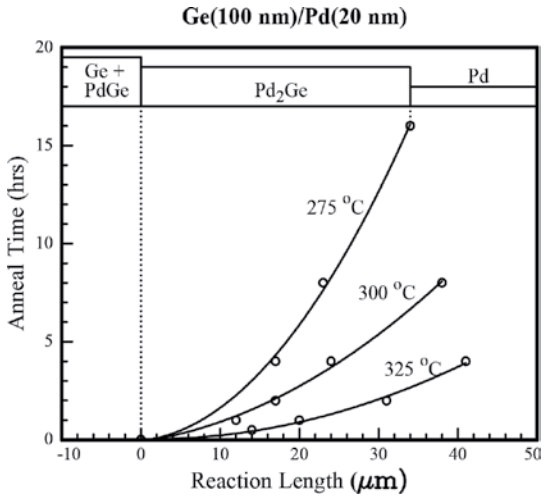


**Figure 15.** A plot of reaction length against the time of annealing for the phase $Pd_2Ge$ at temperatures 275, 300, and 325°C.

growth constants, $K_\beta = x_\beta^2/t$ . Arrhenius plots were then produced by plotting the logarithm of the diffusional growth constants versus the reciprocal of the product between the Boltzmann constant and the absolute temperature (i. e. $1/k_BT$), the results are presented in **Figure 14**.

From the slopes of these plots, the activation energy of diffusional growth for the combined lateral growth of $Ni_3Ge_2$ and $Ni_5Ge_3$ was determined to be $0.9 \pm 0.1$ eV while that corresponding to the rate of exposure of NiGe was $1.1 \pm 0.1$ eV.

The two phases, PdGe and $Pd_2Ge$, which were observed to form in the thin film study of the Pd-Ge system were also the only two observed in the lateral diffusion couples. The growth region outside the original island interface, labeled as region B in **Figure 8**, consisted of the phase $Pd_2Ge$. The original island region, labeled as region A in **Figure 8**, consisted of PdGe at the bottom while

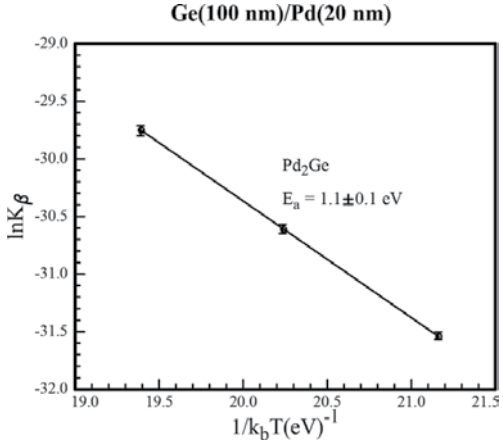


**Figure 16.** Arrhenius plot, $\ln K_\beta$ versus $1/k_bT$, showing temperature dependence of Ge diffusion rate through $Pd_2Ge$, yielding an average activation energy of $1.0 \pm 0.1$ eV.

at the top there was unreacted Ge intermingled with PdGe. There was only a very little and unworkable region of completely exposed PdGe without intermingled unreacted Ge, it was therefore not possible to obtained data for the growth or exposure rates of the phase PdGe. The growth of the $Pd_2Ge$ region was monitored at the temperatures 275, 300, and 325°C. The periods of annealing were chosen so as to obtain a reasonable range of growth widths at each of the three temperatures; results are presented in **Figure 15**. Parabolic growth characteristics were observed.

Arrhenius plots were obtained from the data presented in **Figure 15**, in the same way as explained for the Ni/Ge lateral diffusion couples. **Figure 16** is an Arrhenius plot showing the temperature dependence of the Ge diffusion rate through $Pd_2Ge$.

The average activation energy determined from the plot in **Figure 16** was $1.0 \pm 0.1$ eV.

## 5. Conclusion

The movement of inert markers during the formation of palladium and nickel germanides was continuously monitored in conventional thin film couples using in situ RBS. The comparative contribution of each atomic species to the diffusion process during the formation of the phases was determined. Any changes of the comparative contributions of the atomic species during the phase growth process were studied. $Ni_5Ge_3$ and NiGe were observed to form in the Ni/Ge system with $Ni_5Ge_3$ being the first to form. Nickel was the only diffusing species during the formation of $Ni_5Ge_3$. Both Ni and Ge were observed to diffuse during the formation of NiGe. The diffusion of Ge was dominant in the initial stages of the reaction but Ni diffusion becomes the prominent growth mechanism thereafter. The only phases observed to form in the Pd/Ge system were PdGe and $Pd_2Ge$, the latter being the first. Both Pd and Ge are observed to diffuse during $Pd_2Ge$ and PdGe formation. Palladium is however the dominant diffusing species during both $Pd_2Ge$ and PdGe formation, being responsible for around 60% of the diffusion during $Pd_2Ge$ formation and 65% of diffusion during PdGe formation. The results obtained for the first phase formation are in agreement with previously reported data. To the best of our knowledge this is the first time that the dominant diffusing species during NiGe and PdGe formation has been quantitatively determined, as mentioned earlier NiGe and PdGe are the most promising candidates for ohmic contacts in germanium-based technology [2, 3]. Our conventional thin film investigation has shown that the metal is the dominant diffusing species during the formation of the first phase. This is in agreement with the $Cu_3Au$ ordered rule [40] which states that the majority diffusing element in an intermetallic ordered structure is the one with the highest diffusion coefficient. This rule was however not applicable to lateral diffusion couples.

**Table 2** summarizes our results for the thin film and lateral diffusion couples in terms of the phase-formation sequences, phase-formation temperatures and diffusing species during the respective phase growths.

As presented in **Table 1**, the formation of $Ni_5Ge_3$ and NiGe was a common feature in the thin film and lateral diffusion couple results. However, $Ni_3Ge_2$ was only observed in lateral diffusion couple samples. Lateral diffusion couples provide a qualitative pointer to the dominant diffusing species in a system, without the need to interpose markers between coupling layers.

| Phase - formation characteristics | Thin film couples | | Lateral diffusion couples | |
|---|---|---|---|---|
| Phases observed | $Ni_5Ge_3$, NiGe, $Pd_2Ge$, PdGe | | $NiGe$, $Ni_3Ge_2$, $Ni_5Ge_3$, $Pd_2Ge$, PdGe | |
| Phase-formation sequence | 1st | $Ni_5Ge_3$, $Pd_2Ge$ | Simultaneous lateral growth of phases | |
| | 2nd | NiGe, PdGe | | |
| Phase-formation temperatures | $Ni_5Ge_3$ | 150°C | Lateral reactions commenced at around 300°C in both the Ni/Ge and Pd/Ge systems | |
| | $Pd_2Ge$ | 140–150°C | | |
| | NiGe | 250°C | | |
| | PdGe | 180°C | | |
| Diffusing species | $Ni_5Ge_3$ | Ni | Combined growth of $Ni_3Ge_2$/$Ni_5Ge_3$ | Ge |
| | NiGe | Ni is the DDS; Ge diffusion observed during the early stages of growth. | Exposure of NiGe | Ge |
| | $Pd_2Ge$ | 60% Pd and 40% Ge | Limited exposure of $Pd_2Ge$ | Ge |
| | PdGe | 65% Pd and 35% Ge | PdGe | Ge |

**Table 2.** Summary of the results for the thin film and lateral diffusion couples in terms of the phase-formation sequences, phase-formation temperatures and diffusing species during the respective phase growths in the Ni/Ge and Pd/Ge systems.

The results from both diffusion couples with Ni islands on a Ge film and vice-versa indicate that Ge was the dominant diffusing species during germanide growth. The growth in the lateral diffusion couples was found to obey the $t^{1/2}$ law, indicating a diffusion-controlled process. The magnitude of the activation energy of the combined lateral growth of $Ni_3Ge_2$ and $Ni_5Ge_3$ was found to be $0.9 \pm 0.1$ eV, and that of the rate of exposure of NiGe was $1.1 \pm 0.1$ eV. The two phases, PdGe and $Pd_2Ge$, which were observed to form in the thin film study of the Pd/Ge system were also the only two observed in the lateral diffusion couples. The average activation energy determined for the lateral growth of $Pd_2Ge$ is $1.0 \pm 0.1$ eV. The magnitudes of the activation energies calculated for all phases in this study suggest that the lateral diffusion reactions were not driven by surface diffusion but rather by diffusion through the interior of the lateral diffusion couples; typical values for surface diffusion being around 0.6 eV [41].

## Acknowledgements

The authors would like to thank the Materials Research Division of iThemba LABS, Faure for their kind assistance and use of their facilities. We thank the South African National Research Foundation (NRF) and the Zambian National Science and Technology Council (NSTC) for their financial support. The authors would also like to acknowledge the support that this work received from the CREA programme of the KULeuven, the Inter-University Attraction Pole and the Fund for Scientific Research of Flanders.

## Author details

Adrian Habanyama[1]* and Craig M. Comrie[2]

*Address all correspondence to: adrian.habanyama@cbu.ac.zm

1 Department of Physics, Copperbelt University, Kitwe, Zambia

2 Department of Physics, University of Cape Town, Rondebosch, South Africa

## References

[1] Brunco DP, De Jaeger B, Eneman G, Mitard J, Hellings G, Satta A, Terzieva V, Souriau L, Leys FE, Pourtois G, Houssa M, Winderickx G, Vrancken E, Sioncke S, Opsomer K, Nicholas G, Caymax M, Stesmans A, Van Steenbergen J, Mertens PW, Meuris M, Heyns MM. Germanium MOSFET devices: Advances in materials understanding, process development and electrical performance. Journal of the Electrochemical Society. 2008;**155**: H552-H561

[2] Gaudet S, Detavernier C, Kellock AJ, Desjardins P, Lavoie C. Thin film reaction of transition metals with germanium. Journal of Vacuum Science and Technology. 2006; **A24**:474

[3] Kittl JA, Opsomer K, Torregiani C, Demeurisse C, Mertens S, Brunco DP, Materials Science and Engineering. 2008;**144**:B154-B155

[4] Hökelek E, Robinson GY. A comparison of Pd Schottky contacts on InP, GaAs and Si. Solid State Electronics. 1981;**24**:99

[5] Rhoderick EH, Williams RH. Metal-Semiconductor Contacts. Oxford: Clarendon Press; 1988

[6] Baraff GA, Schlüter M. Binding and formation energies of native defect pairs in GaAs. Physical Review B. 1986;**33**:7346

[7] Asubay A, Güllü Ö, Türüt A. Determination of the laterally homogeneous barrier height of thermally annealed and unannealed Au/p-InP/Zn-Au Schottky barrier diodes. Applied Surface Science. 2008;**254**:3558

[8] Peng CY, Yang YH, Lin CM, Yang YJ, Huang CF, Liu CW. Process strain induced by nickel germanide on Ge substrate. In: 9th International Conference on Solid-State and Integrated Circuit Technology (ICSICT) Proceedings. 2008. pp. 681-683

[9] Hallstedt J, Blomqvist M, Persson POA, Hultman L, Radamson HH. The effect of carbon and germanium on phase transformation of nickel on $Si_{1-x-y}Ge_xC_y$ epitaxial layers. Journal of Applied Physics. 2004;**95**:2397

[10] Thanailakis A, Northrop DC. Metal-germanium Schottky barriers. Solid State Electronics. 1973;**16**:1383-1389

[11] Jin LJ, Pey L, Choi WK, Fitzgerald EA, Antoniadis DA, Pitera AJ, Lee ML, Chi DZ, Tung CH. The interfacial reaction of Ni with (111) Ge, (100) $Si_{0.75}Ge_{0.25}$ and (100) Si at 400 °C. Thin Solid Films. 2004;**462**:151-155

[12] Nemouchi F, Mangelinck D, Bergman C, Clugnet G, Gas P. Simultaneous growth of $Ni_5Ge_3$ and NiGe by reaction of Ni film with Ge. Applied Physics Letters. 2006;**89**:131920

[13] Patterson JK, Park BJ, Ritley K, Xiao HZ, Allen LH, Rockett A. Kinetics of Ni/a-Ge bilayer reactions. Thin Solid Films. 1994;**253**:456-461

[14] Gaudet S, Detavernier C, Lavoie C, Desjardins P. Reaction of thin Ni films with Ge: Phase formation and texture. Journal of Applied Physics. 2006;**100**:034306

[15] Majni C, Ottaviani G, Zani A. Growth kinetics of $Pd_2Ge$ and PdGe. Journal of Non-Crystalline Solids. 1978;**29**:301

[16] Knaepen W. Characterization of solid state reactions and crystallization in thin films using in situ X-ray diffraction. [PhD thesis] Ghent: University of Ghent; 2010

[17] Scott DM, Pai CS, Lau SS. Thin film reaction investigation by backscattering spectroscopy – W Marker Study of $Pd_2Ge$ formation. Proceedings of the Society of Photographic Instrumentation Engineers (SPIE). 1984;**463**:40-45

[18] Marshall ED, Wu CS, Pai CS, Scott DM, Lau SS. Metal-germanium contacts and germanide formation. Materials Research Society Symposium Proceedings. 1985;**47**:161

[19] Brunco DP, Opsomer K, De Jaeger B, Winderickx G, Verheyden K, Meuris M. Observation and suppression of nickel germanide overgrowth on germanium substrates with patterned $SiO_2$ structures. Electrochemical and Solid-State Letters. 2008;**11**:H39-H41

[20] Zhang SL, Ostling M. Metal silicides in CMOS technology: past, present and future trends. Critical Reviews in Solid State and Materials Sciences. 2003;**28**:1

[21] Nemutudi RS, Comrie CM. Churms CL. Study of Pt/Ge interactions in a lateral diffusion couple by microbeam rutherford backscattering spectrometry. Thin Solid Films. 2000;**358**: 270

[22] Zheng LR, Hung LS, Mayer JW, Majni G, Ottaviani G. Lateral diffusion of Ni and Si through $Ni_2Si$ in Ni/Si couples. Applied Physics Letters. 1982;**41**:646

[23] Zheng LR, Hung LS, Mayer JW. Silicide formation in lateral diffusion couples. Journal of Vacuum Science and Technology. 1983;**A1**:758

[24] Zheng LR, Hung LS, Mayer JW. Lateral diffusion of platinum through $Pt_2Si$ in Pt/Si. Thin Solid Films. 1983;**104**:207-213

[25] Chen SH, Zheng LR, Barbour JC, Zingu EC, Hung LS, Carter CB, Mayer JW. Lateral-diffusion couples studied by transmission electron microscopy. Materials Letters. 1984;**2**: 469-476

[26] Blanpain B, Mayer JW, Liu JC, Tu KN. Kinetic description of the transition from a one-phase to a two-phase growth regime in Al/Pd lateral diffusion couples. Journal of Applied Physics. 1990;**68**:3259-3267

[27] Blanpain B, Mayer JW, Liu JC, Tu KN. Layered growth of the quasicrystalline decagonal $Al_3Pd$ phase in Al/Pd lateral diffusion couples. Physical Review Letters. 1990;**64**:2671

[28] Blanpain B, Liu JC, Lilienfeld DA, Mayer JW. Simultaneous growth of a crystalline phase and a quasicrystalline phase in lateral Al-Pd diffusion couples. Philosophical Magazine Letters. 1990;**61**:21-27

[29] Liu JC, Mayer JW, Barbour JC. Phase formation of $NiAl_3$. Journal of Applied Physics. 1988;**64**:651

[30] Liu JC, Mayer JW, Barbour JC. Kinetics of $NiAl_3$ and $Ni_2Al_3$ phase growth on lateral diffusion couples. Journal of Applied Physics. 1988;**64**:656

[31] Liu JC, Mayer JW. Aluminum and Ni-silicide lateral reactions. Journal of Materials Research. 1990;**5**:334-340

[32] Ding PJ, Talevi R, Lanford WA, Hymes S, Murarka SP. Use of a raster microbeam to study lateral diffusion of interest to microelectronics. Nuclear Instruments & Methods B. 1994;**85**:17

[33] de Waal HS. The effect of diffusion barriers, stress and lateral diffusion on thin-film phase formation. [PhD thesis]. South Africa: University of Stellenbosch; 1999

[34] Doolittle LR. Algorithm for rapid simulation of Rutherford backscattering spectra. Nuclear Instruments and Methods B. 1985;**9**:344-351

[35] Comrie CM, Smeets D, Pondo KJ, van der Walt C, Demeulemeester J, Knaepen W, Detavanier C, Habanyama A, Vantomme A. Determination of the dominant diffusing species during nickel and palladium germanide formation. Thin Solid Films. 2012;**526**:261-268

[36] Chilukusha D, Pineda-Vargas CA, Nemutudi R, Habanyama A, Comrie CM. Microprobe PIXE study of Ni-Ge interactions in lateral diffusion couples. Nuclear Instruments and Methods in Physics Research B. 2015;**363**:161-166

[37] Vantomme A, Degroote S, Dekoster J, Langouche G, Pretorius R. Concentration-controlled phase selection of silicide formation during reactive deposition. Applied Physics Letters. 1999;**74**:3137-3139

[38] Perrin C, Mangelinck D, Nemouchi F, Labar J, Lavoie C, Bergman C, Gas P. Nickel silicides and germanides: Phases formation, kinetics and thermal expansion. Materials Science and Engineering. 2008;**154**:163

[39] Smith GA, Luo L, Gibson WM. Ion channeling study of nickel metal growth on Ge<111> at room temperature. Journal of Vacuum Science and Technology. 1991;**A9**:646

[40] d'Heurle FM, Gas P, Lavoie C, Philibert J. Diffusion in intermetallic compounds: The ordered $Cu_3Au$ rule, its history. Zeitschrift für Metallkunde. 2004;**95**:852-859

[41] Eckertova L. Physics of Thin Films. 2nd ed. New York: Plenum Press; 1986

Chapter 8

# Transition Metal Aluminide Coatings and Initial Steps on Additive Manufacturing

Núria Cinca i Luis

Additional information is available at the end of the chapter

http://dx.doi.org/10.5772/intechopen.72582

**Abstract**

During the last decades, Fe-, Ni- and Ti-based aluminides have been studied in terms of bulk materials with an effort to develop alloying and processing strategies to overcome their low ductilities and toughness compared to conventional alloys. Whenever significant improvements can be addressed in this direction, they will be opened to an extensive range of industrial applications, especially those related to high temperature resistance requirements. In parallel, progressing interest has also been focused on their application as protective layers. This chapter is intended to provide a review of the evolution that has been made mainly during the last two decades of the several coating technologies devoted for this purpose. From thick to thin coatings are revised, with insight into coating microstructures and properties as well. Lack of space has forced the selection of those technologies arising most interest within last years; therefore, the content will follow this order: joining (laser cladding and electrospark deposition), thermal spraying (high velocity oxygen fuel and cold spraying) and physical vapor deposition (magnetron sputtering and cathodic arc deposition).

**Keywords:** intermetallic, coating, overlay, repair, corrosion, wear

## 1. Introduction

Due to their intrinsic outstanding properties, intermetallic compounds (IMCs) have found application to coat other materials, either to improve surface resistance of an industrial substrate component to environmental attack or to create a beneficial intermediate layer between the substrate and another coating material [1, 2]. As coatings, a wide range of techniques have been employed to deposit them, either at low temperatures such as plating or at high temperatures by hot dipping, joining, thermal spraying and so on. Many intermetallic coatings have been produced for a wide range of applications and different technological interest; however, the scientific community has been mainly focusing during the last decades on the study of

those coatings for high temperature protection of industrial components. One of the primary users of high-temperature coatings is the gas turbine engine industry for commercial and military aircraft, industrial power generation and marine applications. One possible application could therefore be for the protection against oxidation of external and internal surfaces of turbine blades and vanes to fight oxidation and hot corrosion. Other applications would include turbines for coal gasification combined cycle power plants in components of fast breeder reactors or superheater tubes in the incinerator of waste to energy plants. Those IMC coating materials of interest rely on aluminide, chromide or silicide intermetallics because they can form protective oxide films of $Al_2O_3$, $Cr_2O_3$ or $SiO_2$ [1–3].

Transition metal aluminides as bulk materials are seen as potential candidates for future substitution of superalloys since they can also offer significant reductions in density. Within this group, Fe, Ni and Ti aluminides are mainly considered, although Co-Al, Nb-Al, Pt-Al, Ru-Al alloys as well as other trialuminide alloys ($Al_3X$ where X can be Ti, Zr, Hf, V, Nb or Ta) are also reviewed, even with some works dealing with coatings [4–8].

Nickel and iron aluminides especially provide excellent oxidation resistance in the range 1100–1400°C due to their high aluminum contents and high melting points, although many times spallation problems can be important [9, 10]. **Table 1** provides the critical ordering temperature ($T < T_c$ long-range order while $T > T_c$ short-range order), melting temperature and the maximum use temperatures of the main compounds of potential industrial interest. As it can be seen, their corrosion resistance extends to temperatures at which these alloys have limited or poor mechanical strength. Because of the limitation on balancing loading capabilities with high temperature corrosion resistance, together with poor room temperature ductility, some processing problems, as well as low strength and creep properties at high temperatures of some intermetallics [11], their commercialization is still limited; therefore, their use as coatings to provide resistance to other materials offers increasing suitable possibilities. The purpose of the present chapter is to offer an overview of the most recent advances on this topic.

**Table 2** presents the main characteristics of the most usual coating techniques employed for the production of intermetallic coatings. The use of pack cementation, slurry, hot dipping and chemical vapor deposition was the first initially established [12]; the fundamentals of such

| Intermetallic | Critical ordering T | Melting point | Maximum use temperature (°C) | |
|---|---|---|---|---|
| | | | Strength limit | Corrosion limit |
| $Ni_3Al$ | 1390 | 1390 | 1100 | 1150 |
| NiAl | 1640 | 1640 | 1200 | 1400 |
| $Fe_3Al$ | 540/760 | 1540 | 700 | 1200 |
| FeAl | 1250 | 1250 | 800 | 1200 |
| $Ti_3Al$ | 1100 | 1600 | 760 | 650 |
| TiAl | 1460 | 1460 | 1000 | 800 |

**Table 1.** Temperature limits for iron, nickel and titanium aluminides.

| | |
|---|---|
| Slurry | Applying a powder mixture of aluminum or an aluminum alloy with an activator along with a binder either by spraying or by brushing followed by a diffusion heat treatment at a temperature of 1000–1200°C |
| Hot dipping | Immersion of the substrate into a molten metal pool and diffusion in the solid state during dipping or subsequent thermal treatment |
| Pack cementation | *In situ* chemical vapor deposition (CVD) batch process where the substrate is buried in a mixture of the master alloy powder (powder of the element or elements to be deposited on the surface of the parts, such as Cr and/or Al, Cr and/or Si), an halide salt activator and an inert filler powder |
| Chemical vapor deposition | Precursor gases (often diluted in carrier gases) are delivered into the reaction chamber at approximately ambient temperatures. As they pass over or come into contact with a heated substrate, they react or decompose forming a solid phase and are deposited onto the substrate |
| Joining techniques | Welding processes where the powder in liquid phase, upon reaction with the substrate metal, forms the intermetallic compound. The coating material is melted in contact with the substrate |
| Thermal spraying | The feedstock coating material (in powder, wire or rod form) is heated to a molten or semimolten state some distance from the substrate. The resultant heated particles are accelerated and propelled toward a prepared surface by either process gases or atomization jets |
| Physical vapor deposition | A solid metal is vaporized in a high vacuum environment and deposited on the substrate |

**Table 2.** Main characteristics of diffusion and overlay coatings.

technologies are based on the formation of the intermetallic through the interaction of a reactant that contains Al with the primary elements composing the substrate alloy. Many of these techniques have in common that rely on diffusion processes to form the intermetallic. The behavior of diffusion coatings strongly depends on the composition of the substrate alloys because the alloy participates in the formation of the coating. As a result, these coatings do not offer wide flexibility for the incorporation of minor elements. In order to face this limitation, the "overlay"-type coatings were developed with minimal direct contribution of the substrate alloys. The present chapter will thus mainly focus on these overlay processes such as thermal spraying, joining or physical vapor deposition that actually consist of an alloy of a specially designed composition, i.e. feedstock intermetallic, to be deposited on the component surface. The coating thicknesses deposited by the above overlay joining and thermal spray methods are of the order of ~200 μm and higher. Physical vapor deposition (PVD) techniques enable the deposition of coatings in the nanometer to micron thickness range. Thermal spraying and joining techniques can be considered as fusion processes. Each process results in different coating microstructures, thus also having a direct influence on the final properties (**Figure 1**).

We will also explore the concepts of rapid prototyping and additive manufacturing applied to IMCs, which are acquiring relevant interest. The conventional production process for bulk components on intermetallic compounds is casting, which leads to a partial oxidation and grain growth owing to aging at high temperature for a long time [9, 10]. The direct manufacturing of 3D articles of these materials is complex due to the brittleness at low temperatures inherent in intermetallics. Moreover, the subsequent sample machining leads to a noticeable wear of the cutting tool.

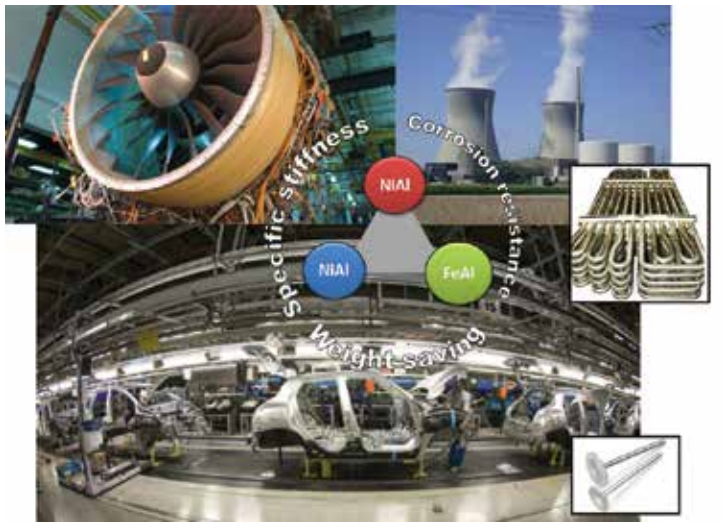


**Figure 1.** Fields of application where intermetallic coatings can be applied.

On that concern, rapid prototyping actually refers to the rapid production of prototypes for several objectives, including ergonomic and visual trials, assessment of functional performance and supporting parts to other processes. By contrast, additive manufacture technologies (AMTs) involve any manufacturing process using layer-by-layer or drop-by-drop processes. Usually, these AMTs are used for obtaining prototypes, rather than large-scale production. However, recently, more and more AMTs are employed for final components, especially when complex geometries need to be produced, or for the incorporation of special functionalities [13]. Some of the above-mentioned processes can also then be regarded as potential technologies for additive manufacturing, which can outperform conventional hot-pressing consolidation of powder due to their less complexity, lower energy consumption, higher productivity and therefore lower production costs [14].

## 2. Overlay coatings

### 2.1. Joining techniques

Welding involves a range of technologies suitable for the application of thick coatings, from 1 to 50 mm or more, of metallic materials. The available processes are manual metal arc (MMA), metal inert gas (MIG), tungsten inert gas (TIG), plasma transferred arc (PTA), etc.; Çam et al. [15] reviewed the use of these techniques for intermetallics. A part from improving the surface properties, they can be used for cosmetic repair of casting defects as well as for the assembly of components. Alternatively, the laser cladding process is increasingly used instead of PTA (Plasma Transferred Arc) welding and uses a laser as source of heat. It outperforms conventional welding methods like TIG for advanced weld repair applications. Typically coatings from 0.5 to 3 mm thicknesses can be build-up with laser cladding. Instead

of using a filler rod, consumable electrode or a previously applied paste, it uses powder as feedstock material to form the coating, which is carried into the melt pool by an inert gas through a powder nozzle.

Although PTA and laser cladding are technologies dating from about the same period, i.e. the 1960s, laser cladding has received more attention in this decade for possible production of additive manufacturing of aluminides; therefore, in order to avoid overextension of the present chapter, the emphasis is highlighted on laser cladding and references to PTA intermetallic coatings can be found in the literature as reported at the beginning of this section.

Laser cladding uses a powder-fed or wire-fed system and the resulting coatings possess extremely dense and pore-free microstructures. They are bonded to the substrate through an excellent metallurgical union, have uniform composition and coating thickness. Laser coating also produces very low dilution and small affected zone to the base material [16]. Laser cladding will be here revised as an option for additive manufacturing purposes. Also other wire feeding systems have appeared to be suitable for the build-up of intermetallic structures such as the so-called wire-arc additive manufacturing (WAAM) process [17, 18].

Furthermore, for repair purposes, electrospark deposition (ESD) has also been used to deposit intermetallics and this will briefly revised; this is a process based on pulsed micro-welding, working slower than previous processes and with maximum thicknesses of about 2-3 mm. In order to deposit the electrode material, electrical pulses of short duration are used [19].

### *2.1.1. Laser cladding*

#### *2.1.1.1. Fe-Al coatings*

Previous works with gas tungsten arc (GTA) and gas metal arc (GMA) welding techniques indicate that when the clad has an aluminum content above 10 wt.%, cold cracking in the iron aluminide cladding occurs in a similar manner to that observed in bulk samples [20, 21]. High-quality clads were produced by proper optimization of the pulsed laser-assisted powder deposition (LAPD) process conditions on mild steel; however, since Al plus Fe powders were used as feedstock, inhomogeneous phase distribution was obtained rather than the stoichiometric $Fe_3Al$ or FeAl phases which are the ones of interest for possessing enough Al content to form a continuous oxide surface layer [22]; notice then that those works required the mixing of the two base metals. Cheng and He [23] produced real overlays as defined before when employing $Fe_3Al$ powders; they observed a fine dendritic structure with some cracking in the coatings, whereas none when using a mixed powder of Fe and Al, as well as Bax et al. [24], who achieved completely crack-free single-phase $Fe_3Al$ and FeAl coatings with hardness values HV0.1–300 on mild steel and HV0.1–500 on pure nickel, respectively. The shift in composition in comparison to the initial powder composition (45/55 at.% ratio) is reported to be caused during the mixing or laser cladding process.

In addition, FeAl intermetallic matrix composite coatings with TiC as reinforcement have been produced for wear resistance at high temperatures [25, 26]; TiC is found to be a suitable reinforcement because of its excellent high temperature stability, high hardness and low density;

a transition from abrasive wear to adhesive wear was found when the load was increased for such tested coatings.

Whereas previous cited works usually dealt with coatings deposited on steel substrates, Tomida and Nakata [27] deposited on A5052 commercial Al-Mg alloy substrate to improve its surface hardness and wear resistance for possible application in automobile industry, railway cars, aircraft, etc.

Abboud et al. [28] as well as Chen and Wang [25] used a one-step process instead of preplacing the powder on the substrate and then passing the laser, which offers higher flexibility enabling the use of such technique for rapid prototyping. Apart from coating, laser cladding has therefore gained importance within this decade for 3D manufacturing purposes. This might be a good solution to solve the drawbacks encountered for bulk processing, also when problems concerning porosity, bond strength and thermal expansion coefficients mismatch between the coating and the substrate may arise.

There are some reports on additive manufacturing of iron aluminides, i.e. 3D laser cladding, laser metal deposition (LMD), laser engineered net shaping (LENS) and selective laser melting (SLM) processes [29–36]. SLM derives from the selective laser sintering (SLS) process because instead of sintering or partial melting, complete melting of powder occurs; also for SLS post-processing is required. Song et al. [29] reached a hardness value in SLM pieces about 750 HV0.3, harder than those FeAl coatings deposited by high velocity oxy-fuel spraying and also higher than hot forging (680 HV0.3) or by mechanical milling + explosive shock wave consolidation (683 HV0.5) [37]. A large-scale collaborative German project explored the possibilities for the production of parts from iron aluminide-based alloys by ALM for automotive, aeronautics and energy conversion applications by means of SLM and LMD with a Fe-28 at.% Al feedstock powder. Defect-free samples were produced whose mechanical properties are highly dependent on the internal stresses. SLM samples were only ductile above 200°C while LMD samples

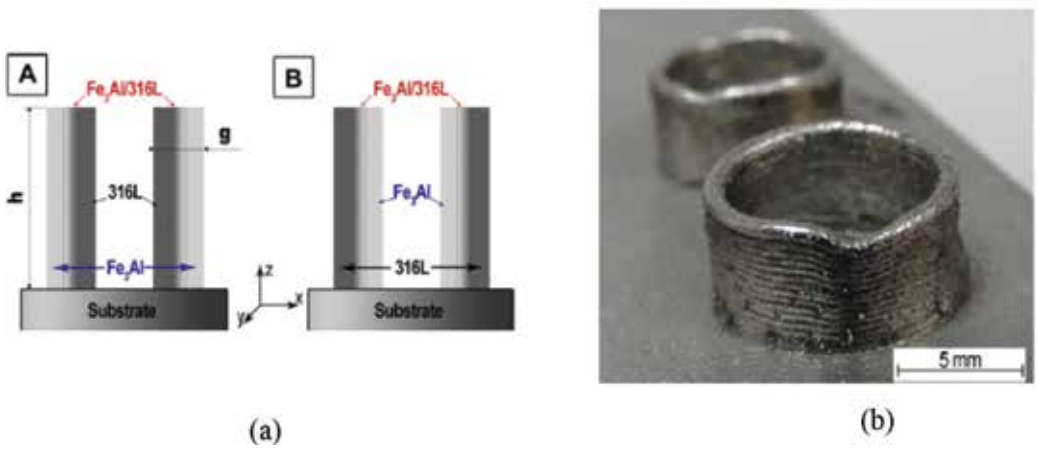


**Figure 2.** Laser cladded tubes: (a) scheme of the composition of each structural component: A—316 L/$Fe_3Al$ and B—$Fe_3Al$/316 L, and (b) first technological trials [34].

are already ductile at room temperature [29]. Michalcová et al. [36] recently explored three different strategies for strengthening iron aluminides at high temperatures using LAM: (i) increasing the ordering temperature D03 ↔ B2 Fe–30Al–10Ti (at.%), (ii) precipitation of borides (Fe–30Al–5Ti–0.7B) and (iii) generation of coherent A2 + L21 microstructures (Fe–22Al–5Ti). Dense samples could be generated with yield stress and compressive creep strength matching that of the as-cast alloys above 600°C and even higher at lower temperatures, being dependent on the building direction. No general improvement of ductility was observed.

LENS has been mostly used for obtaining functionally graded materials (FGMs), either $Fe_3Al$/SS316L or Fe/FeAl [30, 33, 34], allowing to produce tubes with good shape and a high metallurgical quality (**Figure 2**). LENS enables the production of metal components through a process of metal powder sintering aided with pre-designed three-dimensional computer-aided design (CAD) models. On account of the "layer by layer" building mode, the chemistry of each layer being build-up can be different, and thus, the LENS technique can produce composition gradients in near-net-shape components without using any additional intermediate steps.

*2.1.1.2. Ni-Al coatings*

Mostly nickel [28, 38–40] and steel [28, 41–45] substrates were employed for the fabrication of laser cladding nickel aluminide coatings, the composition being either controlled by using two powder feeders and selecting the powder feeder rates [28] or by mixing the desired amount of nickel and aluminum powders that are preplaced on the substrate and then selecting the laser power density to generate the melt pool [45]; from the first work, a compositional gradient was obtained, whereas single-phase adherent NiAl coatings free from pores and cracks could be produced afterwards. Depending on the operating conditions, a dendritic, cellular or equiaxial structure can be obtained, and the optimum one has resulted that leading to a dense and fine dendrite microstructure that leads to improved wear rates, i.e. about $14 \times 10^{-5}$ $mm^3/Nm$ under sliding conditions. Up to a hardness value of 750 HV0.2 could be pursued by the addition of phosphorous, also resulting in a refined cellular microstructure ($Ni_3Al + Ni_3P$) near the interface; in that case, the microstructure of the coating was however composed of γ-Ni, $Ni_3Al$ and NiAl rather than a uniform single phase [40]. Also by the increased yttrium addition, the dendrites were gradually refined [46].

As well as for iron aluminides, a great focus has been done on the preparation of intermetallic composite coatings with TiC or WC particulate reinforcement. Chen et al. [35, 36] tried with a 35 and 20 at.% Al ratios in the raw material of elemental powder blends resulting in NiAl-$Ni_3$(Al,Ti,C) and NiAl-$Ni_3$Al-TiC composition with dendritic structure and a hardness around 650 and 750 HV0.2, respectively. The NiAl-$Ni_3$Al-TiC laser clad coating exhibited excellent wear resistance not only at room temperature but also at 600°C in dry sliding wear test conditions. The adhesive wear seems to be prevented thank to the high strength of the interatomic bonds of the intermetallic matrix, providing a firm support for TiC particles and resisting metallic adhesion during metallic dry sliding wear. The cavitation erosion resistance of laser clad nickel aluminide composite coatings is also ameliorated by the use of TiC as well as the work hardening ability of the NiAl-$Ni_3$Al [43, 44].

LENS was employed to obtain not only nickel aluminides with various compositions but also with composition gradient [47]; cracking problems were solved by preheating the substrate. Due to problems in mixing with a single feeder, two feeders were used for the Ni and Al powders, so that the in situ reactive alloying was successful.

*2.1.1.3. Ti-Al coatings*

Titanium aluminide intermetallic coatings produced by laser cladding were employed to protect titanium and aluminum specimens. On aluminum substrates, Ti + Al powders were preplaced to produce $Al_3Ti$ reinforced with $TiB_2$, TiC and SiC so that the wear resistance could be improved; in order to produce an adherent layer, the process was optimized to minimize the melting of the base material [48]. On titanium substrates, either pure Ti or its alloys, such as Ti6Al4V, which are extensively used in aeronautical, marine and chemical industries, the use of intermetallic layers is aimed at improving its wear and oxidation resistance at temperatures above 500°C [49–55]. In most of the cases, just by preplacing the Al powder in the right portion, $Ti_3Al$, TiAl or $TiAl_3$ layers can be achieved [52, 53], but this implies a high dilution with the base material. Guo et al. [50] found the following hardness order $Ti_3Al$ > TiAl > $TiAl_3$ and the main conclusions derived from their studies are that, under the same sliding conditions, the wear resistance tendency followed the same order as the hardness, with the higher Ti content exhibiting the highest resistance.

Other authors used Ti + Al powders [29, 49, 51] and some observed an increase in hardness when increasing the Al content, contrarily to what is reported in the previous paragraph. The wear rate and mechanisms change according to normal load and composition [54].

Few used TiAl alloy powders, i.e. $TiAl_3$ [54] or TiAl [55, 56] compositions; Li et al. [54] also uses $TiB_2$, $Al_2O_3$ and nano-$Y_2O_3$ but the best results on the volume wear loss approach to 2 $mm^3$, whereas by using TiC, TiN or SiC, one order of magnitude lower is reached.

Zhang et al. [56] also used TiAl alloys, i.e. Ti482Nb0.4Ta and Ti48Al2Cr2Nb (at.%) powders to be deposited onto stainless steel, a Nb alloy, a Ti alloy and TiAl alloy and produced 3D components through the LENS technology; final microstructure, either an equiaxed, metastable $\alpha_2$-$Ti_3Al$ or massive $\gamma$, is very influenced by the processing parameters. Also LMD was used for building up components from Ti–47Al–2.5 V–1Cr and Ti–40Al–2Cr (at.%) intermetallic alloys. Fully lamellar (FL) microstructure consisted of $\gamma$-TiAl and $\alpha_2$-$Ti_3Al$ was formed in the as-laser deposited $\gamma$-TiAl samples [57].

However, with laser cladding, the quality of the coating may vary significantly due to small changes in the process variables such as laser power, beam velocity and powder feed rate. Optimizing the set of parameters is of crucial importance for the control of the microstructure. Therefore, for prototyping operations, its use is still limited. However, undergoing developments in high-power diode lasers (HPDL), fiber lasers and control units based on knowledge offers promising capabilities for industrial benefits.

On the other hand, the ability to have automatization control of the laser/material feed system, precise thermal energy dosing and coating integrity makes laser cladding suitable over other processes such as high velocity oxy-fuel (HVOF) and cold spray (CS).

http://dx.doi.org/10.5772/intechopen.72582

*2.1.2. Electrospark deposition*

FeAl compound has proved to be resistant in corrosion environments such as in molten salts. Therefore, their use for corrosion protection of austenitic stainless steels used as bipolar plates and cell housing materials appears to be promising. Frangini and Masci [58] were pioneers on directly depositing FeAl through ESD with no apparent oxide content or crack formation within the layer; its corrosion in (Li + K) carbonate molten salts showed some degradation at long exposure times. More recently, these coatings were oxidized by using a DC plasma oxidation technique to grow alumina films, which despite being the metastable gamma alumina, it presented very good barrier properties [59]. Lower interest has been devoted to the Ni-Al system where instead pure alloyed layers, Ni-Cr-NiAl [60] and Al-$NiAl_3$ [61], have been produced.

Gradual titanium aluminide coatings onto $\gamma$-TiAl substrates were produced by Li et al. [62], mainly presenting $TiAl_3$ on the top with a good oxidation resistance at 800°C but less at 900°C. Electrospark deposition has been recently explored in combination with ultrasonic impact treatment reaching up to 540 HV.

## 2.2. Thermal spray

One of the major advantages of thermal spray technologies compared to the previous ones is the minimum heat input to the substrate, the so-called heat affected zone present in welding processes, here is absent. Thus, materials with very high melting points can be applied without modifying the properties of the component and without excessive thermal distortion of the part. An additional advantage is the capability of recoating damaged deposits without changing previous dimensions or properties.

The raw material (in powder, wire or rod form) is deposited onto the substrate by propelling the energetic particles by means of high-pressure carrier gas. The particles can be fully or partially melted on impact with the substrate creating cohesive bonds with each other and adhesive bonds with the substrate. The resulting microstructure is lamellar with the characteristic "splats," which attach each other after undergoing very high cooling rates.

Thermal spray processes can be classified according to the energy source, differing from the respective characteristic gas temperatures and particle velocities. When a combustion is used to heat up the material, the existing processes are detonation gun, flame spray and high-velocity oxygen fuel, whereas when it is based on electric energy, plasma spray and arc spray are found. Further modifications of those such as vacuum plasma spray (VPS), high-velocity suspension flame spraying (HVSFS) or suspension plasma spraying (SPS) also exist [63].

More lately, cold spray (CS) has raised the interest of many scientists. Unlike the previous processes, CS is a solid-state process, which offers many advantages in front of conventional thermal spraying: avoids oxidation and undesirable phases, retains the properties of the starting materials, induces low residual stresses, results in a cold-worked microstructure with high-density and high-hardness, allows spraying of thermally sensitive materials, requires minimum surface preparation and implies a safer process due to the absence of high-temperature gas jets, radiation and explosive gases [63].

Recently, the principal findings on thermal spraying of transition metal aluminides were reviewed [64]. Since the larger production of intermetallic coatings has been produced by means of HVOF, the last studies are here reported, as well as those of CS, whose goal is trying to resemble to bulk structures.

*2.2.1. High-velocity oxygen fuel*

*2.2.1.1. Fe-Al coatings*

$Fe_3Al$ and FeAl coatings were produced by HVOF with the aim to improve oxidation and wear performance. They have been mostly applied on steel substrates as well as light alloys [65–69]. A wide range of feedstock compositions have been investigated along the years; different alloying elements have been introduced to the feedstock powders, i.e. Cr, Zr, B, Mo, Ni, as well as ceramic particles such as $CeO_2$, WC, TiC, TiN, $TiB_2$, for different purposes, from decreasing the spallation phenomena during high temperature oxidation to introduce ceramic reinforcement to decrease wear rates.

Typical microstructural features that can be found are the occurrence of molten or partially melted FeAl or $Fe_3Al$ particles, with different amount of Al-depletion, intersplat oxidation and porosity depending on the spraying parameters. Playing with different ranges of particle sizes also results in quite different structures but, mostly, molten splat areas exhibit columnar grains while the rest is equiaxed.

Up to 479 HV0.4 and even 520 HV0.5 hardness values were achieved for iron aluminides, while even 650 HV0.2 can be reached when ceramic particles are introduced [65]. Usually, the higher the microhardness is, the higher the wear resistance. Performance in sliding, abrasive and erosion testing conditions has been investigated, and the wear resistance is governed by the wear mechanisms taking place, i.e. adhesive through material transfer, delamination by fatigue, abrasive and oxidation wear can be encountered depending on the load, sliding speed, counterpart material and so on [68–70]. Dry sliding has been ultimately investigated also at high temperatures with rates in the order of $2.11 \times 10^{-5}$ $mm^3$ $N^{-1}$ $m^{-1}$ at 400°C and unnoticeable wear track at 800°C with a $Si_3N_4$ counterpart ball and 5 N load [70]. The use of intermetallic matrix for composite coatings has also been studied here as a good strategy for improving wear as it was reviewed for laser cladding coatings; in this case, not only TiC [65] but also WC [69], $CeO_2$ [68] and TiN-$TiB_2$ [66] cermets have been synthesized. One of the best wear performances was the coating where 10 wt.% of BN and 20 wt.% of Ti were added to starting $Fe_3Al$ powder leading to $8 \times 10^{-7}$ $mm^3$/Nm with an alumina ball and 10 N load.

The performance of iron aluminide in gaseous corrosion, molten salt corrosion, erosion-corrosion, aqueous corrosion, oxidizing, carburizing and sulfidizing properties has been quite investigated. The moderate and high temperature conditions have been the mostly studied. They possess the ability to form compact aluminum oxide layers due to their high Al content; at high temperatures (>900°C), the occurrence of a stable $\alpha$-$Al_2O_3$ layer is highly desirable, but some spallation can be induced if less stable oxides are present; the relative diffusion kinetics of Fe and Al upon exposure can induce the formation of voids at the coating-oxide layer interface [64].

At high oxidizing temperatures, additional points to consider are: ability to suppress cracking when external stresses are applied or induced thermally, as well as mismatch in the coefficient thermal expansion of the coating and substrate. Also, lower porosity reduces the effective surface area and increases the life service.

Thermal spray iron aluminide coatings have been tested in high temperature gaseous environments [64], but to the author's knowledge, very few findings were observed concerning their use in hot corrosion conditions [71]. These authors reported that no degradation (corrosion and wear) was noticed on the Fe-25% Al-Zr plasma and HVOF coatings sprayed onto low carbon steel heat exchanger tubes tested in a new industrial plant burning very poor fuel; however, this work is not explicit on the coating structures and corrosion evolution. Coal combustion atmospheres can be simulated by testing the coatings in sulfidizing mixture of gases. Coating microstructure can strongly affect its resistance to sulfur penetration [72]. By adding $CeO_2$, the sulfidation resistance was improved [73].

Finally, Shankar highlights the interest on aqueous corrosion mainly for two reasons [74]; firstly, to test durability of these alloys when they are either stored ideally or during working conditions in a corrosive atmosphere. Secondly, since these materials are less expensive compared to conventional stainless steels, they are also considered for room temperature applications in replacement of stainless steels, such as pipes and tubes for heating elements, and in distillation and desalination plants. It is also worth to consider that in order to avoid the use of strategic elements, such as Cr and Ni, these materials are also considered for biomaterials applications, for example bone joints and surgical instruments. Primarily then, their low temperature electrochemical behavior has been tested in simulated human body fluids (Hank's solutions) [75], NaCl [76], $H_2SO_4$ [77] and NaOH [78]. For thermal sprayed coatings, just few authors have dealt with the topic [79, 80].

*2.2.1.2. Ni-Al coatings*

In analogy to the Fe-Al system, nickel aluminide coatings also intend to produce uniform coatings with target NiAl or $Ni_3Al$ compositions. Like it occurred in the microstructure of Fe-Al-based coatings, HVOF NiAl and $Ni_3Al$ coatings typically present Ni-rich regions along the splat boundaries, as well as oxides and the intermetallic at the splat core.

Concerning mechanical properties, up to 470 HV0.1 of hardness value was obtained for NiAl HVOF coatings [81] and even higher up to 750 HV0.1 when nanocrystalline powders are used [82], which have made them also attractive for wear resistance even in slurry conditions [83]. Recently, Benegra et al. [84] compared the abrasive behavior of HVOF and PTA NiAl coatings and reported similar results. At room temperature and dry sliding conditions, friction coefficients as low as 0.3 at 90 N can be obtained with a AISI 52100 steel pin [85]. Like FeAl, nickel aluminides have been proposed as matrix phases for wear performance at high temperatures [86–88]; in erosion conditions, NiAl–40$Al_2O_3$ coatings showed lower sensitivity to the test temperature in front of chromium carbide cermet coatings. Wang et al. [89] investigated the high temperature wear behavior (600–900°C) of NiAl-$Al_2O_3$-TiC composites against SiC under dry sliding conditions on a ball-on-disc test; they exhibited excellent self-lubricating property.

$\alpha$-$Al_2O_3$, nickel spinels and oxides were formed during oxidation of HVOF NiAl coatings above 900°C [90]. The addition of ceria was also used for the improvement of carburization resistance, by creating corrosion products acting as diffusion barrier [91], but giving lower efficiency for the erosion resistance compared to nonheat-treated coatings [92].

To the author knowledge, no aqueous corrosion works have been found for NiAl HVOF coatings; some exist for plasma-sprayed deposits in 0.01 M $H_2SO_4$ electrolyte solution at ambient temperature [93], with lower current densities and higher aluminum content.

*2.2.1.3. Ti-Al coatings*

Few articles have dealt on HVOF spraying of titanium aluminides and those few ones are based mainly on the TiAl with additions of Cr, Fe [94–97] or even $Al_2O_3$ incorporation [98]. TiAl-based alloys can be more sensitive to the high temperature oxidation occurring within the flame resulting in high oxidation [99].

The hardness and wear performance of plane titanium aluminide HVOF coatings have not been much investigated unlike other of the conventional processes such as plasma spraying, whose hardness values can reach 589 HV at room temperature [100]. As in the other reviewed cases, the use of such intermetallics has also been used to form composite coatings to improve the wear resistance of Ti6Al4V substrates [101]. The sliding wear resistance is reported to be higher for $\gamma$-TiAl-$Al_2O_3$ HVOF, followed by $\gamma$-TiAl-$Al_2O_3$ APS and, finally, by $\gamma$-TiAl APS. In addition, HVOF $\gamma$-TiAl-$Al_2O_3$ coatings exhibited lower wear rate at 700°C compared to uncoated hardened H13 tool steels [102]. Under non-lubricated conditions, the wear resistance of $\gamma$-TiAl-$Al_2O_3$ HVOF at RT is higher than $\gamma$-TiAl-$Al_2O_3$ HVOF at 700°C, and this, in turn, higher than RT H13 at RT. Also, carbide reinforcement was introduced but for APS coatings.

As far as the oxidation resistance is concerned, mixed $Al_2O_3$-$TiO_2$ layers are usually formed on titanium aluminides, resulting in less protection capabilities than $Al_2O_3$ scales. By alloying further elements to $Ti_3Al$ and TiAl, this can be improved [103]. Also $TiAl_3$ + Al coatings have been sprayed to achieve better sprayability avoiding the brittleness of the intermetallic and reporting improved performance at 700°C. APS, VPS and HVOF coatings were also tested under cyclic and isothermal oxidation tests at 700 and 900°C [104]. HVOF coatings have shown good cyclic oxidation resistance, reporting that service temperature might be increased by 150°C more than the steel substrate material. No spallation was there observed, while some studies concerning LPPS (low pressure plasma spray) coatings, indicated cracking failure during deposition or early oxidation testing, when coatings are applied on Ti and TiAl [105].

Ti-Al blends were also sprayed by warm spraying, which has been lately studied for the deposition of titanium aluminides given their sensitivity to oxidation. This allows working at decreased temperatures of combustion gas via mixing with nitrogen. After heat treatments, $Ti_3Al$, TiAl and $TiAl_3$ were formed with significant porosity that developed during the heat treatment was caused mainly by Kirkendall effect [106].

### 2.2.2. Cold spray

#### 2.2.2.1. Fe-Al coatings

CS of iron aluminide coatings has been produced with feedstock compositions Fe + Al, Fe(Al) and FeAl. The easiest way is by co-spraying the elemental powders or ball-milled powders with a solid solution composition, thus avoiding the challenges of the high strength and brittleness of the intermetallic compound, but this needs annealing post-processing to achieve the desired composition [107]. Direct cold spraying of intermetallic Fe 40 at.% Al particles has been just attempted by Cinca et al. [108], and dense coatings have been achieved (**Figure 3a**). The study of the spraying parameters revealed that in order to obtain good deposition, a narrow window of selected parameters need to be selected. More investigations need to be pursued concerning the influence of the anomaly yield strength behavior of this material as well as the performance under the typical high strain rates of the cold spray process; some studies in this direction are being undergone through the analysis of the as-sprayed deposits by the EBSD technique, which is showing considerable grain refinement not only at particle boundaries but also all along the upper part of the coating (**Figure 3b**) [109], probably because those particles are impinging on the first layers which are stiffer compared to the stainless steel substrate; splats of individual powder particles can be suspected; some examples are indicated by dotted ellipses. Assuming that, the large deformed grains are primarily located inside the splashes, which are surrounded by fine-grained material due to high strain rate deformation at the intersplat boundaries. Fracture surface features indicate the presence of ductile fracture most probably induced by softening (**Figure 3c**).

The cavitation wear and corrosion resistance of such Fe 40 at.% Al coatings have been characterized [110]. They exhibited reasonably good cavitation performance in fresh water with a low wear rate. In addition, the isothermal and cyclic oxidation at 900°C up to 300 h has shown that the coating keeps unaltered; most promising, **Figure 3d** shows the coating cross section

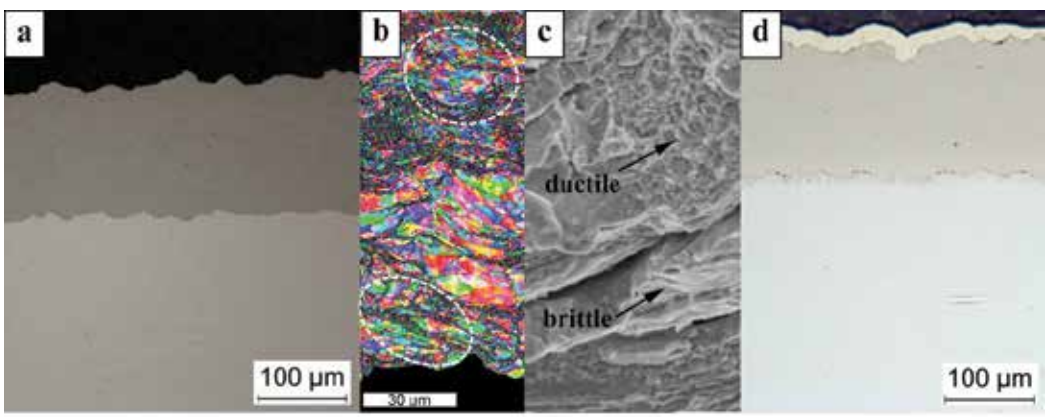


**Figure 3.** Cold sprayed Fe 40 at.% Al coating: (a) as-sprayed cross section, (b) orientation distribution map—EBSD, (c) fracture surface and (d) cross section after exposure at chlorinating environment.

after exposure at 650°C for 500 h in $N_2$ + 6% $H_2O$ + 15% $CO_2$ + 4% $O_2$ + 0.1% $SO_2$ + 500 ppm HCl, indicating no damage at all (**Figure 3d**), which evidences the great capabilities of such materials under aggressive industrial environments [111].

*2.2.2.2. Ni-Al coatings*

Also, blends of elemental powders and ball-milled Ni + Al powders were deposited by cold spray [112–114]. When a mixture of powders is used as feedstock, the microstructure is non-homogeneous in composition and an annealing treatment is required afterwards [112], while the composition along the coating is more homogeneous when starting from the mechanically alloyed powders [113]. The microstructure of cold-sprayed NiAl deposits was also compared to that of HVOF and APS coatings through electrical measurements, proving that their resistivity values strongly depend on splat interface areas and porosity distribution; the presence of interparticle porosity within CS deposits results in higher electrical resistivities [115].

More recently, Azarmi et al. [116] investigated the performance of cold sprayed Ni–$Ni_3Al$ composite coatings on aluminum substrates as an industrial material can be used under harsh service conditions. The compound coatings presented higher strength as well as elastic modulus values compared to pure Ni coatings given the increased amount of dislocations and hardening in $Ni_3Al$.

*2.2.2.3. Ti-Al coatings*

In order to improve high-temperature oxidation resistance, orthorhombic $Ti_2AlNb$ alloy substrates, promising lightweight materials for the aeronautic industry, were coated with $TiAl_3$-Al composite coatings; the feedstock was a blend and needed a heat treatment of the as-sprayed deposit to enable the formation of the composite. During oxidation at 650, 800 and 950°C for 1200 h, the aluminum led to alumina; less protective intermetallics resulting from Al depletion of the $TiAl_3$ alloy and (Ti, Nb)$Al_x$ compounds were formed [117–120]. Also, Ti-46Al-8.5Nb-1Ta (at.%) particles were deposited on a commercial alloy IMI-834 and the metastable phases present in the feedstock later transformed to the equilibrium ordered $\gamma$-TiAl and $\alpha_2$-$Ti_3Al$ phases when heat treatment was applied to the as-sprayed deposit [121].

## 2.3. Physical vapor deposition

In PVD processes, reduced pressures are necessary for the coating deposition by condensation from neutral or ionized atoms of metals. Of all the possible PVD techniques, magnetron sputtering and cathodic arc vapor deposition usually result in adherent and dense thin layers at relatively low temperatures. In addition to the dense structure, PVD layers exhibit a nanocrystalline microstructure, which further enhances the adhesion and hardness properties of thin protective coatings.

Intermetallic aluminide coatings produced by PVD processes are mainly investigated to increase oxidation and corrosion resistance of several steel materials, rather than for improving the wear resistance as has been reported in previous coating technologies.

As far as the Fe-Al system is concerned, Fe-40% Al [122] and Fe-45% Al [122–124] were produced, studying the high temperature oxidation resistance. Magnetron sputtered Fe-45% Al

coatings containing different nominal compositions ranging 6.5–45 wt.% Cr and 0.5% Zr were deposited on bulk FeAl and 304 stainless steel. The scale spallation was diminished by the addition of such alloying elements during thermal cycling at 1000 and 1100°C. The resistance to scale spallation was even superior than bulk iron aluminides. The nanostructure of PVD coatings has been reported to improve the oxide scale adherence due to the reduction of the thermal stresses and inducing an anchoring effect as result of the formed oxide intrusions.

Cathodes of Fe-40% Al and Fe-45% Al composition were used by Paldey and Deevi [122] to deposit iron aluminides by means of cathodic arc evaporation, which uses a higher energy input than PVD sputtering processes, and it was observed a reduction of the mass gain during isothermal oxidation at 800°C of 440C steel by four times and also improved the oxidation resistance up to 1000°C of 304SS.

The cyclic thermal oxidation was also evaluated for NiAl PVD coatings to be employed as bond coats in thermal barrier coating (TBC) systems [125]; such bond coats have the role of (i) reducing the mismatch in thermal expansion coating of typically superalloy substrates and ceramic upper coatings and (ii) improving the oxidation resistance. He et al. [125] investigated three routes for the Ni30Al70 deposition on 304 SS and Inconel 600 alloy plates, i.e. arc ion plating (AIP), electron beam evaporative ion plating (EBIP) and sputter ion plating (SIP); description of such techniques can be found elsewhere. The AIP was formed by $NiAl_3$ and $Ni_2Al_3$ phases; the SIP was dominated by $NiAl_3$ and less $Ni_2Al_3$, while EBIP was rather formed by minor $Ni_2Al_3$ in mainly Al. Although such differences in composition, the oxidation resistance was improved at 800 and 1100°C for the two substrates, although by means of different protection mechanisms. Another technique, here cathodic arc plasma (CAP), was used by Chang et al. [126] with the aim to improve the cavitation wear resistance of AISI 1045 steel substrates with $Ni_3Al$ coating through the following target compositions: Ni52Al48, Ni60Al40 and Ni70Al30; the cavitation performance was ameliorated by 10 times to the bare substrate in fresh water and twice in 3.5 wt.% NaCl. Potentiodynamic polarization tests also indicated an improvement on the corrosion resulting in higher corrosion potentials and lower corrosion current densities.

Titanium aluminides seem to have been more extensively studied by PVD methods. Ti-51Al-12Cr at.% magnetron sputtered layers were applied to γ-TiAl substrates and then covered by yttria partially stabilized zirconia to form TBCs. Such layers did not provide long-term protection at 900°C [127].

Predominantly, $(Al,Cr)_2O_3$ films were found to be protective on the TiAlCrN, TiAl55CrSiYN and TiAl60CrSiYN layers deposited by PVD on titanium aluminide alloys, thus improving the isothermal oxidation resistance at 900°C [128].

Good thermal stabilities up to 700°C of titanium aluminide films on $SiO_2$ substrates prove them as candidates for materials for high temperature electronics [129].

When using sputtering, titanium aluminide thin films have been manufactured by the use of different targets: (i) a target of an Al disk mounted on a Ti disk, (ii) one target of titanium and another of aluminum, (iii) the intermetallic target [130–133]. A part from the high temperature performance, the microstructure evolution [131–133], crystallization kinetics [133] and mechanical properties [130] have also been investigated. In some cases, a proper annealing treatment was necessary to achieve the target composition within the deposited film.

## 3. Final remarks

To sum up, thick coating deposition techniques such as welding-related processes can provide significant advantages for repairing purposes and good adhesion being achieved due to the metallurgical bonding mechanism. However, as it is reviewed, uniform compositions are reached hardly, the heat affected zone can induce alteration in substrate microstructure and properties and surface cracking is common resulting from thermal mismatch between the coating and substrate due to their different crystal structure, especially for the Fe-Al and Ti-Al system.

Each depositing method results in its characteristic coating microstructure, also determining of the final properties. Given the interest regarding high temperature applications, usually thick transition aluminide coatings are required in order to form a continuous and stable $Al_2O_3$ layer, especially in the case of titanium aluminides, where thin layers often result in oxide scales containing large amounts of $TiO_2$ which exhibits limited protection. In that case, intermediate coating methods such as thermal spray technologies can be of interest, although good bond strength requires proper mechanical anchoring, also related to convenient matching of thermal expansion coefficients between the coating and substrate.

The oxidation performance up to 900°C in isothermal and cyclic testing conditions and even higher temperatures has raised an interest for nickel and iron aluminides for aeroengines and power generation industries, while that of titanium aluminides has been more focused also for automobile parts. Their degradation in other harsh environments as well as for wear resistance has become frequently investigated during the last decade, giving importance to the use of intermetallic as promising metal matrix for composite coatings in high temperature wear applications.

The use then of intermetallics as coatings can be expanded as long as new compositions can reach protection at more aggressive environments.

Finally, the manufacture of components via additive manufacture technologies occupies more and more references in the literature. Up to this moment, Ni-, Fe- and Ti-based aluminides have been investigated through laser processes. Clearly, this seems to be the trend for the future. Nowadays, additive manufacturing technologies are gaining more importance; especially for this type of materials, where several fabrication issues arising from conventional technologies might be a concern, the build-up of near net shape components through the use powders can be of great interest. The effort, however, is need to be focused on achieving uniform compositions without disparity of undesired phases that may lower the mechanical properties.

## Author details

Núria Cinca i Luis

Address all correspondence to: nucilu7@gmail.com

Department of Materials Science and Physical Chemistry, Universitat de Barcelona, Martí i Franques, Barcelona, Spain

## References

[1] Sauthoff G. Intermetallics. New York: Wiley-VCH Verlagsgesellschaft; 2007. 165 p. ISBN: 978-3-527-61540-7

[2] Cahn RW. Intermetallics: New physics. Contemporary Physics. 2001;**42**(6):365-375

[3] George EP, Yamaguchi M, Kumar KS, Liu CT. Ordered intermetallics. Annual Review of Materials Science. 1994;**24**:409-451

[4] Tabaru T, Hanada S. High temperature strength of Nb-Al-base alloys. Intermetallics. 1998;**6**:735-739

[5] Yeh CL, Yeh CC. Preparation of CoAl intermetallic compound by combustion synthesis in self-propagating mode. Journal of Alloys and Compounds. 2005;**388**(2):241-249

[6] Wolff IM. Toward a better understanding of ruthenium aluminide. Journal of the Minerals Metals & Materials Society. 1997;**49**(1):34-39

[7] Kumar KS, Liu CT. Ordered intermetallic alloys, part II: Silicides, trialuminides, and others. The Journal of The Minerals, Metals & Materials Society. 1993;**45**(6):28

[8] Bax B, Pauly C, Leibenguth P, Woll K, Mücklich F. Synthesis of B2-RuAl coatings on mild steel by laser cladding. Surface and Coatings Technology. 2012;**206**(19-20):3931-3937

[9] Deevi SC, Sikka VK. Nickel and iron aluminides: An overview on properties, processing and applications. Intermetallics. 1996;**4**:357-375

[10] Deevi SC, Sikka VK, Liu CT. Processing, properties and applications of nickel and iron aluminides. Progress in Materials Science. 1997;**42**:177-192

[11] Morris DG, Muñoz-Morris MA. Intermetallics: Past, present and future. Revista de Metalurgia. 2005:498-501

[12] Bose S. High Temperature Coatings. Butterworth-Heinemann: Elsevier; 2007. 312 p. ISBN: 978-0-7506-8252-7

[13] Isaza JF, Aumund-Kopp C. Additive Manufacturing Approaches. In: Structural Materials and Processes in Transportation. Weinheim: Wiley-VCH Verlagsgesellschaft; 2013. pp. 549-566. DOI: 10.1002/9783527649846

[14] Krasnowski M, Kulik T. Nanocrystalline FeAl matrix composites reinforced with TiC obtained by hot-pressing consolidation of mechanically alloyed powders. Intermetallics. 2007;**15**:1377-1383

[15] Çam G, Koçak M. Progress in joining of advanced materials part 1: Solid state joining, fusion joining, and joining of intermetallics. Science and Technology of Welding and Joining. 1998;**3**(3):105-126

[16] Vuoristo P, Tuominen J, Nurminen J. Laser coating and thermal spraying – process basics and coating properties. In: Conference proceedings: ITSC 2005. Basel, Switzerland: International Thermal Spray Conference & Exposition; 2005

[17] Shen C, Pan Z, Ma Y, Cuiuri D, Li H. Fabrication of iron-rich Fe–Al intermetallics using the wire-arc additive manufacturing process. Additive Manufacturing. 2015;**7**:20-26

[18] Shen C, Liss K, Pan Z, Wang Z, Li X, Li H. Thermal cycling of $Fe_3Al$ based iron aluminide during the wire-arc additive manufacturing process: An in-situ neutron diffraction study. Intermetallics. 2018;**92**:101-107

[19] Sahin O, Ribalko AV. Electrospark deposition: mass transfer. In: Mass Transfer – Advanced Aspects. InTech; 2011. DOI: 10.5772/24339. Available from: http://cdn.intechopen.com/pdfs/23531/InTech-Electrospark_deposition_mass_transfer.pdf

[20] Banovic SW, Dupont JN, Tortorelli PF, Marder AR. The role of aluminum on the weldability and sulfidation behavior of iron-aluminum cladding. Welding Journal. 1999; **78**(1):23-30

[21] Maziasz PJ, Goodwin GM, Liu CT, David SA. Effects of minor alloying elements on the welding behavior of FeAl alloys for structural and weld-overlay cladding applications. Scripta Materialia. 1992;**27**:12:1835-1840

[22] Corbin SF, Toyserkani E, Khajepour A. Cladding of a Fe-aluminide coating on mild steel using pulsed laser assisted powder deposition. Materials Science and Engineering A. 2003;**354**(1-2);48-57

[23] Cheng G, He Y. Preparation of deposited coating of Fe-Al intermetallic compound by laser cladding. Transactions of the China Welding Institute; 2006

[24] Bax B, Schäfer M, Pauly C, Mücklich F. Coating and prototyping of single-phase iron aluminide by laser cladding. Surface and Coatings Technology. 2013;**235**:773-777

[25] Chen Y, Wang HM. Growth morphology and mechanism of primary TiC carbide in laser clad TiC/FeAl composite coating. Mater Letters. 2003;**57**:1233-1238

[26] Chen Y, Wang HM. Microstructure and wear resistance of laser clad TiC reinforced FeAl intermetallic matrix composite coatings. Surface and Coatings Technology. 2003; **168**:30-36

[27] Tomida S, Nakata K. Fe-Al composite layers on aluminum alloy formed by laser surface alloying with iron powder. Surface and Coatings Technology. 2003;**174-175**:559-563

[28] Abboud JH, Rawlings RD, West DRF. Functionally graded nickel-aluminide and iron-aluminide coatings produced via laser cladding. Journal of Materials Science. 1995; **30**:5931-5938

[29] Song B, Dongs S, Liao H, Coddet C. Fabrication and microstructure characterization of selective laser-melted FeAl intermetallic parts. Surface and Coatings Technology. 2012; **206**:4704-4709

[30] Rolink G, Vogt S, Sencekova L, Weisheit A, Poprawe R, Pal M. Laser metal deposition and selective laser melting of Fe-28 at.% Al. Journal of Materials Research. 2014;**29**:2036-2043

[31] Durejko T, Lipinski S, Bojar Z, Bystrycki J. Processing and characterization of graded metal/intermetallic materials: The example of Fe/FeAl intermetallics. Materials & Design. 2011;**32**:2827-2834

[32] Song B, Dong S, Liao H, Coddet C. Manufacture of Fe-Al cube part with a sandwich structure by selective laser melting directly from mechanically mixed Fe and Al powders. International Journal of Advanced Manufacturing Technology. 2013;**69**(5-8):1323-1330

[33] Shishkovsky I, Missemer F, Kakovkina N, Smurov I. Intermetallics synthesis in the Fe-Al system via layer by layer 3D laser cladding. Crystals. 2013;**3**:517-529

[34] Durejko T, Zietala M, Polkowski W, Czujko T. Thin Wall tubes with $Fe_3Al$/SS316L graded structure obtained by using laser engineered net shaping technology. Materials & Design. 2014;**63**:766-774

[35] Durejko T, Zietala M, Lazinska M, Lipinski S, Polkowski W, Czujko T, Varin RA. Structure and properties of the Fe3Al-type intermetallic alloy fabricated by laser engineered net shaping (LENS). Materials Science and Engineering A. 2016;**850**:374-381

[36] Michalcová A, Sencekova L, Rolink G, Weisheit A, Pesicka J, Stobik M, Palm M. Laser additive manufacturing of iron aluminides strengthened by ordering, borides or coherent Heusler phase. Materials & Design. 2017;**116**:481-494

[37] Muñoz-Morris MA, Dodge A, Morris DG. Structure, strength and toughness of nanocrystalline FeAl. Nanostructured Materials. 1999;**11**:873-885

[38] Chen Y, Wang HM. Microstructure of laser clad TiC/NiAl-$Ni_3$ (Al, Ti, C) wear-resistant intermetallic matrix composite coatings. Materials Letters. 2003;**57**:2029-2036

[39] Chen Y, Wang HM. Microstructure and wear resistance of a laser clad TiC reinforced nickel aluminides matrix composite coating. Materials Science and Engineering A. 2004; **368**:80-87

[40] Liu K, Li Y, Wang J. In-situ reactive fabrication and effect of phosphorous on microstructure evolution of Ni/Ni-al intermetallic composite coating by laser cladding. Materials & Design. 2016;**105**:171-178

[41] Zhong M, Xu X, Liu W, Sun H. Laser synthesizing NiAl intermetallic and TiC reinforced NiAl intermetallic matrix composite. Journal of Laser Application. 2004;**16**(3):160-166

[42] Duraiselvam M, Galun R, Siegmann S, Wesling V, Mordike BL. Particle-laden liquid impact erosion characteristics of laser clad Ni-based intermetallic matrix composites with TiC and WC reinforcements. Lasers in Engineering. 2005;**15**:355-373

[43] Duraiselvam M, Galun R, Wesling V, Mordike BL, Reiter R, Oligmüller J. Cavitation erosion resistance of AISI 420 martensitic stainless steel laser-clad with nickel aluminide intermetallic composites and matrix composites with TiC reinforcement. Surface and Coatings Technology. 2006;**201**:1289-1295

[44] Duraiselvam M, Galun R, Wesling V, Mordike BL. Laser clad WC reinforced Ni-based intermetallic-matrix composites to improve cavitation erosion resistance. Journal of Laser Application. 2006;**18**:297-304

[45] Yu Y, Zhou J, Chen J, Zhou H, Guo C, Wang L, Yang L. Preparation, microstructure and tribological behavior of laser cladding NiAl intermetallic compound coatings. Wear. 2012; **274-275**:298-305

[46] Wang CS. Defence Technology. Influence of yttrium on microstructure and properties of NiAl alloy coatings prepared by laser cladding. Defence Technology. 2014;**10**:22-27

[47] Lu W, Dupont JN. In-situ reactive processing of nickel aluminides by laser-engineered net shaping. Metallurgical and Materials Transactions A. 2003;**34A**:2633-2641

[48] Uenishi K, Kabayashi K. Formation of surface layer based on $Al_3Ti$ on aluminum by laser cladding and its compatibility with ceramics. Intermetallics. 1999;**7**:553-559

[49] Abboud J, West DRF, Rawlings RD. Functionally gradient titanium-aluminide composites produced by laser cladding. Journal of Materials Science. 1994;**29**:3393-3398

[50] Guo B, Zhou J, Zhang S, Zhou H, Pu Y, Chen J. Phase composition and tribological properties of Ti-Al coatings produced on pure Ti by laser cladding. Applied Surface Science. 2007;**253**:9301-9310

[51] Pu Y, Guo B, Zhou J, Zhang S, Zhou H, Chen J. Microstructure and tribological properties of in situ sunthesized TiC, TiN, and SiC reinforced Ti3Al intermetallic matrix composite coatings on pure Ti by laser cladding. Applied Surface Science. 2008;**255**:2697-2703

[52] Li J, Chen C, Squartini T, He Q. A study on wear resistance and microcrack of the $Ti_3Al$/TiAl + TiC ceramic layer deposited by laser cladding on Ti6Al4V alloy. Applied Surface Science. 2010;**257**:1550-1555

[53] Guo B, Zhou J, Zhang S, Zhou H, Pu Y, Chen J. Tribological properties of titanium aluminides coatings produced on pure Ti by laser surfase alloying. Surface and Coatings Technology. 2008;**202**:4121-4129

[54] Li J, Chen C, Wang D. Surface modification of titanium alloy with laser cladding RE oxides reinforced $Ti_3Al$-matrix composites. Composites: Part B. 2012;**43**:1207-1212

[55] Cárcel B, Serrano A, Zambrano J, Amigó V, Carcel AC. Laser cladding of TiAl intermetallic alloy on Ti6Al4V. Process optimization and properties. Physics Procedia. 2014; **56**:284-293

[56] Zhang XD, Brice C, Mahaffey DW, Zhang H, Schwedner K. Characterization of laser-deposited TiAl alloys. Scripta Materialia. 2001;**44**:2419-2424

[57] Qu HP, Li P, Zhang SQ, Li A, Wang HM. The effects of heat treatment on the microsctructure and mechanical property of laser melting deposition γ-TiAl intermetallic alloys. Materials & Design. 2010;**31**:2201-2210

[58] Frangini S, Masci A. Intermetallic FeAl based coatings deposited by the electrospark technique: Corrosion behavior in molten (Li + K) carbonate. Surface and Coatings Technology. 2004;**184**:31-39

[59] Jamnapara NI, Frangini S, Alphonsa J, Chauhan NL, Mukherjee S. Comparative analysis of insulating properties of plasma and thermally grown alumina films on electrospark aluminide coated 9Cr steels. Surface and Coatings Technology. 2015;**266**:146-150

[60] Paustovskii AV, Alfintseva RA, Pyatachuk SG, Treshchenko VS, Novikova VI, Mordovets NM. Properties of spark-deposited Ni–Cr–NiAl coatings. Powder Metall Metal Ceramics. 2009:**48**(7-8):429-434

[61] Heard DW, Brochu M. Development of a nanostructure microstructure in the Al–Ni system using the electrospark deposition process. Journal of Materials Processing Technology. 2010;**210**:892-898

[62] Li Z, Gao W, Yoshihara M, He Y. Improving oxidation resistance of $Ti_3Al$ and TiAl intermetallic compounds with electro-spark deposit coatings. Materials Science and Engineering A. 2003;**347**:243-252

[63] Fauchais PL, Heberlein JVR, Boulos M. Thermal spray fundamentals: From powder to part, springer. Science. 2014

[64] Cinca N, Guilemany JM. Thermal spraying of transition metal aluminides: An overview. Intermetallics. 2012;**24**:60-72

[65] Amiriyan M., Alamdari HD, Blais C, Savoie S, Schulz R, Gariépy M. Dry sliding wear behavior of $Fe_3Al$ and $Fe_3Al$/TiC coatings prepared by HVOF. Wear. 2015: **342-343**(15):154-162

[66] Pougoum F, Schmitt T, Martinu L, Ewa J, Sapieha K, Savoie S, Schulz R. Wear behavior of $Fe_3Al$-TiN-$TiB_2$ HVOF coatings: A comparative study between in situ and ex situ powder processing routes. Ceramics International. 2017;**43(**11):8040-8050

[67] Thiem PG, Chornyi A, Smirnov IV, Krüger M. Comparison of microstructure and adhesion strength of plasma, flame and high velocity oxy-fuel sprayed coatings from an iron aluminide powder. Surface and Coatings Technology. 2017;**324**:498-508

[68] Wang Y, Yan M. The effect of $CeO_2$ on the erosion and abrasive wear of thermal sprayed FeAl intermetallic alloy coatings. Wear. 2006;**261**:(11-12);1201-1207

[69] Xu B, Zhu Z, Ma S, Zhang W, Liu W. Sliding wear behavior of Fe–Al and Fe–Al/WC coatings prepared by high velocity arc spraying. Wear. 2004;**257**:1089-1095

[70] Cinca N, Dosta S, Cano IG, Guilemany JM, Cygan S, Jaworska L, Senderowski C. Sliding wear behavior of Fe–Al coatings at high temperature. In: International Thermal Spray Conference 2017. Düsseldorf, Germany DVS-German Welding Society

[71] Magnee A, Offergeld E, Leroy M, Lefort A. Fe-Al intermetallic coating applications to thermal energy conversion advanced systems. In: Proceedings of the 15th Thermal Spray Conference. Vol. 2. Nice, France. ASM International; 1998; pp. 1091-1096

[72] Natesan K. Corrosion performance of iron aluminides in mixed-oxidant environments. Materials Science and Engineering A. 1998;**258**(1-2):126-134

[73] Xiao C, Chen W. Sulfidation resistance of $CeO_2$-modified HVOF sprayed FeAl coatings at 700°C. Surface and Coatings Technology. 2006;**201**:3625-3632

[74] Shankar Rao V. A review of the electrochemical corrosion behaviour of iron aluminides. Electrochimica Acta. 2004;**49**:4533-4542

[75] Rodríguez-Díaz RA, Uruchurtu-Chavarín J, Molina-Ocampo A, Porcayo-Calderón J, González-Pérez M, López-Oglesby JM, Gonzalez-Rodríguez JG, Juárez-Islas JA. Corrosion behavior of Fe-Al alloy modified with Cr and Ti in simulated physiological human media. International Journal of Electrochemical Science. 2013;**8**:958-972

[76] Osório WR, Peixoto LC, Goulart PR, Garcia A. Electrochemical corrosion parameters of as-cast Al–Fe alloys in a NaCl solution. Corrosion Science. 2010;**52**:2979-2993

[77] Kowalski K, Łosiewicz B, Budniok A, Kupka M. Effect of alloying on corrosion resistance of B2 FeAl alloy in aqueous solution of sulfuric acid. Materials Chemistry and Physics. 2011;**126**:314-318

[78] Sharma G, Singh PR, Sharma RK, Gaonkar KB, Ramanujan RV. Aqueous corrosion behavior of iron aluminide intermetallics. Journal of Materials Engineering and Performance (JMEP). 2007;**16**:779-783

[79] Ji G, Elkedim O, Grosdidier T. Deposition and corrosion resistance of HVOF sprayed nanocrystalline iron aluminide coatings. Surface and Coatings Technology. 2005;**190**:406-416

[80] Senderowski C, Chodala M, Bojar Z. Corrosion behavior of detonation gun sprayed Fe-Al type intermetallic coating. Materials. 2015;**8**:1108-1123

[81] Hearley JA, Little JA, Sturgeon AJ. The effect of spray parameters on the properties of high velocity oxy-fuel NiAl intermetallic coatings. Surface and Coatings Technology. 2000; **123**:210-218

[82] Hu W, Li M, Fukumoto M. Preparation and properties of HVOF NiAl nanostructured coatings. Materials Science and Engineering A. 2008;**478**:1-8

[83] Scrivani A, Ianelli S, Rossi A, Groppetti R, Casadei F, Rizzi G. A contribution to the surface analysis and characterisation of HVOF coatings for petrochemical application. Wear. 2001;**250**:107-113

[84] Benegra M, Santana ALB, Maranho O, Pintaude G. Effect of heat treatment on wear resistance of nickel Aluminide coatings deposited by HVOF and PTA. Journal of Thermal Spray Technology. 2015;**24**(6):1111-1116

[85] Enayati MH, Karimzadeh F, Jafari M, Markazi A, Tahvilian A. Microstructural and wear characteristics of HVOF-sprayed nanocrystalline NiAl coating. Wear. 2014;**309**:192-199

[86] Wang B, Lee SW. Erosion-corrosion behaviour of HVOF NiAl–$Al_2O_3$ intermetallic-ceramic coating. Wear. 2000;**239**:83-90

[87] Wang Z, Zhou L, Guo J, Hu Z, Mocaxue X. Wear bahavior of in situ composite NiAl-$Al_2O_3$-TiC at high temperature. Tribology. 2008;**28**(6):497-502

[88] Culha O, Celik E, Ak Azem NF, Birlik I, Toparli M, Turk A. Microstructural, thermal and mechanical properties of HVOF sprayed Ni–al-based bond coatings on stainless steel substrate. Journal of Materials Processing Technology. 2008;**204**:221-230

[89] Wang Z, Zhou L, Guo J, Hu Z. Wear bahavior of in situ composite NiAl-$Al_2O_3$-TiC at high temperature. Available from: http://en.cnki.com.cn/Article_en/CJFDTOTAL-MCXX200806003.htm

[90] Hearley JA, Little JA, Sturgeon AJ. Oxidation properties of NiAl intermetallic coatings prepared by high velocity oxy-fuel thermal spraying. In: Proceedings of the 15th Thermal Spray Conference. Vol. 2. Nice, France. ASM International; 1998. pp. 89-94

[91] Wang Y, Chen W. Microstructures, properties and high-temperature carburization resistances of HVOF thermal sprayed NiAl intermetallic-based alloy coatings. Surface and Coatings Technology. 2004;**183**(1):18-28

[92] Wang Y, Yang Y, Yan MF. Microstructures, hardness and erosion behavior of thermal sprayed and heat treated NiAl coatings with different ceria. Wear. 2007;**263**:371-378

[93] Starosta R. Properties of thermal spraying Ni-al alloy coatings. Advanced Materials Science. 2009;**9**(1):30-40

[94] Cao P, Gabbitas B, Salman A, Zhang DL, Han ZH. Consolidation of TiAl powder by thermal spray processes. Advanced Materials Research. 2007;**29-30**:159-162

[95] Hao-Hsin HJ, Lung CY, Liang J. Reciprocating wear properties of thermal sprayed titanium aluminide–alumina composite coatings. Surface and Coatings Technology. 2004; **182**:363-369

[96] Dewald D, Austin M, Laitila E, Mikkola D., Cubic titanium trialuminide thermal spray coatings – A review. Journal of Thermal Spray Technology. 2001;**10**:1:111-117

[97] Khor KA, Murakoshi Y, Takashi M, Sano T. Microstructure changes in plasma sprayed TiAl coatings after hot isostatic pressing. Journal of Materials Science Letters. 1996; **15**:1801-1804

[98] Salman A, Gabbitas B, Li J, Zhang D. Tribological properties of thermally sprayed TiAl-$Al_2O_3$ composite coating: In: IOP Conference Series Materials Science and Engineering. Vol. 4. 2009. pp. 1-5

[99] Lee JK, Oh MH, Lee HK, Wee DM. Plasma-sprayed Al-21Ti-23Cr coating for oxidation protection of TiAl alloys. Surface and Coatings Technology. 2008;**202**(5):599-602

[100] Honda K, Hirose A, Kobayashi KF. Properties of titanium-aluminide layer formed by low pressure plasma spraying. Materials Science and Engineering A. Structural Materials: Properties, Microstructure and ProcessingStructural Materials: Properties, Microstructure and Processing. 1997;**222**(2):212-220

[101] Hao-Hsin HJ, Lung CY, Liang J. Reciprocating wear properties of thermal sprayed titanium aluminide-alumina composite coatings. Surface and Coatings Technology. 2004;**182**:363-369

[102] Salman A, Gabbitas B, Li J, Zhang D. Tribological properties of thermally sprayed TiAl-$Al_2O_3$ composite coating. In: IOP Conference Series Materials Science and Engineering. 2009;**4**:1-5

[103] Shemet V, Tyagi AK, Becker JS, Lersch P, Singheiser L, Quadakkers WJ. The formation of protective alumina-based scales during high-temperature air oxidation of $\gamma$-TiAl alloys. Oxidation of Metals. 2000;**54**(3-4):211-235

[104] Honda K, Hirose A, Kobayashi KF. Properties of titaniumealuminide layer formed by low pressure plasma spraying. Materials Science and Engineering A. 1997;**222**(2):212-220

[105] Dewald D, Austin M, Laitila E, Mikkola D. Cubic titanium trialuminide thermal spray coatings – A review. Journal of Thermal Spray Technology. 2001;**10**(1):111-117

[106] Sienkiewicz J, Kuroda S, Molak RM, Murakami H, Araki H, Takamori S, Kurzydlowski KJ. Fabrication of TiAl intermetallic phases by heat treatment of warm sprayed metal precursors. Intermetallics. 2014;**49**:57-64

[107] Wang H-T, Li C-J, Yang G-J, Li C-X. Cold spraying of Fe/Al powder mixture: Coating characteristics and influence of heat treatment on the phase structure. Applied Surface Science. 2008;**255**:2538-2544

[108] Cinca N, List A, Gärtner F, Guilemany JM, Klassen T. Influence of spraying parameters on cold gas spraying of iron aluminide intermetallics. Surface and Coatings Technology. 2015;**268**:99-107

[109] Dietrich D, Cinca N, Sokołowski P, Drehmann R, Pawlowski L, Guilemany JM, Lampke T., Adiabatic shear loading on thermal spray coatings studied by EBSD. In: 16th European Microscopy Congress, Lyon (France), 2016. Poster Contribution

[110] Cinca N, List A, Gärtner F, Guilemany JM, Klassen T. Coating formation, fracture mode and cavitation performance of Fe40Al deposited by cold gas spraying. Surface Engineering. 2015;**31**(11):853-859

[111] Cinca N, Dosta S, Cano IG, Guilemany JM, Pflumm R, Rudolphi M, Galetz M. Isothermal and cyclic oxidation of CGS and HVOF iron aluminide coatings. In: International Thermal Spray Conference, Dusseldorf (Germany) 2017. Poster Contribution

[112] Lee H, Shin H, Ko K. Effects of gas pressure of cold spray on the formation of Al-based intermetallic compound. The Journal of Thermal Spray Technology. 2009;**19**:(1-2);102-109

[113] Zhang Q, Li C, Wang X, Ren Z, Li C, Yang G. Formation of NiAl intermetallic compound by cold spraying of ball-milled Ni/Al alloy powder through postannealing treatment. The Journal of Thermal Spray Technology. 2008;**17**:(5-6):715-720

[114] Bacciochini A, Bourdon-Lafleur S, Poupart C, Radulescu M, Jodoin B. Ni-Al nanoscale energetic materials: phenomena involved during the manufacturing of bulk samples by cold spray. The Journal of Thermal Spray Technology. 2014;**23**(7);1142-1148

[115] Sharma A, Gambino RJ, Sampath S. Anisotropic electrical properties in thermal spray coatings. Acta Materialia. 2006;**54**(1):59-65

[116] Azarmi F, Tangpong XW, Chandanayaka T. Investigation on mechanical properties of cold sprayed Ni–$Ni_3Al$ composites. Surface Engineering. 2015;**31**(11):832-839

[117] Kong L, Lu B, Cui X, Du H, Li T, Xiong T. Oxidation behavior of $TiAl_3$/Al composite coating on orthorhombic-$Ti_2AlNb$ based alloy at different temperatures. The Journal of Thermal Spray Technology. 2010;**19**(3):650-656

[118] Shen L, Kong L, Xiong T, Du H, Li T. Preparation of $TiAl_3$-Al composite coating by cold spraying. Transactions of the Nonferrous Metals Society of China. 2009;**19**:879-882

[119] Kong LY, Shen L, Lu B, Yang R, Cui XY, Li TF, Xiong TY. Preparation of $TiAl_3$-Al composite coating by cold spray and its high temperature oxidation behavior. The Journal of Thermal Spray Technology. 2010;**19**(6):1206-1210

[120] Novoselova T, Celotto S, Morgan R, Fox P, O'Neill W. Formation of TiAl intermetallics by heat treatment of cold-sprayed precursor deposits. Journal of Alloys and Compounds. 2007;**436**:69-77

[121] Gizynski M, Miyazaki S, Sienkiewicz J, Kuroda S, Araki H, Murakami H, Pakiela Z, Yumoto A. Formation and subsequent phase evolution of metastable Ti-Al alloy coatings by kinetic spraying of gas atomized powders. Surface and Coatings Technology. 2017;**315**:240-249

[122] PalDey S, Deevi SC. Cathodic arc deposited FeAl coatings: Properties and oxidation characteristics. Materials Science and Engineering. 2003;**A355**:208-215

[123] Liu Z, Gao W. Effects of chromium on the oxidation performance of β-FeAlCr coatings. Oxidation of Metals. 2000;**54**(3-4):189-209

[124] Liu Z, Gao W, Wang F. Oxidation resistance of magnetron sputter deposited ß-FeAl+ Zr coatings. High Temperature Material Processes. 2000;**19**(6):419-426

[125] He JL, Yu CH, Leyland A, Wilson AD, Matthews A. A comparative study of the cyclic thermal oxidation of PVD nickel aluminide coatings. Surface and Coatings Technology. 2002;**155**:67-79

[126] Chang JT, Yeh CH, He JL, Chen KC. Cavitation erosion and corrosion behavior of Ni–Al intermetallic coatings. Wear. 2003;**255**:162-169

[127] Braun R, Fröhlich M, Braue W, Leyens C. Oxidation behaviour of gamma titanium aluminides with EB-PVD thermal barrier coatings exposed to air at 900°C. Surface and Coatings Technology. 2007;**202**:676-680

[128] Dosbaeva GK, Veldhuis SC, Yamamoto K, Wilkinson DS, Beake BD, Jenkins N, Elfizy A, Fox-Rabinovich GS. Oxide scales formation in nano-crystalline TiAlCrSiYN PVD coatings at elevated temperature, Int. Journal of Refractory Metals & Hard Materials. 2010;**28**:133-141

[129] Kim HC, Theodore ND, Gadre KS, Mayer JW, Alford TL. Investigation of thermal stability, phase formation, electrical, and microstructural properties of sputter-deposited titanium aluminide thin films. Thin Solid Films. 2004;**460**:17-24

[130] Vieira MT, Trindade B, Ramos AS, Fernandes JV, Vieira MF. Mechanical characterisation of γ-TiAl thin films obtained by two different sputtering routes. Materials Science and Engineering A. 2002;**329-331**:147-152

[131] Senkov N, Uchic MD. Microstructure evolution during annealing of an amorphous TiAl sheet. Materials Science and Engineering A. 2003;**340**:216-224

[132] Wang Z, Shao G, Tsakiropoulos P, Wang F. Phase selection in magnetron sputter-deposited TiAl alloy. Materials Science and Engineering A. 2002;**329-331**:141-146

[133] Banerjee R, Swaminathan S, Wiezorek JMK, Wheeler R, Fraser HL. Crystallization of amorphous phase in sputter-deposited Ti-Al alloy thin films. Metallurgical and Materials Transactions A: Physical Metallurgy and Materials Science. 1996;**27A**:2047-2050

Chapter 9

# Physical Properties of Yttrium-Rhodium and Yttrium-Copper B2-Type Rare Earth Intermetallic Compounds: First Principles Study

Abdessamad Sekkal, Mohamed Sahlaoui and Abdelnour Benzair

Additional information is available at the end of the chapter

http://dx.doi.org/10.5772/intechopen.73189

**Abstract**

The electronic structure of B2-YCu and YRh intermetallic compounds which crystallize in the CsCl structure has attracted the attention of the scientific world because of their excellent mechanical properties. The advantage of studying these materials is to answer of some industrial request in the materials that resist for high temperature and high oxidation resistance. However, high ductility has been observed in these compounds at room temperature. In this present work, we employed ab initio calculation methods while basing on the full-potential linearized augmented plane wave (FP-LAPW) method within density functional theory implanted in the Wien-2 k code, which is used to examine the various properties of these materials (YCu, YRh) like structural, electronic, and elastic properties. The results obtained are in good agreement with those found in other theoretical studies and experimental data.

**Keywords:** intermetallic compounds, electronic structure, elastic properties, FP-LAPW method

## 1. Introduction

The intermetallic compounds typically possess chemical, physical, and mechanical properties superior to those of ordinary metals. They have many applications in engineering due to their high melting points, high tensile strength, good stiffness, low density, high corrosion, and oxidation resistances at elevated temperature [1, 2]. However, the brittle comportment and low ductility of these intermetallics at ambient temperature severely limit their application.

The previous studies revealed that the brittleness of intermetallic systems increases when the symmetry of the unit cell decreases and the number of atoms by unit cell increases [3]. In 2003, it has been discovered by scientists at Ames Laboratory (Iowa University) that a new type of binary stoichiometric rare earth intermetallic compounds possesses high ductility at room temperature [4–6]. They have B2 CsCl-type structure with equal atomic ratios and have R-M formula, where R is the rare earth and M is the transition metal. YCu and YRh are typical members of this family of B2 ductile rare earth intermetallics. Furthermore, many experimental and theoretical works have examined these compounds. The phase stability, elastic constants, and electronic structure of YCu have been recently studied by ab initio calculations [7–9]. The electronic properties of YCu and YRh were calculated by Khadeer et al. [10] utilizing TB-LMTO technique. The crystal-field (CF) parameters and electronic structure of YRh and YCu crystals were calculated by Divis and Kuriplach [11]. In the last years, an ab initio study of structural, elastic, and electronic properties of YRh has been reported in Refs. [12–14]. The dissociation and core properties of dislocations in YCu were investigated by using the generalized Peierls-Nabarro formalism [15]. The ductility mechanism of YCu and YRh has been determined in Ref. [12]. Chouhan et al. [16] have also studied the electronic, thermoelastic, and mechanical properties of YCu. The rare earth ions in intermetallic compounds are generally trivalent [17]. The result indicates that YRh has more significant ductility than YCu. To understand some of the physical properties of these compounds, the electronic structures of these compounds are required. In this chapter, we present ab initio calculations of the properties of YRh and YCu compounds, including the structural parameters, elastic constants, band structure, and density of state (DOS), which are computed and compared with the available theoretical and experimental results.

## 2. Methodology

In this work, we have employed the full-potential linearized augmented plane wave (FP-LAPW) method [18, 19] as implanted in the Wien-2 k code developed by Blaha et al. [20]. The exchange and correlation effects are described in the framework of the density functional theory with the parameterization of Perdew et al. [21]. To confirm the convergence of our calculations, we carefully investigate the dependence of total energy of the cutoff energy and the k-point set mesh according to the Monkhorst pack grid [22]. The unit cell is divided into no overlapping muffin-tin spheres of radius $R_{MT}$ and an interstitial region, where the Kohn-Sham wave functions are expressed in spherical harmonic functions within spheres and plane waves in the remaining space of unit cell. We use the value of $R_{MT}$. $K_{max}$ equal to 8 which determines the matrix size, where $K_{max}$ is the PW cutoff and $R_{MT}$ is the muffin-tin radius. Basis functions, charge density, and potential were expanded inside the muffin-tin spheres in spherical harmonic functions with cutoff $l_{max} = 10$ and in Fourier series in the interstitial region. The iteration process was repeated until the calculated total energy of the crystal converged to less than 0.5 mRy/unit cell. A mesh of 35 special k-points is used in the irreducible wedge of the Brillouin zone. We have taken the $R_{MT}$ for Y, Cu, and Rh equal to 2.0, 1.87, and 2.3 a.u., respectively. YRh and YCu crystallize in the B2 CsCl-type structure with space group Pm3m-*N*° 221, where Rh and Cu atoms are occupied (½, ½, ½) position and Y occupy (0, 0, 0) position. The following basic orbital is used:

http://dx.doi.org/10.5772/intechopen.73189

Y: $5s^2$, $5p^0$, $4d^1$

Cu: $4s^1$, $3d^{10}$, $4p^0$

Rh: $5s^2$, $5p^0$, $4d^8$

## 3. Lattice parameters and elastic properties

As a first step, the total energy of YCu and YRh was calculated at many different volumes around equilibrium fitted to Murnaghan's equation of state [23] from which we obtained the equilibrium structural parameters. This is performed by applying hydrostatic pressure by changing the lattice parameters while keeping the c/a and b/a ratios constant with the optimized volume. The variation of the total energy with the relative volume for YCu and YRh compounds is given in **Figure 1(a, b)**. The calculated equilibrium lattice parameter and the bulk modulus of each of these compounds, which are in the B2 structure, are compared with the available experimental data and some theoretical results. They are tabulated in **Table 1**. The calculated lattice parameters and the bulk modulus (B) for YCu are in good agreement with those measured experimentally. Hence, we can conclude that the computation parameters and conditions selected in the present work should be suitable. The calculated values of the Bulk modulus (B) are 70.149 and 108.507 GPa for YCu and YRh compounds, respectively, indicating a disagreement with those found by Khadeer and coworkers [10] which indicates values of 97.49 GPa for YCu and 49 for YRh obtained by TB-LMTO method within the atomic sphere approximation (ASA). The difference is essentially due to the fact that they used the LDA approximation with relativistic effect, while we have used the GGA approximation. So, there are no experimental results available to us for YRh compounds. We have also calculated the elastic constants ($C_{11}$, $C_{12}$, and $C_{44}$) in B2 phase at the equilibrium volume for these cubic compounds using the method discussed in detail in Ref. [28]. In all cases the comparison is quite agreeable. The largest

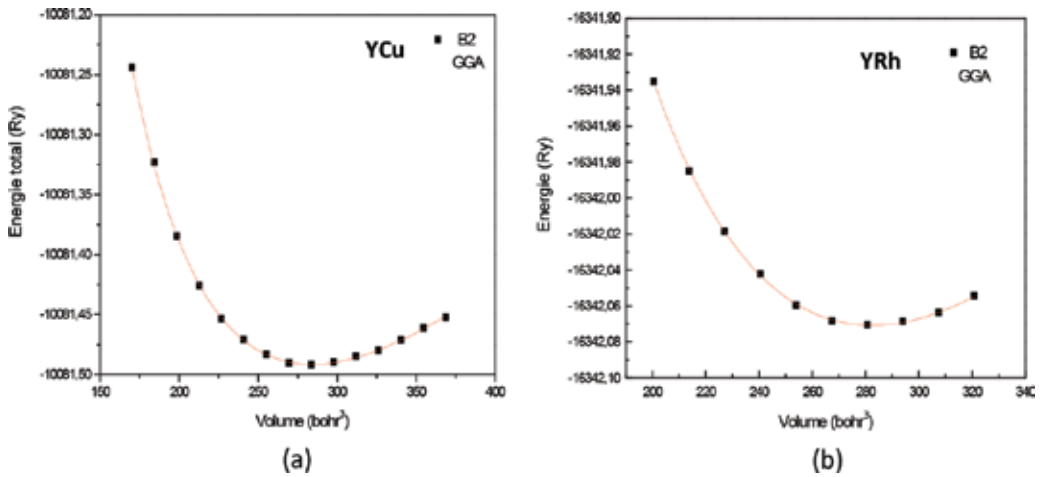


**Figure 1.** Calculated total energies as a function of volume in B2 phase for YCu (a) and YRh (b).

| | YCu | | | YRh | | |
|---|---|---|---|---|---|---|
| | **Present** | **Exp.** | **Other theories** | **Present [14]** | **Exp.** | **Other theories** |
| $a_0$ (A°) | 3.47 | 3.477 [7] | 3.475 [24], 3.418 [10], 3.478 [16] | 3.47 | 3.408 [11], 3.415 [12] | 3.368 [12], 3.43 [13] |
| B (GPa) | 70.14 | 70.1 [7], 70.0 [25] | 97 [10], 70 [7], 70 [25], 69.8 [16] | 108.50 | / | 113.4 [12], 115.78 [13], 49 [10] |
| $C_{11}$ (GPa) | 116.94 | 113.4 [7] | 117.7 [26], 113.6 [12], 116 [7], 114.4 [25], 121.9 [16] | 133.48 | / | 171.0 [12], 186.47 [13] |
| $C_{12}$ (GPa) | 46.43 | 48.4 [7] | 47.2 [26], 48.4 [12], 47 [7], 47.8 [25], 49.1 [16] | 96.01 | / | 83.6 [12], 80.44 [13] |
| $C_{44}$ (GPa) | 32.05 | 32.3 [7] | 36.1 [26], 36.8 [12], 35 [7], 34.3 [25], 35.7 [16] | 20.14 | / | 38.4 [12], 51.64 [13] |
| *G* (GPa) | 33.33 | 32.38 [27] | 35.25 [26], 35.9 [16] | 19.57 | / | / |
| *B*/*G* | 2.10 | 2.140 [7] | 1.977 [26], 1.944 [16] | 5.54 | / | / |
| *A* | 0.90 | 0.99 [7] | 1.02 [26], 0.98 [16] | 1.07 | / | / |
| ν | 0.284 | 0.299 [7] | 0.286 [26], 0.289 [16] | 0.41 | / | / |
| *E* (GPa) | 133.333 | 85.1 [16] | 91.80 [26], 92.7 [16] | 78.31 | / | / |

Note that the values of our calculations are given at T = 0 K values, while the experiments are given at room temperature.

**Table 1.** Lattice parameter and elastic constants ($C_{ij}$) for YCu and YRh compounds. The bulk modulus (*B*), shear modulus (*G*), elastic anisotropy (*A*), Poisson's ratio (*ν*), Young's modulus (*E*) and available experimental values are also given.

discrepancy between theory and experiment is the value for $C_{12}$ for YCu, where the difference is approximately 4.24%. The value for $C_{11}$ is also different by 3%. Our calculated positive value of the elastic constants ($C_{12} > 0$, $C_{11} > 0$, $C_{44} > 0$, and $C_{11} + 2C_{12} > 0$) is an indication of the mechanical stability of YCu and YRh. There are no experimental results available to us for YRh compound. We hope that our present work will stimulate some more works in the YRh compound.

In addition, the elastic constants are correlated to numerous macroscopic parameters as the shear modulus (*G*), Young's modulus (*E*), Poisson's ratio (*ν*), and the elastic anisotropy (*A*). The results obtained by our method (FP-LAPW) of calculation are presented in **Table 1**, including the experimental data and those obtained by other numerical approaches.

The polycrystalline shear modulus is associated with the resistance to plastic deformation, while the bulk modulus represents the opposition to band rupture. The polycrystalline shear modulus is described by equation [7]:

$$G = \frac{C_{11} - C_{12} + 3C_{44}}{5} \tag{1}$$

as well as the bulk modulus (*B*) is given by the following equation:

$$B = \frac{C_{11} + 2C_{12}}{3} \tag{2}$$

Young's modulus expresses the rigidity of the material. For a cubic structure, it is related to the shear modulus and bulk modulus by [29]

$$E = \frac{9BG}{3B+G} \tag{3}$$

The relation between Poisson's ratio and the elastic constants is expressed by

$$\nu = \frac{C_{12}}{C_{11}-C_{12}} \tag{4}$$

It is well known that microcracks are easily induced in the material due to the significant elastic anisotropy. Hence, it is very important to calculate the elastic anisotropy factor ($A$) in order to improve their mechanical durability. The elastic constants can be described by the following expression [7]:

$$A = 2\frac{c_{44}}{c_{11}-c_{12}} \tag{5}$$

The elastic constants ($C_{ij}$) permit calculation of Pugh's factor [30] for these materials investigated here. Pugh proposed that for materials with melting temperature above 900°C, the bulk modulus ($B$) divided by the shear modulus ($G$) predicts whether the material is expected to deform in a ductile or brittle manner: if $B/G > 1.75$, then the ductile behavior is predicted, else the materials have brittle behavior. Therefore, using the relation between the bulk modulus ($B$), shear modulus ($G$), and the elastic constants ($C_{ij}$), the ratio $B/G$ can be calculated for RM (M = Cu and Rh). From **Table 1**, the value of Pugh's factor (2.104) for YCu is consistent with the recent theoretical and experimental studies.

The calculated Poisson's ratio (ν) and the anisotropy constant ($A$) are also given in **Table 1**. For YCu, one can observe that the calculated value of the elastic anisotropy ($A$) is inferior to the experimental value [7]; the error is around 8%. For Poisson's ratio ($\nu$), we find a good agreement with the theoretical studies and the experimental data. The values of anisotropy factor calculated are close to unity signifying that the YCu and YRh studied have isotropic elasticity.

In **Table 1**, we also observed that the YCu material has a low bulk modulus (70.149 GPa) and a relatively low B/G ratio (2.104), which reflects a high value of shear modulus (G). As a result, YCu undergoes a lower deformation than YRh compound. YRh is more ductile than YCu (due to the relatively low shear modulus (19.578 GPa) and high bulk modulus (108.507 GPa)) and has less rigid structure ($E_{(YRh)} < E_{(YCu)}$). This tendency underlines proportionality found between the toughness and the ductility.

## 4. Band structure calculation and density of state (DOS)

In this section, it is interesting to examine the electronic structure for YCu and YRh compounds at equilibrium volume using the accurate full-potential linearized augmented plane

wave (FP-LAPW) method with PBE-GGA approximation. The calculated band energies along the higher symmetry directions are presented in **Figure 2**. It can be seen that both materials possess a large dispersions of the free electrons around Γ point and an overlap of the bands, which confirm us the metallic character. The overall band profiles obtained in the present work are in fairly good agreement with the tight-binding linear muffin-tin orbital (TB-LMTO) calculations [10, 11] using the LDA approximation. In **Figure 2a**, the bands in the energy domain between −4 and −2 eV are largely predominant by the *d* states of the Cu atom. The bands near the Fermi energy (EF) are due to Y-d states. Some bands lying around −3.0 eV, following along the direction + Γ are nearly flat, indicating that the recovery of the orbital between the neighboring atoms is more restricted, and other bands of high energy that are around 4.0 eV present a large dispersion. For YRh, below the Fermi energy, the bands are predominantly by Rh-d states, while at high energies, one can find bands due to Y-d states. A pseudo-gap was also observed at the Fermi energy level. The bands are narrow. They are characterized by a doubly degeneration of bands in the point Γ; it is due to the cubic symmetry of crystals (**Figure 2b**).

The density of state (DOS) for YCu and YRh compounds is calculated in B2 phase by the method of the standard tetrahedron [29]. The total and partial densities of states have also been plotted for both YCu and YRh and are shown in **Figures 3** and **4**, respectively. From these figures, the following observations have been made. For YCu, we find that the large occupied peak is located at energy range between −6.0 and −1.9 eV in valence region, which is dominated by Cu-d state below the Fermi energy ($E_F$ = 0.621 eV). In the

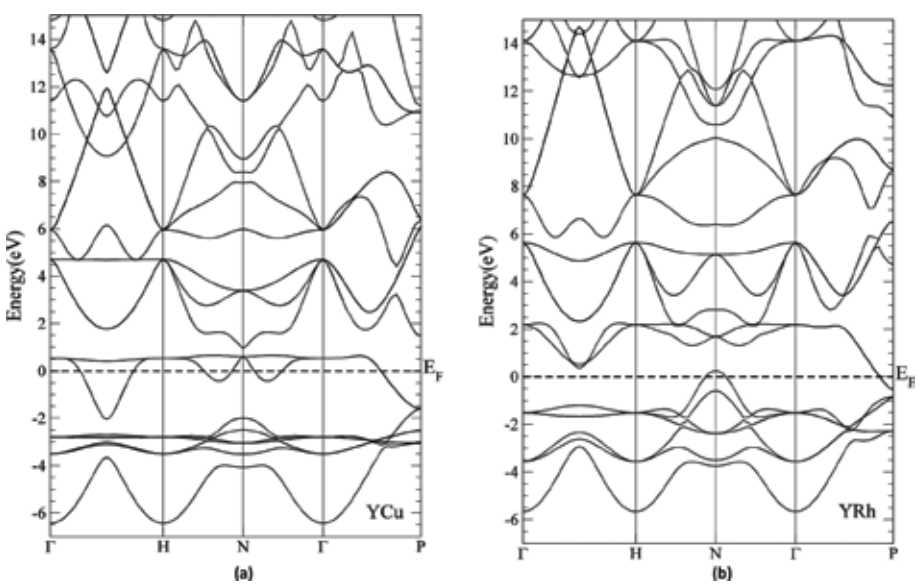


**Figure 2.** Band structure for YCu (a) and YRh (b) in B2 phase.

http://dx.doi.org/10.5772/intechopen.73189

conduction band above the Fermi level, the states are mainly due to Y-d state. The DOS of YRh (**Figure 4**) is similar to YCu, while the large occupied peak is dominated by the Rh-d state in the valence band (states below the Fermi level $E_F$ = 0.773 eV). At higher energy around 4 eV, one can find DOS mainly due to Y-d states. The location of the Fermi level near a local minimum in the DOS is very important for the stability of these binary rare earth intermetallic compounds. We have also observed that the densities of states at the Fermi level *N (EF)* are different to zero which indicates the metallic character for YRh and YCu.

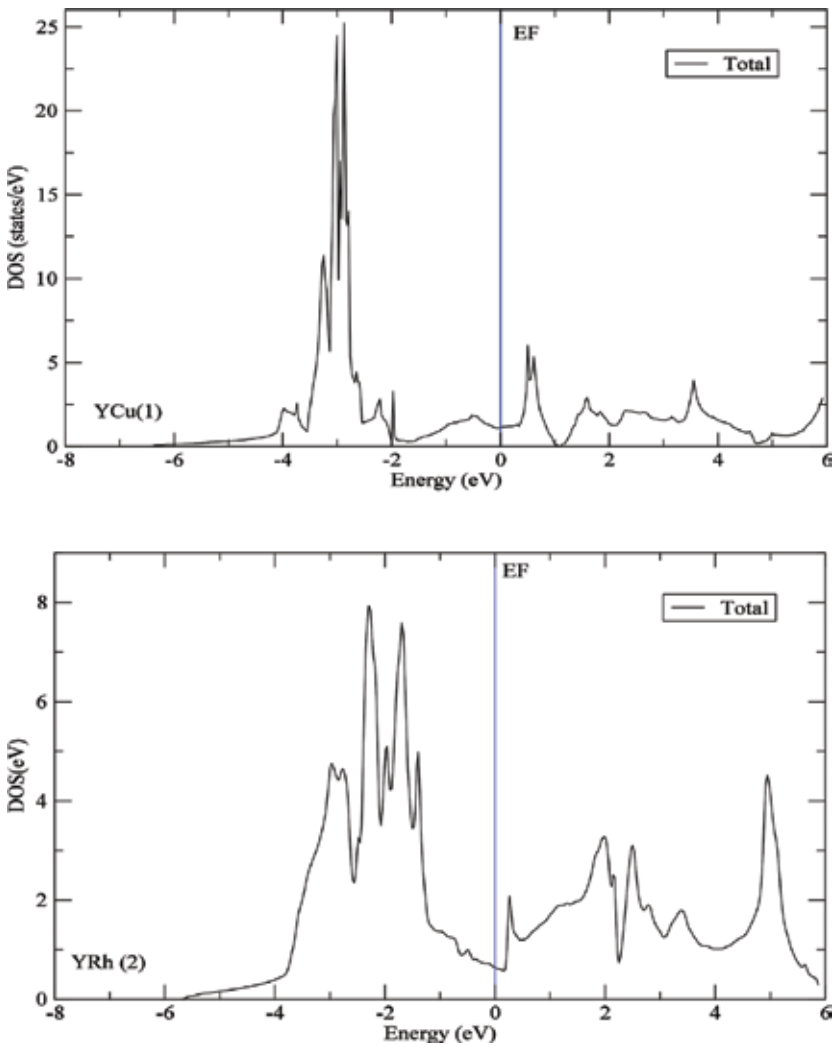


**Figure 3.** Total densities of states of YCu (1) and YRh (2) in the B2 structure.

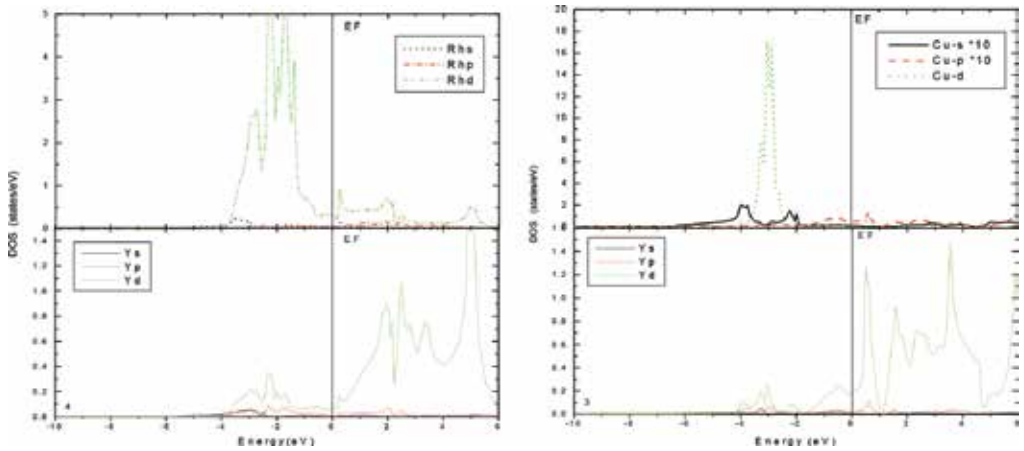


**Figure 4.** The partial electronic densities of YCu (1) and YRh (2) in the B2 structure.

## 5. Conclusion

In this chapter, we have investigated the structural, electronic, and elastic properties of YCu and YRh B2 rare earth intermetallics by means of the full-potential linearized augmented plane wave (FP-LAPW) approach. The use of the PBE-GGA approximation for the exchanging correlation potential allowed us to obtain good values of the electronic structure. The value of the bulk modulus obtained in YRh material is in disagreement with those found by the method TB-LMTO. This difference can be justified later by the experience. Our calculations demonstrate that the YM (M = Cu and Rh) ductile materials are significantly different than previously studied intermetallic B2 compounds. The elastic constants have significantly more isotropic behavior, and Poisson's ratio is smaller than theoretical value (<0.25) indicating that these materials are compressible. The calculated band structure and density of state (DOS) were in good agreement with other theoretical calculations. The remarkable characteristic is that the total density of state (DOS) of these B2 rare earth intermetallics is similar. In addition, there are no experimental studies on the bulk modulus and elastic properties of YRh compound. Hopefully, these results will encourage further experimental works on YRh intermetallics to test and refine the theoretical works. So, it may be interesting to perform high-pressure X-ray diffraction studies on this compound.

## Author details

Abdessamad Sekkal[1,2], Mohamed Sahlaoui[3,4] and Abdelnour Benzair[5]

*Address all correspondence to: asekkal.ph@gmail.com

1 Ecole Supérieure des Sciences Appliquées d'Alger, Algérie

2 Division Etude et Prédiction de Matériaux, Unité de Recherche Matériaux et Energies Renouvelables, Département de Physique, Faculté des Sciences, Université Abou Bekr Belkaid, Tlemcen, Algérie

3 Theoretical Physics Laboratory, Abou Bekr Belkaid University, Tlemcen, Algeria

4 Ecole Supérieure en Sciences Appliquées de, Tlemcen, Algérie

5 Département de Physique, Faculté des Sciences, Université' Djilali Liabes, Sidi Bel Abbés, Algeria

## References

[1] Medvedeva NI, Mryasov ON, Gornostyrev YN, et al. First-principles total-energy calculations for planar shear and cleavage decohesion processes in B2-ordered NiAl and FeAl. Physical Review B. 1996;**54**:13506-13514

[2] Schoeck G. The core structure of dissociated dislocations in NiAl. Acta Materialia. 2001; **49**:1179-1187

[3] Russell AM. Ductility in intermetallic compounds. Advanced Engineering Materials. 2003;**5**:9

[4] Gschneidner KA, Russell AM, Pecharsky A, et al. A family of ductile intermetallic compounds. Nature Materials. 2003;**2**:587-591

[5] Zhang Z, Russell AM, Biner SB, Gschneidner KA, Lo CCH. Fracture toughness of polycrystalline YCu, DyCu, and YAg. Intermetallics. 2005;**13**:559

[6] Russell AM, Zhang Z, Lograsso TA, Lo CCH, Pecharsky AO, Morris JR, Ye Y, Gschneidner KA, Slager AJ. Mechanical properties of single crystal YAg Acta. Materialia. 2004;**52**:4033-4040

[7] Morris JR, Yiying Y, Lee YB, Harmon NB, Gschneidner KA, Russell AM. Ab initio calculation of bulk and defect properties of ductile rare-earth intermetallic compounds. Acta Materialia. 2004;**52**:4857

[8] Shi YJ, Du YL, Chen G, Chen GL. First principle study on phase stability and electronic structure of YCu. Physics Letters A. 2007;**368**:495-498

[9] Gschneidner Jr KA et al. Influence of the electronic structure on the ductile behavior of B2 CsCl-type AB intermetallics. Acta Materialia. 2009;**57**:5876-5881

[10] Khadeer Pasha SK, Sundareswari M, Rajagopalan M. Ab initio study of the electronic structure of some B2 intermetallic compounds. Physica B. 2004;**348**:207

[11] Divis M, Kuriplach J. Crystal field in rare earth intermetallics with CsCl structure. Physica B. 1995;**205**:353

[12] Wu Y, Hu W, Han S. First principles calculation of the elastic constants, the electronic density of states and ductility mechanism of the intermetallic compounds: YAg, YCu and YRh. Physica B. 2008;**403**:3792

[13] Bushra F, Chouhan SS, Nikita A, Sanyal SP. Density functional study of XRh (X = Sc, Y, Ti and Zr) intermetallic compounds. Computational Materials Science. 2014;**89**:205-215

[14] Sekkal A, Benzair A, Faraoun HI, Aourag H, Merad G. Structural and thermoelastic properties of the B2–YX (X=Cu, Mg and Rh) intermetallic compounds Condensed matter. Physica B. 2010;**405**:2831-2835

[15] Chen Q, Ji M, Wang CZ, Ho KM, Biner SB. Core properties of dislocations in YCu and YAg B2 intermetallic compounds. Intermetallics. 2010;**18**:312-318

[16] Chouhan SS, Soni P, Pagare G, Sanyal SP, Rajagopalan M. Ab-initio study of electronic and elastic properties of B2-type ductile YM (M=Cu, Zn and Ag) intermetallics. Physica B. 2011;**406**:339-344

[17] Fulde P, Loewenhaupt M. Magnetic excitations in crystal-field split 4f systems. Advances in Physics. 1986;**34**:589-661

[18] Madsen GKH, Blaha P, Schwarz K, Sjöstedt E, Nordström L. Efficient linearization of the augmented plane-wave method. Physical Review B. 2001;**64**:195134

[19] Schwarz K, Blaha P, Madsen GKH. Electronic structure calculations of solids using the WIEN2k package for material sciences. Computer Physics Communications. 2002;**147**:71

[20] Blaha P, Schwarz K, Madsen GKH, Kvasnicka D, Wien JL. An Augmented Plane Wave Plus Local Orbitals Program for Calculating Crystal Properties. Vienna, Austria: Vienna University of Technology; 2001

[21] Perdew JP, Wang Y. Accurate and simple analytic representation of the electron-gas correlation energy. Physical Review B. 1992;**45**:13244

[22] Monkhorst HJ, Pack JD. Special points for Brillouin-zone integrations. Physical Review B. 1976;**13**:5188

[23] Murnaghan FD the Compressibility of Media under Extreme Pressures. Proceedings of the National Academy of Sciences of the United States of America. 1944;**30**:244

[24] Shi Y J, Du Y L, Chen G, Chen G L. First principle study on phase stability and electronic structure of YCu. Physics Letters A. 2007;**368**:495

[25] Uğur G, Civi M, Uğur S, Soyalp F, Ellialtıoğlu R. Structural, electronic and elastic properties of YCu from first principles. Journal of Rare Earths. 2009;**27**:661-663

[26] Wu Y, Hu W. Elastic and brittle properties of the B2-MgRE (RE = Sc, Y, Ce, Pr, Nd, Gd, Tb, Dy, Ho, Er) intermetallics. European Physical Journal B. 2007;**60**:75

[27] Tao X, Ouyang Y, Liu H, Feng Y, Du Y, Jin Z. Elastic constants of B2-MgRE (RE = Sc, Y, La–Lu) calculated with first-principles. Solid State Communications. 2008;**148**:314

[28] Mehl MJ. Pressure dependence of the elastic moduli in aluminum-rich Al-Li compounds. Physical Review B. 1993;**47**:2493

[29] Mayer B, Anton H, Bott E, Methfessel M, Sticht J, Schmidt PC. Ab-initio calculation of the elastic constants and thermal expansion coefficients of Laves phases Intermetallics. 2003;**11**:23-32

[30] Pugh SF. XCII. Relations between the elastic moduli and the plastic properties of polycrystalline pure metals. Philosophical Magazine. 1954;**45**:823-843

Chapter 10

# Effect on Heat Treatment and Doping of Cubic $NaZn_{13}$-Type $La_{0.7}Pr_{0.3}(Fe,Si)_{13}$ for Magnetic Refrigerator Application

Muhamad Faiz Md Din, Jianli Wang and

Mohd Taufiq Ishak

Additional information is available at the end of the chapter

http://dx.doi.org/10.5772/intechopen.75607

**Abstract**

Soft ferromagnetic cubic $NaZn_{13}$-type $La_{0.7}Pr_{0.3}Fe_{11.4}Si_{1.6}$ has turned out to be a standout amongst the most fascinating compounds for investigating substantial magnetocaloric effect (MCE) on the grounds that the attractive properties of this compound shows large enough spontaneous magnetization for applications, strongly doping dependent, and as well as delicate soft ferromagnetism. These impacts can be attributed to the itinerant electron metamagnetic (IEM) transition especially around the first-order magnetic transition region. However, this compound is difficult to frame by the basic cementing process because of the inherent deficiency of the peritectic response, $\gamma$-Fe + La → $La(Fe,Si)_{13}(\tau_{1a})$, which frequently brings about a blended microstructure of $\alpha$-Fe + $La(Fe,Si)_{13}(\tau_{1a})$ + $LaFeSi(\tau_4)$. Additionally, dependability of $La(Fe_xSi_{1-x})_{13}$ is no middle-of-the-road stage and common solvency amongst Fe and La in the Fe-La framework as a reality is represented by response dispersion as indicated by magnetic and electronic states' contribution. From this point of view, the structure, attractive properties and MCE of this compound have been talked about in detail as indicated by various temperatures and times of the annealing treatment. In addition, efficiently contemplating on the doping impact from various concentrations of transition metal elements such as Copper (Cu) and Chromium (Cr) on Iron (Fe) in the $La_{0.7}Pr_{0.3}Fe_{11.4}Si_{1.6}$ compound is likewise discussed.

**Keywords:** intermetallic, structure properties, magnetocaloric effect, magnetic properties, magnetic application

## 1. Introduction

Attractive refrigeration moves toward becoming more solid to supplant the ordinary refrigeration frame work due to its favourable circumstances utilizing magnetocaloric effect (MCE) application. This innovation has brought huge points of interest as high refrigeration efficiency, environment friendly, practical of volume size, cheapest, nondangerous, and out of sound pollution draw in to additionally look into, contrasted/compared to conventional gas pressure refrigeration system. The MCE was initially found by Warburg [1] in 1881, and since the discovery of the giant magnetocaloric effect at room temperature in 1997 [2], attractive materials with expansive MCE have been widely examined tentatively and hypothetically in the previous two decades. Up to the present time, various materials with impressive magnetic

| Nominal composition | Condition of case study | Ref |
|---|---|---|
| $La(Fe_{13-x}Si_x)$<br>Different of Si concentration | Tc found to increase from 195 K for Si=1, 195 K for Si=1.2, 210 K for Si=1.43, 222 K for Si=1.6 and 231 K for Si=1.8 | [7] |
| $La(Fe_xSi_{1-x})_{13}$<br>Different of Fe concentration | Tc found to decrease from 208 K for Fe=11.4, 195 K for Fe=11.44, 188 K for Fe=11.57 and 184 K for x=11.7 | [9] |
| $LaFe_{11.4}Si_{1.6}$ | Tc=209 K | [10] |
| $LaFe_{10.98}Co_{0.22}Si_{1.8}$ | Tc=242 K | |
| $LaFe_{11.13}Co_{0.71}Al_{1.17}$ | Tc=279 K | |
| $La_{0.7}Pr_{0.3}(Fe_{13-x}Si_x)$<br>Different of Si concentration | Tc found to increase from 168 to 218 K for Si=1.5 to Si=2.0 | [11] |
| $LaFe_{10.6}Si_{2.4}$ | Tc=242 K | [12] |
| $LaFe_{11.44}Co_{0.13}Si_{1.43}$ | Tc=205 K | [13] |
| $LaFe_{11.44}Co_{0.39}Si_{1.17}$ | Tc=240 K | |
| $LaFe_{11.44}Co_{0.52}Si_{1.04}$ | Tc=250 K | |
| $LaFe_{11.4}Si_{1.6}$ | Tc=200 K | [14] |
| $La_{0.9}Er_{0.1}Fe_{11.4}Si_{1.6}$ | Tc=205 K | |
| $La_{0.7}Er_{0.3}Fe_{11.4}Si_{1.6}$ | Tc=214 K | |
| $LaFe_{11.4}Si_{1.6}$ | Large MCE with reversible magnetic phase transition at Tc | [8] |
| $La_{1-x}R_xFe_{11.5}Si_{1.5}$<br>R=Ce, Pr, Nd | Tc found to increase up to 11% when 30% of La replaced by R element | [15] |
| $La(Fe_xSi_{1-x})_{13}H_y$<br>Doping of Hydrogen<br>y= 0, 0.5, 1.0 and 1.5 | Tc found to increase from 195 to 330 K for y=0 to 1.5 | [19] |
| $La_{0.7}Pr_{0.3}Fe_{11.4-x}Cu_xSi_{1.6}$<br>Different of Cu concentration | Tc found to increase from 197 K for x=0, 210 K for x=0.06, 218 K for x=0.12, 224 K for x=0.23 and 230 K for x=0.34 | [25] |
| $La_{0.7}Pr_{0.3}Fe_{11.4-x}Cr_xSi_{1.6}$<br>Different of Cr concentration | Tc found to decrease from 197 K for x=0 to 180 K for x=0.06 and start to increase till 185 K for x=0.12, 190 K for x=0.23 and 195 K for x=0.34 | [26] |

**Table 1.** Brief summary of previous study related to $La_{0.7}Pr_{0.3}Fe_{11.4}Si_{1.6}$ compound.

entropy change values have been observed, for example, $Gd_5Si_2Ge_2$ [2], $NdMn_{2-x}T_xSi_2$ (T = transition metal = Cr, Cu, V, Ti) [3–5], $MnAs_{1-x}Sb_x$ [6] and $La(Fe,Si)_{13}$ [7–9].

The cubic $NaZn_{13}$-type $La(Fe,Si)_{13}$ winds up noticeably as one of the intriguing compounds to investigate large MCE because of their attractive properties, for example, firmly doping reliant, sufficiently extensive unconstrained charge and delicate soft ferromagnetism [10–12]. These impacts can be attributed to the itinerant electron metamagnetic (IEM) change in the region of the primary request progress temperature. Doping other attractive rare earth elements, for example, Pr, Nd, Ce, Er and Gd, substitute the La position which was utilized to change the temperature and diminish the critical field of 3*d*-metamagnetic progress in $La(Fe,Si)_{13}$ compound [13–15] in light of the fact that the rare earth-Fe magnetic coupling in this system shows a solid reliance on the kind of the rare earth element, respectively.

The cubic $NaZn_{13}$ type is difficult to be formed by regular solidification process because of the characteristic inadequacy of a peritectic response, $\gamma$-Fe + L → $La(Fe,Si)_{13}(\tau_{1a})$, which frequently results in the blended microstructure of $\alpha$-Fe + $La(Fe,Si)_{13}(\tau_{1a})$ + $LaFeSi(_{\tau 4})$ [16]. Many researchers set up this compound treatment in the range of 1173–1323 K for at least 10 days to produce the $NaZn_{13}$-type structure [17–19]. However, the peritectic response temperature in $La(Fe,Si)_{13}$ is around 1673 K regarding the La-Fe quasi table diagram [20] and the temperature was found to be more beneficial in the shorting-stage change process [21] as demonstrated by Liu et al. [22] and Chen et al. [23]. Both these groups revealed that the readiness in temperature range around 1323–1623 K can create most measures of the $NaZn_{13}$-type structure. **Table 1** indicated the variable case study related to the $NaZn_{13}$ type which showed different physical properties' behaviour in substitution or doping effect on the $La(FeSi)_{13}$ compound, respectively.

According to Shen et al. [24] findings, substituting La with other rare earth component can prompt surprising improvements of magnetic entropy change. However, these behaviors come with an expansion hysteresis loss as the nature of first-order magnetic transition. In this chapter, we clarify in detail the impact of different temperature-annealing processes on the structure and magnetic properties of $La_{0.7}Pr_{0.3}Fe_{11.4}Si_{1.6}$. The influence of Cu and Cr doping with the substitute of Fe in the $La_{0.7}Pr_{0.3}Fe_{11.4}Si_{1.6}$ compound on magnetic properties and magnetocaloric effect was also explained.

## 2. The phase relation between low temperature with long-time annealing (LTA) and high temperature with short-time annealing (HTA)

### 2.1. Structural properties

It was all around acknowledged that the stage level of impurity structure in the $NaZn_{13}$-type compound is dependent on the procedure of preparation process [25, 26]. Starting there, the $La_{0.7}Pr_{0.3}Fe_{11.4}Si_{1.6}$ compound was chosen to be set up with two different annealing treatments with low-temperature annealing (LTA) at 1323 K for 14 days and high-temperature annealing (HTA) at 1523 K for 4 h to elucidate which method is more advantageous and forms a better

$NaZn_{13}$-type structure. Results from XRD diffraction (as indicated in **Figure 1**) show that the HTA with less time can form a bigger number of the NaZn13– compound structure phase compared to LTA with long-time annealing process. LTA produces substantially an amount of impurity, LaFeSi and $\alpha$-Fe phase in the $La_{0.7}Pr_{0.3}Fe_{11.4}Si_{1.6}$ compound.

It is shown in **Table 2** that the LTA procedure brings about less amount of the $NaZn_{13}$ structure though the peritectic reaction alludes to refined structure. This behaviour happens with respect to non-equilibrium solidification phenomenon regarding the uncompleted peritectic response $\gamma$-Fe + L → $La(Fe,Si)_{13}(\tau_{1a})$ [16]. At the point when the annealing temperature is higher, the speed of the dispersion of atom is just large during the high temperature and solid-phase diffusion reaction process. Along these lines, it unmistakably happens that while expanding the annealing temperature to 1523 K for 4 h (HTA), the measure of the $NaZn_{13}$ structure steadily formed will eliminate nearly all of the LaFeSi structure and decrease the amount of the $\alpha$-Fe structure. The Retiveld refinement is indicated in **Table 2** and it is shown that the weight of $NaZn_{13}$ structure increases from 69% at LTA to 96% while the weight amount of LaFeSi and the $\alpha$-Fe stage at HTA is found to decrease. The constitutions of the formed $NaZn_{13}$ structure in 1523 K for 4 h of annealing treatment are in concurrence with other groups [22, 23]. However, it was hard to shape a single-structure sample by the bulk synthesis technique as a low cooling rate of the solidification procedure which will deliver an inhomogeneous structure to the sample. That is the reason, with a specific method in order to stay away from recrystallization of $\alpha$-Fe and the LaFeSi structure, the samples were quickly quenched in water.

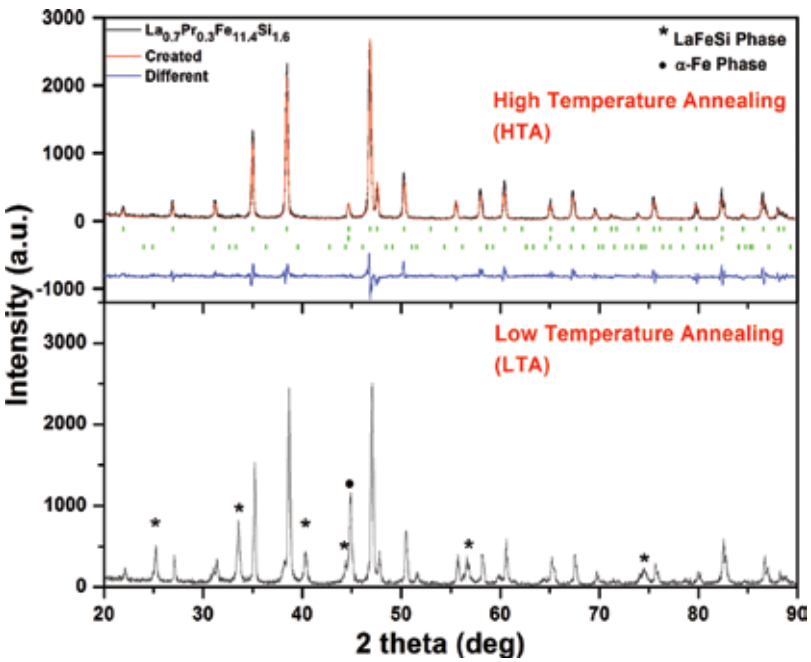


**Figure 1.** Room temperature X-ray diffraction patterns of $La_{0.7}Pr_{0.3}Fe_{11.4}Si_{1.6}$ produced by the HTA and LTA processes.

http://dx.doi.org/10.5772/intechopen.75607

| Nominal composition | Heat treatment (T(K)/t) | Phase | Wt% | Refined composition | Lattice parameter, a (Å) |
|---|---|---|---|---|---|
| $La_{0.7}Pr_{0.3}Fe_{11.4}Si_{1.6}$ | 1323 K/14 days | $Nazn_{13}$ | 69.05 | $La_{0.7}Pr_{0.3}Fe_{14.1}Si_{2.1}$ | 11.45104 |
| | (LTA) | $\alpha$-Fe | 19.42 | | 2.86435 |
| | | LaFeSi | 11.53 | | |
| $La_{0.7}Pr_{0.3}Fe_{11.4}Si_{1.6}$ | 1523 K/4 hours | $Nazn_{13}$ | 96.12 | $La_{0.7}Pr_{0.3}Fe_{11.00}Si_{1.6}$ | 11.45845 |
| | (HTA) | $\alpha$-Fe | 3.56 | | 2.86563 |
| | | LaFeSi | 0.32 | | |

**Table 2.** Synthesis conditions (heat treatment process) and results of the structural characterization (phase observed, analyzed compositions, and lattice parameter of the $NaZn_{13}$, $\alpha$-Fe, and LaFeSi phases) for LTA and HTA from XRD.

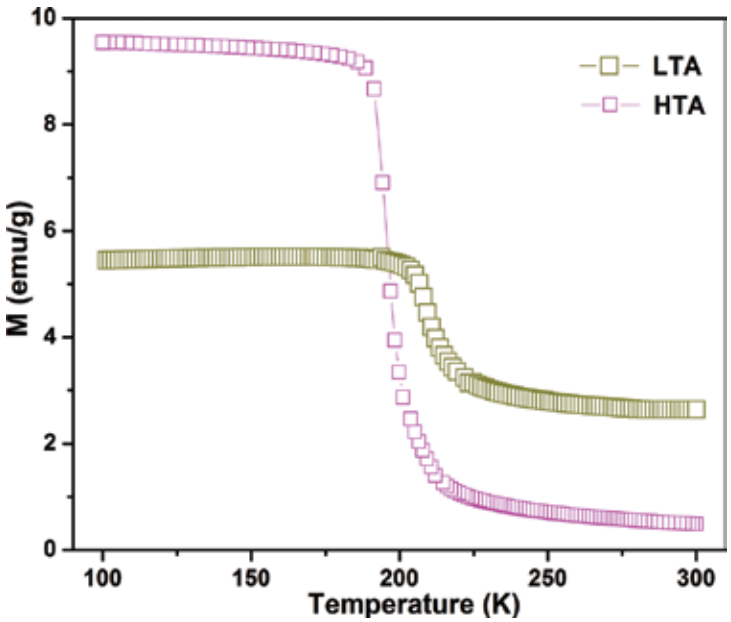


**Figure 2.** Temperature dependence of magnetization of $La_{0.7}Pr_{0.3}Fe_{11.4}Si_{1.6}$ for LTA and HTA.

## 2.2. Magnetic properties

**Figure 2** demonstrates the temperature dependent of magnetization measured under the low magnetic field of 0.01 T in temperature range from 100 to 300 K of the $La_{0.7}Pr_{0.3}Fe_{11.4}Si_{1.6}$ compound for LTA and HTA. The TC values were characterized as a maximum of dM/dT from **Figure 2**. It found that TC of the $La_{0.7}Pr_{0.3}Fe_{11.4}Si_{1.6}$ compound from LTA treatment is ~ 200 K which is 13 K higher than HTA treatment as ~197 K. Furthermore, LTA has different magnetic phase transition characteristics because of the different Si concentration in the $NaZn_{13}$ phase compared to HTA, in which LTA is formed with higher Si concentration and contributes to expand TC and changes the magnetic state from first-order to second-order transition in this case study. Moreover, LTA treatment also interfaced to produce more impurity such as $\alpha$-Fe and

LaFeSi structure and decrease the main $NaZn_{13}$ structure content with respect to temperature and time during annealing process, which troubles in solution treatment at low temperature directly increasing the Si concentration behaviour. In **Table 2**, it is shown from XRD refinement that the concentration of Si in the $NaZn_{13}$ structure for LTA is higher compared to HTA. As far as the impacts of expanding the Si concentration in the $NaZn_{13}$ structure is concerned, we suggest that this marvel adds to expanding the value of $T_C$ and changes the magnetic phase transition. Comparative phenomena likewise have been reported by Bo Liu et al. [27].

Magnetic hysteresis loss (as shown by the territory encased between ascending and descending branches of the magnetization curves) is additionally normal for first-order magnetic transition. The magnetization curves obtained for $La_{0.7}Pr_{0.3}Fe_{11.4}Si_{1.6}$ (LTA and HTA) for fields in the range B = 0–5 T around their ferromagnetic ordering temperatures have been studied respectively [25]. This information was obtained for increasing and decreasing fields at 5 K and 2 K intervals at 200 K around $T_C$, consequently giving data about magnetic hysteresis loss effect as discussed using the below Equation [28].

$$\text{Magnetic hysteresis loss} = \int_{\text{decrease } H}^{\text{increase } H} (\partial M)_H \, dH \tag{1}$$

As exhibited in **Figure 3**, examination of the magnetic hysteresis loss around the ferromagnetic ordering temperatures for $La_{0.7}Pr_{0.3}Fe_{11.4}Si_{1.6}$ (LTA and HTA) is up to ~ 12.4 J $kg^{-1}$ (demonstrated value for B = 0–5 T as appropriate to compare) for $La_{0.7}Pr_{0.3}Fe_{11.4}Si_{1.6}$ (HTA) at $T_C$ ~ 197 K, while almost no magnetic hysteresis loss of ~ 0.1 J $kg^{-1}$ is found for $La_{0.7}Pr_{0.3}Fe_{11.4}Si_{1.6}$ (LTA) around $T_C$ ~ 210 K. It is exhibited that the field which actuated the first-order magnetic transition from paramagnetic to ferromagnetic was eminently debilitated by the more Si concentration in LTA which demonstrated second-order magnetic transition as a contrast with HTA which showed

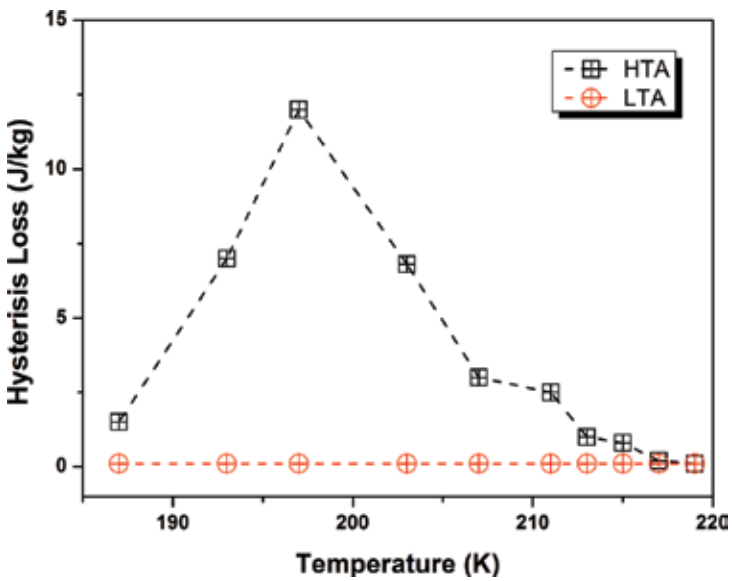


**Figure 3.** Comparison of the magnetic hysteresis losses for $La_{0.7}Pr_{0.3}Fe_{11.4}Si_{1.6}$ produced by the HTA and LTA process under magnetic fields over the ranges *B* = 0–5 T.

first-order magnetic transition. The upside of the sample without hysteresis loss expands the proficiency of magnetic refrigerator application [29] which is of little vitality loss during temperature change in the cycle operation system.

### 2.3. Magnetocaloric effect

Giant MCE value and magnetic entropy changes are generally accompanied with a first-order magnetic transition because of an extensive rate of change in magnetic field. Even these materials have been preferred in terms of the MCE value compared to second-order material; the issues of thermal and magnetic hysteresis loss are impossible to solve. So as to fulfill the reasonableness of various tests and related logical ways to deal with, calculation of the isothermal entropy change, $-\Delta S_M$, in this study, has been characterized from the decreased field of magnetization measurement by the Maxwell relation [30, 31]:

$$-\Delta S_M(T, H) = \int_0^H \left(\frac{\partial M}{\partial T}\right)_H dH \quad (2)$$

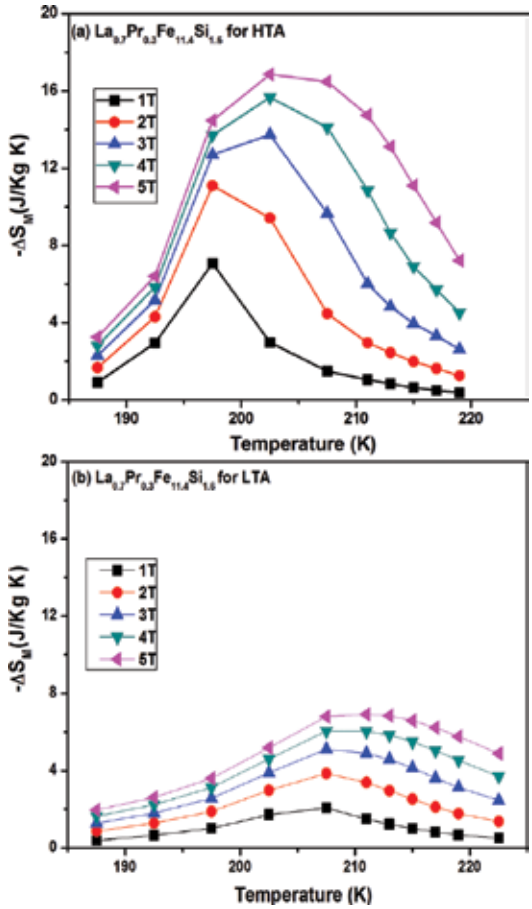


**Figure 4.** Magnetic entropy change, $-\Delta S_m$, for a 0–5 T change in field of $La_{0.7}Pr_{0.3}Fe_{11.4}Si_{1.6}$ for (a) HTA and (b) LTA compounds as a function of temperature.

The $-\Delta S_M$ peak gradually broadens toward higher temperatures with increasing magnetic field (from $\Delta B$ = 0–5 T) as shown in **Figure 4(a)** and **(b)** for $La_{0.7}Pr_{0.3}Fe_{11.4}Si_{1.6}$ (LTA and HTA) related to behaviour of a field-induced transition from the paramagnetic to ferromagnetic state, respectively. The changes in magnetic entropy for $La_{0.7}Pr_{0.3}Fe_{11.4}Si_{1.6}$ (LTA and HTA) around their ferromagnetic ordering temperatures as indicated in **Figure 4** are calculated from decreasing applied fields in order to satisfy the isothermal entropy change and suitability of different experiments [32]. The MCE values are $-\Delta S_M \sim 16.8$ J kg$^{-1}$ K$^{-1}$ at $T_C$ = 197 for HTA and decrease to $-\Delta S_M \sim 7.9$ J kg$^{-1}$ K$^{-1}$ at $T_C$ = 200 K for LTA. The decrease in the value of $-\Delta S_M$ is related to increase in Si and there is less magnetization moment concentration in $La_{0.7}Pr_{0.3}Fe_{11.4}Si_{1.6}$ (LTA) compared to $La_{0.7}Pr_{0.3}Fe_{11.4}Si_{1.6}$ (HTA). This phenomenon indicated that $La_{0.7}Pr_{0.3}Fe_{11.4}Si_{1.6}$ (HTA) is more favorable and advantageous compare to $La_{0.7}Pr_{0.3}Fe_{11.4}Si_{1.6}$ (LTA) as a refrigerant in the magnetic refrigerator application.

## 3. The influence of phase and properties in $La_{0.7}Pr_{0.3}Fe_{11.4}Si_{1.6}$ with partial substitution of Cu for Fe

### 3.1. Structural properties

$La_{0.7}Pr_{0.3}Fe_{11.4-x}Cu_xSi_{1.6}$ (x = 0–0.34) is prepared using the HTA method. As indicated in **Table 3**, the amount of $\alpha$-Fe and LaFeSi phases increases with Cu-doping contribution. This behaviour occurs when we substitute Cu for Fe in $La_{0.7}Pr_{0.3}Fe_{11.4}Si_{1.6}$ and it affected the bulk diffusion rate controlling factor of homogenization in the $NaZn_{13}$–type structure. **Table 3** shows the LaFeSi and $\alpha$-Fe phase fractions in $La_{0.7}Pr_{0.3}Fe_{11.4-x}Cu_xSi_{1.6}$ which increases with the increasing Cu substitution while the $NaZn_{13}$ phase decreases from 96% at x = 0 to 85% at x = 0.34. In the La-Fe-Si ternary system, the substitution new element directly influences the La-Si and Fe-Si bonding as discussed in detail from the previous study [27]. The substitution of Cu into Fe in $La_{0.7}Pr_{0.3}Fe_{11.4}Si_{1.6}$ produces the differences in relation between the La-Si and La-Fe pairs, changing the interatomic distances which contribute to affecting the structural stability of the $NaZn_{13}$ structure. As discussed by Fujita et al. [19], that diffusion, also sensitive to modification of both the electronic structure and lattice spacing, then agrees well with this study which takes in different atomic radii of Cu (1.28 Å) and Fe (1.24 Å).

### 3.2. Magnetic properties

As indicated in **Table 3**, increase in Cu doping in $La_{0.7}Pr_{0.3}Fe_{11.4}Si_{1.6}$ will increase the $T_C$ and change the magnetic phase transition from first- to second-order type. This behaviour found that related exchange interactions exist between Fe-Fe in the Fe-rich rare earth intermetallic compounds. It is related to the phenomenon when the separation of the Fe–Fe pair is smaller than 2.45 Å, the exchange interaction will be negative but the interaction is positive at larger Fe–Fe distances as similarly reported by other group [31]. Based on the fact that the atomic radius of Fe is smaller than that of Cu, increase in Cu concentration doping will increase the lattice parameter and the Fe-Fe distance then will enhance the positive interactions with increasing $T_C$.

| **Nominal composition $La_{0.7}Pr_{0.3}Fe_{11.4-x}Cu_xSi_{1.6}$** | **X = 0** | **x = 0.06** | **x = 0.12** | **x = 0.23** | **x = 0.34** |
|---|---|---|---|---|---|
| Phase (Wt%) | Nazn13 (96.12%) | Nazn13 (91.68%) | Nazn13 (88.20%) | Nazn13 (86.83%) | Nazn13 (85.20%) |
| | $\alpha$-Fe (3.56%) | $\alpha$-Fe (7.33%) | $\alpha$-Fe (9.06%) | $\alpha$-Fe (10.15%) | $\alpha$-Fe (10.63%) |
| | LaFeSi (0.32%) | LaFeSi (0.99%) | LaFeSi (2.74%) | LaFeSi (3.02%) | LaFeSi (4.16%) |
| Lattice parameter, a (Å) | 11.45845 | 11.46035 | 11.46274 | 11.46495 | 11.46621 |
| Tc (K) | 197 | 210 | 218 | 224 | 230 |
| $-\Delta S_M$ (J/kg K) | 17 | 12 | 9 | 7 | 5 |
| RCP (J/Kg) | 400 | 330 | 300 | 280 | 245 |
| MS ($\mu$B/ f.u.) at 5 K | 22.8 | 22 | 21.6 | 21 | 21.4 |

**Table 3.** Results of the structural characterization (phase observed, analyzed compositions, and lattice parameter of the $NaZn_{13}$, $\alpha$-Fe, and LaFeSi phases) magnetic and magnetic entropy change for $La_{0.7}Pr_{0.3}Fe_{11.4-x}Cu_xSi_{1.6}$ (x = 0, 0.06, 0.12, 0.23, 0.34) [25].

As details included in **Table 3**, the compounds were found to exhibit ferromagnetic behaviour with a saturation magnetization below 24 $\mu_B$/f.u. [25]. However, it is shown that the replacement Cu for Fe will reduce the saturation magnetization field in $La_{0.7}Pr_{0.3}Fe_{11.4-x}Cu_xSi_{1.6}$ according to the characteristics of Cu as a diamagnetic element. As we assume no contribution from the Pr moment with increasing Cu content, the average moment of the Fe can be derived from the total moment. It is indicated that substituting Fe by Cu leads to a decrease in the average moment of the Fe in $La_{0.7}Pr_{0.3}Fe_{11.4}Si_{1.6}$. This agrees well with x = 0.34; the value of the saturation magnetization is higher than expected. The saturation magnetization is higher because the total moment is included with a large amount of the $\alpha$-Fe moment in $La_{0.7}Pr_{0.3}Fe_{11.06}Cu_{.34}Si_{1.6}$.

### 3.3. Magnetocaloric effect

The values of $-\Delta S_M$ around $T_C$ that have been derived from the decrease in magnetic field are shown in **Table 3** as a function of temperature with a 0–5 T change in the field for $La_{0.7}Pr_{0.3}Fe_{11.4-x}Cu_xSi_{1.6}$ (x = 0–0.34) compounds. It is shown that the $-\Delta S_M$ peak gradually becomes broader at higher temperatures with increasing magnetic field from 1 to 5 T as characteristic of the field-induced IEM transition from the paramagnetic to the ferromagnetic state particularly around temperatures above $T_C$. Furthermore when there is increase in the concentration of Cu in $La_{0.7}Pr_{0.3}Fe_{11.4-}Si_{1.6}$, the $-\Delta S_M$ decreases from 17 J/kgK for x = 0 to 5 J/kgK for x = 0.34 as it is proved that Cu is dilute and not a magnetic element.

The relative cooling power (RCP) is very important and related to the magnetic refrigerator application performance. Using the full width at half maximum of the peak in the temperature dependence of the magnetic entropy change $-\Delta S_M$ and the maximum of the entropy variation $-\Delta S_M^{max}$, the value of RCP has been calculated using the following formula [19, 33]:

$$RCP = -\Delta S_M^{max} \delta T^{FWHM} \quad (3)$$

A summary of RCP values and other magnetic characterization parameters listed in **Table 3** for $La_{0.7}Pr_{0.3}Fe_{11.4-x}Cu_xSi_{1.6}$ (x = 0, 0.06, 0.12, 0.23, 0.34) compounds is presented. The RCP value shows the similar behaviour with MCE which starts to decrease from 400 J/kg for x = 0 to 245 J/kg for x = 0.34 on application of a B = 0–5 T, respectively.

## 4. The influence of phase and properties in $La_{0.7}Pr_{0.3}Fe_{11.4}Si_{1.6}$ with partial substitution of Cr for Fe

### 4.1. Structural properties

The x-ray diffraction analysis at room temperature in **Table 4** showed that Cr concentration contributes to an increase in the amount of $\alpha$-Fe and LaFeSi phases from the beginning to x = 0.06. However it was found to increase from x = 0.12 to x = 0.34. We suggest this behaviour to be related to bulk diffusion rate controlling factor of homogenization in the cubic $NaZn_{13}$–type phase structure (space group *Fm3c*) by substitution of Cr for Fe. **Table 4**, shows that the weight fraction of the $NaZn_{13}$ structure decreases from 96% at x = 0 to 85% at x = 0.06 and then increases to 97% with increasing Cr content till x = 0.34. The replacement of Cr for Fe into $La_{0.7}Pr_{0.3}Fe_{11.4}Si_{1.6}$ starts to produce large differences between the La-Si and the La-Fe pairs which effect to decrease the stability on clusters of the $NaZn_{13}$ phase. That diffusion is also sensitive to modification of both the electronic structure and lattice spacing [34] agrees with the phenomenon of lattice parameter *a*, which decreases from 11.458 Å at x = 0 to 11.451 Å at x = 0.34; even Cr atomic radius is larger than Fe and at different electronic environments (Fe ~ $3d^64s^2$ and Cr ~ $3d^54s^1$, respectively).

### 4.2. Magnetic properties

The temperature dependence of the magnetization for calculated $T_C$ of $La_{0.7}Pr_{0.3}Fe_{11.4-x}Cr_xSi_{1.6}$ compound is measured under magnetic field of 0.01 T as shown in **Table 4**. $T_C$ was found to

| **Nominal composition $La_{0.7}Pr_{0.3}Fe_{11.4-x}Cr_xSi_{1.6}$** | **X = 0** | **x = 0.06** | **x = 0.12** | **x = 0.23** | **x = 0.34** |
|---|---|---|---|---|---|
| Phase (Wt%) | Nazn13 (96.12%) | Nazn13 (85.90%) | Nazn13 (92.60%) | Nazn13 (94.00%) | Nazn13 (97.60%) |
| | $\alpha$-Fe (3.56%) | $\alpha$-Fe (10.6%) | $\alpha$-Fe (6.00%) | $\alpha$-Fe (4.70%) | $\alpha$-Fe (2.30%) |
| | LaFeSi (0.32%) | LaFeSi (3.55%) | LaFeSi (1.40%) | LaFeSi (1.30%) | LaFeSi (0.20%) |
| Lattice parameter, a (Å) | 11.45845 | 11.45560 | 11.4540 | 11.45240 | 11.45180 |
| Tc (K) | 197 | 180 | 185 | 190 | 195 |
| $-\Delta S_M$ (J/kg K) | 17 | 12 | 14.2 | 15.6 | 17.5 |
| RCP (J/Kg) | 400 | 365 | 380 | 400 | 420 |

**Table 4.** Results of the structural characterization (phase observed, analyzed compositions, and lattice parameter of the $NaZn_{13}$, $\alpha$-Fe, and LaFeSi phases) magnetic and magnetic entropy change for $La_{0.7}Pr_{0.3}Fe_{11.4-x}Cr_xSi_{1.6}$ (x = 0, 0.06, 0.12, 0.23, 0.34) [26].

decrease from 197 K at x = 0 to 180 K at x = 0.06 and then increase to 185 K at x = 0.12 until 195 K at Cr concentration where x = 0.34. This variation of temperature occurs related to the more presence of $\alpha$-Fe and LaFeSi phase (impurity) at lower Cr concentration and starts to decrease that amount by increasing Cr until x = 0.34, respectively. The variation of the $T_C$ values with the Cr content in these compounds occurs according to two types of exchange interactions existing between Fe-Fe in the Fe-rich rare earth intermetallic compounds as discussed in detail somewhere else [26].

Magnetic hysteresis is one characteristic of the first-order magnetic transition as discuss in the previous section. It can be seen that the M-B curves exhibit almost no magnetic hysteresis for x = 0.34 which is found to be similar of the characteristic at x = 0 but did not change the first-order magnetic transition behaviour [26]. The phenomenon will provide the advantage of the sample with higher IEM transition and will contribute to enhance the value of magnetic entropy change [11, 23, 35].

### 4.3. Magnetocaloric effect

The values of $-\Delta S_M$ around $T_C$ have been derived from the magnetic data and are indicated in **Table 4** for $La_{0.7}Pr_{0.3}Fe_{11.4-x}Cr_xSi_{1.6}$ compounds. $-\Delta S_M$ was found to decrease from 17 J $kg^{-1}$ $K^{-1}$ at x = 0 to 12 J $kg^{-1}$ $K^{-1}$ at x = 0.06 and then increase to 14.2 J $kg^{-1}$ $K^{-1}$ at x = 0.12 until it reaches 17.5 J $kg^{-1}$ $K^{-1}$ at x = 0.34 which is larger than Gd (10.2 J $kg^{-1}$ $K^{-1}$). The relative cooling power (RCP) is defined by Eq. (3). It can clearly list at **Table 4** that the RCP values increase from 365 J $kg^{-1}$ at x = 0.06 to 420 J $kg^{-1}$ at x = 0.34 under 0–5 T field applied. The RCP value at x = 0.34 is slightly higher than the parent compound as indicated by the promising material of the $La_{0.7}Pr_{0.3}Fe_{11.06}Cr_{0.34}Si_{1.6}$ compound.

## 5. Conclusion

A systematic investigation of the structural and magnetic characterization of $La_{0.7}Pr_{0.3}Fe_{11.4}Si_{1.6}$ for HTA and LTA samples has been carried out. The results show that the HTA offers more advantages in solving the problem of non-equilibrium solidification behaviour due to the incomplete peritectic reaction $\gamma$-Fe + L → La(Fe,Si)$_{13}$($\tau_{1a}$) that occurs in the LTA process. The HTA sample shows promising values of $-\Delta S_M$ with very small hysteresis loss. This indicates that the elevated temperature in HTA plays an important role to form the $NaZn_{13}$-type structure in the $La_{0.7}Pr_{0.3}Fe_{11.4}Si_{1.6}$ compound.

Furthermore, the substitution of Cu for Fe in $La_{0.7}Pr_{0.3}Fe_{11.4-x}Cu_xSi_{1.6}$ leads to a decrease the magnetic entropy change but eliminates hysteresis loss. Increasing the Cu concentration also changes the magnetic-phase transition type from first to second order which in effect reduces the characteristics of IEM transition. The Curie temperature, $T_C$, increases with increasing Cu concentration. This phenomenon is related with the increase in the lattice parameter and the modification of the composition. The compound with a small amount of Cu substitution shows a promising magnetic performance for magnetic refrigerator application, with no hysteresis loss and reasonable RCP.

In conclusion, substitution of Cr for Fe $La_{0.7}Pr_{0.3}Fe_{11.4-x}Cr_xSi_{1.6}$ compound leads to decreases in lattice parameter but variation behaviour on $T_C$. The variation of $T_C$ with increasing Cr

concentration can be understood in terms of sensitive changes of Fe1-Fe2 and Fe2-Fe2 distances. Analysis of the magnetisation data demonstrates that the order of magnetic phase transition around $T_C$ is consistent on the first-order type even when x = 0.34 for $La_{0.7}Pr_{0.3}Fe_{11.4-x}Cr_xSi_{1.6}$ compounds. Replacement of Fe by Cr leads to a reduction of the magnetic entropy change from x = 0 to x = 0.06; however, it starts to enhance again when one increases Cr concentration until x = 0.34.

## Acknowledgements

The authors thank the National Defense University of Malaysia for financial support of this research. M. F, Md Din acknowledges the Ministry of Higher Education Malaysia for an FRGS Grant (FRGS/1/2015/SG06/UPNM/03/3).

## Author details

Muhamad Faiz Md Din[1,2]*, Jianli Wang[2] and Mohd Taufiq Ishak[1]

*Address all correspondence to: mfmd999@uowmail.edu.au

1 Department of Electrical and Electronic Engineering, Faculty of Engineering, National Defence University of Malaysia, Kuala Lumpur, Malaysia

2 Institute for Superconducting and Electronic Materials, University of Wollongong, Wollongong, NSW, Australia

## References

[1] Warburg E. Annals of Physics (Leipzig). 1881;**13**:141-164

[2] Pecharsky VK, Gschneidner JKA. Giant Magnetocaloric effect in Gd_{5}(Si_{2}Ge_{2}). Physical Review Letters. 1997;**78**(23):4494-4497

[3] Din MFM et al. Magnetic properties and magnetocaloric effect of $NdMn_{2-x}$ $Ti_x$ $Si_2$ compounds. Journal of Physics D: Applied Physics. 2013;**46**(44):445002

[4] Din MFM et al. Magnetic phase transitions and entropy change in layered $NdMn_{1.7}Cr_{0.3}Si_2$. Applied Physics Letters. 2014;**104**(4):p. 042401

[5] Din MFM et al. Magnetic properties and magnetocaloric effect of NdMn2−xCuxSi2 compounds. Journal of Applied Physics. 2014;**115**(17):17A921

[6] Wada H, Tanabe Y. Giant magnetocaloric effect of $MnAs_{1-x}Sb_x$. Applied Physics Letters. 2001;**79**(20):3302-3304

[7] Gutfleisch O, Yan A, Muller KH. Large magnetocaloric effect in melt-spun LaFe13−xSix. Journal of Applied Physics. 2005;**97**(10):10M305-10M303

[8] Hu FX et al. Influence of negative lattice expansion and metamagnetic transition on magnetic entropy change in the compound LaFe11.4Si1.6. Applied Physics Letters. 2001;**78**(23):3675-3677

[9] Fujieda S, Fujita A, Fukamichi K. Large magnetocaloric effect in La(FexSi1−x)13 itinerant-electron metamagnetic compounds. Applied Physics Letters. 2002;**81**(7):1276-1278

[10] Hu FX et al. Great magnetic entropy change in La(Fe, M ) 13 ( M = Si, Al) with co doping. Chinese Physics. 2000;**9**(7):550

[11] Shen J et al. Magnetocaloric properties of the La0.7Pr0.3Fe13âˆ'xSix compounds. Journal of Magnetism and Magnetic Materials. 2009;**321**(15):2336-2339

[12] Zhang XX et al. Magnetic entropy change in Fe-based compound $LaFe_{10.6}Si_{2.4}$. Applied Physics Letters. 2000;**77**(19):3072-3074

[13] Fujita A, Fukamichi K. Giant volume magnetostriction due to the itinerant electron metamagnetic transition in $La(Fe\text{-}Si)_{13}$ compounds. Magnetics, IEEE Transactions on. 1999;**35**(5):1796-1798

[14] Balli M et al. Magnetic and magnetocaloric properties of La1âˆ'xErxFe11.44Si1.56 compounds. Journal of Magnetism and Magnetic Materials. 2007;**313**(1):43-46

[15] Jia L et al. Magnetic coupling between rare-earth and iron atoms in the La1−x Rx Fe11.5 Si1.5 (R=Ce, Pr, and Nd) intermetallics. Applied Physics Letters. 2008;**92**(18)

[16] Raghavan V. Fe-La-Si (iron-lanthanum-silicon). Journal of Phase Equilibria. 2001;**22**(2): 158-159

[17] Palstra TTM et al. Study of the critical behaviour of the magnetization and electrical resistivity in cubic La(Fe, Si)13 compounds. Journal of Magnetism and Magnetic Materials. 1983;**36**(3):290-296

[18] Fujita A, Fukamichi K. Control of large magnetocaloric effects in metamagnetic compounds by hydrogenation. Journal of Alloys and Compounds. 2005;**404-406**(0):554-558

[19] Fujita A, Fujieda S, Fukamichi K. Relative cooling power of $La(Fe_xSi_{1-x})13$ after controlling the curie temperature by hydrogenation and partial substitution of Ce. Journal of Magnetism and Magnetic Materials. 2007;**310**(2, Part 3):e1006-e1007

[20] KA. Gschneidner. Journal of Rare Earth Alloys (D. Van Nostrand Co., Inc., Princeton, N.J.). 1961:pp. 187-188

[21] Louzguine-Luzgin DV, Inoue A. Relation between time–temperature transformation and continuous heating transformation diagrams of metallic glassy alloys. Physica B: Condensed Matter. 2005;**358**(1-4):174-180

[22] Liu T et al. Structure and magnetic properties of shortly high temperature annealing $LaFe_{11.6}Si_{1.4}$ compound. Journal of Alloys and Compounds. 2009;**475**(1-2):672-675

[23] Chen X, Chen Y, Tang Y. High-temperature phase transition and magnetic property of $LaFe_{11.6}Si_{1.4}$ compound. Journal of Alloys and Compounds. 2011;**509**(34):8534-8541

[24] Shen J et al. Effect of R substitution on magnetic properties and magnetocaloric effects of $La_{1-x}R_xFe_{11.5}Si_{1.5}$ compounds with R = Ce, Pr and Nd. Chinese Physics B. 2009;**18**(5):2058

[25] Md Din MF et al. Effects of Cu substitution on structural and magnetic properties of $La_{0.7}Pr_{0.3}Fe_{11.4}Si_{1.6}$ compounds. Intermetallics. 2013;**36**(Supplement C):1-7

[26] Din MFM et al. Effects of Cr substitution on structural and magnetic properties in $La_{0.7}Pr_{0.3}Fe_{11.4}Si_{1.6}$ compound. Journal of Applied Physics. 2014;**115**(17) 17A942

[27] Liu Xu B, Altounian Z, Ryan DH. Structure and magnetic transition of $LaFe_{13-x}Si_x$ compounds. Journal of Physics: Condensed Matter. 2003;**15**(43):7385

[28] Shamba P et al. Reduction of hysteresis losses in the magnetic refrigerant $La_{0.8}Ce_{0.2}Fe_{11.4}Si_{1.6}$ by the addition of boron. Journal of Applied Physics. 2011;**109**(7):p. 07A940-07A943

[29] Shen J et al. Reduction of hysteresis loss and large magnetic entropy change in the $NaZn_{13}$-type LaPrFeSiC interstitial compounds. Applied Physics Letters. 2007;**91**(14): 142504-142503

[30] Morrish AH. The Physical Principles of Magnetism. New York: Wiley; 1965 Chapter 3

[31] Feng-xia H et al. Magnetic entropy change in $La(Fe_{0.98}Co_{0.02})$ 11.7 Al 1.3. Journal of Physics: Condensed Matter. 2000;**12**(46):L691

[32] Caron L et al. On the determination of the magnetic entropy change in materials with first-order transitions. Journal of Magnetism and Magnetic Materials. 2009;**321**(21):3559-3566

[33] Balli M et al. Effect of interstitial nitrogen on magnetism and entropy change of $LaFe_{11.7}Si_{1.3}$ compound. Journal of Magnetism and Magnetic Materials. 2009;**321**(2):123-125

[34] Fujita A, Yako H. Stability of metallic, magnetic and electronic states in NaZn13-type $La(Fe_xSi_{1-x})13$ magnetocaloric compounds. Scripta Materialia. 2012;**67**(6):578-583

[35] Md Din MF et al. Magnetic phase transitions and entropy change in layered $NdMn_{1.7}Cr_{0.3}Si_2$. Applied Physics Letters. 2014;**104**(4):042401

*Edited by Mahmood Aliofkhazraei*

Intermetallic compounds are usually brittle with high melting points. Their properties are often found among ceramic and metallic materials. In most cases, their hot corrosion resistance and simultaneously hardness are important. One of the main applications of intermetallic compounds is for superalloy turbine blades in which they show appropriate high-temperature-related properties. This book collects new developments about intermetallic compounds and their recent usages.

Published in London, UK


IntechOpen

ISBN 978-1-83881-298-0